NON-LINEAR COUPLING OF SCALES OF OCEAN VARIABILITY AND IMPLICATIONS FOR DOWNSCALING

by

Anna Katavouta

Submitted in partial fulfillment of the requirements
for the degree of Doctor of Philosophy

at

Dalhousie University
Halifax, Nova Scotia
October 2015

To the loving memory of my father

and to my mother who has supported me in all my endeavours.

TABLE OF CONTENTS

List of Tables . . . . . **vii**

List of Figures . . . . . **ix**

Abstract . . . . . **xviii**

List of Abbreviations and Symbols Used . . . . . **xix**

Acknowledgements . . . . . **xxvi**

Chapter 1 Introduction **1**

1.1 Ocean Downscaling 3

1.2 Objectives and Technical and Scientific Questions 7

1.3 Outline and Structure of Thesis 8

Chapter 2 Overview of Ocean Downscaling and Data Assimilation **10**

2.1 Definitions of Scales in the Atmosphere and Ocean 10

2.2 Empirical Evidence of Coupling Between Scales 12

2.3 Overview of Dynamical Downscaling 16

2.4 Theoretical Motivation for Proposed Downscaling Approach 18

2.4.1 Error Free Large Scales 18

2.4.2 Imperfect Large Scales 20

2.4.3 Relationship to Atmospheric Spectral Nudging 22

2.5 Downscaling and Assimilation of Local Observations 24

2.6 Summary 25

Chapter 3 Downscaling using an Idealized Quasi-Geostrophic Model . . . **26**

3.1 The Quasi-Geostrophic Model 26

3.2 Definition and Variation of Scales 32

3.3 Statistical Prediction of Small Scales from Large Scales 35

3.4 Prediction of Small Scales using Spectral Nudging and Data Assimilation 38
3.4.1 Runs Description 39
3.4.2 Results 41

3.5 Summary 47

Chapter 4 A One-Way Nested Model of the Northwest Atlantic and Adjacent Shelf Seas 48

4.1 The Global HYCOM/NCODA System 49
4.1.1 Description 49
4.1.2 Initial Assessment of the Global System 51

4.2 The NEMO Modelling Framework 58
4.2.1 Governing Equations 58
4.2.2 Boundary Conditions 59
4.2.3 Subgrid Scale Physics 60
4.2.4 Horizontal and Vertical Grid 62
4.2.5 Open Lateral Boundary Conditions 62

4.3 Configuration and Forcing of the Regional Model 63

4.4 Summary 67

Chapter 5 Evaluation of the One-Way Nested Regional Model 69

5.1 Tides 70
5.1.1 Tidal Elevation 70
5.1.2 Tidal Residual Circulation 72
5.1.3 Impact of Stratification on Tides 76
5.1.4 Impact of Stratification on M_2 77
5.1.5 Physical Interpretation of the Seasonal Changes in M_2 Tidal Speed 80
5.1.6 Impact of Stratification on K_1 91

5.2 Synoptic Variability 94
5.2.1 Sea Level and Storm Surges 94
5.2.2 Temperature and Salinity 97

5.3 Seasonal Cycle and Mean State 104
5.3.1 Sea Level 104
5.3.2 Temperature and Salinity 110

5.3.3 Currents 116

5.4 Summary 127

Chapter 6 Downscaling the Northwest Atlantic and Adjacent Shelf Seas . 128

6.1 Motivation for the New Downscaling Method 129
6.1.1 Spatial and Temporal Variability 129
6.1.2 Internal Variability 133
6.1.3 Lateral Open Boundaries 135

6.2 Spectral Nudging and its Implementation in GoMSS 136
6.2.1 Regional Model Primitive Equations with Spectral Nudging . . . 136
6.2.2 Length Scale Separation 137
6.2.3 Parameter Choices 138

6.3 Impact of Spectral Nudging on Prediction Skill 140
6.3.1 Deep Water and Shelf Break 140
6.3.2 Shelf 148

6.4 Effect of Spectral Nudging on Wavenumber Spectra of Sea Level, Current and Vorticity 160
6.4.1 Dynamical Background 161
6.4.2 Variance 163
6.4.3 Wavenumber Spectra 166

6.5 Summary 173

Chapter 7 Summary and Discussion 174

7.1 Summary 175

7.2 Answer to Questions posed in the Introduction 179

7.3 Future Work 181

Appendix A Optimal Ensemble Size 185

Appendix B Comparison of Tidal Currents and Observations 190

B.1 Model Evaluation using Moored Current Meter Observations 191

B.2 Model Evaluation using HF Radar Observations 192

Appendix C Regional Model Seasonal Cycle: Comparison with Climatology 195

Appendix D Autocovariance and Power Spectral Density 205

Appendix E Spectral Nudging Implemented only in the Deep Water 207

Bibliography 212

LIST OF TABLES

Table 3.1 Parameter values for the quasi-geostrophic model. 27

Table 3.2 Description of the model runs. 30

Table 3.3 The minimum wavelengths (in km) of the large scale, the number of observations, and radius of influence (in km) as a function of k^c. . . 34

Table 4.1 Main characteristics of the global system and regional model. . . . 51

Table 4.2 Parameter values for the NEMO model. 63

Table 5.1 Summary of the three runs used to evaluate the Tides in GoMSS. . . 70

Table 5.2 Ability of Run1 to predict tidal elevations at the 39 locations shown in Figure 4.11. 72

Table 5.3 Mean and standard deviation of the differences in tidal elevation amplitude (cm) and phase (degrees) between winter (superscript w) and summer (superscript s) according to Run2. 77

Table 5.4 Comparison of observed and predicted sea level anomalies at four tide gauge locations. 96

Table 5.5 Comparison of observed and predicted sea level anomalies. GoMSS was driven by CFSR atmospheric forcing. 97

Table 5.6 The normalized mean square error (NMSE) for the global system and GoMSS based on the observed temperature profiles for 2012 (Figure 5.19), binned over three depth ranges. 99

Table 5.7 The NMSE of the global system and GoMSS based on the observed salinity profiles (Figure 5.19). 99

Table 5.8 The normalized mean square error (NMSE) of the global system and GoMSS based on the temperature and salinity glider observations. 102

Table 5.9 The mean difference between temperature and salinity glider observations and the global system and GoMSS. 104

Table 5.10 Fit of the global system and GoMSS to observed mean flows in winter for three depth ranges. 126

Table 5.11 Fit of the global system and GoMSS to observed mean flows in summer. 126

Table 6.1 Main characteristics of GoMSS with spectral nudging (GoMSS$^+$). . 137

Table 6.2 Correlation between sea level from the global system, GoMSS and GoMSS$^+$ and the satellite observations in the deep water, the shelf break and the the shelf (areas separated by the horizontal lines in Figure 6.11). 145

Table 6.3 Normalized mean square error (NMSE) for GoMSS$^+$ based on comparison with the observed temperature and salinity profiles for 2012 (Figure 5.19), binned over three depth ranges. 153

Table 6.4 The normalized mean square error (NMSE), and the mean difference, between the temperature and salinity glider observations and GoMSS$^+$.154

Table 6.5 Fit of GoMSS$^+$ to observed mean flows in winter and summer for three depth ranges. The regression coefficient $\hat{\beta}_1$ is given in polar form (vector scale and rotation, in degrees). 158

Table E.1 Correlation between sea level from GoMSS$^+$ (with no-nudging on the shelf) and the satellite observations in the deep water, the shelf break and the the shelf (areas separated by the horizontal lines in Figure 6.11). 209

Table E.2 Normalized mean square error (NMSE) for GoMSS$^+$ with no-nudging on the shelf based on comparison with the observed temperature and salinity profiles for 2012 (Figure 5.19), binned over three depth ranges. 210

LIST OF FIGURES

Figure 1.1 Snapshots of sea surface height from the real time global system for 3 December 2009 in the Kuroshio region (left panel) and 4 December 2009 in the Gulf Stream region (right panel). 3

Figure 1.2 Observed hourly sea level (top panel), atmospheric pressure (middle), and their normalized integrated power spectral density (bottom panel) at Halifax for 2010. 5

Figure 2.1 The position of the altimeter track, and the standard deviation and the skewness of the sea level profiles through time as a function of position along the track. 12

Figure 2.2 Hovmöller diagrams of sea level variability, about the time mean, along the altimeter track. 14

Figure 2.3 Differences between the observed and the reconstructed sea level along the altimeter track shown in 2.1. 15

Figure 3.1 The model domain, grid spacing, and specific points and section referenced in the text. 29

Figure 3.2 Two typical snapshots of sea level from run EN (upper panels) and the mean and standard deviation of the run (lower panels). 30

Figure 3.3 Holvmöller diagram of sea level variability along the zonal section defined by $y = 1500$ km in Figure 3.1. 31

Figure 3.4 Time-averaged sea level (*McCalpin and Haidvogel*, 1996). 32

Figure 3.5 Snapshot of a typical sea level field about the long term mean (top left), and its decomposition into large and small scales (bottom left and right respectively) for $k^c = 2$. 35

Figure 3.6 Normalized small scale variance as a function of k^c for the 13 year long validation run (run VA, see Table 3.2). 36

Figure 3.7 Statistical prediction of the small scales from the large scales. . . . 38

Figure 3.8 Typical snapshots of sea level (day 600) from the truth (a), forecast (b), spectral nudging (c) and hybrid (d) runs. 42

Figure 3.9 Time variation of the mean square difference between the truth run and the forecast and assimilation runs. 44

Figure 3.10 Dependence of the small scale error on k^c. 45

Figure 4.1 The 1/12° grid of the global HYCOM/NCODA real-time nowcast/forecast system. 50

Figure 4.2 The mean, standard deviation and skewness of sea level observed by satellite altimeters (AVISO product, upper panels) and predicted by the global system (lower panels). 52

Figure 4.3 Locations of the six CTD profiles (C1 to C6, blue asterisks), the glider path (red line crossing the Scotian Shelf), and five tide gauges (A1 to A5, magenta asterisks) used to validate the global system. . 53

Figure 4.4 Temperature vertical profiles from CTD measurements (black), the global system (red), and GoMSS (blue). 54

Figure 4.5 Salinity vertical profiles from CTD measurements (black), the global system (red), and GoMSS (blue). 55

Figure 4.6 Temperature section observed by a glider (left panel) operating along the Halifax Line (red line in Figure 4.3), the global system (middle) along the same path, and their difference (right panel) during 11-31, July 2012. 56

Figure 4.7 Salinity section from the glider and the global system. 56

Figure 4.8 Daily (snapshots) sea level anomalies observed by coastal tide gauges (black) and predicted by the global system (red) at Halifax and Yarmouth for 2010. 57

Figure 4.9 The geographical coordinate system (λ, ϕ, z) and the curvilinear coordinate system ($\mathbf{i}$,$\mathbf{j}$,$\mathbf{k}$). 60

Figure 4.10 Arrangement of variables on the C-grid. 62

Figure 4.11 The GoMSS model domain (inset panel) along with major bathymetric features, place names and observation locations. 64

Figure 4.12 M_2 amplitude (top panels) and phase (bottom panels) from the global FES2004 model (left panels) and GoMSS (right panels). . . 66

Figure 4.13 Comparison of observed and predicted (FES2004) tides for 39 locations and the following frequencies: M_2, S_2, N_2, K_1 and O_1. . 68

Figure 5.1 Comparison of the amplitude and phase of five tidal constituents based on observations and predicted by Run1 for specific locations shown in Figure 4.11. 71

Figure 5.2 Speed of the tidal residual current predicted by Run1. 74

Figure 5.3 The tidal residual circulation in the vicinity of Georges Bank and Browns Bank calculated by Run1. 74

Figure 5.4 The tidal residual circulation in the vicinity of Cape Sable calculated by Run1. 75

Figure 5.5 The tidal residual circulation in the vicinity of Sable Island calculated by Run1. 76

Figure 5.6 M_2 surface tidal current ellipses predicted by Run2 for winter (blue) and summer (red). 79

Figure 5.7 Seasonal differences in the speed of the M_2 surface current, summer - winter. 80

Figure 5.8 Seasonal difference in M_2 tidal current speed (summer-winter) based on radial radar observations (top panel) and Run2 (bottom panel). 81

Figure 5.9 Seasonal variation of the vertical structure of the cross isobath M_2 tidal current on the northern slope of Georges Bank (location 67.75°W, 42.28°N). 82

Figure 5.10 Hourly snapshots of density, over a complete M_2 tidal cycle during 10 July 2010, along a vertical section north of Georges Bank. . . . 84

Figure 5.11 Variation of density at 20 m depth along a section running from the top of Georges Bank to the Gulf of Maine (section A-C, Figure 4.11). 85

Figure 5.12 Effect of smoothing the bathymetry on the variation of density at 20 m depth along a section running from the top of Georges Bank to the Gulf of Maine. 87

Figure 5.13 Effect of separating barotropic and baroclinic flow components on the striations. 88

Figure 5.14 Predictions of perturbation density and surface velocity by the *Laurent et al.* (2003) model. 90

Figure 5.15 K_1 surface tidal current ellipses predicted by Run2 for winter (blue) and summer (red). 92

Figure 5.16 Seasonal differences in the speed of the K_1 surface current, summer - winter. 93

Figure 5.17 Comparison of observed (black) and predicted (red) hourly sea level anomalies at Halifax and Yarmouth for 2010. 95

Figure 5.18 Comparison of observed (black) and predicted (red) hourly sea level anomalies at Portland and Boston for 2010. 96

Figure 5.19 Locations of all available CTD profiles for 2012. 98

Figure 5.20 Snapshots of sea surface temperature from GHRSST (left panels), the global system (middle panels) and GoMSS (right panels) near Sable Island (represented by white color) and the Gully. 100

Figure 5.21 Temperature section observed by a glider (left panel) operating along the Halifax Line (red line in Figure 4.3), GoMSS (middle) along the same path, and their difference (right panel) during 11-31, July 2012. 101

Figure 5.22 Salinity section from the glider and GoMSS. 102

Figure 5.23 Surface temperature from GoMSS (blue), the global system (red) and observed by a buoy (black) located near Halifax Harbour (blue point on the inset). 103

Figure 5.24 The mean, standard deviation and skewness of sea level based on satellite observations (AVISO, upper panels) and GoMSS (lower panels, tides removed). 105

Figure 5.25 Variation of monthly mean sea level at North Sydney, Halifax, and Yarmouth based on tide gauge observations (black), and predictions from GoMSS (blue) and the global system (red). 106

Figure 5.26 The altimeter track (black thick line). 107

Figure 5.27 Hovmoller diagram of sea level along the Halifax Line (Figure 5.26) based on the coastal altimeter dataset (top panel), and predictions by the global system (middle panel) and GoMSS (bottom panel). . 108

Figure 5.28 Hovmoller diagram of sea level along the Halifax Line (Figure 5.26) based on the coastal altimeter dataset (top panel), and predictions by the global system (middle panel) and GoMSS (bottom panel). . 109

Figure 5.29 Standard deviation of sea level from coastal altimetry (black), the global system (red) and GoMSS (blue) along the altimeter track shown in Figure 5.26. 110

Figure 5.30 Separation of GoMSS domain into 4 sub-domains used to examine the seasonal variation of temperature and salinity. 111

Figure 5.31 TS diagrams for winter for the climatology (left panels), GoMSS (middle panels) and the global system (right panels) for depths greater than 50 m. 113

Figure 5.32 TS diagrams for summer. 114

Figure 5.33 Seasonal mean currents based on current meters observations. . . . 117

Figure 5.34 The observed (red arrows) and the global system (every 3 grid points) winter mean currents averaged over the top 100 m. 120

Figure 5.35 The observed (red arrows) and the global system (every 3 grid points) summer mean currents averaged over the top 100 m. 121

Figure 5.36 The observed (red arrows) and GoMSS (every 8 grid points) winter mean currents averaged over the top 100 m. 122

Figure 5.37 The observed (red arrows) and GoMSS (every 8 grid points) summer mean currents averaged over the top 100 m. 123

Figure 5.38 Seasonal mean currents normal to a section crossing the Scotian Shelf (see inset). 124

Figure 5.39 Seasonal mean currents normal to a section radiating from Cape Sable at the western end of Nova Scotia. 124

Figure 6.1 Spatial autocorrelations for temperature for the global system (left panel) and GoMSS (right panel) for the 6 reference locations indicated by the black stars 130

Figure 6.2 Spatial autocorrelation for salinity for the global system (left panel) and GoMSS (right panel). 131

Figure 6.3 Temporal autocorrelation of temperature for the global system (red) and GoMSS (blue) for the five locations shown by red stars. 132

Figure 6.4 Temporal autocorrelation of salinity for the global system (red) and GoMSS (blue) for the five locations shown by red stars. 133

Figure 6.5 Correlation of colocated temperature (left panel) and salinity (right panel) from the global system and GoMSS. 134

Figure 6.6 Response of the 1st to 4th order low-pass Butterworth filters as a function of wavenumber normalized by the cutoff wavenumber. . . 138

Figure 6.7 Coastal attenuation of the nudges by the Butterworth filter. 139

Figure 6.8 Sea surface temperature snapshots for 29 July, 2010 from satellite observations, the global system, GoMSS and GoMSS$^+$ (top panels). 142

Figure 6.9 Correlation of colocated (left panel) temperature and (right panel) salinity from the global system and GoMSS$^+$. 143

Figure 6.10 The cumulative variance of sea surface temperature in the deep water as a function of wavelength ($\overline{\Phi(\lambda_n)}$), determined by the footprint of the moving average filter. 144

Figure 6.11 Hovmoller diagram of sea level along the Halifax Line (Figure 5.26) based on the coastal altimeter dataset (first panel), and predictions by the global system (second panel), GoMSS (third panel) and GoMSS$^+$ (fourth panel). 146

Figure 6.12 Standard deviation of sea level from coastal altimetry (black), the global system (red), GoMSS (green) and GoMSS$^+$ (blue) along the altimeter track shown in Figure 5.26. 147

Figure 6.13 The observed (red arrows) and GoMSS$^+$ (every 8 grid points) winter mean currents averaged over the top 100 m. 149

Figure 6.14 The observed (red arrows) and GoMSS$^+$ (every 8 grid points) summer mean currents averaged over the top 100 m. 150

Figure 6.15 Temperature vertical profiles from CTD measurements (black), and predictions by GoMSS (blue) and GoMSS$^+$ (red). 151

Figure 6.16 Salinity vertical profiles from CTD measurements (black), GoMSS (blue) and predictions by GoMSS$^+$ (red). 152

Figure 6.17 Temperature section observed by a glider (left panel) operating along the Halifax Line (red line in Figure 4.3), GoMSS$^+$ (middle) along the same path (and times), and their difference (right panel) during 11-31, July 2012. 154

Figure 6.18 Salinity section from the glider and GoMSS$^+$. 155

Figure 6.19 Hovmoller diagram of sea level along the Halifax Line (Figure 5.26) based on the coastal altimeter dataset (first panel), and predictions by the global system (second panel), GoMSS (third panel) and GoMSS$^+$ (fourth panel). 156

Figure 6.20 GoMSS$^+$ Seasonal mean currents normal to a section crossing the Scotian Shelf (see Figure 5.38) and to a section radiating from Cape Sable (see Figure 5.39). 157

Figure 6.21 Seasonal differences in the maximum speed of the M_2 surface current, summer - winter predicted by GoMSS$^+$. 159

Figure 6.22 Sea surface height variance (top panels), eddy kinetic energy (middle panels) and eddy enstrophy (bottom panels) for the global system, GoMSS and GoMSS$^+$ at the ocean surface. 165

Figure 6.23 The two lines (red and blue) along which the wavenumber spectra are estimated. 166

Figure 6.24 Sea level variance (top panels), turbulent kinetic energy (middle panels) and turbulent enstrophy (bottom panels) wavenumber spectra from the global system (red), GoMSS (green) and GoMSS$^+$ (blue) at the ocean surface along the line in deep water (blue line) shown in Figure 6.23. 169

Figure 6.25 Sea level variance (top panels), turbulent kinetic energy (middle panels) and turbulent enstrophy (bottom panels) wavenumber spectra from the global system (red), GoMSS (green) and GoMSS$^+$ (blue) at the ocean surface along the line on the shelf (red line) shown in Figure 6.23. 171

Figure 6.26 Hovmoller diagrams of vertical relative vorticity at the surface normalized by the planetary vorticity, along the deep ocean line (blue line) in Figure 6.23 based on the global system (left panel), GoMSS (middle panel) and GoMSS$^+$ (right panel). 172

Figure 7.1 Trajectories of particles released along the shelf break 200 m isobath (thick black line) based on GoMSS. 183

Figure A.1 Correlation function between the point represented by black dot and the rest of the grid points. 186

Figure A.2 Typical snapshots (day 200) of sea level difference between the truth and forecast (left top panel), the analysis using the small ensemble (right top panel), the medium ensemble (left bottom panel), and the large ensemble (right bottom panel). 188

Figure A.3 Time variation of the mean square difference between the truth run and the forecast and the analysis runs, for different ensemble sizes. 189

Figure B.1 Evaluation of the surface tidal currents predicted by Run2 and Run1. 192

Figure B.2 Evaluation of the M_2 surface tidal currents predicted by Run2 and Run1 using the total radar data as observations. 194

Figure C.1 The 4 sections for which the vertical profiles for temperature and salinity are presented. 198

Figure C.2 The seasonal mean surface temperature from the climatology (left panels), GoMSS (middle panels) and the global system (right panels), during winter (top panels) and during summer (bottom panels). 198

Figure C.3 Similar to Figure C.2 for salinity. 199

Figure C.4 The seasonal mean temperature from the climatology (left panels), GoMSS (middle panels) and the global system (right panels) at 100 m depth, during winter (top panels) and during summer (bottom panels). 199

Figure C.5 Similar to Figure C.4 for salinity 200

Figure C.6 The seasonal mean temperature profile along section S1, from the climatology (left panels), GoMSS (middle panels) and the global system (right panels), during winter (top panels) and during summer (bottom panels). 200

Figure C.7 The seasonal mean salinity profile along section S1, similar to Figure C.6. 201

Figure C.8 The seasonal mean temperature profile along section S2, similar to Figure C.6. 201

Figure C.9 The seasonal mean salinity profile along section S2, similar to Figure C.6. 202

Figure C.10 The seasonal mean temperature profile along section S3, similar to Figure C.6. 202

Figure C.11 The seasonal mean salinity profile along section S3, similar to Figure C.6. 203

Figure C.12 The seasonal mean temperature profile along section S4, similar to Figure C.6. 203

Figure C.13 The seasonal mean salinity profile along section S4, similar to Figure C.6. 204

Figure E.1 Horizontal attenuation of $\gamma \quad (\phi(x, y))$. 208

Figure E.2 Correlation of colocated temperature (left panel) and salinity (right panel) from the global system and GoMSS$^+$ with no-nudging on the shelf. 209

Figure E.3 Temperature vertical profiles from CTD measurements (black), and predictions by GoMSS (blue) and GoMSS$^+$ with no-nudging on the shelf (red). 210

Figure E.4 Salinity vertical profiles from CTD measurements (black), GoMSS (blue) and predictions by GoMSS$^+$ with no-nudging on the shelf (red). 211

ABSTRACT

The objectives of this study are to develop better methods for dynamically downscaling ocean conditions, and to improve understanding of the physical processes controlling variations on regional scales.

Motivated by the study of *Henshaw et al.* (2003), the predictability of small scale variability from the time history of the associated large scales is investigated. This leads to a practical method for assimilating large scale information in order to recover small scale variability. The method is similar to spectral nudging of limited area atmospheric models but it is modified for ocean applications.

The method is first applied to an idealized ocean model that captures the most relevant oceanographic non-linearity: baroclinic instability. Numerical experiments show that important features of the ocean circulation, including the position of a meandering mid-ocean jet and the associated eddies, can be recovered from the time history of a small number of large scale modes. A hybrid approach is then proposed for assimilating both the large scales and additional point observations from a limited number of locations that, alone, are too sparse to recover the small scales using traditional assimilation methods. It is shown that the assimilation of sparse observations improves significantly the accuracy of the recovered small scales after the correct large scales have been ingested by the model.

A high resolution model of the Gulf of Maine, Scotian Shelf and adjacent deep ocean is then developed based on the Nucleus for European Modelling of the Ocean to downscale fields from a well known global operational system, specifically the US Naval Oceanography system based on the HYbrid Coordinate Ocean Model. The regional model is validated, using observations and results from previous studies, and weaknesses associated with simple one-way nesting are identified. The new downscaling method is shown to overcome these weaknesses. The implications for more realistic downscaling of ocean conditions are discussed.

In the process of developing more accurate ocean downscaling methodologies, new regional oceanographic features of scientific interest and practical importance (e.g., seasonal variations of tidal current speed) are identified and explained.

LIST OF ABBREVIATIONS AND SYMBOLS USED

Abbreviation	Description
AVISO	Archiving, Validation and Interpretation of Satellite Oceanographic Data
CFSR	Climate Forecast System Reanalysis
CORE	Coordinated Ocean-ice Reference Experiment
CTD	Conductivity, Temperature, Depth
DBDB	Digital Bathymetric Data Base
DFO	Department of Fisheries and Ocean
EKE	Eddy Kinetic Energy
EnKF	Ensemble Kalman Filter
EnOI	Ensemble Optimal Interpolation
EZ	Eddy Enstrophy
FES2004	Finite Element Solution 2004
FC	Forecast
FNMOC	Fleet Numerical Meteorology and Oceanography Center
HF	High frequency
HYCOM	Hybrid Coordinate Ocean Model
GEM	Global Environmental Multiscale Model
GDEM	Generalized Digital Environmental Model
GHRSST	Group for High Resolution Sea Surface Temperature
GODAE	Global Ocean Data Assimilation Experiment
GoMSS	Gulf of Maine and Scotian Shelf regional model
LANL	Los Alamos National Laboratory
LEGOS	Laboratoire d'Etudes en Gophysique et Ocanographie Spatiales
MICOM	Miami Isopycnic Coordinate Ocean Model
MODAS	Modular Ocean Data Assimilation System
MVOI	Multivariate Optimal Interpolation

Abbreviation	Description
NAVGEM	Navy Global Environmental Model
NAVOCEANO	Naval Oceanographic Office
NCEP	National Centers for Environmental Prediction
NCODA	Navy Coupled Ocean Data Assimilation
NEMO	Nucleus for European Modelling of the Ocean
NERACOOS	Northeastern Regional Association of Coastal and Ocean Observing Systems
NMSE	Normalized Mean Square Error
NODC	National Oceanographic Data Center
NOAA	National Oceanic and Atmospheric Administration
NOGAPS	Navy Operational Global Prediction System
NRL	Naval Research Laboratory
QG	Quasi-Geostrophic
RDPS	Regional Deterministic Prediction System
SP	Spin Up
SSMI	Special Sensor Microwave Imager
SST	Sea Surface Temperature
TA	Training
TKE	turbulent kinetic energy
TR	Truth
TS	Temperature and Salinity
US	United States
VA	Validation

Symbol	Description	Units
Chapter 2		
E	Ensemble member	
f	Forcing	
H	Matrix relating the observations and the model state vectors	
I	Orthogonal matrix	
K	Kalman gain	

Symbol	Description	Units
N	Number of elements	
P	Covariance matrix of the estimate	
R	Covariance matrix of the observation error	
U	Spatial matrix	
y	Observations	
$\mathcal{L}$	Linear dynamical terms	
$\mathcal{N}$	Non-linear function	
$\mathcal{P}^L$	Projection operator for the large scales	
$\mathcal{P}^S$	Projection operator for the small scales	
γ	Nudging coefficient	
ν	Stochastic model error	
Σ	Covariance matrix	
σ	Standard deviation	
ψ	General oceanographic variable	
Chapter 3		
a	Fourier coefficient for sea level	m
A_h	Scale selective horizontal	
	friction coefficient	$\mathrm{m}^2\ \mathrm{s}^{-1}$
A_b	Biharmonic scale selective horizontal	
	friction coefficient	$\mathrm{m}^4\ \mathrm{s}^{-1}$
F	Forcing	
f_0	Coriolis parameter	s^{-1}
g'	Reduced gravitational acceleration	$\mathrm{m\ s}^{-2}$
H	Reference thickness of the upper layer	m
h	Interface anomaly	m
J	Jacobian	
K	Kalman gain	
k	Wavenumber	m^{-1}
L_x	Zonal extent of model	km
L_y	Meridional extent of model	km
N	Number of elements	

Symbol	Description	Units
n	Grid point	
r	Linear drag coefficient	s^{-1}
S	Sample covariance matrix	
y	Observation vector	
α_s	Asymmetry of the zonal wind stress	
β	Beta coefficient	$\mathrm{m}^{-1}\ \mathrm{s}^{-1}$
γ	Nudging coefficient	
Δ	Size of grid boxes	km
Δt	Time step	s
η	Sea level	m
ρ	Density	$\mathrm{kg\ m}^{-3}$
τ_0	Wind stress amplitude scale	Pa
ψ	General oceanographic variable	
Chapter 4		
A_h^T	Horizontal eddy diffusivity coefficient	$\mathrm{m}^2\ \mathrm{s}^{-1}$
$A_h^{\mathbf{u}}$	Bilaplacian horizontal eddy viscosity coefficient	$\mathrm{m}^4\ \mathrm{s}^{-1}$
A_v^T	Vertical eddy diffusivity coefficient	$\mathrm{m}^2\ \mathrm{s}^{-1}$
$A_v^{\mathbf{u}}$	Vertical eddy viscosity coefficient	$\mathrm{m}^2\ \mathrm{s}^{-1}$
c	Speed of external gravity waves	$\mathrm{m\ s}^{-1}$
C_D	Bottom drag coefficient	
$D^{\mathbf{u},T,S}$	Small scale physics parametrization	
$F^{\mathbf{u},T,S}$	Surface forcing	
f	Coriolis acceleration	s^{-1}
g	Gravitational acceleration	$\mathrm{m\ s}^{-2}$
H	Water depth	m
P	Pressure	Pa
S	Salinity	PSU
T	Temperature	°C
$\mathbf{u}$	Horizontal velocity	$\mathrm{m\ s}^{-1}$
$\mathbf{w}$	Vertical velocity	$\mathrm{m\ s}^{-1}$

Symbol	Description	Units
$\mathcal{R}$	Matrix associated with slope between surfaces	
Δt	Time step	s
η	Sea surface height	m
ρ	Density	kg m^{-3}
Chapter 5		
A	Tidal elevation amplitude	m
$A(x)$	Amplitude of total velocity	m s^{-1}
f	Coriolis acceleration	s^{-1}
h	Water depth	m
H	Water depth of idealized step model	m
k	Wavenumber	m^{-1}
N	Buoyancy frequency	s^{-1}
R^2	Measure of model fit	
S	Salinity	PSU
T	Temperature	°C
U_n	Amplitude of n mode velocity	m s^{-1}
$\mathbf{u}$	velocity	m s^{-1}
α	Wave slope	
β	Regression coefficient	
δ	Normalized height of step	
δv	Difference in maximum tidal velocity between winter and summer	m s^{-1}
ϵ	Error	
ζ	Relative vorticity	s^{-1}
ϕ	Tidal elevation (current) phase	degrees
σ	Standard deviation	
ω	Frequency	s^{-1}
Chapter 6		
k	Wavenumber	km^{-1}
K	Dimensionless constant	
R^2	Measure of model fit	

Symbol	Description	Units
S	Salinity	PSU
T	Temperature	°C
$\mathbf{u}$	Horizontal velocity	m s^{-1}
z	Depth	m
$\mathcal{E}(k)$	Energy spectrum	m^3 s^{-2}
$\mathcal{P}^L$	Projection operator for the large scales	
$\mathcal{S}(k)$	Sea Level variance spectrum	m^3
$\mathcal{Z}(k)$	Enstrophy spectrum	m s^{-2}
β	Regression coefficient	
γ	Nudging coefficient	
ϵ	Energy flux	m^2 s^{-3}
ζ	Relative vorticity	s^{-1}
η	Enstrophy flux	s^{-3}
λ	Wavelength	km
$\Phi(\lambda)$	Temperature cumulative variance	$°C^2$
Appendix A		
C	Gaspari and Cohn function	
N	Number of ensemble members	
z	Distance between grid points	m
R_o	Radius of influence	m
Appendix B		
γ^2	Scalar measure of tidal ellipses error	
$\mathbf{u}$	Tidal current	m s^{-1}
P	Tidal constituent period	s
Appendix D		
E	Expected value	
f	Frequency	s^{-1}
k	Wavenumber	m^{-1}
$R(\tau)$	Autocovariance for lag τ	
$r(\tau)$	Autocorrelation for lag τ	
$S(f)$	Power spectral density	

Symbol	Description	Units
X	Field value	
τ	Time lag	s
χ	Space lag	m
Appendix E		
$h(x, y)$	Regional model bathymetry	m
h_0	Bathymetry cutoff	m
z	Depth	m
γ	Nudging coefficient	

ACKNOWLEDGEMENTS

I would like to thank Dr. Keith R. Thompson for his support, help, inspiration, encouragement and unlimited patience during the last five years. It was a real honour to have him as my supervisor. I would also like to thank the members of my supervisor committee, Dr. Katja Fennel, Dr. Daniel Kelley, and Dr. Jinyu Sheng for their helpful comments and contributions. A special thank you to Dr. Youyu Lu, a member of my supervisor committee, this work would not have been possible without the expertise and time that he devoted helping me address various scientific and technical problems. It was a pleasure collaborating with him.

Many thanks to Dr. Keith Haines, my external examiner, for making the trip from United Kingdom for my defence. His constructive comments and suggestions have helped improve this thesis and strengthen my knowledge on various subjects.

I am particularly grateful to Dr. John Loder for his collaboration and support, and to Dr. David Greenberg for his many constructive and insightful comments.

Thank you to the staff and faculty of the Department of Oceanography, and to my fellow graduate students. Thank you to Dr. Christopher Taggart for all his support and encouragement. Thank you to Drs Li Zhai and Jean-Philippe Paquin, I really enjoyed interacting with you. Thank you to Franziska Broell, Jessica Carrière-Garwood, Dr. Fatemeh Chegini, Jean-Pierre Auclair and Dr. Simon Higginson, my academic brother, for their friendship.

Last, but not least, I would like to thank my family: my mother, Kleopatra Sarantakou, my grandmother, Erasmia Sarantakou, my stepfather, Alexandros Vogiatzakis and my boyfriend, Brendan Crozier, for all the love and psychological support that they have provided throughout my journey.

Finally, this work would not have been possible without the data and source code provided freely by Drs Emmanuel Devred, Neil Fisher, David Hebert, Richard Karsten, and by various organizations including: Aviso, the Department of Fisheries and Oceans Canada, NOAA, NERACOOS, HYCOM consortium and NEMO. Funding for this project was provided by the Ocean Tracking Network (OTN) Canada through a strategic network

Grant (NETGP 375118-08) from the Natural Science and Engineering Research Council of Canada (NSERC), and the Marine Environmental Observation Prediction and Response Network (MEOPAR), one of Canada's Network of Centers of Excellence.

CHAPTER 1

INTRODUCTION

Numerical ocean circulation models are now used widely to forecast ocean conditions with lead times of hours to days (e.g. *Burnett et al.*, 2002; *Smedstad et al.*, 2003). To make realistic projections of climate change under different anthropogenic scenarios, all climate system components (e.g., atmosphere, ocean and sea ice) and their interaction must be modelled explicitly. Thus, ocean models, as part of climate models, are also used to project ocean variability decades to centuries into the future (ocean climate, e.g., *Griffies et al.*, 2005). Ocean models are also used extensively to reconstruct past ocean conditions (i.e., hindcast), particularly for regions and periods for which few, if any, observations are available. Another important role for ocean models is in understanding the dynamics of undersampled environments like the ocean; models are used to test, and sometimes validate, hypotheses based on observations or theory (*Griffies*, 2006).

The idea of forecasting weather by solving a system of non-linear partial differential equation was first introduced by Vilhelm Bjerknes in the early 1900's. Based on this idea Lewis Fry Richardson envisioned a scheme for weather forecasting (*Richardson*, 1922), in which, to quote, "*A myriad computers are at work upon the weather of the part of the map where each sits, but each computer attends only to one equation or part of an equation. The work of each region is coordinated by an official of higher rank. Numerous little night signs display the instantaneous values so that neighbouring computers can read them.*". While Richardson set the foundation for numerical weather prediction, real-time numerical weather prediction only became feasible after the development of the first computers in 1948. Since the time of the first computational numerical weather predictions in the 1950's, tremendous advances in supercomputer power and atmospheric model capabilities have

been made, driven by the demand for better weather predictions and climate projections. However, the computational demands of simulating and resolving the dominant physical processes are a hundred times larger for the global ocean compared to the atmosphere due in large part to the smaller length scales of variability. (The internal Rossby radius of deformation is much smaller in the ocean.) Thus, the capabilities of ocean models, and their realism, have been heavily constrained by the available computational power (*Semtner*, 1995).

Over recent years, ocean modelling has reached " *adolescence*" (*Griffies*, 2006) and started to catch up with atmospheric modelling, due primarily to the large increase in the power of supercomputers. The present generation of ocean models is capable of eddy resolving simulations of the global ocean, allowing for interactions with other climate components (e.g., sea ice, atmosphere) and increased realism due to the assimilation of observations (see *Haines*, 2010, for applications and challenges related to ocean data assimilation). Two well known, new generation operational ocean systems with global domains and relatively high resolution are the US Naval Oceanography Office system based on HYbrid Coordinate Ocean Model (HYCOM, *Chassignet et al.*, 2009) and the MERCATOR system based on the Nucleus for European Modelling of the Ocean framework (NEMO, *Molines et al.*, 2014). An example of the realism of this new generation of ocean models is shown in Figure 1.1, where the position of the Gulf Stream and the Kuroshio predicted by the HYCOM global system is compared with observations.

Despite these advances in global ocean modelling, many regional practical problems (e.g., investigating the movement of marine animals) require even higher resolution (several km). However, the variability on regional scales is often controlled, to a practically significant degree, by processes operating on large scales (e.g., basin and possible global scales). To illustrate, the physical conditions observed on the Scotian Shelf bordering the Northwest Atlantic are controlled by the Labrador Current, the outflow from the Gulf of St Lawrence and the position of the Gulf Stream (*Smith et al.*, 1978; *Hannah et al.*, 2001). One way in which modellers are responding to this multi-scale challenge is by developing models with unstructured grids or nested structured grid models, with the highest resolutions reserved for the region of primary interest.

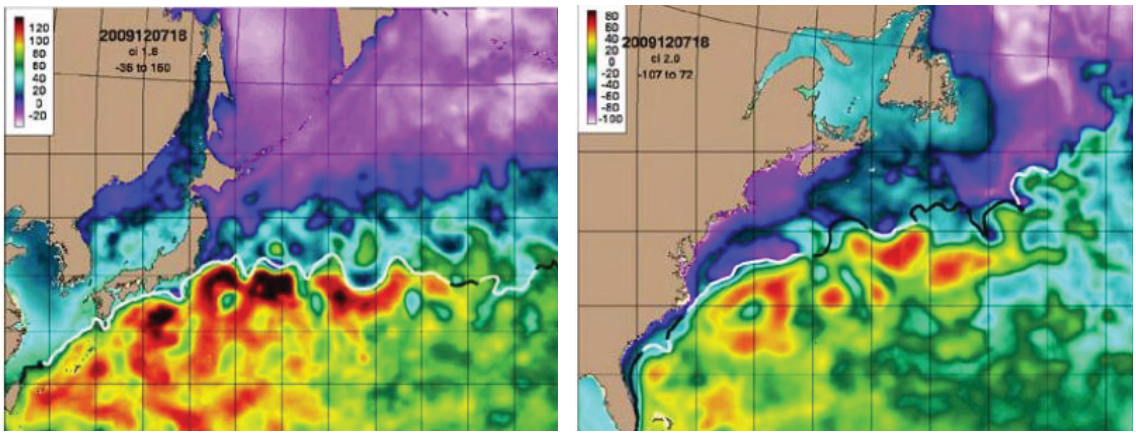

Figure 1.1: Snapshots of sea surface height from the real time global system for 3 December 2009 in the Kuroshio region (left panel) and 4 December 2009 in the Gulf Stream region (right panel). The black line shows an independent frontal analysis of sea surface temperature observations performed by the Naval Ocean. The figures are from *Chassignet et al.* (2009)

.

1.1 Ocean Downscaling

Downscaling refers to the process by which high resolution regional features are derived from coarser scale patterns. Downscaling is important for many ocean applications where high resolution is necessary in specific regions, e.g., interpreting the movement of marine animals, marine search and rescue, oil spill mitigation, and calculating the probability of extreme events (essential for the design of offshore structures).

Dynamical downscaling of the ocean conditions is commonly achieved by developing high resolution regional models that are driven by large scale fields (e.g., coarser resolution models) at their lateral open boundaries. Such an approach is sometimes called one-way nesting. Ideally, the regional model acts like a magnifying glass that reveals the fine detail associated with the large scale fields introduced at the lateral boundaries. In practice this is a challenging problem for the following reasons:

- Internal variability: Even if the large scales are known perfectly the regional models will be affected by internally generated variability. This internal variability may lead to decoupling of the regional model solution and the large scale fields used to drive it (*Giorgi and Bi*, 2000; *Caya and Biner*, 2004; *Rinke et al.*, 2004; *Alexandru et al.*, 2009; *Laprise et al.*, 2012).

- Error in the large scales: For most practical applications, the large scales will not be known perfectly. For example our knowledge of the large scale may come from a low resolution global model, or a reanalysis based on all available observations for a given period. For both estimates, the large scales will be imperfect, e.g., the low resolution global model may have a crude representation of non-linear processes such as baroclinic instability and may misrepresent the location and intensity of large scale current, and the reanalysis may be seriously affected by observations and interpolation errors.

- Boundary conditions specification: The treatment of the lateral boundary conditions of the regional models is known to be ill posed (no set of boundary conditions can assure a stable and unique solution) and several, *ad hoc* boundary condition treatments have been proposed (*Davies*, 1976; *Marchesiello et al.*, 2001; *Blayo and Debreu*, 2005) depending on the application.

It is well known that widely-varying spatial scales of oceanic motion can interact due to the non-linearity of the governing momentum equation. A remarkable study by *Henshaw et al.* (2003) showed that the small scale modes of variability of the solution to the unforced, three-dimensional Navier-Stokes equation and Burger's equation can be partially recovered from the time history of a few of the large scale modes. This suggests that the time-evolution of the large scales can be used to guide ocean reconstructions, predictions and projections over limited areas. Note however that *Henshaw et al.* (2003) identified situations that the small scales are not coupled with the large scales and so cannot be reconstructed.

The atmospheric community has considerable experience with downscaling and dealing with the problems listed above (e.g., *de Elia et al.*, 2002; *Denis et al.*, 2002; *Laprise*, 2003). Thus, the idea that the large scales may be used to guide the small scales reconstruction is not new in the atmospheric community and a method that nudges the large scales of high resolution models towards the prediction of known large scales, the atmospheric spectral nudging method, has been proposed and successfully applied in the past (*Waldron et al.*, 1996; *von Storch et al.*, 2000).

Even though spectral nudging has been shown to be effective for atmospheric models, it is not clear at first sight that it will work for ocean models. There are four main reasons:

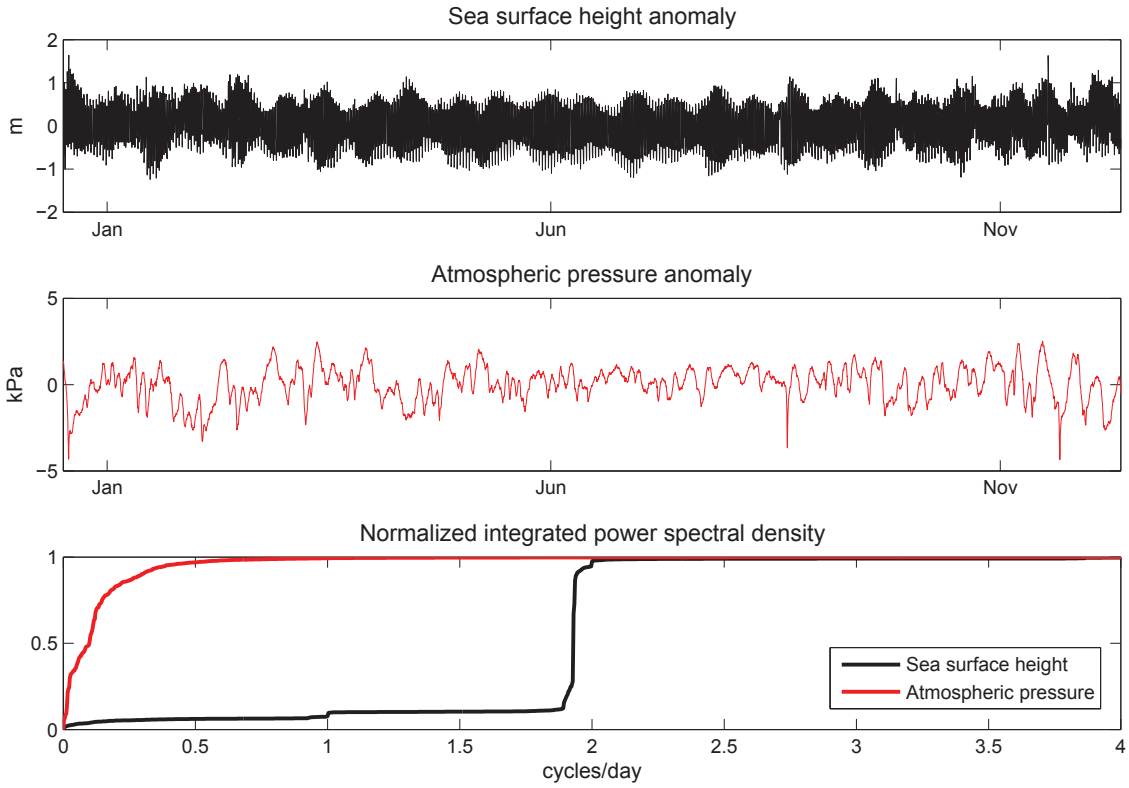

Figure 1.2: Observed hourly sea level (top panel), atmospheric pressure (middle), and their normalized integrated power spectral density (bottom panel) at Halifax for 2010. Both time series are plotted about their long term means.

i) the internal Rossby radius of deformation of mid-latitude oceans is typically 10 times smaller than in the atmosphere, leading to much smaller spatial scales of variability ; ii) coastal boundaries have a dominant impact on the ocean circulation and they couple spatial scales of variability; iii) there are relatively few observations of the ocean for assimilation compared to the atmosphere (leading to less accurate estimates of the large scale); iv) the ocean has a "longer memory" than the atmosphere but is also strongly affected by the tides which influence not only variability on daily time scales but also the mean through processes such as ocean mixing and tidal rectification.

To illustrate the multiple scales operating in the ocean, consider the variability of two equivalent variables for the ocean and the atmosphere: sea level and atmospheric pressure, both observed at the same representative mid-latitude coastal location. Figure 1.2 shows

observed hourly sea level and atmospheric pressure at Halifax for 2010, both referenced with respect to their long term means. The sea surface height signal is strongly affected by tides and also exhibits high frequency variability. The atmospheric pressure has lower frequency variability than the sea surface height (events that last several days), the result primarily of storms. To explore further the variability of these two variables, the normalized integrated power spectral density (equivalent to the normalized cumulative summation of the periodogram calculated through a Fourier transform) is also presented in Figure 1.2. Around 70% of the power for the atmospheric pressure is in the storm band (2-20 days) and there is almost no power for frequencies higher than 1 cycle/day (less than 1%) as expected. The power distribution of the sea level record has a very different character with large steps indicating a large amount of power is concentrated at specific frequencies. Specifically, around 90% of the power is due to the semi-diurnal tides and 4% is in the diurnal tidal band. Focusing on the low frequencies only (time scales exceeding 20 days) relatively more power is found at longer time scales for sea level (50% of the low frequency power is found below 100 days) compared to atmospheric pressure (less than 20% of the low frequency power is found below 100 days), confirming that the ocean has a "longer memory" than the atmosphere.

As it will become clear in the following chapters, the spatial scales of the atmosphere and ocean are also very different. For example, although tides are a very long length scale phenomenon in the deep ocean, their impact on the hydrography and circulation of continental shelf seas can be quite localized (e.g., tidal mixing and formation of residual currents).

Despite the differences between the atmosphere and the ocean there are reasons to believe that the ocean's large scales can be used to guide the reconstruction of the small scales because the different length scales of variability are coupled through the non-linearity of the governing equations, the surface forcing, and the reflection of Rossby waves by western boundaries (*Pedlosky*, 1987).

The above discussion provides the motivation to i) extend the analysis of *Henshaw et al.* (2003) to flow regimes that approximate those of the real ocean, ii) assess if atmospheric spectral nudging will work in the ocean, and iii) improve methods for downscaling ocean conditions.

1.2 Objectives and Technical and Scientific Questions

The overall objective of this thesis is to develop and evaluate methods for improving the dynamical downscaling of ocean conditions. The development is based in part on advances in atmospheric downscaling (*Waldron et al.*, 1996; *von Storch et al.*, 2000) but focuses on ocean applications. To achieve this objective a two track approach, based on an idealized and a realistic ocean model, is used. For the first track I use a quasi-geostrophic ocean model that captures the most relevant oceanographic non-linearity in order to test the predictability of small scales of ocean variability given the time history of the large scales. This is essentially an extension of the study of *Henshaw et al.* (2003) to flow regimes relevant to the ocean. For the second track, I develop a realistic high resolution model of the Gulf of Maine and Scotian Shelf region, validate it against observations and previous studies, identify the weaknesses associated with the simple one-way nesting method, and apply a new downscaling method to generate more accurate simulations.

To realize the overall objective I will address the following specific questions related to ocean downscaling:

- Is there evidence of coupling across length scales in the real ocean on which to base effective downscaling methods?
- Can the time history of the large scales be used to recover the small scale variability (as proposed by *Henshaw et al.*, 2003) of flow regimes that exist in the real ocean?
- Is spectral nudging of large scales a viable method for ocean downscaling? If so can it be supplemented by the assimilation of local observations to produce more accurate simulations of the small scales?
- Can the existing global ocean forecast systems, in particular the 1/12° HYCOM/NCODA global operational system, provide realistic large scales for the Northwest Atlantic?
- Can the global system's representation of the hydrography and circulation of the Northwest Atlantic be improved by high resolution and explicit representation of tides?
- Does one-way nesting lead to unrealistic features? How does it compare with the spectral nudging method?

Perhaps not surprisingly, in attempting to answer the above questions, new scientific questions emerge. The high resolution regional model of the Gulf of Maine and Scotian Shelf region, developed as part of the second track mentioned above, generates several features that are absent in the global system. For example, the prognostic simulation of variability over a wide range of time scales (tides to seasons) allows the investigation of the effect of the seasonal variation of ocean properties on the tides and vice-versa. Several interesting features arise from this dynamical interaction, some of which are identified and explained for the first time. More specifically I tackle the following scientific questions:

- How does the spectral nudging method modify the transfer of energy and enstrophy between large and small scales?
- How large are the seasonal changes in the tides and what is their spatial distribution?
- What are the physical mechanism responsible for large seasonal variations in tidal currents in the Gulf of Maine and on top of Georges Bank?

1.3 Outline and Structure of Thesis

In Chapter 2, the coupling between the different length scales is discussed. Observations and theoretical arguments based on *Henshaw et al.* (2003) are used to investigate the predictability of the small scale features from large scale patterns. A downscaling method is proposed and its association with atmospheric spectral nudging is discussed. A method that combines this downscaling method with local observations is also discussed.

In Chapter 3, the analysis of *Henshaw et al.* (2003) is extended to flow regimes closer to that of the real ocean. Specifically, an idealized but highly non-linear, wind forced mid-latitude ocean model is used to assess the extent to which the time history of the large scales can be used to recover unstable mid ocean jets and their associated eddies. Using the same model, I also investigate if the combination of spectral nudging with assimilation of local observations is viable for the ocean.

In Chapter 4, the realism of the 1/12° HYCOM/NCODA system in the Northwest Atlantic is investigated. The configuration of a new, high resolution regional model for the Gulf of Maine and Scotian Shelf region is described.

In Chapter 5, I investigate the improvements of the regional model over the global system and its weaknesses. Extensive comparisons with observations on different time scales (e.g., tidal, synoptic, seasonal) are conducted. I focus on the interaction between seasonal and tidal time scales, and several interesting features that arise from this interaction are identified and explained.

In Chapter 6 the internal variability of the regional model, and its divergence from the global system, are investigated. The new downscaling method is applied to constrain this decorrelation. The improvement in the downscaling ability of the regional model is then discussed.

A summary of the main conclusions of this thesis is presented in Chapter 7.

CHAPTER 2

OVERVIEW OF OCEAN DOWNSCALING AND DATA ASSIMILATION

In this chapter, the coupling between the different length scales of ocean variability is discussed. Specifically, the predictability of smaller scale features from large scale patterns in the real ocean is investigated using observations and theoretical arguments based on the study of *Henshaw et al.* (2003). The relevance of the coupling between the length scales to downscaling the ocean conditions is examined and a downscaling method is proposed. The proposed method is similar to a method that has been used extensively to downscale atmospheric conditions.

The definition of length scales in the atmosphere and ocean is presented in section 2.1. Evidence for the coupling between the different length scales in the ocean are described in section 2.2. In section 2.3, I provide a brief overview of the dynamical downscaling of the ocean. The theoretical background for the proposed dynamical downscaling method, and its association with a similar method used to downscale atmospheric conditions, is provided in section 2.4. An approach that combined the downscaling method and the assimilation of local observations is discussed in section 2.5. In section 2.6 I summarize the main points of this chapter.

2.1 Definitions of Scales in the Atmosphere and Ocean

Processes in the atmosphere and ocean create variability that occurs over a wide range of length and time scales. Typically, large scale phenomena "live" longer. The definition of scales is not rigid because different processes may generate overlapping scales of

variability. There are however three dominant scales of variability in the atmosphere (*Orlanski*, 1975): the synoptic scale, the mesoscale and the microscale. Synoptic scales in the atmosphere are on the order of 1000 km and last from days to weeks. Mesoscale atmospheric phenomena have length scales ranging from five to several hundred km and last from minutes to days. The atmospheric microscale corresponds to variability that typically lasts less than a few minutes and has length scales less than about 1 km.

The Rossby radius of deformation is a length scale of fundamental importance in both the ocean and atmosphere. It is the length scale at which the effect of the Earth's rotation becomes as important as the effect of buoyancy (e.g., *Gill*, 1982). In the atmosphere, the Rossby radius of deformation is on the order of 1000 km. For synoptic scale variability, the flow is approximately geostrophic (Coriolis term balances the pressure gradient) and hydrostatic. Mesoscale variability occurs on scales less than the Rossby radius and ageostrophic motion becomes important. In the vertical the hydrostatic approximation is however still generally valid because mesoscale processes have a small aspect ratio (vertical scale/horizontal scale). Microscale variability occurs on scales where the ageostrophic motion is dominant and the hydrostatic approximation is not valid.

The internal (mode 1) Rossby radius in the ocean typically ranges between 10 km to 300 km, and is therefore much smaller than its atmospheric counterpart. In addition, the time scales of variability in the ocean are much longer than in the atmosphere (e.g. ocean eddies can persist for months). In the ocean, mesoscale features have length scales on the order of the Rossby radius (the flow is approximately geostrophic) and have time scales between 10 to 100 days. Therefore, in the ocean, "mesoscale" is usually associated with a particular range of length scales, and the mesoscale features in the ocean are not dynamically equivalent with the mesoscale features in the atmosphere. Additionally, in the ocean, another scale range is often used: the submesoscale. As the name suggests, submesoscale features are smaller than the mesoscale but larger than microscale features (length scale of the order of some km and time scale of hours to a few days). In the submesoscale range, ageostrophic motion becomes important.

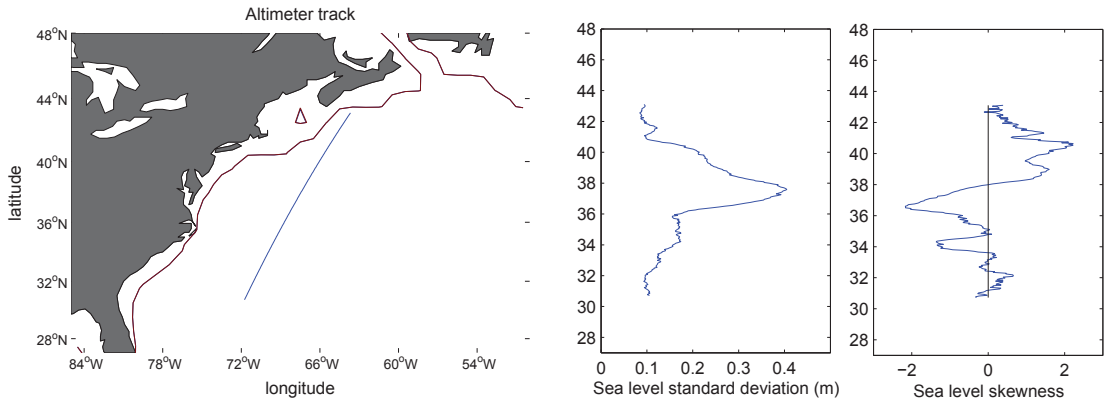

Figure 2.1: The position of the altimeter track, and the standard deviation and the skewness of the sea level profiles through time as a function of position along the track.

2.2 Empirical Evidence of Coupling Between Scales

Although it is possible to separate phenomena into categories based on their length scale, it is important to note that non-linearity may lead to a coupling amongst scales and thus the separation may be somewhat artificial. Perhaps the simplest example of scale interaction in the ocean is turbulence in which the mean circulation feeds energy towards eddies which, in turn, feed energy towards smaller eddies until energy reaches very small scales where viscosity is important and the motion is dissipated. In 1922, Lewis Fry Richardson wrote: "Big whirls have little whirls that feed on their velocity, and little whirls have lesser whirls and so on to viscosity."

Before discussing how non-linear dynamical processes can couple variability on different length scales, observational evidence of scale coupling in the ocean is presented in this section. Specifically horizontal profiles of sea level observed by a spaceborne altimeter along a fixed track are used to demonstrate that the larger scale features along the track can provide information about the smaller scale patterns.

The altimeter track chosen for this demonstration is shown in Figure 2.1. The track was obtained from AVISO and is based on observations by the Jason-2 satellite. This track was chosen because it crosses the Gulf Stream at a longitude where the instantaneous position of the Gulf Stream undergoes large latitudinal variations. Observations were obtained for the period 10/08/08 to 10/02/12 , with a time spacing of 10 days, leading to 128 profiles.

A Hovmöller diagram of the sea level about the long term mean along the track is shown on the top panel of Figure 2.2. The sea level varies greatly with time between 36°N and 40°N (top left panel of Figure 2.2, see also the standard deviation shown in the middle panel of Figure 2.1). A typical sea level profile is shown in the top right panel.

To explore the variability on different length scales, each sea level profile was low pass filtered to suppress variability on length scales shorter than 600 km. The middle left panel of Figure 2.2 is a Hovmöller diagram of the large scale variability. The small scale variability is defined as the difference between the observed and large scale variability. The following question is now asked: How much of the small scale variability can be explained by the large scale variability? To answer this question the following analysis was undertaken:

- The large and small scale fields were separated into training (days 1-96) and validation (days 97-128) datasets.
- The sea level fields were split into large and small scales using the Fourier transform. A length scale of 600 km was used to separate the length scales. The large scale fields from the training period were regressed on the contemporaneous small scale fields.
- The regression coefficients from the training period were used to predict the small scales from the large scales over the validation period

(More details about this approach, and the definition of large and small scales using Fourier transforms, is given in Chapter 3.)

For this particular track, the simple regression approach leads to a successful reconstruction of the small scales from the large scales over the validation period (days 97-128 of the bottom panel, Figure 2.2). Figure 2.3 shows that about 50% of the small scale variability between 36° and 38°N was successfully reconstructed. This implies that the position of the Gulf Stream, and its associated eddies and meanders, can be recovered, to some degree, from large scale information. Figure 2.3 also shows that predictability of the small scales from the large scales drops away from the region with the highest sea level variability (36° to 38°N). Analysis based on other tracks (not shown) reveals that the predictability

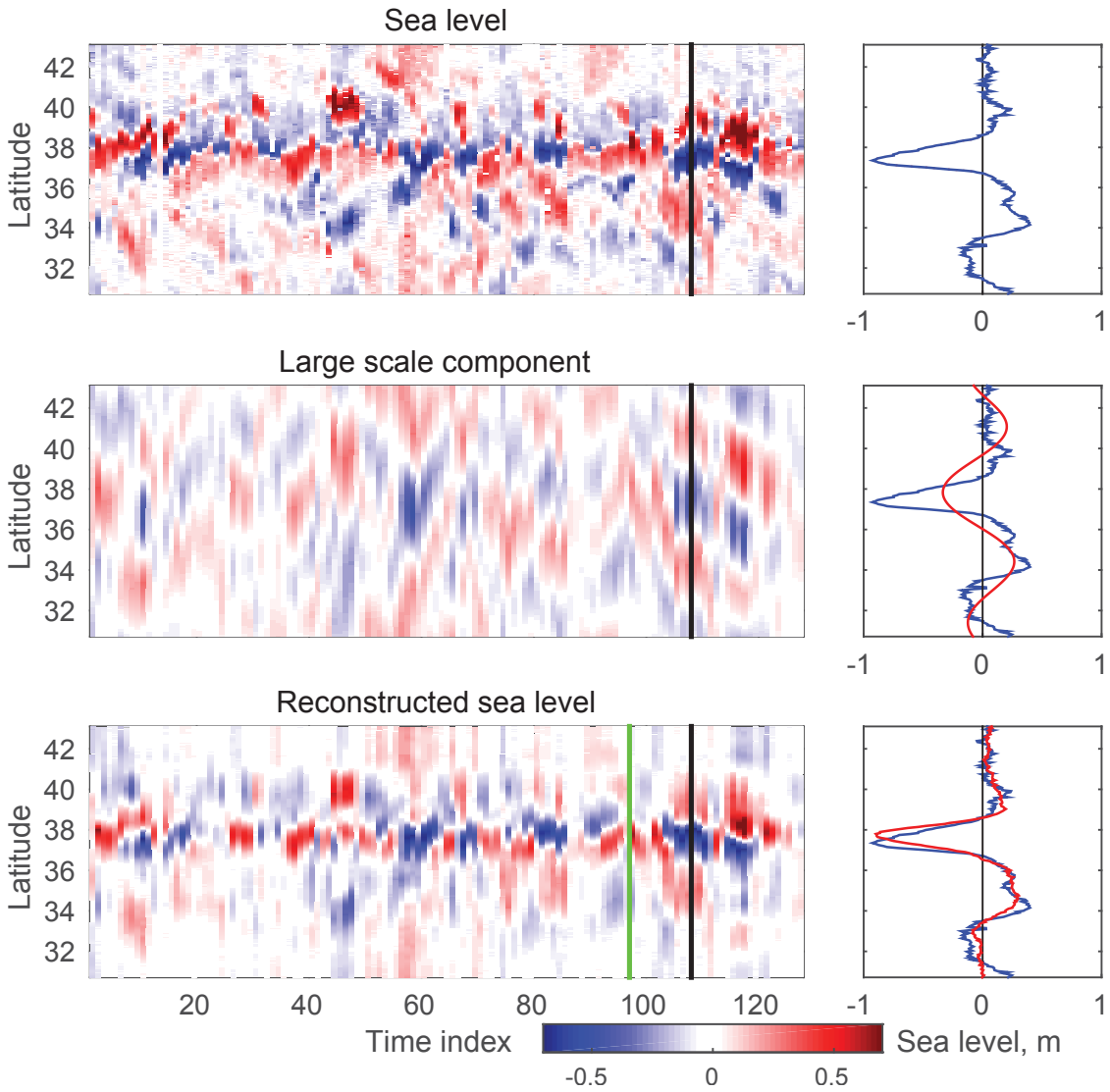

Figure 2.2: Hovmöller diagrams of sea level variability, about the time mean, along the altimeter track. The top Hovmöller diagram includes all length scales. The middle diagram shows the large scales, obtained by low pass filtering each profile to suppress variability with scales less than 600 km. The bottom diagram shows the reconstructed sea level for the training period (days 1-96, top panel-middle panel) and the validation period (days 97-128). The green line shows the boundary between training and validation periods. The blue line in the right panels show the sea level profile for day 108 (black line on the left panels). The red line in the second panel shows the observed large scales. The red line in third panel shows the reconstructed sea level.

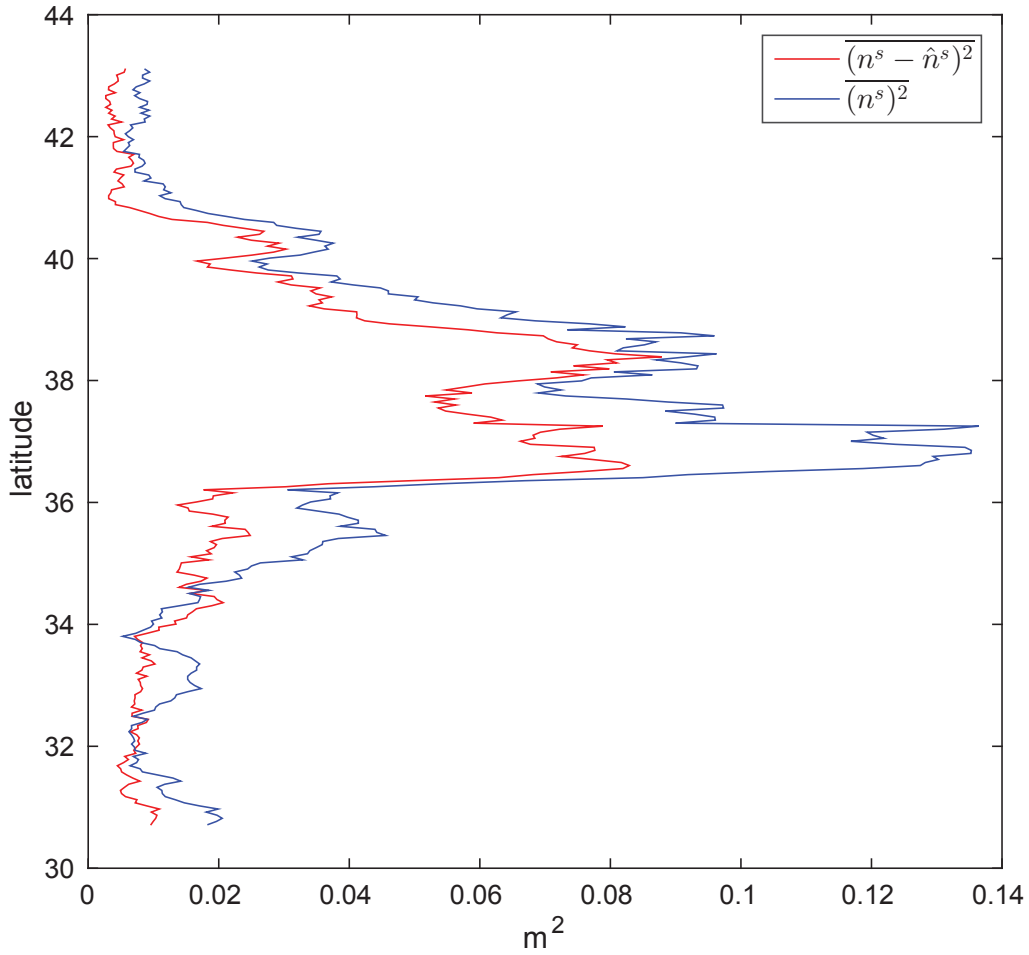

Figure 2.3: Differences between the observed and the reconstructed sea level along the altimeter track shown in 2.1. The blue line shows the averaged square sea level of the observed small scales for the validation period (days 97-128). The red line shows the averaged square sea level difference between the observed and the reconstructed small scales for the validation period (day 97-128).

of the small scales from the large scales was also lower for tracks to the east. Thus, in areas where the sea level does not experience any significant short term variation and the variability in the small scales is small, the small scale reconstruction is less accurate.

In summary, this empirical analysis shows that information on the large scale can be used to reconstruct the small scales of ocean variability in regions where non-linear effects are expected to be important. This is important because ocean observations are typically sparse and do not explicitly resolve small scale variability; the above analysis suggests it may be recoverable from the large scale. In the following sections, more detail is provided

on the coupling between scales and the mechanisms that cause it. The implications of this coupling for simulating and predicting small scale ocean variability is also discussed using techniques that take into account the time history of the large scale variability (not just the contemporaneous large scale, as in the simple regression-based approach described above).

2.3 Overview of Dynamical Downscaling

Downscaling refers to the process by which finer resolution features are derived from large scale patterns. In the atmosphere and the ocean, the large (synoptic) scale state is often reasonably well predicted because it is better observed, and more accurately simulated by general circulation models with relatively coarse spatial resolution. By way of contrast, features with scales of tens of kilometers in the atmosphere, and several kilometres in the ocean, are subject to much more uncertainty because they are not well resolved by existing observation networks, and are not included explicitly in the general circulation models.

Downscaling can be achieved by using statistical methods (statistical downscaling) or dynamically based models (dynamical downscaling). In statistical downscaling, an empirical relationship is derived between the large scale and observed small scale local features (e.g., regression analysis, analogue methods, neural networks). This relationship is then used to estimate the small scale patterns from the available observation network and/or the general circulation models. A summary and comparison of some statistical downscaling methods is given by *Wilby and Wigley* (1997). In this thesis I do not discuss statistical downscaling beyond two simple similar examples; one given in the previous section and one discussed in Chapter 3.

In dynamical downscaling, large scale fields (e.g., general circulation model fields, or a reanalysis of the available observations) are used to drive a higher resolution regional model which resolves explicitly the smaller scales. The most popular method for dynamical downscaling is based on nesting a high resolution regional model inside a coarser resolution model (e.g. *Deleersnijder and Lermusiaux*, 2008). Information may be exchanged between the coarser and the finer resolution model (two-way nesting, downscaling and upscaling) or transferred only from the coarser to the higher resolution model (one-way nesting,

downscaling). Two-way nesting can be computationally demanding making the one-way nesting appealing for applications that require long historical reconstructions and projections of the ocean conditions under climate change (e.g., *Sun et al.*, 2012; *Adlandsvik and Bentsen*, 2007). Furthermore, one-way nesting can often adequately represent a physical system, making two-way nesting excessively laborious and unnecessary (*Mason et al.*, 2010).

Typically, in one-way nesting forcing from the coarser model is applied at the lateral boundaries of the regional nested model. This corresponds to the classic view of the regional modelling problem as a boundary problem rather than a downscaling problem (*von Storch et al.*, 2000).

The atmospheric modelling community has considerable experience in using large scale models to specify open boundary conditions for nested high resolution models. In practice it has been found that this approach can be difficult to implement and many studies have focused on its accuracy (e.g., *de Elia et al.*, 2002; *Denis et al.*, 2002; *Laprise*, 2003; *Nutter et al.*, 2004). For example, it is well known that small differences in initial conditions can lead to very different regional simulations after several days of integration, even when the same lateral boundary conditions are imposed (e.g., *Giorgi and Bi*, 2000; *Caya and Biner*, 2004; *Rinke et al.*, 2004; *Alexandru et al.*, 2009; *Laprise et al.*, 2012), unless data assimilation is applied (which is often the case in the global models). Such internally generated variability can have different length scales making it difficult to constrain, particularly when it occurs on the scales of eddies. It has also been observed that the level of internal variability depends on the prevailing synoptic conditions, season, model domain, and simulation period (e.g., *Giorgi and Bi*, 2000; *Caya and Biner*, 2004; *Rinke et al.*, 2004). Whether the internally generated variability should be constrained, and to what degree, is debatable and depends on the application. It is reasonable, however, to expect the regional model to be related to the large scales imposed along its lateral boundaries. Other problems with one way nesting include unrealistic sensitivity to the location of the model's open boundaries and practical difficulties in open boundary specification (e.g., sponge layers, *Davies*, 1976) which may lead to ill-posed mathematical problems (*Staniforth*, 1997). Similar problems have been noted by the ocean modelling community (e.g., *Marchesiello et al.*, 2001; *Blayo and Debreu*, 2005).

To overcome the problems with one way nesting mentioned above, and to limit unrealistic internal variability, a different way of downscaling ocean conditions is discussed in the next two sections.

2.4 Theoretical Motivation for Proposed Downscaling Approach

In a recent study, *Henshaw et al.* (2003) showed that small scale modes of variability of the solution of the unforced Navier Stokes and Burger's equation can be recovered with surprising accuracy from the time history of several large scale modes. This result is of particular relevance to the thesis because it suggests that the time evolution of the large scales contains an important source of small scale information that can be used to guide atmosphere and ocean reconstruction, and prediction, over limited areas. To illustrate how knowledge of the large scales can be used to predict the small scales, a simplified discussion influenced by the study of *Henshaw et al.* (2003) is given below.

2.4.1 Error Free Large Scales

Consider the following non-linear equation that describes the evolution of the ocean variable $\psi(x,t)$:

$$\frac{\partial \psi}{\partial t} = \mathcal{N}(\psi) + \mathcal{L}(\psi) + f \tag{2.1}$$

where $\mathcal{N}(\psi)$ is a non-linear function of ψ, $\mathcal{L}(\psi)$ represents the additional linear dynamical terms, and f denotes the external forcing.

Assume the initial condition is

$$\psi(x,t_0) = \psi_0(x) \tag{2.2}$$

For simplicity I assume that the open boundary conditions are periodic. This excludes coupling of scales caused by reflection of Rossby waves at lateral boundaries.

Following *Henshaw et al.* (2003), the solution of (2.1) and (2.2) is projected onto large and small scales using two projection operators, $\mathcal{P}^L$ and $\mathcal{P}^S$ respectively:

$$\psi^L(x,t) = \mathcal{P}^L\psi(x,t) \tag{2.3}$$

$$\psi^S(x,t) = \mathcal{P}^S\psi(x,t) \tag{2.4}$$

where ψ^L and ψ^S correspond to the large scales and small scales of ψ respectively. The operators are defined such that

$$\psi^L + \psi^S = \psi$$

If the projection operators are based on Fourier transform, and $\mathcal{L}(\psi)$ is a linear combination of spatial derivatives of ψ, then $\mathcal{P}^L$ and $\mathcal{L}$ commute. Applying the two projection operators to (2.1) results in the following pair of coupled equations:

$$\frac{\partial \psi^L}{\partial t} = \mathcal{N}^L(\psi^L + \psi^S) + \mathcal{L}(\psi^L) + f^L \tag{2.5}$$

$$\frac{\partial \psi^S}{\partial t} = \mathcal{N}^S(\psi^L + \psi^S) + \mathcal{L}(\psi^S) + f^S \tag{2.6}$$

where $\mathcal{N}^L$ and $\mathcal{N}^S$ are the projections of $\mathcal{N}(\psi)$ on to the large and small scales, respectively. This pair of equations shows that, as expected, the evolution of the large and small scales are coupled through the non-linear term, $\mathcal{N}(\psi)$. *Henshaw et al.* (2003) showed that even if ψ_0^S is not known, the non-linear coupling may make it possible to recover the time history of the small scales with high accuracy from (2.6) if the time history of ψ^L is known. More specifically, *Henshaw et al.* (2003) attempted to reconstruct the small scale (ψ_r^S) by integrating

$$\frac{\partial \psi_r^S}{\partial t} = \mathcal{N}^S(\psi^L + \psi_r^S) + \mathcal{L}(\psi_r^S) + f^S \tag{2.7}$$

subject to the incorrect initial condition

$$\psi_r^S(x, t_0) = 0$$

Adding this reconstruction to the true large scale gives a reconstruction of the full solution ($\psi^L + \psi_r^S$) that *Henshaw et al.* (2003) call the "playback solution". These authors then examined the differences between the playback and true solution to check how effectively forcing by the large scale can correct for errors in the initial condition of the small scale.

The first example considered by *Henshaw et al.* (2003) was based on Burgers' equation in one dimension. (In the notation of (2.1), ψ corresponds to velocity, $\mathcal{N}(\psi) = -\psi\partial\psi/\partial x$, $\mathcal{L}(\psi) = \nu_B \partial^2\psi/\partial^2 x$ and $f = 0$.) In a set of numerical simulations they showed that the small scale features of the shocks generated by Burgers' equation could be recovered from the large scale defined by a surprisingly small number of Fourier components. Their

second example was based on the incompressible, unforced ($f = 0$) Navier Stokes equation defined in both two and three dimensions. It was again shown that many small scale features could be recovered from the large scale if the large scale contained a significant fraction of the enstrophy and energy in two and three dimensions respectively. Note however that, for both examples, *Henshaw et al.* (2003) identified situations where isolated, small scale features could not be recovered from the large scale.

2.4.2 Imperfect Large Scales

For most practical applications the large scales will not be known perfectly as assumed in the above example. For example, our knowledge of the large scales may come from a low resolution global model, or a reanalysis based on all available observations for a given period. Both estimates of the large scale will be imperfect e.g., the low resolution global model will usually have, at best, only a crude representation of the topography and the non-linear processes such as baroclinic instability, and the reanalysis may be seriously affected by observation and interpolation errors. This is the situation faced by atmospheric scientists who use high resolution regional models to downscale predictions from low resolution atmospheric global models (e.g., *Alexandru et al.*, 2009; *Laprise et al.*, 2012) or reanalysis products (e.g., *Waldron et al.*, 1996; *von Storch et al.*, 2000). Similar concerns over large scale errors apply to the downscaling of ocean conditions derived from low resolution ocean models, reanalysis products, or gridded observations from remote sensing (e.g., global maps of sea level observed by space-borne altimeters).

To recover the small scales using information on the imperfect large scales (e.g., from a reanalysis or a coarse resolution model) methods based on traditional data assimilation can be used. Data assimilation aims to provide an optimal estimate of the true ocean state by combining imperfect models and observations using Bayes Theorem (see *Wikle and Berliner*, 2007, for a historical overview). To illustrate how data assimilation can be used to predict small scale variability from the imperfect large scales, I spatially and temporally discretize (2.1) to give the following time stepping model:

$$\psi_t = \mathcal{D}_t(\psi_{t-1}) + \nu_t \tag{2.8}$$

where ψ_t is the model state vector at time t (with each element corresponding to a specific spatial grid point), $\mathcal{D}_t$ is an operator based on the non-linear and linear dynamics and the

forcing (represented by $\mathcal{N}$, $\mathcal{L}$ and f in (2.1) respectively), and ν_t is a stochastic model error. $\mathcal{D}_t(\psi_{t-1})$ is the one step ahead forecast of the ocean state.

The update equation for (2.8) based on a simple and widely used form of ocean data assimilation is given as:

$$\psi_t = \mathcal{D}_t(\psi_{t-1}) + K_t \left[y_t - H\mathcal{D}_t(\psi_{t-1}) \right] \tag{2.9}$$

where y_t denotes the observations at time t, H relates the observations to the model's state vector and K_t is a time dependent gain matrix. For linear systems Kalman filter theory provides the following updating equation for the gain matrix:

$$K_t = P_{t|t-1} H' (H P_{t|t-1} H' + R_t)^{-1} \tag{2.10}$$

where $P_{t|t-1}$ is the covariance of the error estimate of the background state at time t, given all the observations up to and including time $t-1$, prime notes the transpose of a matrix, and R_t is the covariance of the observation errors.

Instead of point observations, additional information on the true state with uncertainty that depends on length scale is assumed. Let U_L and U_S denote two matrices with columns that describe spatial patterns corresponding to the large and small scales respectively. Let us assume $U = [U_L \; U_S]$ is an othogonal matrix and so the patterns have been normalized and are mutually orthogonal. The square matrix $\mathcal{P}^L = U_L U_L'$ is a projection matrix that can be used to extract the large scales. For example, multiplying ψ_t by $\mathcal{P}^L$ could correspond to: i) Fourier transforming ψ_t, ii) setting coefficients associated with high wavenumbers to zero, and iii) inverse Fourier transforming to get the large scale filtered version of ψ_t.

Assume the additional information on the true state has an error covariance matrix of the form

$$R_t = \sigma_{RL}^2 U_L U_L' + \sigma_{RS}^2 U_S U_S'$$

The first (second) term on the right hand side of this equation defines the uncertainty in the large (small) scales.

Next assume the covariance of the state estimate is of the form:

$$P_{t|t-1} = U \begin{bmatrix} \Sigma_{LL} & \Sigma_{LS} \\ \Sigma_{SL} & \Sigma_{SS} \end{bmatrix} U'$$

where Σ_{LL} and Σ_{SS} control the variance of the large and small scale errors respectively, and Σ_{LS} is their covariance. For simplicity assume Σ_{LL} and Σ_{SS} are diagonal matrices of the form $\sigma_{PL}^2 I$ and $\sigma_{PS}^2 I$, respectively (similar to the form assumed for R_t).

Substituting these forms into (2.10), and using the fact that the additional information is on the large scales, leads to the following expression for the Kalman gain:

$$K_t = \left[\sigma_{PL}^2 + \sigma_{RL}^2\right]^{-1} \left[\sigma_{PL}^2 U_L U_L' + U_S \Sigma_{SL} U_L'\right]$$

This Kalman gain allows us to update both the large and small scales, given the additional information on the large scales. If the covariance between the large and small scales is ignored, the Kalman gain reduces to

$$K_t = \gamma \mathcal{P}^L$$

where

$$\gamma = \frac{\sigma_{PL}^2}{\sigma_{PL}^2 + \sigma_{RL}^2}$$

and γ determines the strength of the large scale nudging.

Using the nudging coefficient γ it follows that (2.9) becomes

$$\psi_t = \mathcal{D}_t(\psi_{t-1}) + \gamma \mathcal{P}^L \left[\tilde{\psi}_t - \mathcal{D}_t(\psi_{t-1})\right] \tag{2.11}$$

where $\mathcal{P}^L$ denotes the projection matrix for the large scales (similar to the large scale operator), and $\tilde{\psi}_t$ is the available information on the true large scales. In practice, if the large scales are known perfectly they will completely replace the large scales of the one-step ahead forecast ($\gamma = 1$); this is similar to the approach of *Henshaw et al.* (2003).

2.4.3 Relationship to Atmospheric Spectral Nudging

In the previous section, the update equation (2.11) for relaxing a model towards "known" large scales was derived from basic principles. This update equation corresponds to a

method that is commonly used to downscale the atmospheric conditions, the so called spectral nudging (*Waldron et al.*, 1996; *von Storch et al.*, 2000), because the nudge is applied only to the large scales. The idea is to nudge the large scales of the regional model to the predictions of a larger scale model (or a reanalysis product) while allowing the small scales to evolve freely. Spectral nudging has been used extensively to accurately downscale atmospheric conditions (e.g., *Waldron et al.*, 1996; *von Storch et al.*, 2000; *Miguez-Macho et al.*, 2004, 2005; *Rockel et al.*, 2008; *Alexandru et al.*, 2009; *Laprise et al.*, 2012). The concept of atmospheric spectral nudging is based on the fact that the small scale details are the result of an interplay between large scale atmospheric flow and small scale regional features such as topography (*von Storch et al.*, 2000).

An important parameter of spectral nudging is the nudging coefficient γ introduced in section 2.4.2. γ controls how strong is the nudging towards the "known" large scales. In general γ reflects the extent to which one believes the "known" large scales over the large scales forecast by the model. If the "known" large scales are not trusted then γ will be close to zero and the nudge will be negligible. On the other hand, if the "known" large scales are believed then γ will be close to unity and the update scheme will simply replace the large scales of the forecast (but not directly affect the small scales), as in the study of *Henshaw et al.* (2003). For downscaling applications the choice of γ is not necessarily based only on the system error statistics and in general it will depend on the specific downscaling application and its optimal value is a subject of ongoing research (e.g., *Omrani et al.*, 2012).

As an aside, *Thompson et al.* (2006) have also proposed a technique called spectral nudging. When their method was initially developed it was called frequency dependent nudging because the differences between the model state and seasonal climatology were bandpass filtered in the time domain before being used to nudge the models time-stepping equations. Later in the development of the technique it was decided to also apply a low wavenumber filter in space in order to allow small scale features in the model state to be unaffected by the nudging. Given that the nudges were now being filtered in both time and space (or equivalently, in the frequency and wavenumber domains) it was decided to replace "frequency dependent nudging" by the more generic term "spectral nudging". In this thesis any application of nudging in the frequency domain will be referred to as "frequency dependent nudging". This will remove any possible confusion with the spectral

nudging technique developed by the atmospheric downscaling community discussed above.

2.5 Downscaling and Assimilation of Local Observations

Suppose that, in addition to information on the large scale, local observations are available. These observations can be assimilated, following the spectral nudging update, to improve the estimate of the ocean state, particularly on the small scales. More specifically, at a time step t, the large scales are first updated using (2.11). The local observations can then be assimilated using a Kalman filter like approach:

$$\psi_t = \psi_t^* + K\left[y_t - H\psi_t^*\right] \tag{2.12}$$

where ψ_t^* is obtained by (2.11) and K is the Kalman gain matrix.

For problems with a large number of variables and non-linear dynamics (e.g., ocean and atmospheric models) an approximation of the Kalman filter is often used. The ensemble Kalman filter (EnKF, *Evensen*, 1997) approximates the covariance matrix of the background state using an "ensemble" of model predictions each advancing through time. The covariance matrix of the background state is approximated by

$$P_{t|t-1} = (N-1)^{-1}\left(E - \bar{E}\right)'\left(E - \bar{E}\right) \tag{2.13}$$

where each column of the matrix E is an ensemble member corresponding to a prediction of the true state at time t, $\bar{E}$ is the ensemble mean (based on averaging over each row of E), and N is the size of the ensemble.

A widely used simplification of the EnKF is provided by the ensemble optimal interpolation (EnOI, *Oke et al.*, 2007, 2008). The EnOI is computationally less demanding, easier to implement, and capable of generating realistic fields. As in the EnKF approach, the gain matrix used in EnOI is based on the statistics of the system. However, in EnOI the covariance matrix of background errors is assumed proportional to the covariance of an ensemble of snapshots of the model state taken from a long model run. Thus, EnOI provides a suboptimal solution in comparison with EnKF because it does not consider the time dependence of the error. However, it is obvious that the computational cost of EnOI is significantly less than EnKF because instead of N (the number of the ensembles

members) models advancing through time, only one long model run is required. Because of its computational efficiency, EnOI is appealing for use in operational ocean models, which are generally computational demanding.

In this study a method that combines both spectral nudging of the large scales and EnOI of point observations from limited locations is applied in an idealized ocean model (as described in Chapter 3).

2.6 Summary

Henshaw et al. (2003) showed, based on dynamical reasoning and idealized numerical experiments, it is possible to reconstruct some of the small scales of variability from the time history of the large scale using Burgers equation and the unforced, incompressible Navier-Stokes equations. Ocean altimeter observations were used to show that indeed there is predictability of small scales from the large scales in the vicinity of the Gulf Stream. This motivated us to propose a practical method for reconstructing, and predicting, ocean fields over limited areas by assimilating large scale information. The method has strong similarities to the spectral nudging approach used to downscale atmospheric conditions. The addition of assimilation of local observations, to further improve the definition of the small scale, was also proposed.

The study of *Henshaw et al.* (2003) was based on idealized experiments. Before applying the proposed downscaling method to a realistic ocean model it is first assessed using a quasi-geostrophic model of two wind driven gyres separated by an unstable mid-ocean jet.

CHAPTER 3

DOWNSCALING USING AN IDEALIZED QUASI-GEOSTROPHIC MODEL

The main goals of this chapter are to (i) extend the analysis of *Henshaw et al.* (2003) to flow regimes closer to those of the real ocean, and (ii) investigate if spectral nudging, supplemented by the assimilation of local observations, is a viable method for ocean downscaling. I am specifically interested in assessing the extent to which the time history of the large scales of a highly non-linear, wind forced mid-latitude ocean can be used to recover the position and intensity of an unstable mid-ocean jet and the associated eddies.

The quasi-geostrophic model is described in section 3.1 and its large and small scales of variability are defined, using Fourier transforms, in section 3.2. A statistical downscaling method is discussed in section 3.3 and the application of the dynamical downscaling method of the previous section is discussed in section 3.4. The results of the study are summarized in section 3.5.

3.1 The Quasi-Geostrophic Model

Quasi-geostrophic models (e.g., *Gill*, 1982) have been used for many years to study ocean eddies and their impact on the general ocean circulation (e.g., *Holland*, 1978). They have also been used extensively in dynamical studies of the separation of western boundary currents (e.g., *Dengo*, 1993; *Özgökmen et al.*, 1997) and the low and high frequency variability associated with unstable mid-ocean jets (e.g., *McCalpin and Haidvogel*, 1996). Realism, strong non-linearity and numerical efficiency are the main reasons a quasi-geostrophic model was chosen for the present study.

Table 3.1: Parameter values for the quasi-geostrophic model.

Parameter	Symbol	Value
Zonal extent of model	L_x	3600 km
Meridional extent of model	L_y	2800 km
Size of (square) grid boxes	Δ	20 km
Time step	Δt	2 hours
Coriolis parameter	f_0	10^{-4} s^{-1}
Beta coefficient	β	10^{-11} m^{-1} s^{-1}
Normalized density difference	$\Delta\rho/\rho_0$	0.002
Reduced gravitational acceleration	g'	0.02 m s^{-2}
Interfacial drag coefficient	r	10^{-7} s^{-1}
Scale selective horizontal friction coefficient	A_h	100 m^2 s^{-1}
Scale selective horizontal friction coefficient	A_b	8×10^{10} m^4 s^{-1}
Reference thickness of the upper layer	H	600 m
Wind stress amplitude scale	τ_0	0.1 Pa
Asymmetry of the zonal wind stress	α_s	0.05

The quasi-geostrophic model used in this study is based on the code developed initially by *McCalpin* (1987). The ocean is represented by two layers of constant density with the lower layer at rest (1.5 layer model). The ocean basin is defined on a beta-plane with closed meridional boundaries at $x = 0, L_x$ and closed zonal boundaries at $y = 0, L_y$. The model is forced by a steady zonal wind with a meridional distribution that drives two gyres separated by a mid-ocean jet.

Following McCalpin(1995), the interface anomaly (h) is assumed to evolve according to

$$(\nabla^2 - \gamma^2)\frac{\partial h}{\partial t} + \frac{g'}{f_0}J(h, \nabla^2 h) + \beta\frac{\partial h}{\partial x} = -r\nabla^2 h + A_h\nabla^4 h - A_b\nabla^6 h + F \qquad (3.1)$$

where $\gamma^2 = f_0^2/g'H$, $g' = g\Delta\rho/\rho_0$ is the reduced gravitational acceleration, β is the latitudinal gradient of the Coriolis parameter (df/dy), H is the reference thickness of the upper layer, J denotes a Jacobian, r is the interfacial drag coefficient, A_h and A_b are horizontal friction coefficients, and F is the forcing. The rest of the notation is standard. The parameter values used in this study are given in Table 3.1.

The horizontal friction coefficients determine the width of the Munk layers at the western boundary. In order to accurately resolve these western boundary layers the Munk layer width associated with the highest order friction term (the hyper-Munk scale) was chosen to exceed one grid interval. The other friction coefficients were chosen so that bottom friction

dominates lateral friction, leading to weak dependence of the solution on A_h and A_b. No normal flow and a partial slip condition, appropriate for the frictional parameterizations used in the model, were imposed at the lateral boundaries. Details of the numerical solution techniques are provided by *McCalpin* (1995).

The forcing in (3.1), due to the wind stress curl, is given by

$$F = -\frac{\pi f_0 \tau_0}{\rho_0 g' H L_y} \sin\left(2\pi \frac{y}{L_y}\right)\left[1 - 4\alpha_s\left(\frac{y}{L_y} - \frac{1}{2}\right)\right]$$

where the coefficient α_s controls the meridional asymmetry of the zonal wind stress (*McCalpin and Haidvogel*, 1996). This form of forcing generates an asymmetrical double gyre circulation with an unstable, meandering mid-ocean jet.

The model domain is shown in Figure 3.1 along with an indication of the grid spacing ($\Delta = 20$ km in both x and y). There are 180 and 140 grid boxes in the zonal and meridional directions respectively (with additional "ghost" boxes in each direction to handle the boundary conditions). The time step of the model is $\Delta t = 2$ hours and the output is saved every 5 days (snapshots).

The model was spun up from a state of rest for several decades. The model was integrated for a further 1000 days to generate a forecast of the ocean state from what will be considered to be an incorrect initial condition. (All of the runs are defined in Table 3.2.) The run continued for 18 years, to generate an ensemble of sea level fields for the estimation of the Kalman gain matrix, and a further 1000 days to generate the so-called "truth" run that used the correct initial condition. In total the run continued for 100 years to generate output for a statistical study of downscaling. A series of additional runs were then performed to see how effectively the assimilation of the large scale information and point observations could correct for an imperfect initial condition.

Two typical sea level fields are shown in the top panels of Figure 3.2. Sea level is linearly related to interface anomaly according to $\eta = -h\Delta\rho/\rho_0$ (i.e., 1.5 layer model). The spatial means of h and η are zero at each time step. A large scale double gyre circulation is evident in the sea level snapshots and the long term mean sea level (lower left panel). As expected, the sea level variability is highest in the vicinity of the mean jet (see standard deviation in the lower right panel), reflecting the effect of meanders and eddies on the time-varying

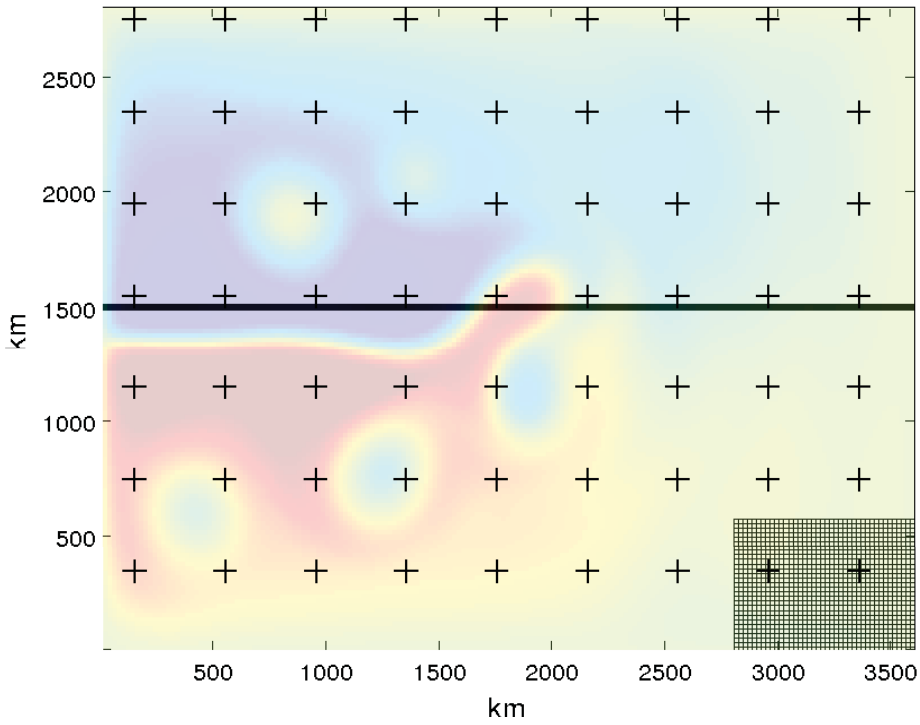

Figure 3.1: The model domain, grid spacing, and specific points and section referenced in the text. The size of the model domain is $L_x = 3600$ km by $L_y = 2800$ km. Part of the model grid is shown in the lower right corner of the domain to give an indication of the model's resolution. The background shading is a typical snapshot of sea surface height (same snapshot as Figure 3.8). The crosses are the fixed locations of the pseudo-observations ($n_{obs} = 63$) used in runs A2 and A3. Note the eddies are not resolved by the observing array. The horizontal line is the section that defines the Holvmöller diagram of Figure 3.3.

circulation.

Another view of the variability is shown by the Hovmöller diagram (Figure 3.3) for the zonal section defined by $y = 1500$ km (Figure 3.1). Rossby waves can be seen propagating westward at their expected, non-dispersive phase speed over the eastern third of the domain. The impact of Rossby wave reflection can be seen within about 400 km of the western boundary. The middle section (400 to 2300 km) exhibits a more complex structure caused by meandering of the unstable mid-ocean jet and its possible interaction with eddies.

The Hovmöller diagram, and sequences of snapshots for this and other runs, show that the circulation can undergo pronounced low frequency changes in both "mean" and variability.

Table 3.2: Description of the model runs. The wind forcing was the same for all runs.

Description	Run	Period	Initial Condition	Assimilation
Spinup	SP	several decades	Rest	No
Forecast	FC	1000 days	End of run SP	No
Ensemble	EN	18 years	End of run FC	No
Truth	TR	1000 days	End of run EN	No
Training	TA	87 years	End of run SP	No
Validation	VA	13 years	End of run TA	No
Spectral nudging	A1	1000 days	End of run SP	Large scales
EnOI	A2	1000 days	End of run SP	Point obs
Hybrid	A3	1000 days	End of run SP	Large scales and point obs

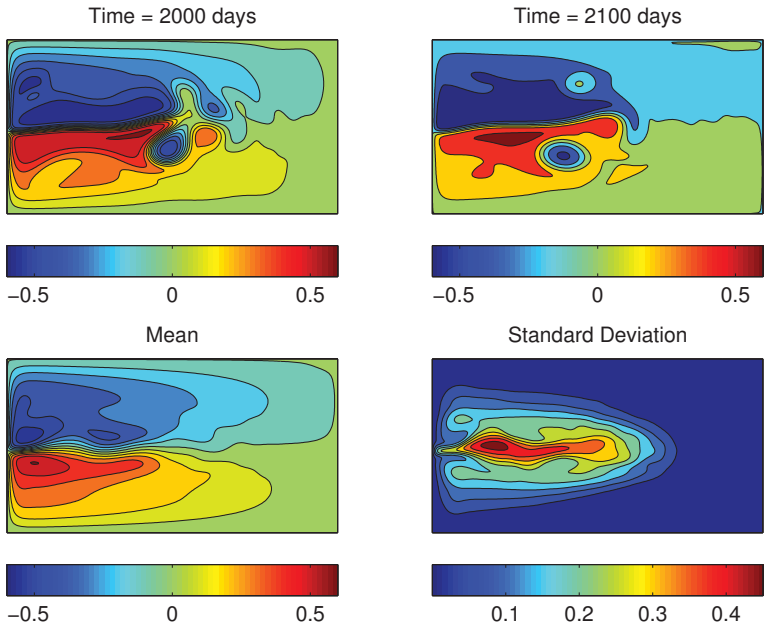

Figure 3.2: Two typical snapshots of sea level from run EN (upper panels) and the mean and standard deviation of the run (lower panels). The sea levels are in m.

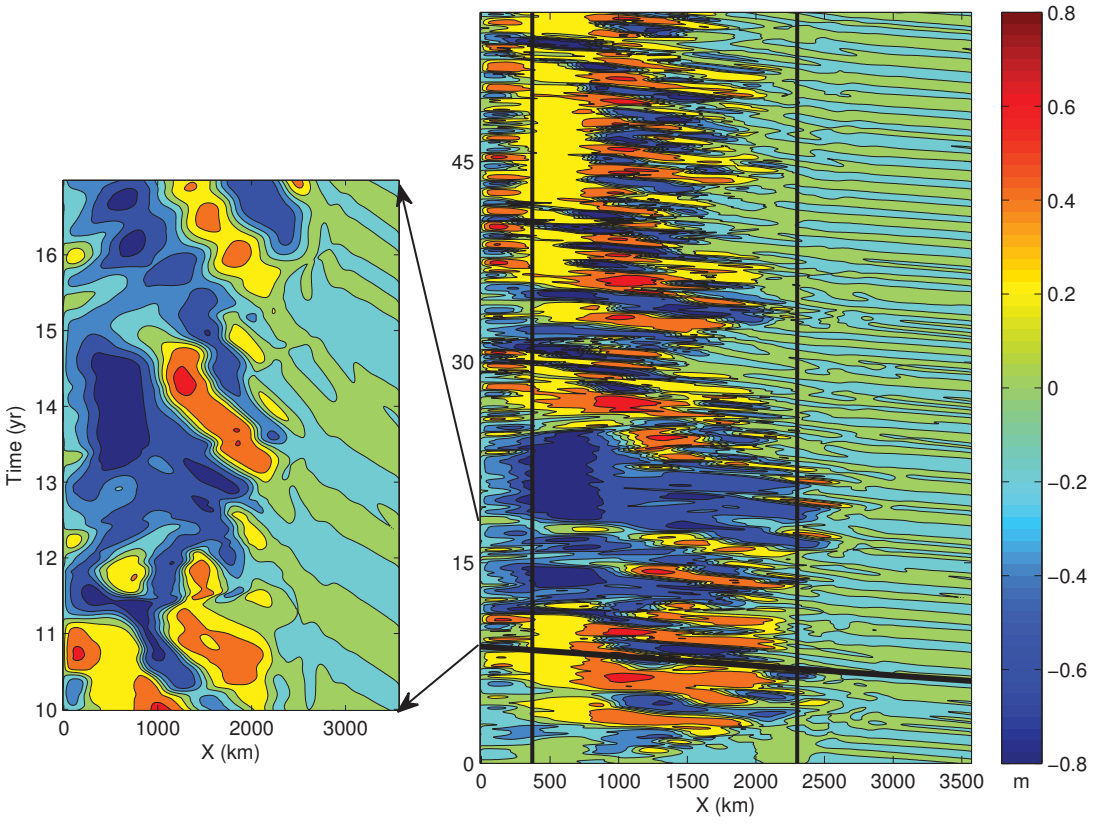

Figure 3.3: Holvmöller diagram of sea level variability along the zonal section defined by $y = 1500$ km in Figure 3.1. The left figure expands the time period 10 to 17 years. The black vertical lines separate the variability into 3 sections. The eastern section (2300 to 3600 km) is dominated by westward propagating baroclinic Rossby waves. The western section (0 to 400 km) is dominated by reflected Rossby waves. The middle section has a more complex behavior, covering a wider range of time and space scales. The black diagonal line shows the theoretical speed of a non-dispersive Rossby wave calculated using $c = -\beta a^2$, where a is the internal Rossby radius of deformation. Sea level is in m.

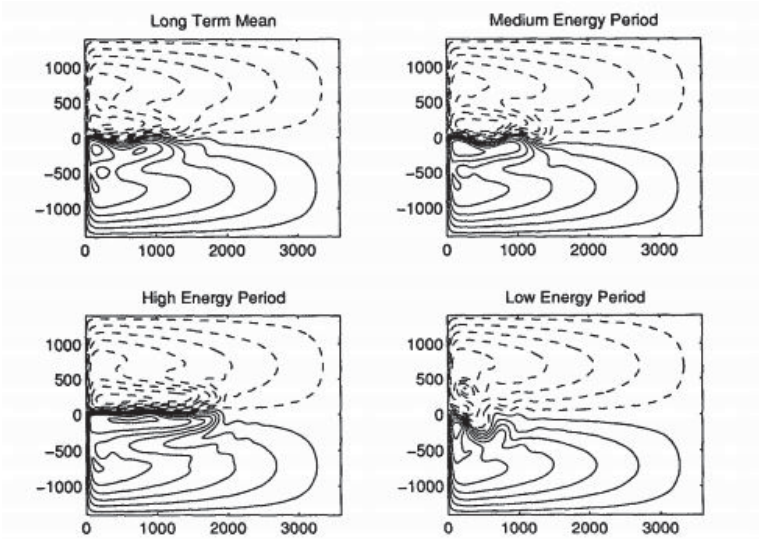

Figure 3.4: Time-averaged sea level (*McCalpin and Haidvogel*, 1996). Upper left is for 200 year record, Uper right is for the intermediate regime (158-168 years period). Lower left is for the weak eddy regime (23-29 years period). Lower right is for the strong eddy regime (70-74 years period). The axes are horizontal distances in km.

Visual examination of the snapshots led us to identify two extreme regimes in the model. In the "weak eddy" regime, the jet meanders are small, the eddies are weak, and the jet penetrates almost half way across the basin. The "strong eddy" regime involves significant meandering, strong eddies, and limited eastward penetration. *McCalpin and Haidvogel* (1996) identified this low frequency variability and associated the strong eddy regime with low total energy, and the weak eddy regime with high total energy. The transition between regimes was observed to be infrequent and irregular (*McCalpin and Haidvogel*, 1996). The time-average of the two extreme regimes, and an intermediate regime, are shown in Figure 3.4. These regimes proved useful in interpreting the assimilation results described later in section 3.4.

3.2 Definition and Variation of Scales

Following *Henshaw et al.* (2003), Fourier transforms are now used to define the large and small scales. Let η_{n_1,n_2} denote the gridded sea level field predicted by the ocean model for a given time and grid point (n_1, n_2) where $0 \leq n_1 \leq N_1 - 1$ and $0 \leq n_2 \leq N_2 - 1$. (For the quasi-geostrophic model, $N_1 = 180$ and $N_2 = 140$.) The Fourier coefficient for

wavenumber (k_1, k_2) is defined by

$$a_{k_1,k_2} = \frac{1}{N_1 N_2} \sum_{n_1=0}^{N_1-1} \sum_{n_2=0}^{N_2-1} e^{-i\phi} \eta_{n_1,n_2}$$

where $\phi = 2\pi(k_1 n_1/N_1 + k_2 n_2/N_2)$, $0 \leq k_1 \leq N_1 - 1$, and $0 \leq k_2 \leq N_2 - 1$.

The large scale component of the sea level field is defined by

$$\eta^L_{n_1,n_2} = \sum_{(k_1,k_2)\in K^L} e^{i\phi} a_{k_1,k_2}$$

where K^L is the set of "low" wavenumbers (k_1, k_2) defined by $N_1/2 - |N_1/2 - k_1| \leq k_1^c$ and $N_2/2 - |N_2/2 - k_2| \leq k_2^c$. To simplify the specification of the critical wavenumbers k_1^c and k_2^c, the single wavenumber k^c is introduced and set $k_1^c = k^c$ and $k_2^c = \max(0, k^c - 1)$. If $k^c = 0$, then only the constant term is included in K^L; in the present example this term is zero because the spatial sum of η is zero at each time step. If $k^c = 1$, only the fundamental in the zonal direction is used. As k^c increases beyond 1, additional zonal and meridional harmonics are used to reconstruct η^L. The reason more zonal than meridional components were used was to ensure roughly equivalent length scales in both directions for a given k^c (see Table 3.3). According to the above definition of K^L, the total number of Fourier components used to reconstruct η^L is $(2k^c + 1)(2k^c - 1)$ for $k^c > 0$.

The small scale component of the sea level field is defined by the wavenumbers not included in K^L and so

$$\eta^S = \eta - \eta^L$$

The decomposition of a typical sea level field into its large and small scale components is illustrated in Figure 3.5 for $k^c = 2$. The original sea level field (top left panel) features pronounced meanders in the midlatitude jet and several eddies. The small scale component (bottom right panel) is dominated by the eddies and jet meanders for this choice of k^c.

The variability of a single sea level field is quantified by

$$S(\eta) = (N_1 N_2)^{-1} \sum_{n_1,n_2} \eta^2_{n_1,n_2}$$

This corresponds to the variance of the sea level field because its spatial mean is zero.

Table 3.3: The minimum wavelengths (in km) of the large scale, the number of observations, and radius of influence (in km) as a function of k^c. The minimum wavelengths in the zonal and meridional directions are given by $L_x^{min} = L_x/2k^c$ and $L_y^{min} = L_y/2(k^c - 1)$ respectively. The number of observations is $n_{obs} = (2k^c + 1)(2k^c - 1)$. The number of observations and the radius of influence are used in assimilation runs A2 and A3.

k^c	L_x^{min}	L_y^{min}	n_{obs}	Radius of influence
1	1800		3	480
2	900	1400	15	480
3	600	700	35	480
4	450	467	63	320
5	360	350	99	320
6	300	280	143	160
7	257	233	195	120
8	225	200	255	80
9	200	175	323	80
10	180	156	399	40
11	164	140	483	40
12	150	127	575	40
13	138	117	675	40

Parseval's Theorem gives the following decomposition of this variance into contributions associated with the large and small scales:

$$S(\eta) = S(\eta^L) + S(\eta^S)$$

The top right panel of Figure 3.5 shows how the normalized variance attributable to the small scales, $S(\eta^S)/S(\eta)$, varies with k^c. As k^c increases the variance of the large scale increases at the expense of the small scale variance, e.g., almost all of the variance is captured by the large scales if the critical wavenumber k^c exceeds about 10 for this particular example.

The above definition of variance can be readily generalized in a straightforward way to cover a sequence of sea level fields, $\eta_1, \ldots \eta_m$, using

$$\overline{S}(\eta_{1,\ldots,m}) = \frac{1}{m} \sum_{t=1}^{m} S(\eta_t)$$

The dependence of $\overline{S}(\eta^S_{1,\ldots m})/\overline{S}(\eta_{1,\ldots m})$ on k^c for a 13 year long run of the model is shown in Figure 3.6. As expected, the result is qualitatively similar to the ratio for the single sea

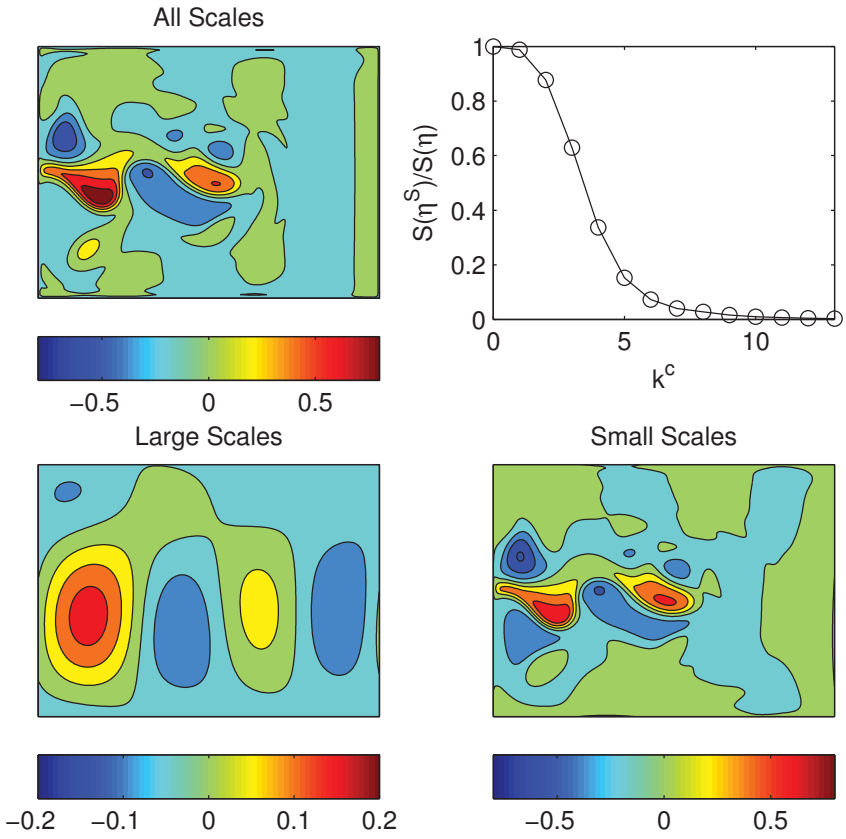

Figure 3.5: Snapshot of a typical sea level field about the long term mean (top left), and its decomposition into large and small scales (bottom left and right respectively) for $k^c = 2$. The top right panel shows $S(\eta^S)/S(\eta)$, the normalized small scale variance, as a function of k^c for the sea level field shown in the top left panel. The sea level field is from the validation run and all sea levels are in m.

level field shown in the top right panel of Figure 3.5.

3.3 Statistical Prediction of Small Scales from Large Scales

Before describing the assimilation runs, it is instructive to first estimate the proportion of small scale variance that can be predicted statistically from the large scale; the results will prove useful in choosing the k^c used in the assimilation experiments described in Section 3.4.

The following approach was used to quantify the proportion of small scale variance

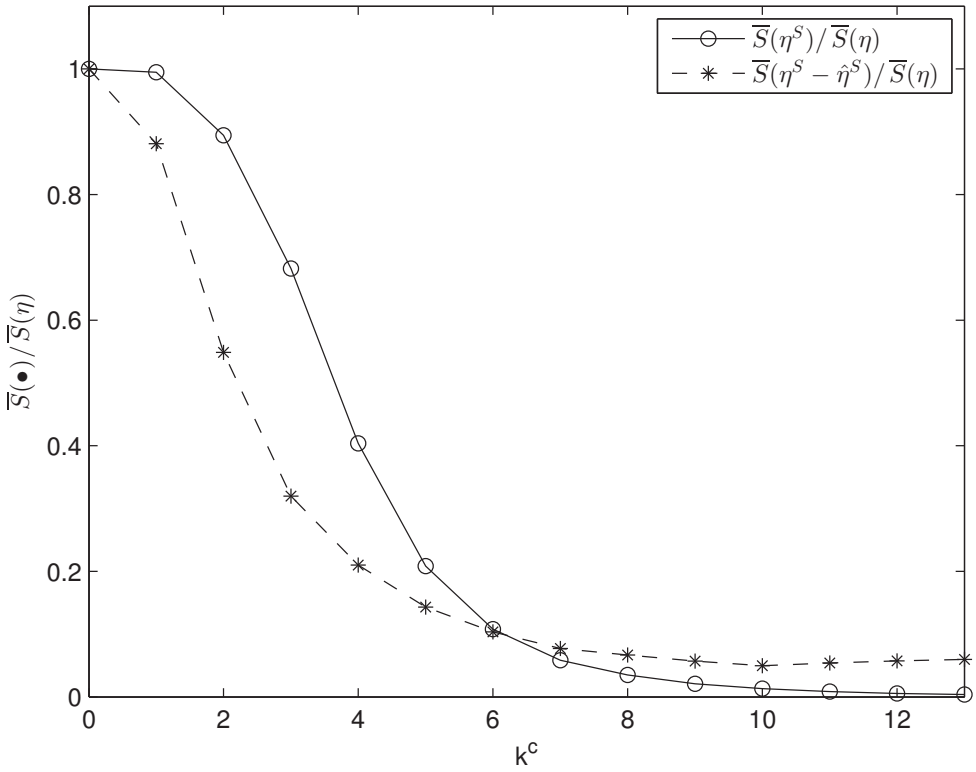

Figure 3.6: Normalized small scale variance as a function of k^c for the 13 year long validation run (run VA, see Table 3.2). The solid line shows $\overline{S}(\eta^S)/\overline{S}(\eta)$. The dashed line shows $\overline{S}(\eta^S - \hat{\eta}^S)/\overline{S}(\eta)$ where $\hat{\eta}^S$ is the prediction of η^S using a multivariate regression model with the large scale Fourier coefficients as inputs (see text for details).

of a sequence of sea level fields that can be linearly predicted by the large scales using a multivariate regression-based approach:

1. Calculate the Fourier coefficients for each of the sea level fields in the sequence.

2. Specify a wavenumber cutoff k^c that defines the large and small scales. Split the time-varying Fourier coefficients into a set of "predictors" (the large scale coefficients) and "responses" (the small scale coefficients).

3. Split the predictors and responses into two disjoint sets corresponding to "training" and "validation" periods.

4. Using only the Fourier coefficients from the training period, regress each response

on the same set of predictors and calculate a matrix of regression coefficients. This matrix converts the large scale information into small scales.

5. Predict the small scales for the validation period using the large scales from the validation period and the regression coefficients from step 4. Denote the estimated small scale field for time t by $\hat{\eta}_t^S$.

6. Calculate the (normalized) mean square error between the true and estimated small scales over the validation period, $\overline{S}(\eta^S_{1,\ldots,m} - \hat{\eta}^S_{1,\ldots,m})/\overline{S}(\eta_{1,\ldots,m})$. If there is coupling between scales this statistic is expected to be less than $\overline{S}(\eta^S_{1,\ldots,m})/\overline{S}(\eta_{1,\ldots,m})$.

Training and validation periods were used to guard against over fitting the regression model; this is a potentially serious problem as the number of predictors becomes large for high k^c. (A similar approach was used in Chapter 2.) In the results shown below, the lengths of the training and validation periods were 87 and 13 years respectively (runs TA and VA respectively, see Table 3.2). The results described below are not sensitive to reasonable choices of training and validation period.

An example showing the prediction of the small scales of a typical sea level field from the validation period is shown in Figure 3.7. Clearly for this particular field and choice of $k^c = 2$, the regression based approach gives a remarkably good reconstruction of the small scales (this is the case for different times). It is also encouraging to note that small scale variability is recovered over much of the region dominated by jet meanders and eddies. To quantify how well the above approach works over a sequence of fields, Figure 3.6 shows $\overline{S}(\eta^S_{1,\ldots,m} - \hat{\eta}^S_{1,\ldots,m})/\overline{S}(\eta_{1,\ldots,m})$ for the complete 13 year validation period. For k^c between 0 and 6 the large scales do indeed contain useful information on the small scales. For $k^c > 6$ the reconstructed small scales are not realistic due to overfitting (but note that not much small scale variance remains at such high values of k^c).

Note that using a training period that is based only on one regime (i.e., weak or strong eddy regimes) results in only a slightly less accurate reconstruction of the small scales for all k^c. Thus, even for low k^c, the large scales introduce more information than simply knowledge of the regime.

Although it is encouraging to find significant predictability of small scale variability for $k^c < 6$, large scales corresponding to wavelengths longer than 300 km (Table 3.3),

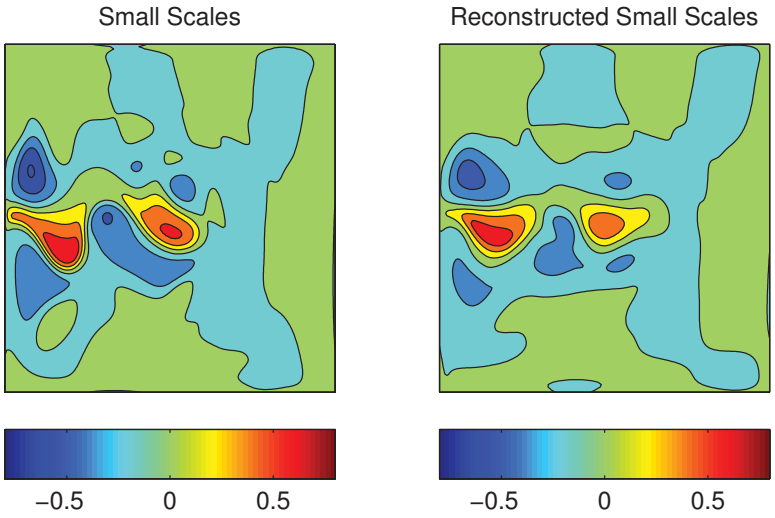

Figure 3.7: Statistical prediction of the small scales from the large scales. The left panel shows a typical small scale sea level field about the long term mean (same as the small scale shown in lower right panel of Figure 3.5, $k^c = 2$). The right panel shows the prediction by a multivariate regression model with the large scale Fourier coefficients as predictors (see text for details). The sea levels are in m.

the regression-based approach almost certainly underestimates the predictability of small scales because it does not take into account the time history of the large scale, and ignores the non-linear dynamics of the quasi-geostrophic model. Data assimilation is used in the next section to extract small scale variability, taking into account both of these missing factors.

3.4 Prediction of Small Scales using Spectral Nudging and Data Assimilation

A series of identical twin experiments is now undertaken to see how much information on the small scales can be recovered from the time history of the large scales. The approach is to first perform a 1000 day simulation of the quasi-geostrophic model to generate the "truth" (run TR, Table 3.2). The "truth" is then decomposed into large (true large scales) and small (true small scales) scale components using the definition described in section 3.2.

Arguably a coarser resolution model could be used to obtain the true large scales.

However, generating the true large scales by degrading the results from a high resolution model (that corresponds to perfectly known large scales) simplifies greatly the investigation and leads to more definitive results.

The true large scales are then assimilated into a run of the quasi-geostrophic model with an incorrect initial condition and it is checked how closely, and quickly, the true small scales are recovered. Based on the regression results described in Section 3.3, k^c is taken to be 4 although some sensitivity studies with varying k^c will be described. The impact of assimilating time series of the truth from a fixed array of n_{obs} locations is also discussed.

One run without assimilation (the forecast run), and three runs with assimilation, are performed. They all use the same erroneous initial condition, i.e., the end of run SP (Table 3.2). In assimilation run A1, only the large scales are assimilated using spectral nudging. In run A2, sea level from n_{obs} locations is assimilated using ensemble-based optimal interpolation (EnOI, see Chapter 2). In run A3, both large scale and point information are assimilated using a hybrid scheme that combines spectral nudging and EnOI (Chapter 2). Further details on the implementation of EnOI and the three assimilation runs are given below.

3.4.1 Runs Description

Run A1: Assimilation of large scales: Spectral nudging is used to nudge the large scales of the model with the wrong initial conditions toward the true large scales using (2.11). A nudging coefficient of $\gamma = 1$ was used. This corresponds to direct insertion, i.e., replacing the large scales of the forecast run by the contemporaneous large scales from the truth run. Using $\gamma = 1$ corresponds to the simplest case were the true large scales are known. In the present idealized setting this choice simplifies greatly the investigation and leads to more definitive results. The nudging was applied every 25 days.

Run A2: Assimilation of point observations Time series of sea level from n_{obs} fixed locations are assimilated using EnOI. This method was chosen because it is widely used, capable of generating realistic fields (e.g., *Evensen*, 2003; *Oke et al.*, 2007, 2008), is easy to implement, and is computationally efficient. As in the Kalman Filter theory the assimilation step is given by (2.9) with gain matrix, K, calculated from (2.10). To calculate K, we must specify H, R and $P_{t|t-1}$. In A2, I assume that the pseudo-observations contain information on both the large and the small scales and their assimilation influence all the

length scales so H is a non square matrix of zeros and ones specified by the locations of the observations. The observations are assumed error free and R is set to zero.

In EnOI, as in the ensemble Kalman Filter, the covariance matrix ($P_{t|t-1}$) is estimated based on an ensemble. For EnOI it is the statistical sample of the model state estimates. In EnKF, each ensemble member is generated individually at each assimilation time step by running the model with different initial conditions (or perturbed forcing fields) for each member (Monte Carlo method). However, in EnOI the $P_{t|t-1}$ is approximated as time-invariant (P) and calculated from a historical ensemble instead (see Chapter 2).

In the present study P was estimated from run EN (see Table 2 for details) using information from all wavenumbers and subsampling every 75 days. The result was an ensemble of size 88. To decide on the size of the ensemble several experiments were conducted with different ensemble sizes (Appendix A).

To avoid long range, unrealistic, spurious correlations the covariance matrix was "localized" by multiplying it, element by element, by a function of distance . This ensured that the covariance between all pairs of grid points fell to zero beyond a given "radius of influence". To represent the localization matrix the function proposed by *Gaspari and Cohn* (1999) was used (see Appendix A). The radius of influence varies depending on the number of the observations (Table 3.3). The assimilation update was made every 25 days, which is appropriate given the model's slowly evolving circulation and eddy field.

Runs A1 and A2 assimilate different information on the true state and so there is no point in comparing them directly. However, to facilitate comparison with run A3, the number of observing locations for run A2 was set equal to the number of large scale Fourier coefficients used in run A1 (i.e., $n_{obs} = (2k^c - 1)(2k^c + 1)$, see Table 3.3). The fixed observing array was laid out in a roughly equispaced grid that covered the model domain.

Run A3: Assimilation of large scales and point observations Spectral nudging is used to assimilate the large scales, and point observations are assimilated to add small scale detail, using the following two step scheme:

$$\begin{aligned} \psi_t^* &= \mathcal{D}_t(\psi_{t-1}) + \gamma \mathcal{P}^L \left[\tilde{\psi}_t - \mathcal{D}_t(\psi_{t-1}) \right] \\ \psi_t &= \psi_t^* + K^S \left(y_t - H\psi_t^* \right) \end{aligned}$$

where K^S is a Kalman gain matrix calculated from the small scale variability of the ensemble (see Chapter 2). This means that the point observations update only the small scales of the model state. As in run A1 $\gamma = 1$.

The number of point observations was set equal to the number of large scale Fourier components assimilated at each time step, i.e., $n_{obs} = (2k^c + 1)(2k^c - 1)$. This ensured that both sources of information would contribute roughly equally to the assimilation. The radius of influence of the point observations was assumed to decrease with increasing n_{obs} as for run A2.

Note that in this idealized setting, the hybrid is used only to address uncertainties in the initial conditions, although it has the capability to address uncertainties in the large scales.

3.4.2 Results

The effectiveness of the three assimilation runs is assessed by checking how closely, and quickly, the true small scales are recovered given that each run starts with a wrong initial condition. Typical snapshots of sea level for day 600 from the truth and forecast runs are shown in Figure 3.8. Although both fields are dominated by a well-defined, mid-basin jet, the small scales exhibit significant differences (e.g., the location of the jet's meanders, the position and intensity of the eddies either sides of the jet). The differences between truth and forecast are more evident in the lower panels of Figure 3.8 which show the small scale components.

The mean square difference of the true and forecast sea level fields through time is shown by the dotted line in the upper panel of Figure 3.9. Overall the mean square difference decreases slowly over the 1000 day integration period. The lower panel shows the mean square difference of the corresponding small scales is more stable through time; the downward trend in $S(\eta_{FC} - \eta_{TR})$ is therefore due to low frequency changes in the large scales of the forecast and truth runs. Note that if the plot is continued it would show periods when $S(\eta_{FC} - \eta_{TR})$ slowly increases. These low frequency changes are related with the regime shifts discussed in Section 3.2 and I will not interpret further the decline over the 1000 day integration period. It is important to note that the difference between run TR and run FC does not tend to zero; the impact of incorrect initial condition used for the forecast run is not forgotten.

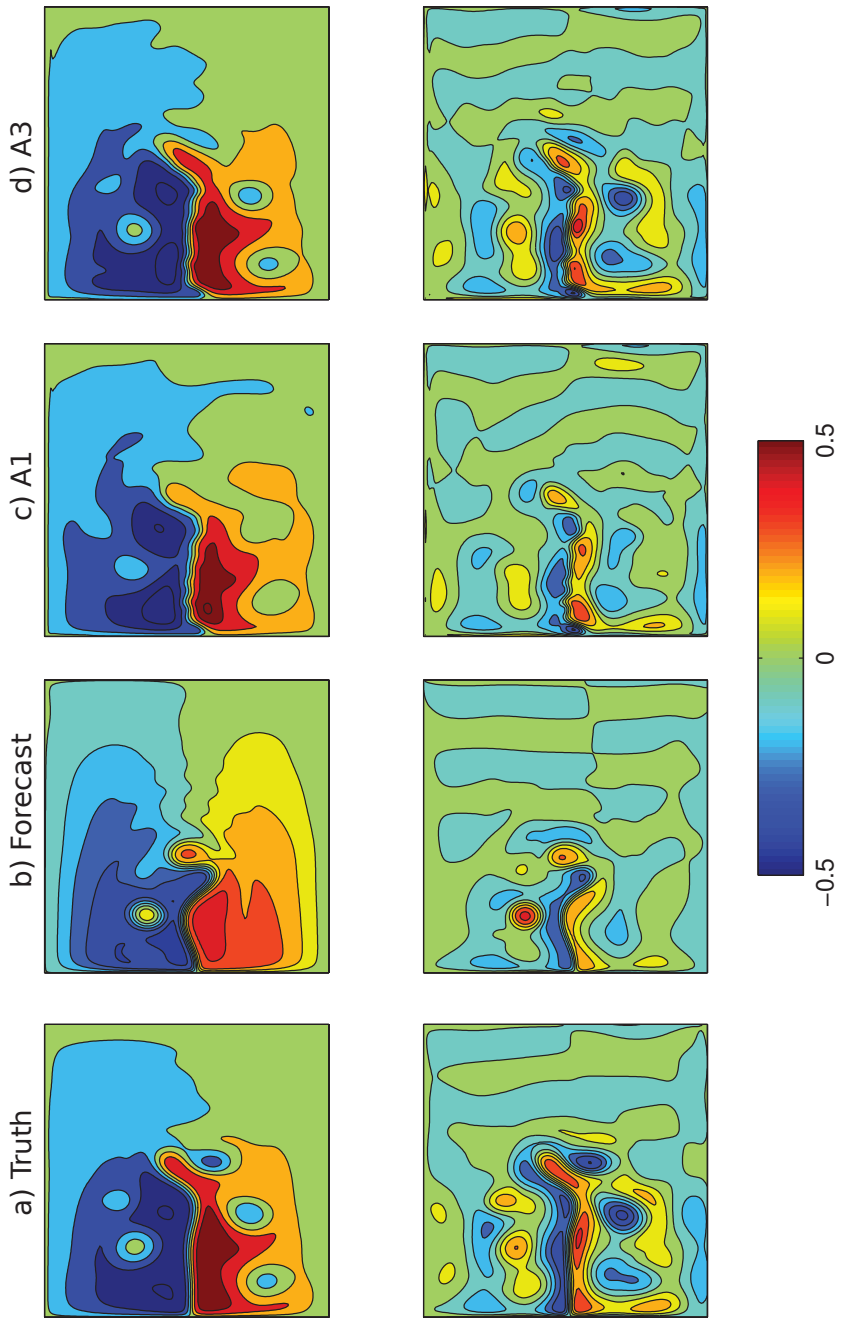

Figure 3.8: Typical snapshots of sea level (day 600) from the truth (a), forecast (b), spectral nudging (c) and hybrid (d) runs. The total sea level fields are shown in the upper panels and the corresponding small scale components are shown directly below. A wavenumber cutoff of $k^c = 4$ was used. Sea level is in m.

The impact of assimilating the large scales is shown in Figure 3.8 for a typical sea level field from run A1. It is encouraging to note that, for this field at least, the assimilation of large scales has improved significantly the accuracy of the reconstructed small scales (bottom panels), e.g., it has removed an unrealistic jet meander and an eddy north of the jet, and started to generate two eddies south of the jet. The assimilation of large scales has also improved significantly the fit to the full fields (upper panel). This is not surprising because the true large scales were inserted directly into the model. A more quantitative assessment of the impact of assimilating the large scales is shown by the dashed lines of Figure 3.9. It is encouraging to note that the assimilation of the large scales has reduced significantly the mean square difference of the small scales, $S(\eta^S_{FC} - \eta^S_{TR})$, even though no information on the true small scales was assimilated.

The assimilation results described above were obtained using a wavenumber cutoff of $k^c = 4$. To determine the sensitivity of the results to this choice of k^c, run A1 was repeated with values of k^c that ranged from 1 to 13. As expected $\overline{S}(\eta^S_{FC} - \eta^S_{TR})$ and $\overline{S}(\eta^S_{A1} - \eta^S_{TR})$ decrease as k^c increases (Figure 3.10) because more variability is assigned to the large scales. For $k^c = 1$ it can be seen that $\overline{S}(\eta^S_{A1} - \eta^S_{TR})$ exceeds $\overline{S}(\eta^S_{FC} - \eta^S_{TR})$ implying that the assimilation of the large scales has degraded the fit. However, for $k^c > 2$ the assimilation of the large scales improves the fit of forecast run. For $k^c = 4, 5$ and 6 spectral nudging of the large scales reduces $\overline{S}(\eta^S_{FC} - \eta^S_{TR})$ by 30%, 52% and 61% respectively.

It is clear from Figure 3.8 (and figures for other times not shown here) that the eddies from run A1 are often too weak in comparison with the truth run and some eddies are missed completely. Such discrepancies are not surprising given the limited amount of information that is being assimilated, and the simplicity of the assimilation scheme. The position of the unstable mid-ocean jet was almost fully recovered in run A1. The eddies near the generation region (i.e., mid-ocean jet) and their interaction with the mid-ocean jet that generates new meanders are also well recovered in run A1. By way of contrast, the eddies that have been moved away from their generation region (i.e., moving westwards to the north and south of the jet) are much weaker in run A1 than the truth run and some of these eddies are not generated at all. This is because these eddies are no longer coupled with the large scales and so they cannot be accurately recovered by run A1. In such a situation, isolated small scale features cannot be generated from the assimilation of the large scales. *Henshaw et al.* (2003) also identified isolated small scale features that cannot

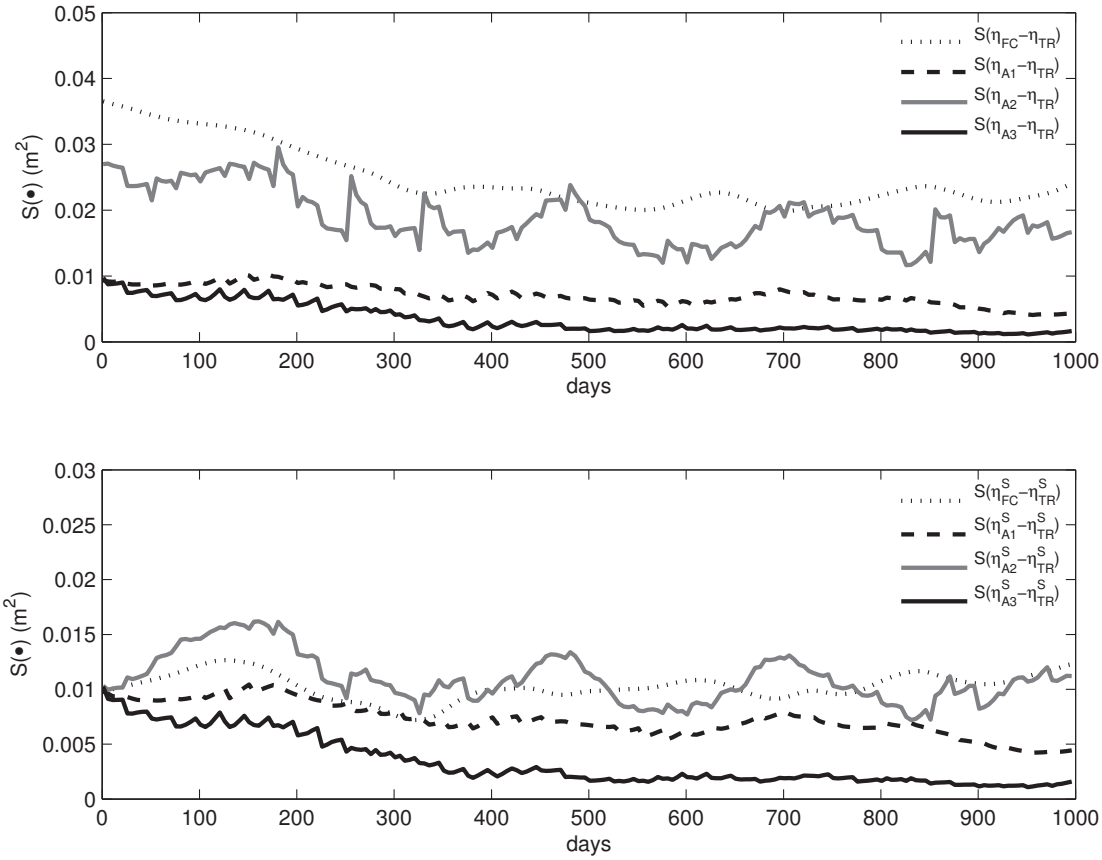

Figure 3.9: Time variation of the mean square difference between the truth run and the forecast and assimilation runs. The upper panel shows results for the full field and the lower panel shows results for the small scales only ($k^c = 4$).

be recovered from the large scales.

The time variation of $S(\eta_{A2} - \eta_{TR})$ is shown in the upper panel of Figure 3.9 for $n_{obs} = 63$ point observations corresponding to $k^c = 4$. (The positions of the observing locations are indicated by the crosses in Figure 3.1.) Overall run A2 improves the fit of the forecast run. If one focuses on the small scales (bottom panel) then the fit of run A2 to the truth is not much better than the forecast run. The large temporal fluctuations of $S(\eta^S_{A2} - \eta^S_{TR})$ are due to the relatively small number of observing locations: there are times when the observing array cannot detect the eddies (see Figure 3.1 for an example) and this inflates $S(\eta^S_{A2} - \eta^S_{TR})$. When eddies are missed, run A2 can give worse small scale results

than the forecast run. Additional runs with denser observing arrays (not shown) confirms that the eddies are better observed and the fluctuations of $S(\eta^S_{A2} - \eta^S_{TR})$ disappear.

The performance of run A2 as a function of k^c, and hence n_{obs}, is shown in Figure 3.10. It is clear that run A2 performs worse than run FC for $k^c < 6$, or equivalently $n_{obs} < 143$. This shows that assimilating a relatively small number of point observations, using a simplistic assimilation method, can degrade the quality of the forecast in the small scales. As the number of observations increases however, run A2 outperforms the forecast run and gives more accurate small scales as expected. It can also be seen from Figure 3.10 that the assimilation of large scales and the assimilation of point observations give almost identical results for $7 < k^c < 14$.

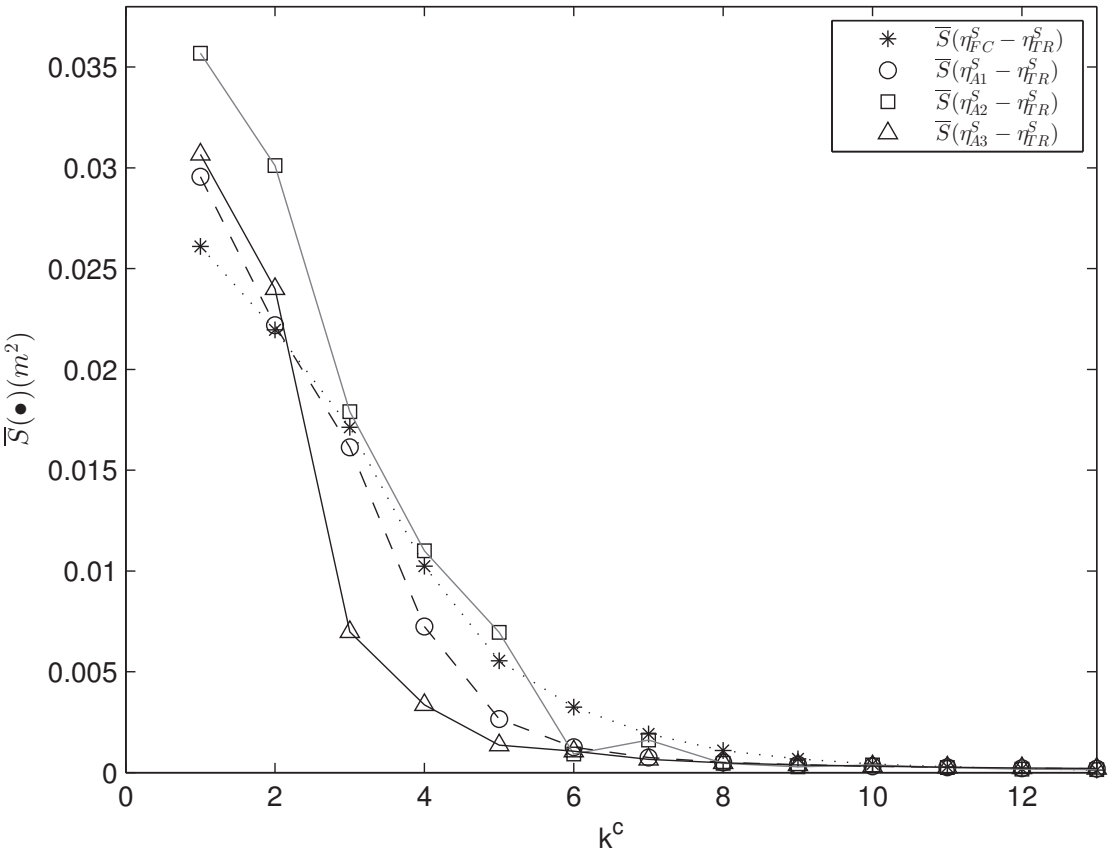

Figure 3.10: Dependence of the small scale error on k^c. The line with asterisks shows the mean square error of the small scales of the forecast run, $\overline{S}(\eta^S_{FC} - \eta^S_{TR})$. The remaining three lines are for run A1 (circles), run A2 (squares) and run A3 (triangles).

The effectiveness of run A3 for $k^c = 4$ and $n_{obs} = 63$ is illustrated by the sea level snapshots shown in Figure 3.8. It is clear, for this snapshot at least, that run A3 predicts the sea level more accurately than run A1, e.g., the eddies are closer to their true intensities and positions, and the isolated eddies are now fully recovered. A more quantitative assessment is provided by the time variation of $\overline{S}(\eta^S_{A3} - \eta^S_{TR})$ shown in Figure 3.9. Clearly the hybrid outperforms runs A1 and A2 for $k^c = 4$ and $n_{obs} = 63$.

The sensitivity of run A3 to the wavenumber cutoff, and number of assimilated point observations, is shown in Figure 3.10. For $k^c < 3$, and thus $n_{obs} < 35$, the mean square error for runs A1 and A3 are similar. For both runs, the assimilation of limited large scale and point information has degraded the forecast. For larger values of k^c and n_{obs} run A3 outperforms runs A1 and A2. For $k^c > 10$, and thus $n_{obs} > 399$, the performance of runs A1 and A3 are both good (i.e., small error variance, as expected). It is encouraging to note that run A3 significantly outperforms run A2 for $k^c < 6$ (compare the lines with triangles and squares in Figure 3.10). This illustrates the benefit of assimilating additional large scale information when all that is available is a set of observations that alias the true variability.

Note, the above results are associated with errors in the initial conditions. To test if the results hold when uncertainties are present in the wind forcing, I performed an additional experiment in which the forecast and the truth runs were generated using different wind forcing. Specifically, I generated the truth using wind stress that varied randomly about τ_0 as an AR(1) process with an e-folding time of 2 years. Thus, the error is only on the large scale wind stress amplitude. The results from the experiment with uncertainty in the wind forcing amplitude were essentially the same as the results from the experiments with uncertainty in the initial condition: assimilation of the large scales significantly improves the recovery of the small scales and the hybrid outperforms the separate assimilation of large scales and limited point observations. Note that when the uncertainty is introduced into the wind forcing, the error from run A1 and A3 does not converge towards zero as in the results with uncertainty in the initial conditions.

3.5 Summary

Following *Henshaw et al.* (2003), I tested if knowledge of the time history of large scale ocean variability may be used to recover the small scale variability of a quasi-geostrophic model. A statistical based approach led to an encouraging reconstruction of the small scales. However this approach underestimates the predictability of the small scales because it ignores the model's non-linearity and the time history of the large scales. In an experiment where these two factors were taken into account using the non-linear quasi-geostrophic model (the spectral nudging run) the recovery of the small scales from the large scales was shown to be more accurate.

Traditional data assimilation techniques (e.g. EnOI) can effectively recover all length scales of variability of the quasi-geostrophic model given a sufficient dense observing array. Reducing the number of the observation locations can reduce significantly the accuracy of the recovered small scales, particularly when the observing array aliases, or completely misses some of the eddies. To address this problem the hybrid method described in section 2 was evaluated. The hybrid method was developed to combine spectral nudging of the large scales with the assimilation of a limited number of point observations to update the small scales. It was shown that if the large scale features are estimated accurately, the assimilation of a limited umber of observations can significantly improve the accuracy of the recovered small scales. The results indicate that in the quasi-geostrophic model spectral nudging can be used to recover a portion of the small scales but it is the combination of spectral nudging and EnOI that leads to the recovery of almost all the small scale variability. This is not surprising given that when the eddies (small scales) are advected away from the region of their generation they become decoupled from the large scales. Thus they cannot be recovered from the large scales and additional information is necessary.

Now that it has been established that spectral nudging can help to improve the accuracy when downscaling ocean flow regimes, the next step is to apply it to a realistic ocean model. In Chapter 6 the application of the above downscaling method in a realistic Northwest Atlantic model is presented; but first the development and realism of this model are discussed in Chapters 4 and 5.

CHAPTER 4

A ONE-WAY NESTED MODEL OF THE NORTHWEST ATLANTIC AND ADJACENT SHELF SEAS

Dynamical downscaling of global ocean fields to the Scotian Shelf, Gulf of Maine and the adjacent deep ocean, based on one-way nesting, is discussed. Specifically, information from the real-time nowcast/forecast, 1/12° global HYCOM/NCODA system is used to specify the open lateral boundary conditions for a higher resolution model of the study region based on NEMO.

The regional model of the study region (GoMSS) differs from the global model in several important respects. Most importantly GoMSS can simulate explicitly dynamical processes and phenomena that are known to be important locally and yet are absent from the global system. Of particular importance is the accurate representation of tidal elevation and currents because they are large in the study region and they can significantly alter local water properties, circulation, and sea surface height through processes such as tidal rectification, and mixing. I also increased the resolution of GoMSS compared to the global system, in both the horizontal and the vertical, in order to resolve explicitly smaller scale features and processes. Two atmospheric forcing datasets are used to quantify the effect of horizontal resolution of air-sea fluxes of heat, fresh water and momentum.

The global system is described in section 4.1 and I show it can provide realistic fields for downscaling to the Northwest Atlantic and adjacent shelf seas. The NEMO modelling framework is described in section 4.2 and the regional configuration is detailed in section 4.3. The atmospheric and tidal forcing datasets are also described, and evaluated, in

section 4.3. The chapter summary is given in section 4.4.

4.1 The Global HYCOM/NCODA System

A brief description of the 1/12° HYCOM/NCODA analysis system (henceforth referred to as the "global system", Table 4.1) is now given with emphasis on the system's configuration. The system's accuracy is also discussed, based on previous studies and through comparison with observations. The comparison is quite limited and meant to show that the global system predictions are reasonable. A more quantitative evaluation of the global system and the regional model is provided in Chapter 5.

4.1.1 Description

The HYbrid Coordinate Ocean Model (HYCOM, *Bleck*, 2002) is a primitive equation, general ocean circulation model based on the Miami Isopycnic Coordinate Model (MICOM) framework. HYCOM uses a hybrid coordinate system in the vertical that combines the three main coordinate types: ρ-levels (isopycnal, density tracking), z-levels (constant fixed depths), and σ-levels (terrain following). Each vertical coordinate type is optimal for different ocean areas. For example, ρ-levels best resolve the deep stratified ocean, z-levels perform well in the surface mixed layer, where high vertical resolution is necessary, and σ-levels are good for shallow coastal regions. The default vertical coordinate in HYCOM transforms smoothly from isopycnal in the open stratified ocean, to terrain following in the shallow coastal regions, and to z-level in the surface mixed layer and unstratified seas.

The HYCOM consortium is a broad collaboration of many partners including the University of Miami, the Naval Research Laboratory (NRL), the Los Alamos National Laboratory (LANL), the U.S Navy at the Naval Oceanographic Office (NAVOCEANO), the Stennis Space Center, the Fleet Numerical Meteorology and Oceanography Center (FNMOC), the National Oceanic and Atmospheric Administration (NOAA) at the National Centers of Environmental Prediction (NCEP), and the Global Ocean Data Assimilation Experiment (GODAE). The main objective of the consortium is to develop a global system based on state of the art models and assimilation methods in order to provide short range ocean forecasts, accurate open boundary conditions for regional models, and initial conditions for climate projections. The real-time nowcast/forecast 1/12° global

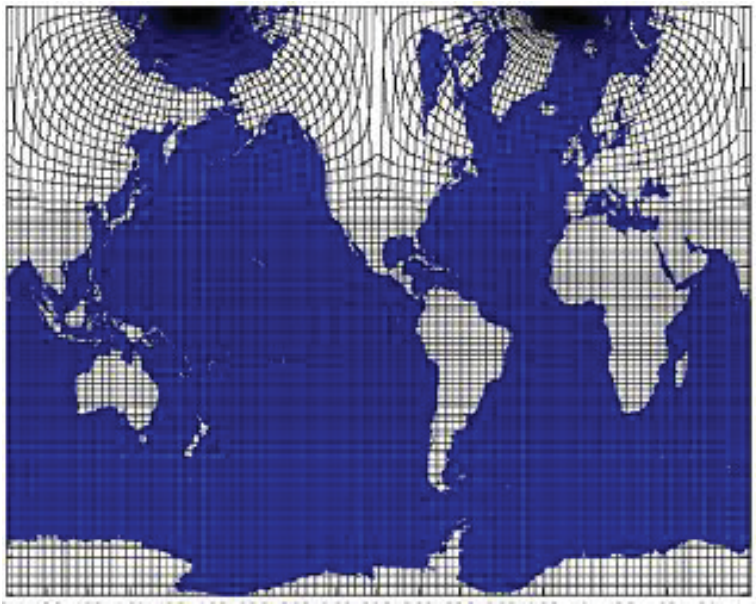

Figure 4.1: The 1/12° grid of the global HYCOM/NCODA real-time nowcast/forecast system.

HYCOM/NCODA (Navy Coupled Ocean Data Assimilation) system is a result of this collaboration (the "global system", Table 4.1).

The global system has a horizontal grid spacing of 1/12° in equatorial regions, about 7 km at mid-latitudes, and 3.5 km at the poles. A Mercator grid is used between 78°S and 47°N; north of this region an Arctic bi-polar patch is used (Figure 4.1). Fields from the global system are available for 32 vertical z-layers (i.e., fixed at depths) with spacing that varies from 10 m near the surface to 500 m at the deepest level. The bathymetry is derived from a quality control NRL Digital Bathymetric Data Base (DBDB2). The surface atmospheric forcing (e.g., wind stress, wind speed, heat flux, precipitation) is obtained from the Navy Operational Global Prediction System (NOGAPS) with a 0.5° resolution for all fields except precipitation which has a 1° resolution. In 2013 the atmospheric forcing switched from NOGAPS to the Navy Global Environmental Model (NAVGEM). There is no tidal forcing in the system. The model is initialized once using January climatology (temperature and salinity) from the Generalized Digital Environmental Model (GDEM3 *Carnes*, 2009). A simple thermodynamic ice model is used (ice formation and melting but no ice motion).

The global system assimilates sea surface height and sea surface temperature observed

Table 4.1: Main characteristics of the global system and regional model.

	Global system	GoMSS	GoMSS+RDPS
Model Framework	HYCOM	NEMO	NEMO
Resolution	1/12°	1/36°	1/36°
Domain	Global	Gulf of Maine, Scotian Shelf, and adjacent deep ocean	Gulf of Maine, Scotian Shelf, and adjacent deep ocean
Atmosph. forcing	NAVGEM/ NOGAPS	CFSR	RDPS
Tidal forcing	No	FES2004	FES2004
Assimilation	NCODA	No	No

by satellites (NAVOCEANO), all available vertical profiles of temperature and salinity from various platforms (e.g., Argo floats, CTDs, moorings), and sea ice concentration from special sensor microwave/imager (SSMI). The analysis updates sea ice concentration, salinity, temperature, dynamic height and currents. The assimilation is performed using multivariate optimum interpolation (MVOI, see *Cummings*, 2005; *Cummings and Smedstad*, 2013). The currents are updated based on the multivariate correlation between velocity and dynamic height (i.e., geostrophic coupling). In MVOI there are two alternative methods to project the sea surface height data to depth in the form of synthetic temperature and salinity profiles: i) using the Modular Ocean Data Assimilation System (MODAS *Fox et al.*, 2002) or ii) using the method developed by *Cooper and Haines* (1996) which directly adjusts the model forecast density field based on the errors between the predicted and the observed sea surface height. The second approach is dynamically more consistent because it relies on model dynamics rather than statistics derived from MODAS; however the global system fields used in this study were generated using the first method because it can correct for errors in stratification and long-term drift.

4.1.2 Initial Assessment of the Global System

The global system has already been extensively validated in several studies (e.g., *Chassignet et al.*, 2007, 2009; *Kelly et al.*, 2007; *Metzger et al.*, 2008). For example, comparison of predictions by the global system and independent observations (*Chassignet et al.*, 2007, 2009; *Kelly et al.*, 2007) has shown that the position of the Gulf Stream and Kuroshio is realistically simulated and the system simulates mixed-layer depth with relatively small error.

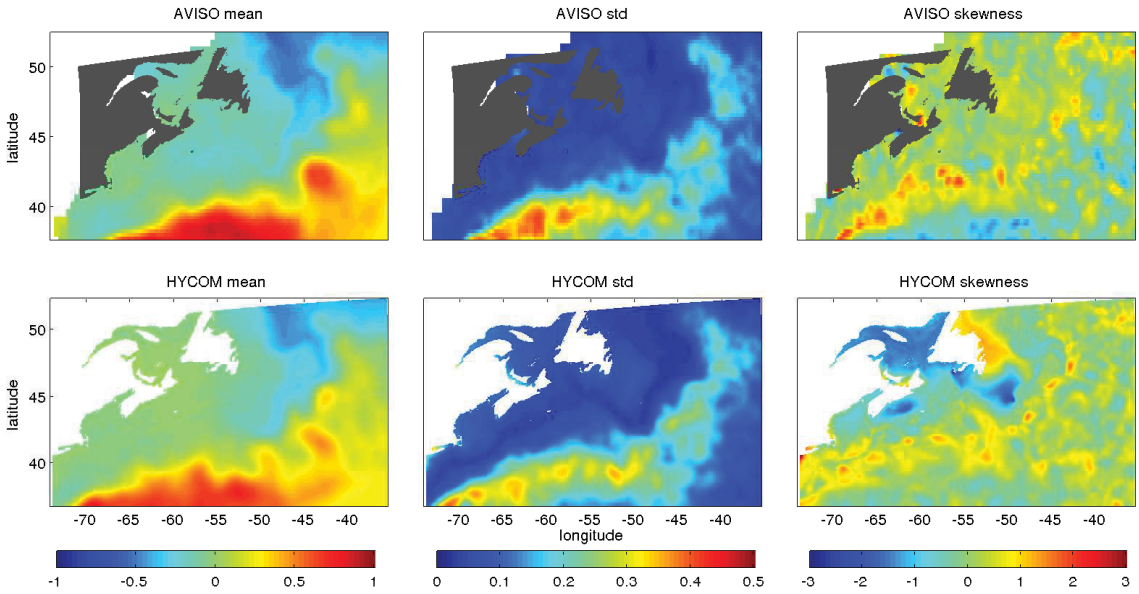

Figure 4.2: The mean, standard deviation and skewness of sea level observed by satellite altimeters (AVISO product, upper panels) and predicted by the global system (lower panels). The mean and standard deviation are in meters, and skewness is nondimensional.

Local observations from satellite altimeters, coastal tide gauges, CTD's and a glider are now used to provide an initial assessment of the global system on the Scotian Shelf and Gulf of Maine, and for the adjacent deep ocean.

The first three moments of sea level variability (mean, standard deviation and skewness) are shown in Figure 4.2 for the global system and gridded satellite altimeter observations from AVISO (Archiving, Validation and Interpretation of Satellite Oceanographic Data). The global system sea surface height estimates are based on daily snapshots for the time period 2010-2012. The AVISO standard deviation and skewness are based on weekly sea level fields between 2010-2012. The AVISO mean was kindly provided by Dr. Simon Higginson; it is based on multiple years (1993-1999) and it represents the mean dynamic topography (mean sea surface minus the geoid *Higginson et al.*, 2011). Because the satellite altimeter observations have large errors near the coast (50 km from the shore) AVISO relaxes the mean sea surface towards an estimate of the geoid there (i.e., the mean sea surface topography becomes zero).

The mean sea surface height of the global system is in good agreement with the altimeter observations. This is not surprising because observations from satellite altimeters have

been assimilated by the global system. The global system's sea surface height variability is large in the vicinity of the Gulf Stream (i.e., high standard deviation) as expected. Skewness is also high in this area and the pattern approximately reflects the mean position of the Gulf Stream and the dominant polarity of the eddy field (*Thompson and Demirov*, 2006); both are generally consistent with the skewness of the observations. Note the global system has lower variability than the observations in the vicinity of the Gulf Stream (lower standard deviation), suggesting that the global system cannot resolve some of the eddy variability and meandering of the Gulf Stream. This implies that higher resolution may be required or a more accurate parametrization scheme for mixing (e.g., the global system may be too diffusive).

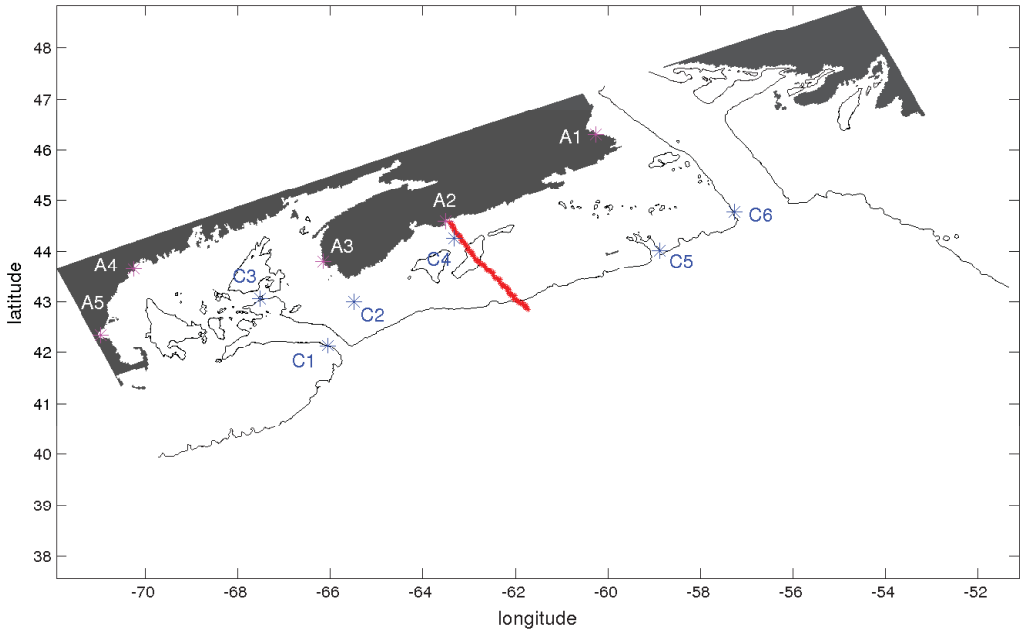

Figure 4.3: Locations of the six CTD profiles (C1 to C6, blue asterisks), the glider path (red line crossing the Scotian Shelf), and five tide gauges (A1 to A5, magenta asterisks) used to validate the global system.

The CTD data used in this study were collected by Fisheries and Oceans Canada and kindly provided by Dr. David Hebert of the Bedford Institute of Oceanography. Temperature and salinity vertical profiles, for 6 locations of interest (Figure 4.3), are shown in Figure 4.4 and 4.5 respectively. The global system is generally in good agreement with the CTD observations during spring, summer and autumn, for the six selected locations.

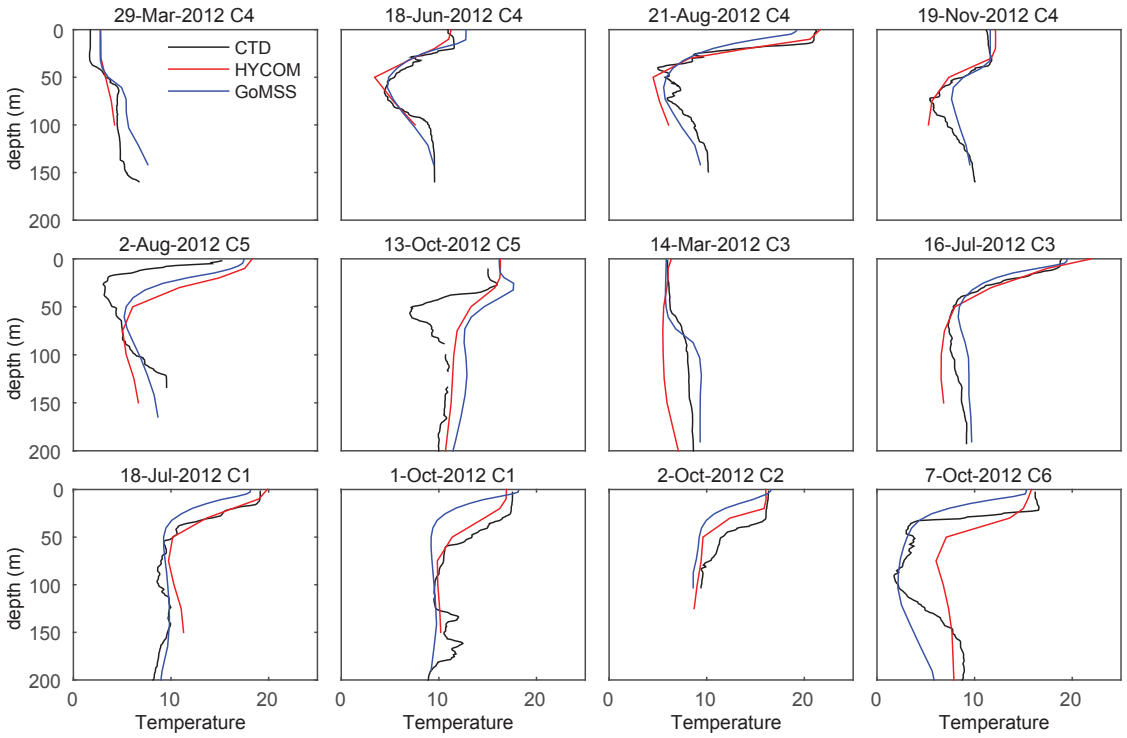

Figure 4.4: Temperature vertical profiles from CTD measurements (black), the global system (red), and GoMSS (blue). The six locations of the profiles are indicated in Figure 4.3. Temperature is in °C

(The agreement generally holds for other locations and dates, not shown.) This agreement is not surprising because all available CTD observations have been assimilated by the global system. There are however still differences. For location C4, during winter, the global system overestimates the salinity at all depths and generates a well mixed water column. This is probably due to the global system's relatively coarse resolution in the vertical (the global system fields are available for 32 z-levels). Additionally, for locations C5 during summer, the global system has generated a deeper thermocline than observed.

The temperature and salinity profiles from a glider operating along the Halifax Line (11-31, July 2012) are shown in Figures 4.6 and 4.7, respectively. The glider path is shown by the red line in Figure 4.3. The glider is operated by the Ocean Tracking Network (OTN). Figures 4.6 and 4.7 show that the global system accurately captures the sea surface layer temperature and salinity. However, for some locations the global system overestimates the mixed layer depth, probably due to its coarse vertical resolution. Generally, the global

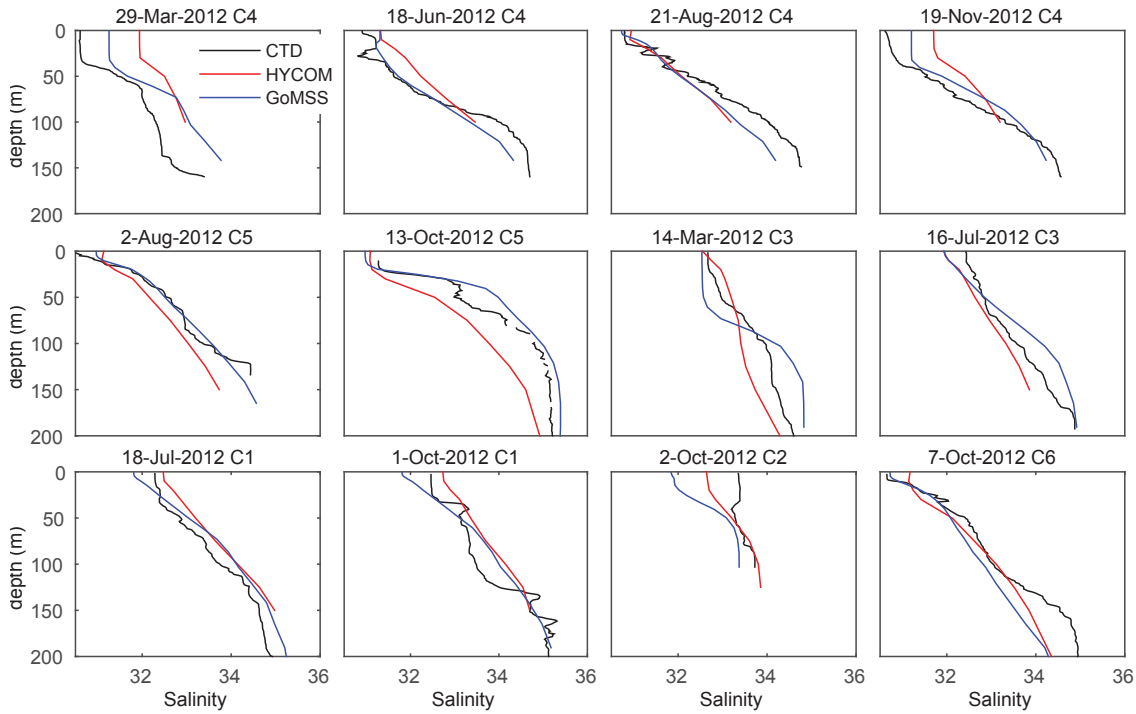

Figure 4.5: Salinity vertical profiles from CTD measurements (black), the global system (red), and GoMSS (blue). The six locations of the profiles are indicated in Figure 4.3. Salinity is in practical salinity units

system has larger errors in deep water where observations are sparse (and so the corrections from the assimilation are weak). Specifically, the global system does not reproduce the well mixed, warm, saline water mass below the pycnocline at the shelf break. (It underestimates both salinity and temperature in this area.)

Daily (snapshots) variations of coastal sea level observed by tide gauges at Halifax and Yarmouth (locations A2 and A3 in Figure 4.3, respectively) are shown in Figure 4.8 for 2010. The tidal gauges are operated by Fisheries and Oceans Canada. Tides and the inverse barometer effect have been removed from the observed hourly time series to facilitate comparison with the global system. During winter, the global system captures most of the high frequency variability at both stations. Specifically, the global system represents accurately the effect of some major storms on sea level (e.g., very low sea level during the first days of February, the first days of September, and the last days of December). However, the global system misses some events like the high sea level during the end of

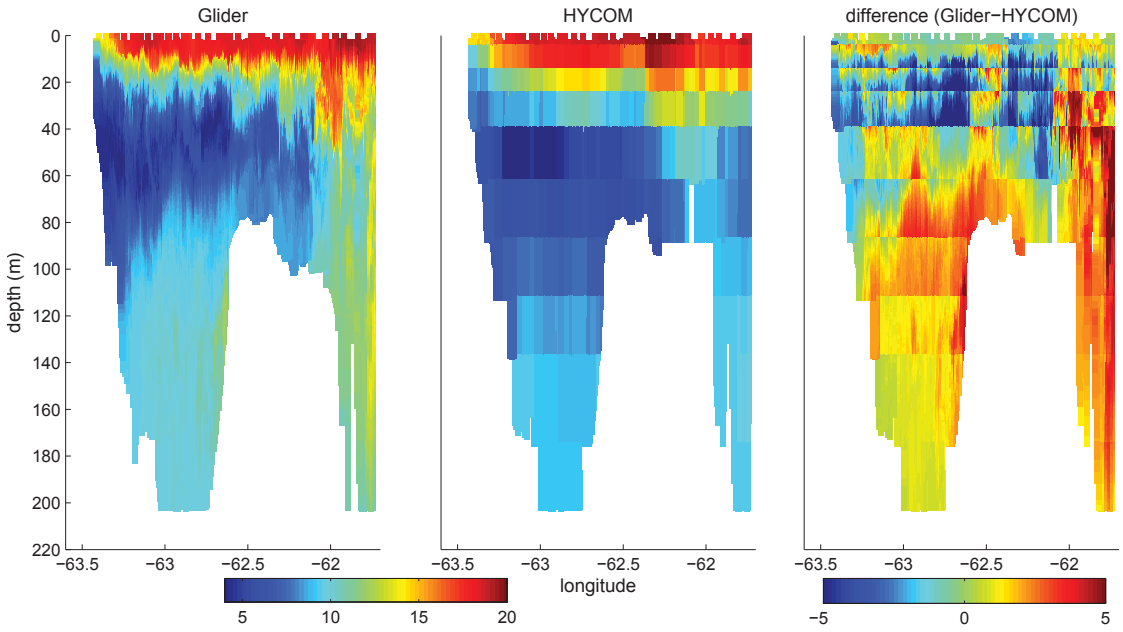

Figure 4.6: Temperature section observed by a glider (left panel) operating along the Halifax Line (red line in Figure 4.3), the global system (middle) along the same path, and their difference (right panel) during 11-31, July 2012. Temperature is in °C.

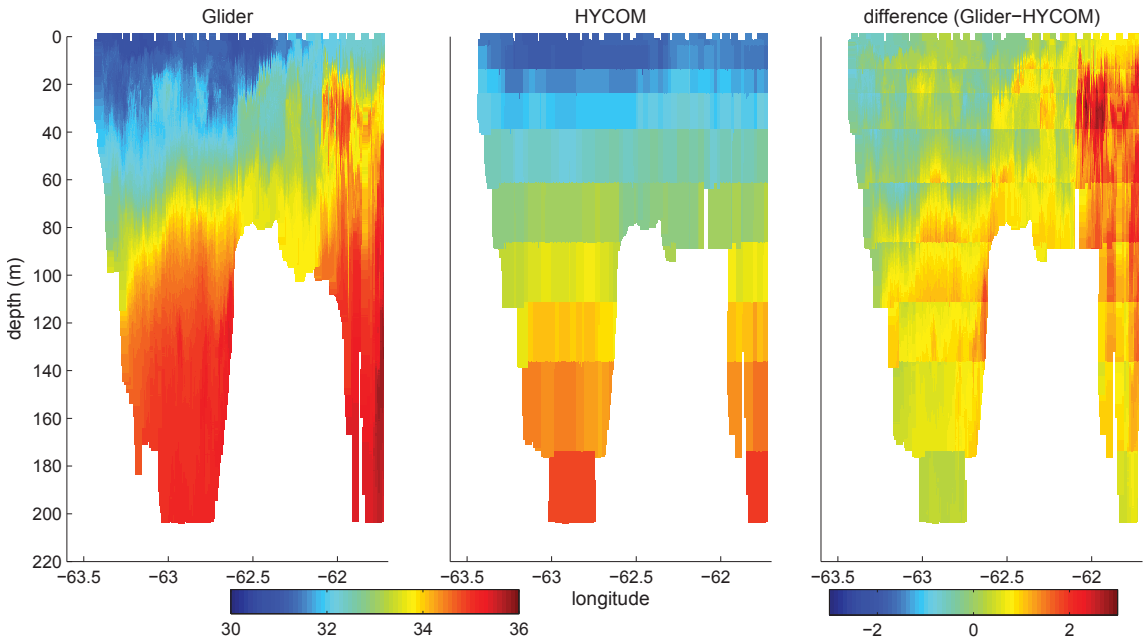

Figure 4.7: Salinity section from the glider and the global system. Same format as Figure 4.6. Salinity is in practical salinity units.

January. Generally, the global system represents well the sea level variability at Halifax and Yarmouth during 2010. This is also the case for different years and locations (not shown). More quantitative comparisons of the global system's output with observations, and comparison with the performance of the regional model, are given in Chapter 5.

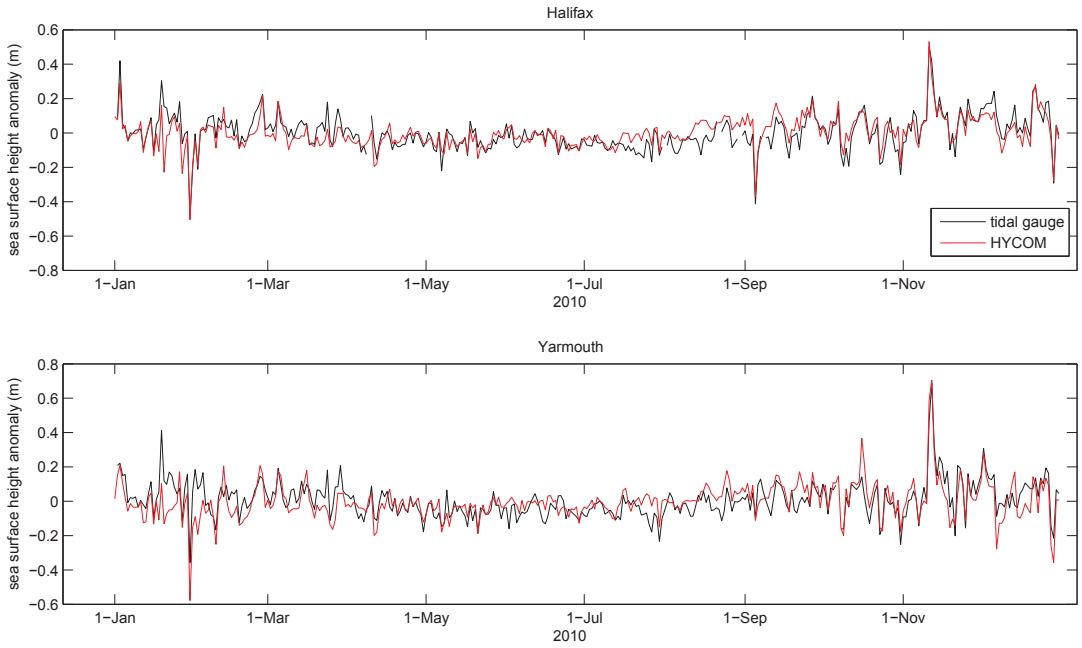

Figure 4.8: Daily (snapshots) sea level anomalies observed by coastal tide gauges (black) and predicted by the global system (red) at Halifax and Yarmouth for 2010. The tide and the inverted barometer effect were removed from the hourly sea level observations before extracting the daily values.

Relatively high horizontal resolution, and realism, are two positive characteristics of the global system. This means that the global system can provide reasonably accurate boundary conditions for higher resolution regional models (*Chassignet et al.*, 2009). I have shown that the global system provides reasonably realistic predictions for the Scotian Shelf, Gulf on Maine and adjacent deep ocean although higher resolution may be necessary to resolve several regional features. Furthermore, the tides are a significant component of the local system that is ignored in the global system. This motivates the following development of a higher resolution regional model that is driven by boundary conditions from the global system using one-way nesting. I decided to base my high resolution regional model on

the Nucleus for European Modelling of the Ocean (NEMO, see section 4.2) framework because it has a build-in algorithm for tidal forcing, and a variety of schemes for the implementation of open lateral boundary conditions.

4.2 The NEMO Modelling Framework

The Nucleus for European Modelling of the Ocean (NEMO) is a state-of-the-art ocean modelling framework for studying the ocean and its interaction with the atmosphere, the sea ice and biogeochemical tracers. The ocean component of NEMO is based on the OPA model (*Madec et al.*, 1998). NEMO has been used in various ocean and sea ice applications (both regional and global) as a stand alone model, but also coupled with the atmosphere. I have used the ocean component of NEMO version 3.1 to develop a high resolution regional model of the Scotian Shelf, Gulf of Maine and adjacent deep ocean.

This section briefly describes the NEMO model, focusing on the numerical schemes used in this study. The description is based on the NEMO manual (*Madec*, 2008) from which further details about NEMO's numerics and code can be found.

4.2.1 Governing Equations

The model's primitive equations are based on the following approximations and assumptions:

1. Spherical earth approximation: Gravity is parallel to the Earth radius.
2. Thin shell approximation: The depth of the ocean is negligible compared to the Earth's radius.
3. Incompressible flow approximation: The divergence of the velocity field is zero.
4. Boussinesq approximation: Density variations are considered only in the buoyancy term.
5. Hydrostatic approximation: The pressure gradient force in the vertical is balanced by the gravitational force.
6. Turbulence closure assumption: Turbulent transport is parametrized in terms of the "mean" state.

Based on these approximations and assumptions, the conservation of momentum, volume, salt and temperature lead to the following governing equations:

$$\begin{aligned}
\frac{\partial \mathbf{u}_h}{\partial t} &= -\left[(\nabla \times \mathbf{u}) \times \mathbf{u} + \frac{1}{2}\nabla(\mathbf{u} \cdot \mathbf{u})\right]_h - f\mathbf{k} \times \mathbf{u}_h - \frac{1}{\rho_o}\nabla_h P + D^{\mathbf{u}} + F^{\mathbf{u}} \\
\frac{\partial P}{\partial z} &= -\rho g \\
\nabla \cdot \mathbf{u} &= 0 \\
\frac{\partial T}{\partial t} &= -\nabla \cdot (T\mathbf{u}) + D^T + F^T \\
\frac{\partial S}{\partial t} &= -\nabla \cdot (S\mathbf{u}) + D^S + F^S \\
\rho &= \rho(T, S, P)
\end{aligned} \tag{4.1}$$

where $\mathbf{u}$ is the 3D vector velocity, the sub-script h denotes the horizontal component, f is the Coriolis acceleration, P is pressure, T is temperature, S is salinity, $D^{\mathbf{u},T,S}$ are parameterizations of small scale physics for momentum, temperature and salinity, and $F^{\mathbf{u},T,S}$ are the "surface forcing term" (e.g wind stress, heat flux and freshwater flux written as interior forces distributed over the top layer). The rest of the notation is standard.

The standard geographical coordinate system has a singular point at the North Pole that is difficult to treat in a global model. A solution is to use a curvilinear geopotential coordinate system. The NEMO model equations are therefore transformed to the curvilinear geopotential coordinate system shown in Figure 4.9.

4.2.2 Boundary Conditions

The ocean is an open system that communicates, interacts and exchanges fluxes with other components of the climate system (e.g., atmosphere, sea ice, land). This interaction can be summarized as follows:

1. Ocean-land interface: The main exchange is the freshwater discharged into the ocean through rivers. This discharge is parameterized as a freshwater flux at the air-sea interface in the vicinity of the river mouth.

2. Ocean-sea floor interface: There is no flow across the ocean bottom (i.e., the bottom normal velocity is zero). The heat and salt exchange between the ocean and its

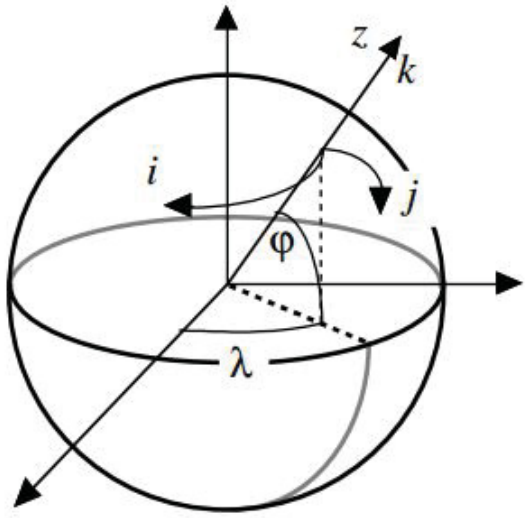

Figure 4.9: The geographical coordinate system (λ, ϕ, z) and the curvilinear coordinate system (**i**,**j**,**k**). From the NEMO manual (*Madec*, 2008).

bottom is neglected. However, momentum is exchanged though friction. The bottom friction is described using a non-linear quadratic parameterization.

3. Ocean-atmosphere interface: The atmosphere and the ocean exchange momentum (wind stress), heat (latent heat, sensible heat, radiation), and freshwater (precipitation-evaporation).

4. Ocean-sea ice interface: Ocean and sea ice exchange momentum, heat and freshwater. In this study ice is not considered, and so this interface does not exist.

4.2.3 Subgrid Scale Physics

The length scales that are resolved explicitly by the model depend on its resolution. However, processes with length scales that are not resolved by the model's mesh (the subgrid scale variability) can exert an important influence on the evolution of the ocean and its steady state. To close the governing equations, the effect of subgrid scale processes is represented entirely in terms of large scale patterns. This is referred to as the turbulent closure hypothesis. In (4.2) the subgrid scale physics is represented by the terms $D^{\mathbf{u}}$, D^{T} and D^{S}.

Due to the strong anisotropy of oceanic motion in the vertical and horizontal, the subgrid scale parameterizations in the vertical and horizontal are treated separately.

4.2.3.1 Subgrid Scale Physics in the Vertical

In the vertical, turbulent motion is not explicitly resolved. The vertical turbulent fluxes are parameterized analogous to molecular diffusion. Specifically, the vertical diffusive operators for momentum and tracers (temperature and salinity) are

$$\begin{aligned} D_v^{\mathbf{u}} &= \frac{\partial}{\partial z}\left(A_v^{\mathbf{u}}\frac{\partial \mathbf{u}_h}{\partial z}\right) \\ D_v^{T} &= \frac{\partial}{\partial z}\left(A_v^{T}\frac{\partial T}{\partial z}\right) \\ D_v^{S} &= \frac{\partial}{\partial z}\left(A_v^{T}\frac{\partial S}{\partial z}\right) \end{aligned} \tag{4.2}$$

where $\mathbf{u}_h$ is the horizontal velocity and $A_v^{\mathbf{u}}$ and A_v^T are the vertical eddy viscosity and diffusivity coefficients respectively. In this study these coefficients are computed from a TKE (turbulent kinetic energy) turbulent closure model. According to this model the eddy viscosity and diffusivity coefficients are computed based on a characteristic length (mixing length scale), and the turbulent kinetic energy found based on shear and buoyancy production, transport and dissipation. The above is valid for the ocean interior. At the surface, the turbulent stress is prescribed based on the wind stress.

4.2.3.2 Subgrid Scale Physics in the Horizontal

The lateral eddy fluxes depend on the model's resolution. In my case the model is eddy resolving (i.e., the model's horizontal grid spacing is around 10 times smaller than the first baroclinic Rossby radius of deformation). For tracers (temperature and salinity) the following lateral second order diffusive operator is used:

$$D_l^T = \nabla \cdot \left(A_l^T \mathcal{R} \nabla T\right) \tag{4.3}$$

where A_l^T is the horizontal eddy diffusivity coefficient (Table 4.2) for tracers, and $\mathcal{R}$ is a matrix associated with the slopes between the surface along which the diffusive operator acts and the model levels. In this study, I assume iso-neutral diffusion for tracers, thus the $\mathcal{R}$ matrix represents the slopes between the iso-neutral and the computational surfaces.

For momentum, I used the following lateral fourth order diffusive operator:

$$D_l^{\mathbf{u}} = \nabla \cdot \left[\mathcal{R}\nabla\left(A_l^{\mathbf{u}}\nabla \cdot \left(\mathcal{R}\nabla \mathbf{u}_h\right)\right)\right] \tag{4.4}$$

where A_l^{u} is the horizontal eddy viscosity coefficient (Table 4.2). I assume the diffusive operator acts along geopotential surfaces for momentum.

4.2.4 Horizontal and Vertical Grid

NEMO uses the C-grid in Arakawa's classification (Figure 4.10). The C-grid consists of cells centred on scalar points with vector points defined at the centre of each face of the cell. All the local points are located at integers or integers and a half value. The ocean mesh is defined in the curvilinear geopotential system. In the vertical, z-levels are used with partial steps for the bottom layer. Thus, the thickness of the bottom layer varies to allow better representation of the bathymetry.

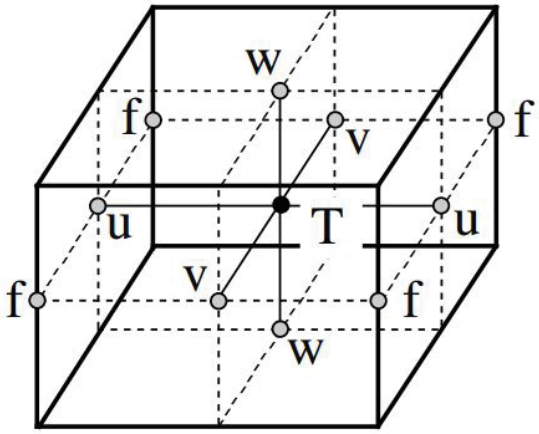

Figure 4.10: Arrangement of variables on the C-grid. T represent the scalar points (temperature, salinity, sea level, etc.), u, v, w represent the vector points (horizontal and vertical velocities), and f indicates vorticity points (relative and planetary). From the NEMO manual (Madec et al., 2012).

4.2.5 Open Lateral Boundary Conditions

When implementing a limited domain configuration the model has to exchange information with the global ocean to close the system. This exchange of information occurs at the open lateral boundaries of the model (the so-called open lateral boundaries). These boundaries allow information from the outer ocean to enter the domain (inflow), and also information generated internally to propagate out without affecting the inner model's solution.

Table 4.2: Parameter values for the NEMO model.

Parameter	Symbol	Value
Barotropic time step	Δt_{bt}	6 s
Baroclinic time step	Δt_{bc}	180 s
Horizontal eddy diffusivity coefficient for tracers	A_l^T	50 m^2 s^{-1}
Bilaplacian horizontal eddy viscosity coefficient	$A_l^{\mathbf{u}}$	10^9 m^4 s^{-1}
Bottom drag coefficient	C_D	5×10^{-3}

Several computational algorithms are available to specify open boundary conditions in NEMO. In this study, I use a "radiation boundary condition" to allow perturbations to leave the model domain with minimum reflection. Specifically, for the barotropic currents I use the Flather radiation scheme (*Flather*, 1976):

$$\overline{u} = \overline{u}_e \pm \frac{c}{H}(\eta - \eta_e) \tag{4.5}$$

where $\overline{u}$ is model's depth average velocity normal to the open boundary, $c = \sqrt{gH}$ is the speed of the external gravity wave, H is the water depth, η is the model's sea surface height, and subscript e indicates that the field is from an external source. Thus the Flather condition radiates away model generated perturbations as gravity waves.

For baroclinic currents, I use a radiation-relaxation type algorithm (Orlanski forward implicit, *Marchesiello et al.*, 2001), with a 10 grid point sponge layer that first estimates if the perturbations propagate in or out of the model domain. If the perturbation is inwards, strong relaxation towards the external source (used to provide the boundary conditions) is applied (1 day). If the perturbation is outwards, the perturbation is allowed to leave the domain with weak relaxation (10 days) towards the external source.

4.3 Configuration and Forcing of the Regional Model

The study region is the Scotian Shelf, Gulf of Maine and adjacent deep ocean off the east coast of Canada. The regional model (GoMSS) domain and the major bathymetric features are shown in Figure 4.11. The model has a horizontal resolution of approximately 1/36° in longitude and latitude (2.8 km average grid spacing). The model has 52 z-levels with a spacing that varies from 0.7 m at the surface to 233 m at the deepest level (4000 m). (A "variable volume level" was used to stretch the thickness of the vertical levels according to

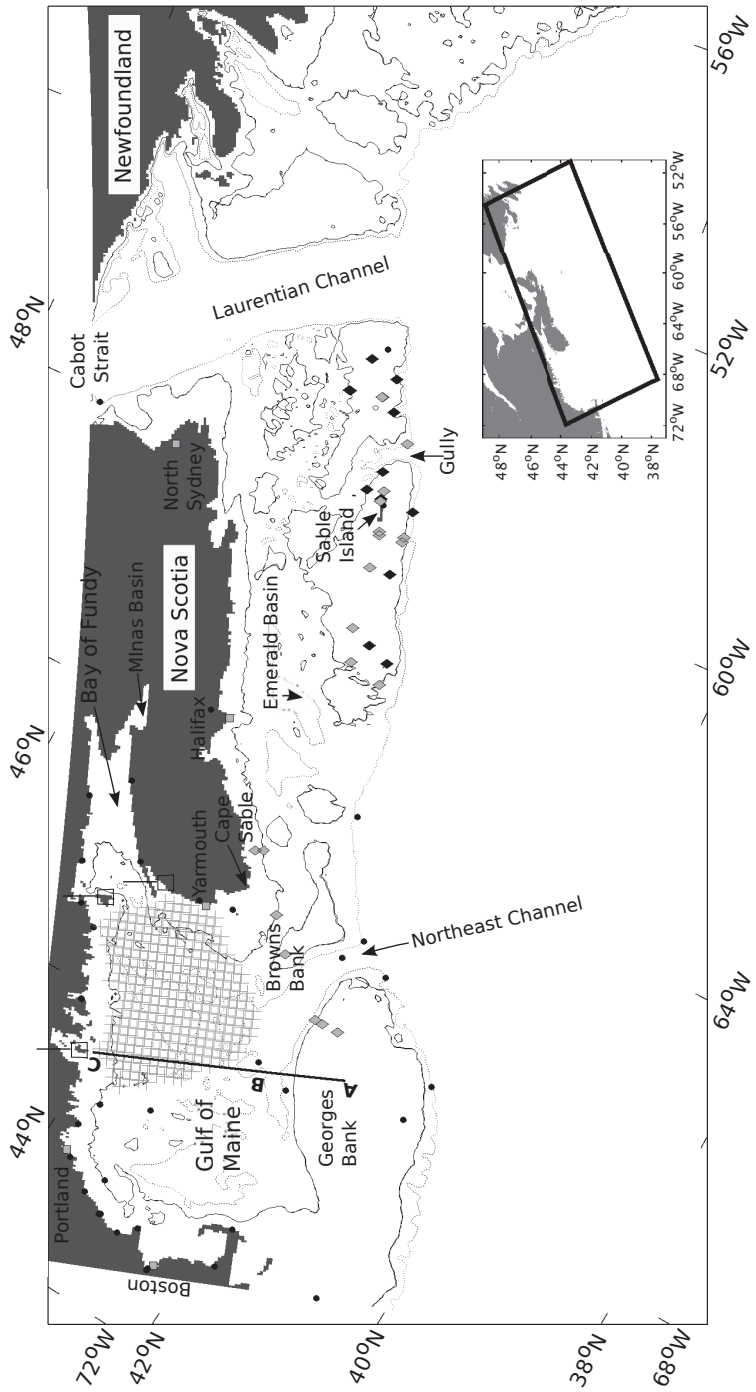

Figure 4.11: The GoMSS model domain (inset panel) along with major bathymetric features, place names and observation locations. The thin black line shows the 100 m isobath and the dotted line shows the 200 m isobath. The black circles show locations of observations of tidal elevation. The diamonds show locations of observations of tidal current (black for winter, gray for summer). The gray squares show the tidal gauge locations. The three rectangular shapes show the locations of the three HF radar antennae and the gray mesh shows the area covered by the HF total data.

Levier et al. (2007). Partial cells are used to better represent the bathymetry.) The model bathymetry is based mostly on the 2 arc-minute Gridded Global Relief Dataset ETOPO2v2 (NOAA, National Geophysical Data Center). Higher resolution data, kindly provided by Professor Richard Karsten (2014, personal communication), was used to improve the bathymetry in the inner Gulf of Maine. All depths exceeding 4000 m were clipped at this value. A barotropic-baroclinic time split approach is used to solve separately for the fast (barotropic) motions and the slower (baroclinic) motions. The barotropic and the baroclinic model time steps are 6 s and 180 s respectively. In this thesis I refer to this model as GoMSS (Table 4.1).

Momentum and buoyancy fluxes at the ocean surface are calculated using output for six atmospheric variables from the global Climate Forecast System Reanalysis (CFSR, *Saha et al.*, 2010) obtained from the U.S National Centers for Environmental Prediction (NCEP). The variables are the wind at 10 m above the ocean surface, air temperature and humidity at 2 m above surface, precipitation and longwave and incoming shortwave radiation. The atmospheric forcing has approximately 0.3° horizontal resolution. The 6-hourly CFSR product is used in this study. CFSR is considered superior to the previous NCEP reanalysis products because (i) it has higher resolution and uses improved assimilation methods, (ii) it is generated considering the ocean, (ii) it includes an interactive sea ice model, and (iv) it assimilates satellite radiances. For more details see *Saha et al.* (2010).

A second atmospheric forcing set was used to conduct some additional Runs (Table 4.1). This set was obtained from the Environment Canada regional deterministic prediction system (RDPS) which is based on the global environmental multiscale model (GEM). RDPS covers North America and has a horizontal resolution of about 15 km (10 km after October 2012). The RDPS fields were obtained through personal communication with Environment Canada meteorologist Mark Pilon. RDPS has higher resolution than CFSR, however it lacks an interactive ocean component. I will focus subsequent discussion on experiments conducted using CFSR. The experiments using RDPS are designed to investigate the sensitivity of GoMSS to the atmospheric forcing.

For river outflow I used monthly climatological values based on the Coordinated Ocean-ice Reference Experiments (CORE) version 2 (*Griffies et al.*, 2012). Because this river dataset is relatively coarse (1°), I limited the river source to only one grid cell in the direction across the coast and spread the river source over more grid cells in the direction along

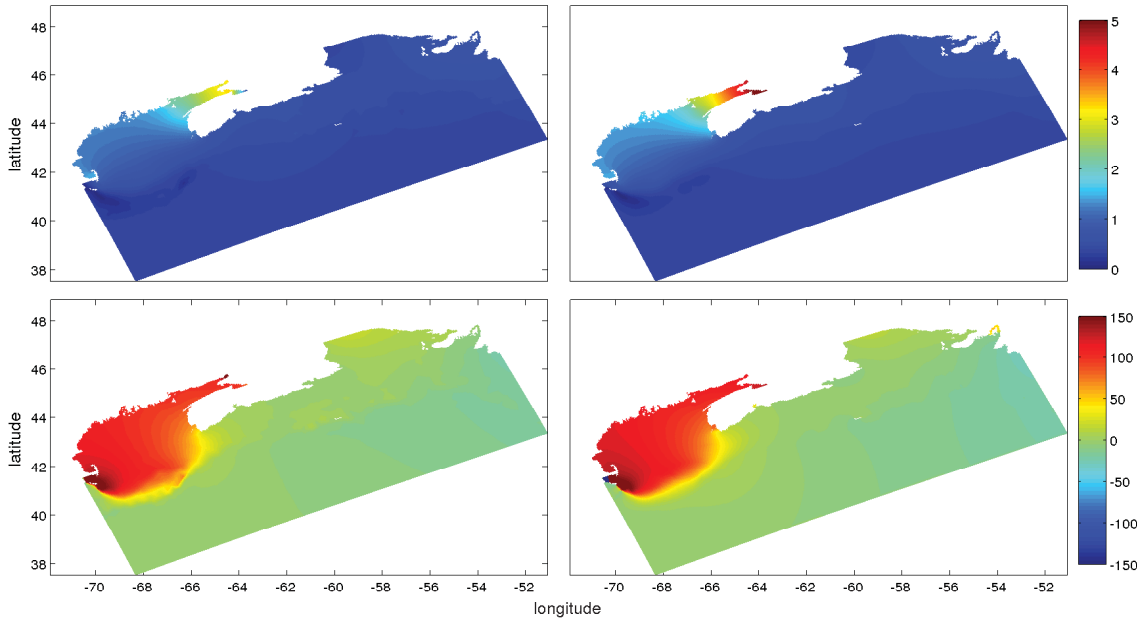

Figure 4.12: M_2 amplitude (top panels) and phase (bottom panels) from the global FES2004 model (left panels) and GoMSS (right panels). The amplitude is in m.

the coast depending on the river's size. The global system uses monthly climatological river values based on the database described by *Barron and Smedstad* (2002). Both the above monthly climatologies are based on the river outflow of about 1000 rivers. Note GoMSS captures better the location of the rivers than the global system because i) it has higher horizontal resolution, ii) represents better the coastline, and iii) spreads the river output along the coast rather than across.

The initial and open lateral boundary conditions of GoMSS (excluding tides) were interpolated from daily temperature, salinity, sea surface height and horizontal current velocity fields from the 1/12° global HYCOM/NCODA analysis (i.e. global system). Temperature and salinity at GoMSS open lateral boundaries are specified using a simple upwind advection scheme with a 10 grid point sponge layer. Different treatments are used for the barotropic and baroclinic current components (see section 4.2.5 for details).

Five tidal constituents (M_2, S_2, N_2, K_1 and O_1) were also used to drive the model through its open lateral boundaries. (The global model does not include tides.) The tidal elevations and transports were obtained from the FES2004 barotropic global tidal model developed by the Laboratoire d'Etudes en Geophysique et Oceanographie Spatiales (LEGOS), France

(*Lyard et al.*, 2006). FES2004 is a finite element model with higher resolution near the coast. Although FES2004 has high resolution near the Scotian Shelf and adjacent seas it does not resolve the Minas Basin and several small harbours along the Scotian coast (Figure 4.12). This is important because the Minas Basin is a major component of the Bay of Fundy system which has the largest tides in the world. (Its resonance frequency is very close to the M_2 tidal frequency.)

Figure 4.13 compares the FES2004 tidal predictions with observed amplitudes and phases at the five chosen frequencies. The comparisons were made for 39 locations on the shelf and shelf break (see Figure 4.11). The observations were obtained from NOAA, Fisheries and Oceans Canada, and Moody et al. (1984). Overall FES2004 is in good agreement with the observations. There is however a tendency for FES2004 to underestimate M_2 and N_2 in the Bay of Fundy.

4.4 Summary

In this chapter I have described the global system and the regional model to be used for ocean downscaling. I have also evaluated the accuracy of the global system because errors and biases in the global fields will propagate to the regional model (i.e., "garbage in, garbage out"). Preliminary comparison with observations shows that the global system provides reasonably realistic local fields in the study area, within the limits of its resolution. This is not surprising because the global system assimilates satellite data and local observations. There are however several phenomena that the global system does not simulate explicitly (e.g., tides). Furthermore, in several areas higher resolution is necessary to resolve local features. GoMSS was designed to overcome these limitations of the global system. In the next chapter, I validate the results from GoMSS, and investigate if GoMSS improves the accuracy of the global system's fields.

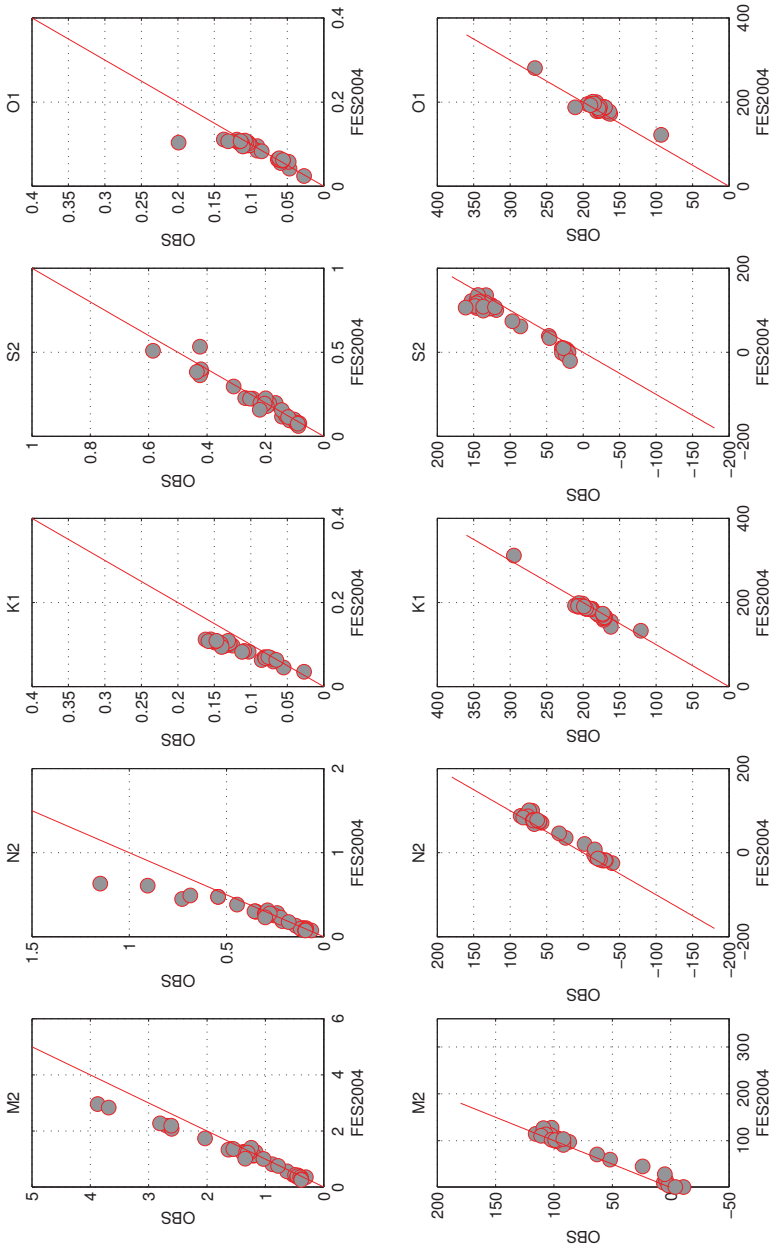

Figure 4.13: Comparison of observed and predicted (FES2004) tides for 39 locations and the following frequencies: M_2, S_2, N_2, K_1 and O_1. The top panels compare the amplitudes and the bottom panels compare phase. The comparison locations are shown in Figure 4.11. The M_2, N_2 and S_2 phases are mapped to $\pm 180^\circ$ to avoid wrap around problems.

CHAPTER 5

EVALUATION OF THE ONE-WAY NESTED REGIONAL MODEL

The regional model was developed to address weaknesses of the global system including the absence of tides and lack of resolution. It is reasonable to believe the global system can be improved by resolving explicitly high resolution features and by introducing the tides, and their interaction with the local ocean conditions and bathymetry (e.g tidal mixing, tidal rectification, internal tides). However, as discussed in chapter 2, the one-way nesting method may not be sufficient to keep the regional model solution consistent with the global system imposed at the lateral boundaries. Thus, even if GoMSS has higher resolution and tides, it is not certain it will accurately simulate the Scotian Shelf and Gulf of Maine variability better than the global system. For example, the regional model may generate erroneous small scale variability, not because the model dynamics is flawed, but because the large scale patterns (that drive the small scale variability) are misplaced (or become decorrelated with the large scale patterns imposed at the lateral boundaries).

To check if GoMSS improves the fields predicted by the global system, its output is evaluated by comparison with observations and a climatology. GoMSS performance is also compared to that of the global system. The evaluation is ordered based on the time scale of variability. In section 5.1 the model tides are compared with observations and results from previous studies. The tidal residual circulation, and the impact of stratification on the tidal circulation, are also discussed. In section 5.2, the model's synoptic variability (timescales of hours to days) is evaluated using observations from tide gauges, CTDs and a glider. In the same section the synoptic variability of the global system and GoMSS are compared. In section 5.3, the model's mean state and seasonality is assessed using an

observed climatology and satellite observations of sea level and surface temperature, and time series observations from tide gauges and current meters. The results of the chapter are summarized in section 5.4.

5.1 Tides

In this section I evaluate GoMSS in terms of its ability to generate realistic tides. For this purpose three runs were performed as summarized in Table 5.1 Run1 is a run forced only by the barotropic tides with no variation in atmospheric forcing or water density. This run was for one year. Run2 is a real ocean simulation run with tides for 3 years (1-January-2010 to 31-December-2012). Run2s is the same as Run2 except for smoothing of the bathymetry in the Gulf of Maine and a reduced run length (1 January, 2010 to 31 December, 2010).

Table 5.1: Summary of the three runs used to evaluate the Tides in GoMSS.

Run name	Period	Density	Atmospheric forcing	Smoothed bathymetry	Tides
Run1	1 year	Constant	Constant, spatially uniform	No	Yes
Run2	2010 to 2012	Varying	CFSR	No	Yes
Run2s	2010	Varying	CFSR	Yes	Yes

5.1.1 Tidal Elevation

Tidal predictions from Run1, driven solely by tidal forcing, are first compared with FES2004 tidal predictions (*Lyard et al.*, 2006) and also observations. I focus on M_2 because it is the dominant tidal constituent over most of the model domain. Figure 4.12 compares spatial maps of the amplitude and phase of M_2 from Run1 (right panels) and FES2004 (left panels). As expected, Run1 amplitude of M_2 is large in the Gulf of Maine, reaching a maximum amplitude (over 5 meters) in the Bay of Fundy. Generally, the M_2 amplitude is small in deep water away from the continental shelf. Run1 and FES2004 predictions of M_2 are qualitatively similar, except in the Minas Basin. (Note the FES2004 model does not resolve Minas Basin.) Similar qualitative agreement is also found for S_2, N_2, K_1 and O_1 (not shown).

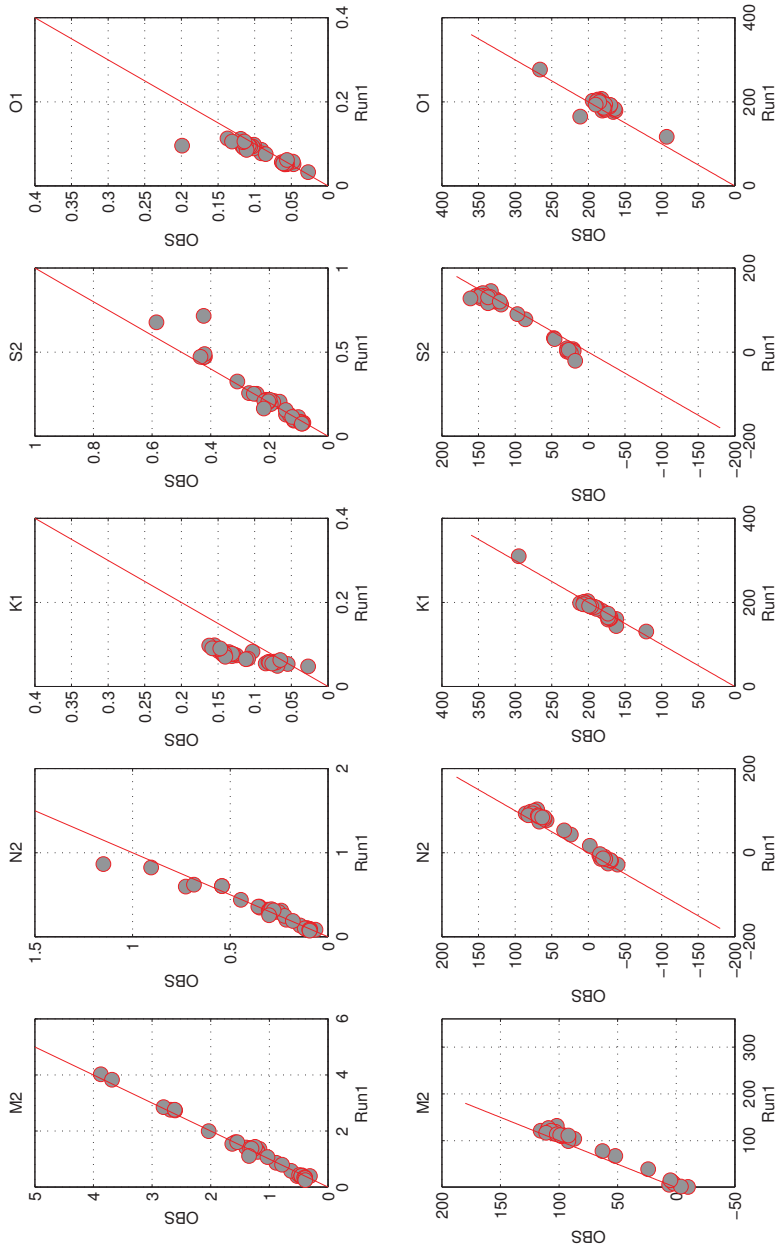

Figure 5.1: Comparison of the amplitude and phase of five tidal constituents based on observations and predicted by Run1 for specific locations shown in Figure 4.11. Results are presented separately for the following constituents: M_2, S_2, N_2, K_1, and O_1. Same format as Figure 4.13.

To provide a quantitative assessment, tidal elevations predicted by Run1 were compared with observed amplitudes and phases of the five tidal constituents (M_2, N_2, S_2, K_1 and O_1) from 39 coastal locations (Figure 4.11). The amplitude and phase of the observed tides and Run1 predictions are directly compared in Figure 5.1. The error statistics are given in Table 5.2. Overall there is no significant bias, and the standard deviation of the errors in amplitude and phase (mapped to $\pm 180^\circ$ to avoid wrap around problems) is small for all five constituents examined (e.g., 9 cm for the amplitude of M_2, and 5.6° for the corresponding phase, averaged over the 39 stations).

Table 5.2: Ability of Run1 to predict tidal elevations at the 39 locations shown in Figure 4.11. The first row shows the observed mean tidal amplitude in cm (averaged over the 39 locations) for the five dominant constituents. The second and fourth rows show the mean of the differences in tidal amplitude (cm) and phase (degrees, mapped to $\pm 180^\circ$) of the predictions and observations. The third and fifth rows show the corresponding standard deviations of the differences in amplitude and phase.

Tidal Constituents	M_2	N_2	S_2	K_1	O_1
mean(A_{obs})	133.3	31.1	21.3	12.0	9.8
mean($A_{obs} - A_{Run1}$)	-2.7	0.5	-1.5	4.6	1.3
std($A_{obs} - A_{Run1}$)	9.4	5.9	5.3	2.3	1.7
mean($\phi_{obs} - \phi_{Run1}$)	-12.4°	-16.1°	12.2°	4.8°	-13.1°
std($\phi_{obs} - \phi_{Run1}$)	5.6°	6.4°	9.8°	5.7°	11.4°

5.1.2 Tidal Residual Circulation

Tides and tidal currents are affected by the following non-linear terms in the governing equations for barotropic flow: the tidal pumping term in the continuity equation, and the advection and bottom friction terms in the horizontal momentum equation. Due to their non-linear effect on the main tidal constituents, a time invariant current can be generated (tidal rectification). I will refer to this time invariant current as the tidal residual current. Additionally, the non-linear interaction between the tidal constituents can also generate energy at other frequencies. For example, the non-linear interaction of M_2 with itself generates the M_4 harmonic constituent, which has half the period of M_2. This effect does not directly affect the mean flow and thus it does not contribute to the tidal residual circulation.

To understand how residual circulation develops on top of a topographic feature (e.g., a sea mountain or ridge) consider the conservation of potential vorticity in the barotropic

case:

$$\frac{D}{Dt}\left(\frac{\zeta + f}{h}\right) = 0 \tag{5.1}$$

where ζ is the relative vorticity (positive for counterclockwise), f is the Coriolis parameter, and h is the total water column depth. Equation (5.1) shows that when a water parcel moves to shallower depth (e.g., over a topographic feature) its relative vorticity will decrease (leading to clockwise rotation) and vive versa. Thus, a fluid parcel that is advected by the tide into shallow regions (e.g., up the slope of a topographic ridge), will obtain negative vorticity, while the opposite happens when the tide reverses and the fluid parcel is advected to deeper water. In the absence of friction, there is no residual current (i.e., the vorticity flux over a tidal cycle is zero) because the current and the vorticity are 90° out of phase. However, in the presence of friction, the vorticity and the current are partially in phase which leads to a mean flow along the ridge (i.e., along isobaths) with the shallow side to the right (in the north hemisphere).

The non-linear contribution of the tides is not reproduced by models without tidal forcing, like the global system discussed in this study. This may not be important on the global scale, however, tidal rectification can significantly alter the regional and local scale circulation. More specifically, it is known that tidal rectification generates small scale circulation features, including gyres, on the Scotian Shelf and in the Gulf of Maine (e.g., *Loder*, 1980; *Greenberg*, 1983; *Naimie et al.*, 1994; *Hannah et al.*, 2001).

The regional tidal residual circulation is estimated by Run1 which is driven solely by tidal forcing (M_2, S_2, N_2, K_1 and O_1 tidal constituents). The speed of the residual current is shown in Figure 5.2. The tidal residual flow is clearly linked to the complex bathymetry (e.g., submarine banks and channels along the Scotian Shelf and the adjacent seas) and several gyres arise due to tidal rectification.

In the Gulf of Maine, Run1 generates a tidal residual circulation that is in good agreement with observations and previous modelling and theoretical studies (e.g., *Loder*, 1980; *Butman et al.*, 1982; *Greenberg*, 1983; *Hannah et al.*, 2001). Specifically, the model generates a clockwise current around Georges Bank (Figure 5.3) and Nantucket Shoals with a speed of about 0.2 m s^{-1} on the north side of the Bank. In the Bay of Fundy there is flow into the Bay along the coast of Nova Scotia and outflow along the coast of New Brunswick; a cyclonic eddy develops between these two flows (not shown), as expected.

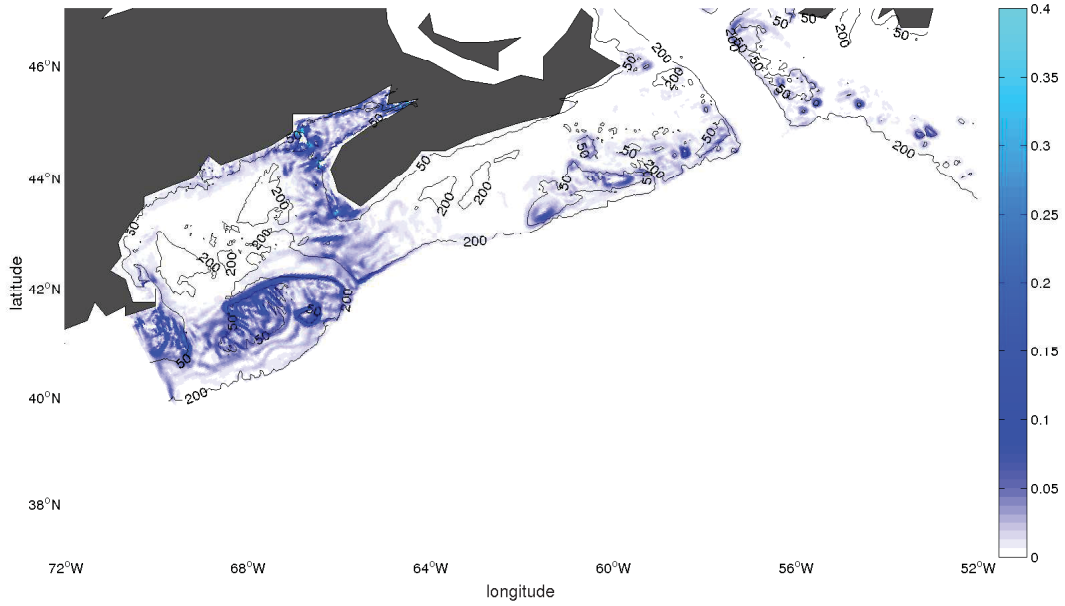

Figure 5.2: Speed of the tidal residual current predicted by Run1. The magnitude is in m s^{-1}.

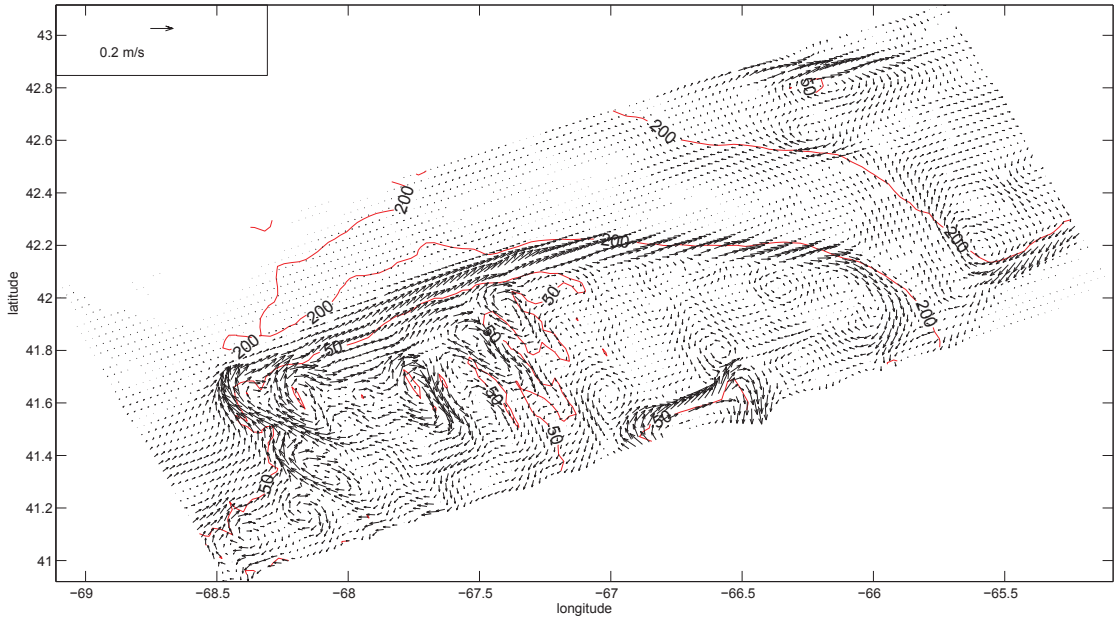

Figure 5.3: The tidal residual circulation in the vicinity of Georges Bank and Browns Bank calculated by Run1. This is a zoom of Figure 5.2.

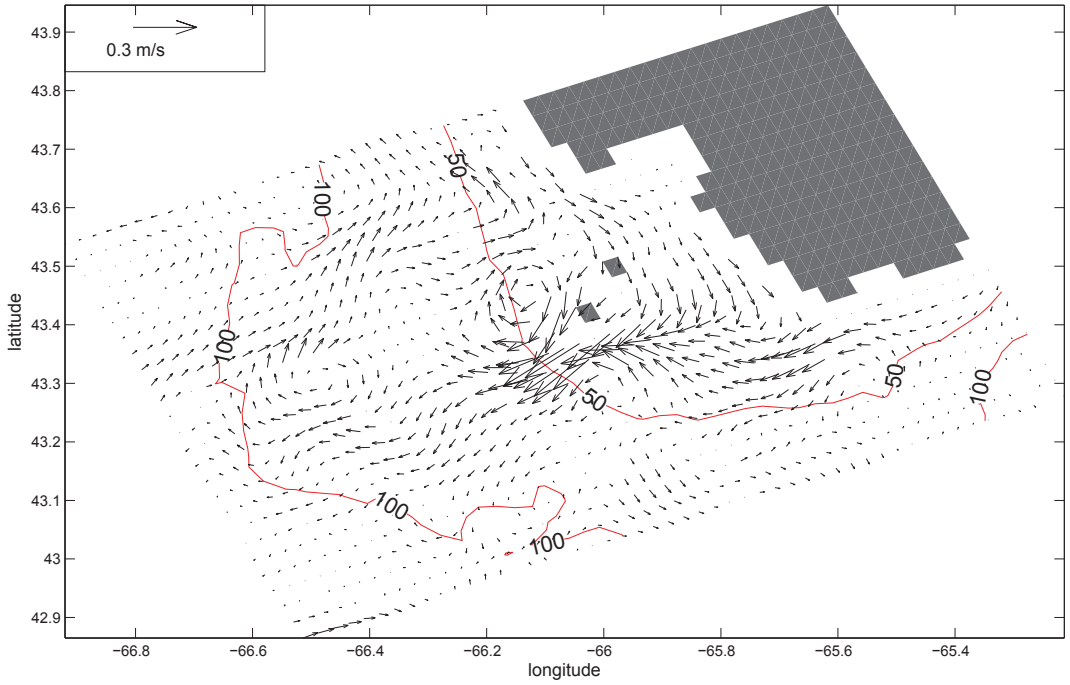

Figure 5.4: The tidal residual circulation in the vicinity of Cape Sable calculated by Run1. This is a zoom of Figure 5.2.

The model also simulates the observed anticyclonic circulation on top of Browns Bank (Figure 5.3), and a strong inflow (up to 0.2 m s^{-1}) near Cape Sable accompanied by weaker return flow along the coast of Nova Scotia (Figure 5.4).

On the Scotian Shelf the tidal residual circulation is weaker, however a strong clockwise current (speeds of 0.1 m s^{-1}) is evident around Sable Island, along with several smaller clockwise gyres associated with the local topography (Figure 5.5). Clockwise circulation around Sable Island has been observed in previous studies (e.g., *Hannah et al.*, 2001) but it has been difficult to confirm the tidal residual current based on the observations or model runs that include atmospheric forcing (e.g., winds). To my knowledge, my results are the first time that the influence of tidal rectification has been modelled with such high resolution in the vicinity of Sable Island. Additionally, the rectified tidal current has speeds that are comparable to the observed speeds means (as I will show in section 5.3), implying that tidal rectification is a major contributor to the observed circulation around Sable Island.

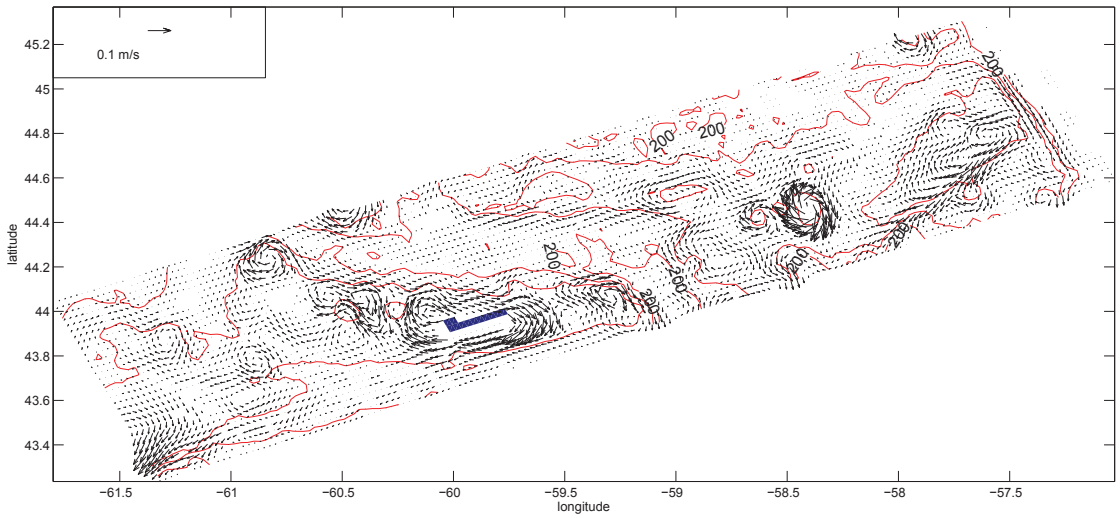

Figure 5.5: The tidal residual circulation in the vicinity of Sable Island calculated by Run1. This is a zoom of Figure 5.2.

Overall, Run1 simulates accurately the tidal residual circulation on the Scotian Shelf and in the Gulf of Maine. However, there are some discrepancies in the residual current speed between Run1 and some previous modelling studies. For example Run1 generates a somewhat faster residual current around Georges Bank than the study of *Greenberg* (1983). This is not surprising because depth-independent models, as in *Greenberg* (1983) may underestimate the magnitude of the flow as pointed out by *Loder and Wright* (1985).

5.1.3 Impact of Stratification on Tides

The vertical stratification of the water column on continental shelves often exhibits a pronounced seasonal cycle. During winter, the upper water column is usually well mixed by strong winds and vertical convection caused by loss of heat by latent and sensible heat fluxes. In shallow water, this well-mixed layer can extend down to, and overlap with, the bottom mixed layer. During summer, the stratification is enhanced in areas where the combination of tidal and background current cannot mix the vertical gradients caused by the increased supply of heat. The front between the stratified and vertically mixed regions is often referred to as a tidal-mixing front and its position in summer can often be predicted by the Simpson-Hunter parameter, h/u^3, where h is the water depth and u is the amplitude of the tidal current (*Simpson and Hunter*, 1974).

Previous modelling and observational studies (e.g., *Loder and Wright*, 1985; *Marsden*, 1986; *Loder et al.*, 1992; *Naimie et al.*, 1994; *Howarth*, 1998; *Cummins et al.*, 2000; *Ohashi et al.*, 2009; *Chen et al.*, 2011; *Müller et al.*, 2014) have shown that stratification of the water column can strongly influence tidal elevations and currents over the continental shelf. More specifically, summer stratification can affect the tides by i) changing internal and bottom friction, and thus the vertical structure of currents, ii) modifying the spatial structure of coastal trapped waves modes and their propagation along the coastal waveguide, iii) generating baroclinic tides. It follows that the tides may experience a seasonal variation due to the seasonal change in density. I now investigate if such a seasonal variation is predicted by Run2. The approach is to compare the Run2 tidal predictions for winter (January-March) and summer (July-September).

The tidal elevations predicted by Run1 do not vary seasonally in contrast to the Run2 predictions which are influenced by changes in stratification. However, in agreement with *Chen et al.* (2011), the seasonal changes in the amplitude and phase of tidal elevation are small (Table 5.3). More specifically, the seasonal changes in M_2 amplitude are less than 10 cm outside the Bay of Fundy, and less than 5 cm outside the Gulf of Maine. The seasonal changes in tidal currents are however much larger and are the focus of the rest of this section. I focus mainly on M_2 because it is the dominant tidal constituent in the study region, however, some results for K_1 are discussed.

Table 5.3: Mean and standard deviation of the differences in tidal elevation amplitude (cm) and phase (degrees) between winter (superscript w) and summer (superscript s) according to Run2. The first row shows the mean tidal elevation amplitude for summer. All results are based on averages over the whole model domain.

Tidal Constituents	M_2	N_2	S_2	K_1	O_1
mean(A^s_{Run2})	53.1	12.2	11.5	5.9	6.0
mean($A^s_{Run2} - A^w_{Run2}$)	1.0	0.2	0.0	0.2	0.0
std($A^s_{Run2} - A^w_{Run2}$)	3.6	0.7	0.4	0.4	0.3
mean($\phi^s_{Run2} - \phi^w_{Run2}$)	-0.1°	0.2°	-0.3°	0.8°	1.6°
std($\phi^s_{Run2} - \phi^w_{Run2}$)	1.0°	1.4°	2.0°	4.1°	9.3°

5.1.4 Impact of Stratification on M_2

M_2 tidal current ellipses from Run2 at the sea surface are shown in Figure 5.6 for both winter (blue) and summer (red). The ellipses exhibit high spatial variability, with strong

tidal currents in the Bay of Fundy (up to 3 m s^{-1}) due to its well-known, near M_2 tidal resonance (*Garrett*, 1972), and also over Georges Bank (0.9 m s^{-1}) due in part to the shallow bathymetry. Over the Scotian Shelf, near the coast, the M_2 currents are negligible, however, they are stronger near the shelf break (about 0.2 m s^{-1}) and Sable Island (up to 0.4 m s^{-1} on the east and the west side of Sable Island). Similarly, near the coast of south Newfoundland, the M_2 currents are generally weak but become stronger over the outer shelf. In deep water, the M_2 currents are generally very weak as expected but they are amplified in the vicinity of the Northeast Channel. This amplification is not evident in Run1 and so it is related to the presence of stratification as I discuss later in this section. The overall distribution, strength and orientation of the M_2 ellipses are generally consistent with previous studies (e.g., *Smith*, 1983; *Hannah et al.*, 2001; *Ohashi et al.*, 2009). Quantitative comparison of Run2 ellipses with observations is discussed in Appendix B.

It is clear from Figure 5.6 that the M_2 currents vary seasonally over most of the model domain. Run1 does not predict such a seasonal variation. Thus, stratification does impact the surface tidal circulation, at least for M_2. To quantify the seasonal variation, Figure 5.7 shows the following difference in maximum M_2 surface current speed between winter and summer:

$$\delta v = \max_t |\mathbf{u}^s(t)| - \max_t |\mathbf{u}^w(t)| \tag{5.2}$$

where $\mathbf{u}^s(t)$ and $\mathbf{u}^w(t)$ are the time-varying M_2 surface currents at a fixed grid point for summer and winter respectively. While it is challenging to observe the differences between winter and summer in the tidal ellipses (Figure 5.6), they are clearly evident in the spatial map of δv (Figure 5.7).

Figure 5.7 clearly indicates large seasonal differences in the speed of the M_2 surface tidal current that exceed 0.1 m s^{-1} in the Gulf of Maine. The differences are largest over Georges Bank, in Bay of Fundy, and in the vicinity of the Northeast Channel where the M_2 currents are stronger during summer. Arguably the most remarkable features of Figure 5.7 are (i) the pattern of ridges (henceforth striations) aligned with Georges Bank in the Gulf of Maine, and (ii) the summer intensification of M_2 current speed over Georges Bank. The striations in δv are due to spatial variability in the summer tidal ellipses. The striations are evident in each summer of Run2 (2010, 2011 and 2012) and they appear at roughly the same location; their amplitude and shape however experience some interannual variability.

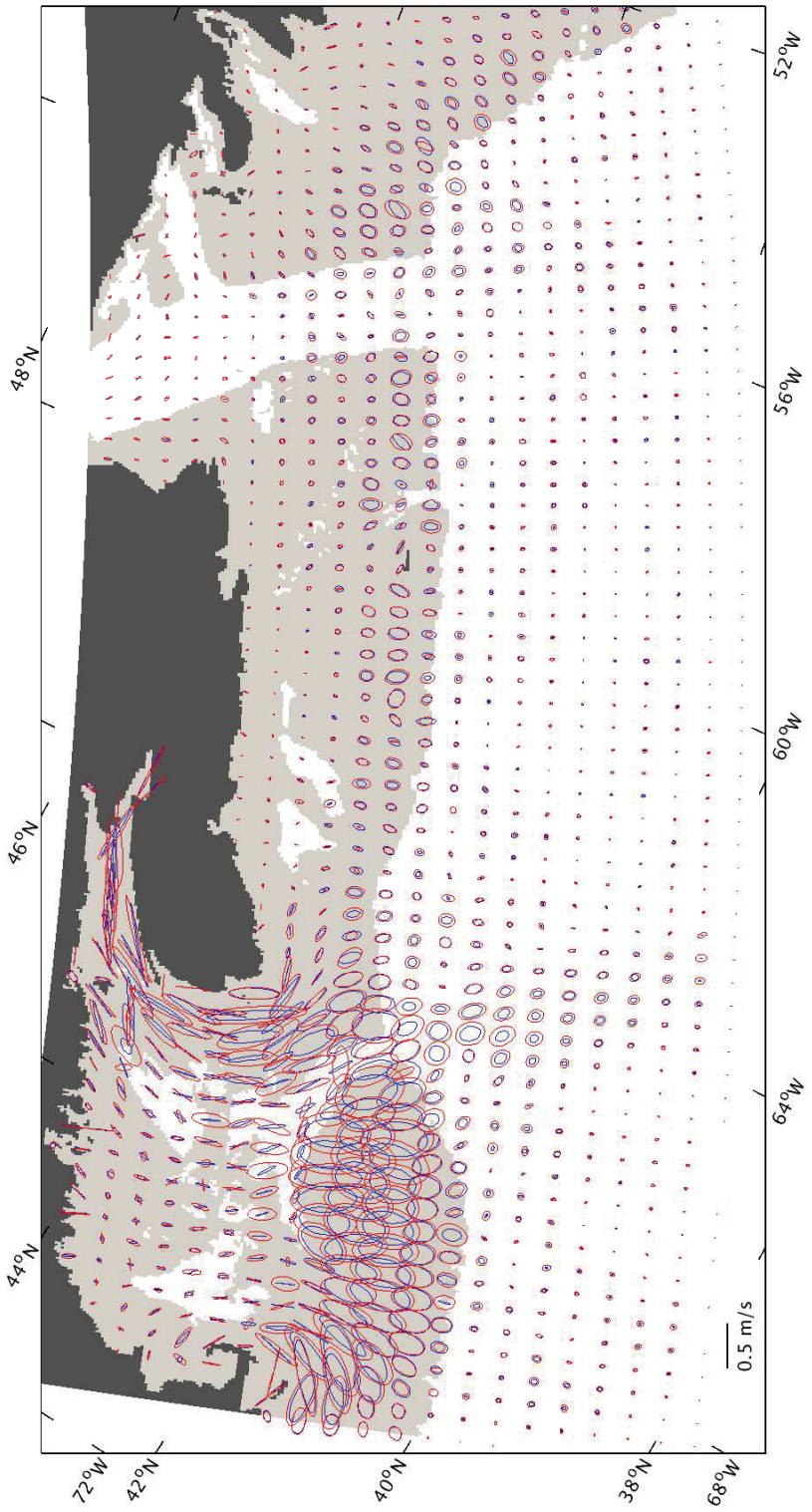

Figure 5.6: M_2 surface tidal current ellipses predicted by Run2 for winter (blue) and summer (red). Ellipses are shown every 10 grid points. The light gray shading shows areas shallower than 200 m.

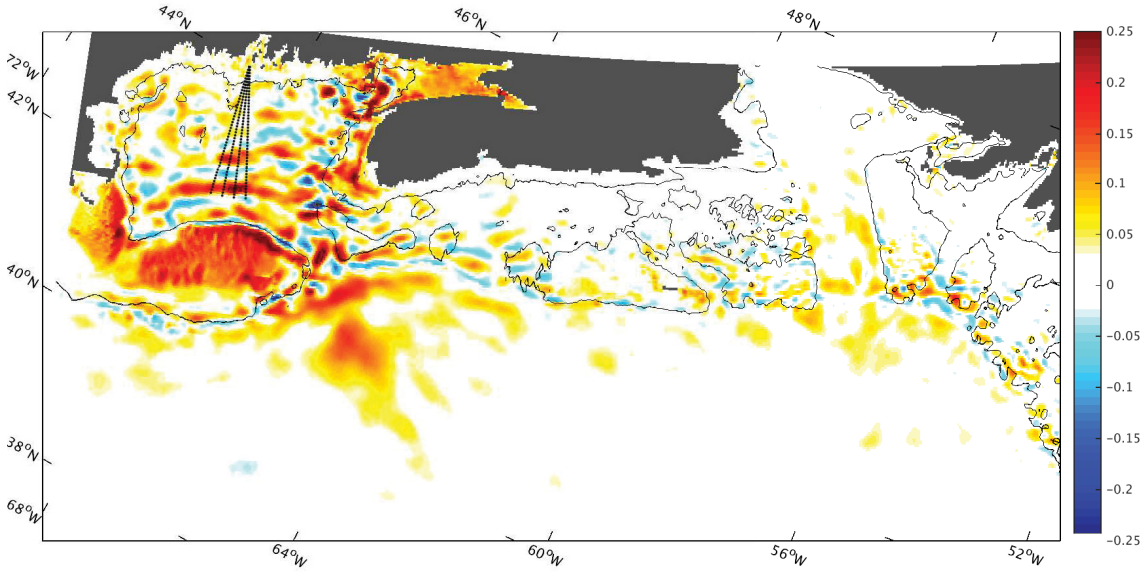

Figure 5.7: Seasonal differences in the speed of the M_2 surface current, summer - winter. The color shading shows δv (in m s^{-1}) based on Run2 for the period 2010-2012. The four dashed lines in the Gulf of Maine are radial paths along which surface currents were measured using an HF radar antenna located at Greens Island, Maine. The thin black line shows the 100 m isobath.

To our knowledge this is the first time that such a spatial pattern in the tidal currents speed has been noted.

Figure 5.8 shows the M_2 radial current maximum speed difference between summer and winter (similar to δv) for the HF radar observations (top panel) and Run2 (bottom panel). (See Appendix B for details about the HF radar observations). The four lines in each panel correspond to the four radar spokes shown in Figure 5.7. Overall the agreement between the results from Run2 and the HF radar observations is encouraging with the observations showing maxima and minima that coincide with locations of the predicted striations.

5.1.5 Physical Interpretation of the Seasonal Changes in M_2 Tidal Speed

North of Georges Bank: The vertical distribution of phase and amplitude of the cross-isobath M_2 current is shown in Figure 5.9 for a location from the north slope of Georges Bank. The profiles are shown for both winter (black) and summer (red). In winter the phase and amplitude gradually change from the surface to the bottom of the water column,

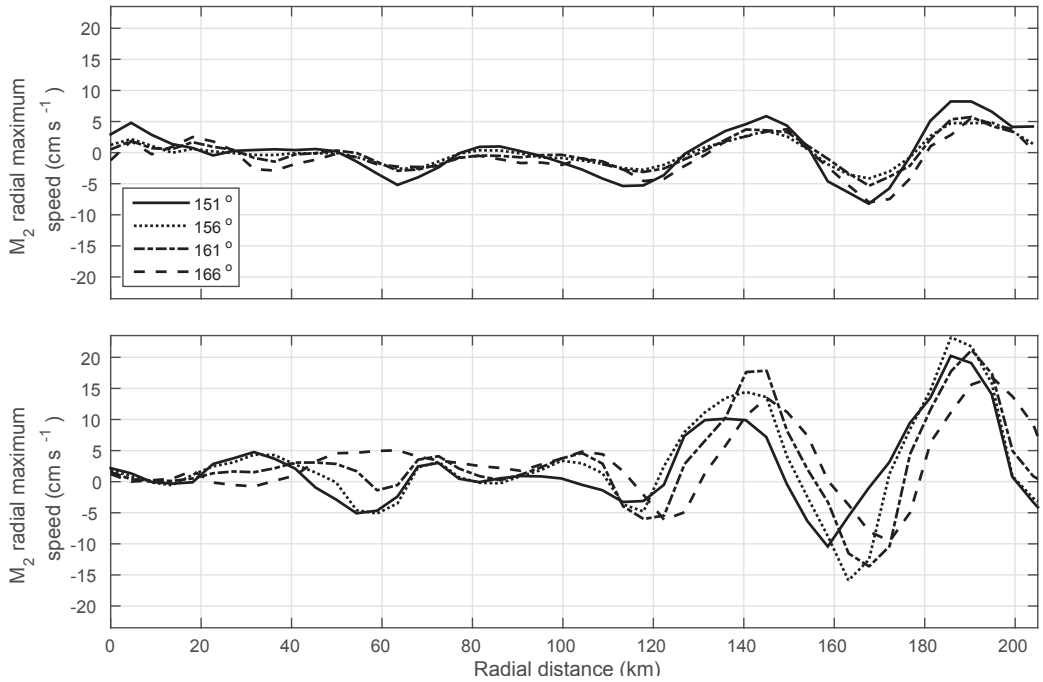

Figure 5.8: Seasonal difference in M_2 tidal current speed (summer-winter) based on radial radar observations (top panel) and Run2 (bottom panel). Each line corresponds to one of the four radial spokes shown in Figure 5.7. The legend shows the angle of each radial spoke with respect to north, measured clockwise. The radial current speeds are estimated from observations from 2011 to 2014 and the Run2 results are for 2010-2012. The x-axis shows radial distance in km with respect to the HF radar antenna at Greens Island (see Figure 5.7).

presumably due to bottom friction. However, in summer, the phase varies much more strongly with depth. This is because the vertical stratification (left panel) is enhanced and affects the tidal current. Thus, on the north slope and off the Bank, the model tide has a significant baroclinic component. This is consistent with previous observational studies (e.g., *Marsden*, 1986). More specifically, Figure 5.9 shows that the cross-isobath M_2 current phase shifts by around 85° between 10 m (above the pycnocline) and 70 m (below the pycnocline). This phase shift is consistent with observations and has been associated with internal tides (e.g., *Marsden*, 1986).

The following questions are now addressed in this subsection: Is the sequence of ridges of summer maximum speeds north of Georges Bank (the "striations") due to internal waves? What is the physical mechanism responsible for their formation? Is GoMSS able to capture the formation of internal waves due to the interaction of tides and bathymetry?

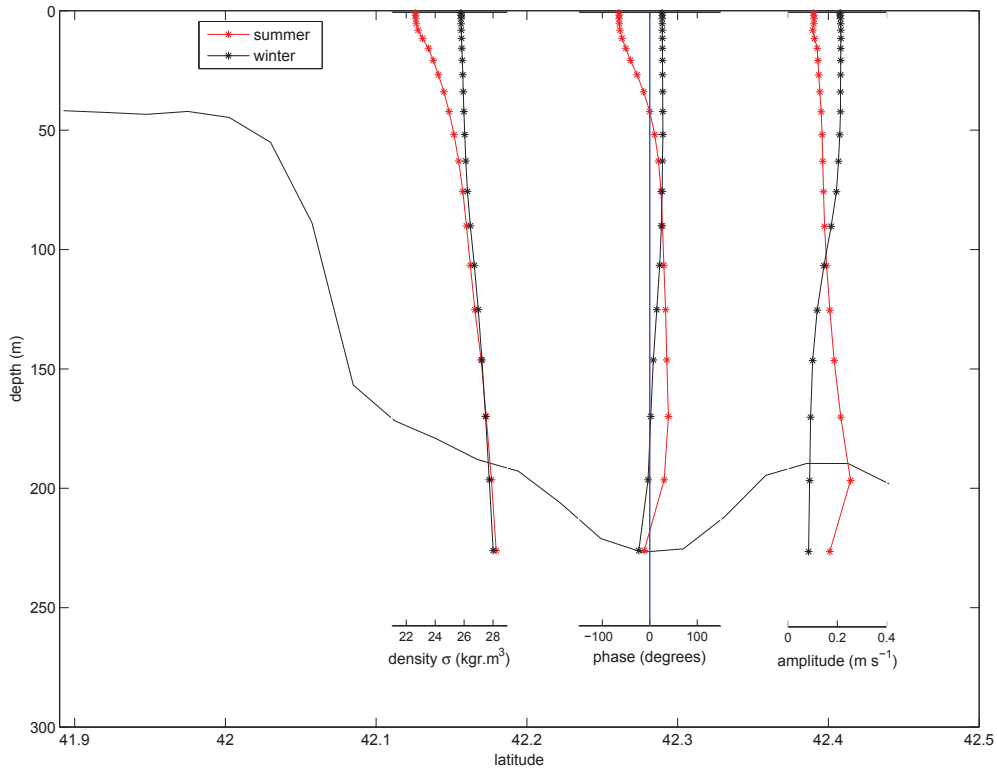

Figure 5.9: Seasonal variation of the vertical structure of the cross isobath M_2 tidal current on the northern slope of Georges Bank (location 67.75°W, 42.28°N). The bathymetry versus latitude is shown by the black line. The density profile is shown in the left subpanel, and the current phase and amplitude are shown in the middle and right subpanels respectively. Profiles for winter and summer are shown in black and red respectively. The horizontal location profile with respect to latitude (42.28°N) is indicated by the position of the y-axis of the middle subpanel. Based on Run2.

To answer these questions I will now explore the link between internal waves and strong tidal flow over steep topography.

It is well known that the flow of a stratified fluid over rapidly changing bathymetry (e.g., banks, ridges, shelf edge) can generate internal waves (e.g.; *Baines*, 1973; *Wunsch*, 1975). When the tide displaces stratified water over sloping bathymetry, it forces internal waves at the tidal frequency that are often referred to as internal tides. Previous studies (e.g., *Marsden*, 1986; *LaViolette et al.*, 1990; *Loder and Horne*, 1991; *Loder et al.*, 1992; *Lamb*, 1994) have shown that internal tides are generated along the north edge of Georges Bank.

Loder et al. (1992) and *Brickman and Loder* (1993) proposed a physical mechanism for the generation of internal tides on the north side of Georges Bank based on the analysis

of current and hydrographic observations from four locations near the Bank edge. Their explanation has been supported by the idealized non-linear, non-hydrostatic numerical modelling study of *Lamb* (1994). *Loder et al.* (1992) and *Brickman and Loder* (1993) argued that, during off-bank tidal flow, a depression in the pycnocline develops over the Bank edge that subsequently separates into two depressions. One depression propagates away from the Bank and the other towards it. The depression that propagates towards the Bank moves more slowly because it moves against the prevailing tidal flow. As the off-bank tidal flow strengthens, the current speed exceeds the expected propagation speed of the internal wave (Froude number >1, super-critical flow) and the bankward propagating depression cannot move onto the Bank. As a result, it becomes trapped and grows, becoming narrower and deeper. At the same time, the flow remains sub-critical in the deeper water off the Bank, thus as the super-critical flow meets the critical flow ahead, a sudden elevation of the ispopycnals occurs at the Bank edge that resembles a hydraulic jump. During the on-bank flow, the isopycnal depression and elevation move onto the Bank, towards the tidal-mixing front. Note the flow is always sub-critical in the deep water off the Bank and so the second depression propagates away from the Bank during both flood and ebb stages of the tidal cycle analogous to the well-known propagation of internal tides from the shelf edge into the deep ocean observed in many regions (*Wunsch*, 1975).

To show GoMSS can generate internal waves along the northern edge of Georges Bank during off-bank flow, the vertical structure of hourly snapshots of Run2 density over a typical tidal cycle is shown in Figure 5.10. (Analysis of temperature and salinity leads to the same conclusions.) The snapshots are for a typical summer M_2 tidal cycle along a section that crosses the northern flank of Georges Bank (section A-B, Figure 4.11). For the first six panels, the flow is off-bank and the tidal front is advected towards the right of each panel (i.e., northwards, toward the deeper water off the Bank). As the off-bank tidal flow strengthens, the isopycnals move downwards and a depression develops near the Bank edge. The depression splits into two: the depression labelled A becomes trapped near the Bank edge where it grows, and depression B propagates northward, away from the Bank. Overall the behaviour of the model is broadly consistent with the conclusions of *Loder et al.* (1992) and *Brickman and Loder* (1993). One difference is that depression A does not propagate onto the Bank. The reason is that our section does not coincide exactly with the observation section of *Loder et al.* (1992) and *Brickman and Loder* (1993) resulting in

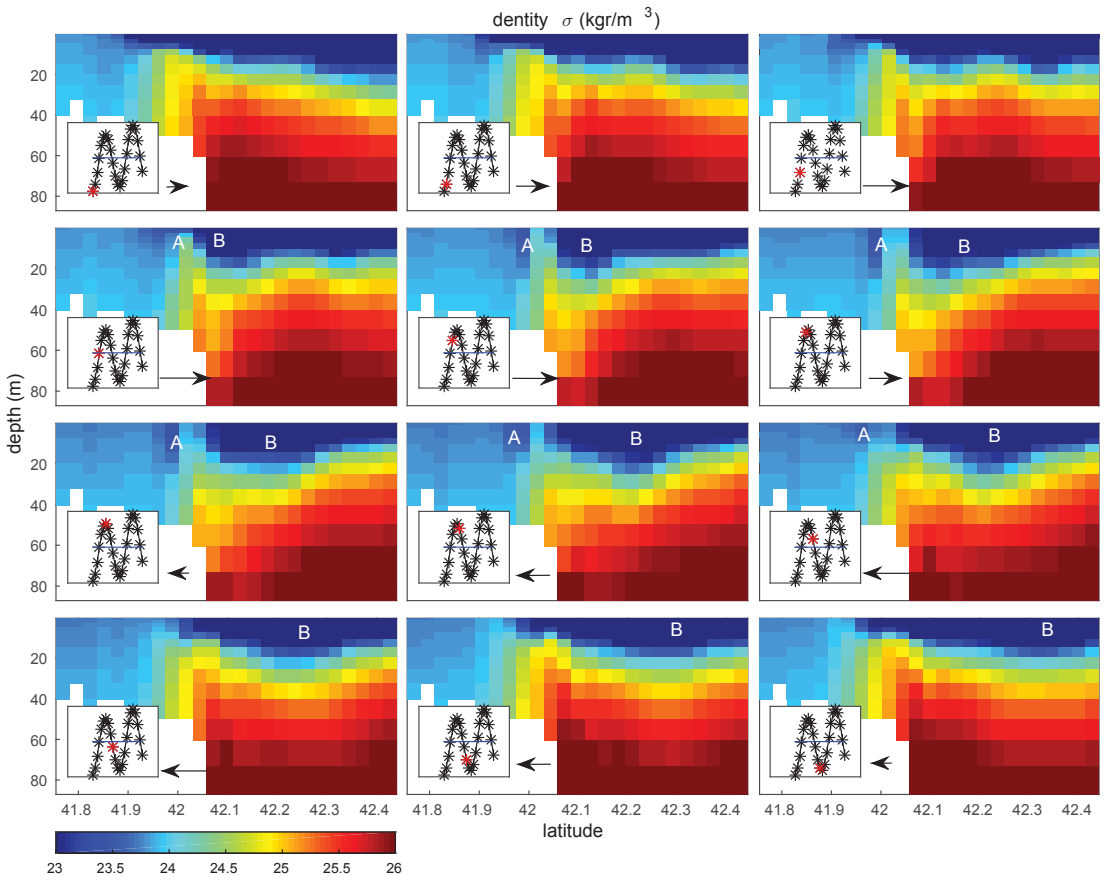

Figure 5.10: Hourly snapshots of density, over a complete M_2 tidal cycle during 10 July 2010, along a vertical section north of Georges Bank. The densities were calculated by Run2 The location of the section is shown by the line labelled A-B in Figure 4.11. The insets are time series of tidal elevation level and the red dot shows the snapshot's position in the tidal cycle. The black arrows at the bottom of each panel show the barotropic tidal current strength and direction, toward or away from the Bank.

the water column at the Bank end being well mixed, thereby suppressing propagation of the depression onto the Bank when the tidal current reverses.

The above behaviour is evident in the model output for the entire summer season. During the other seasons of the year, when the stratification is weaker, only a limited number of examples can be found of the generation and propagation of depressions near the northern edge of Georges Bank; when they do occur, the depressions are not as steep, or well defined, as in summer.

Another view of the tidal variability predicted by Run2 during summer is given by

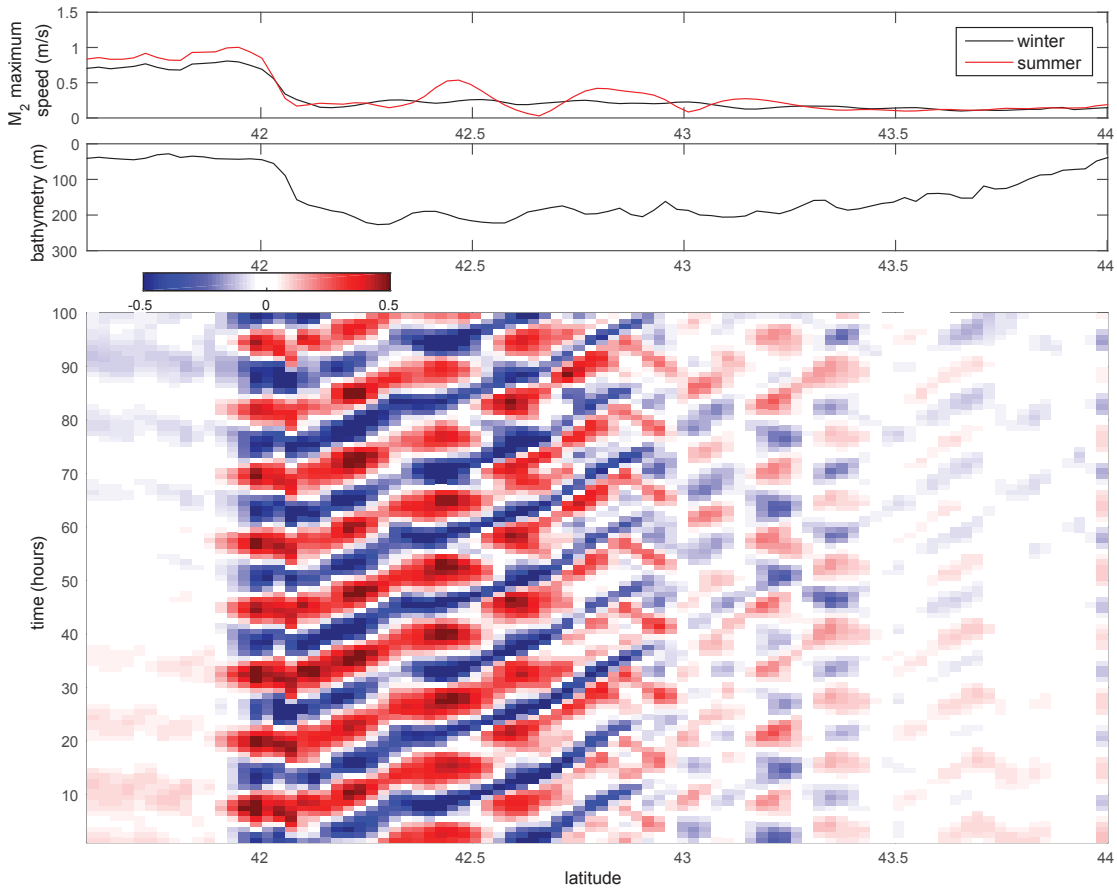

Figure 5.11: Variation of density at 20 m depth along a section running from the top of Georges Bank to the Gulf of Maine (section A-C, Figure 4.11). The top panel shows the maximum M_2 speed at the surface during summer and winter along the section. The middle panel shows the bathymetry along the section. The bottom panel is a Hovmoller diagram of the density anomaly over eight M_2 tidal cycles between 10 and 14 July, 2010. Based on Run2 speeds are in m s^{-1}.

Figure 5.11 which shows the time evolution of density near the pycnocline, along a section running from Georges Bank to the coast of Maine (section A-C section, Figure 4.11). The bottom panel is a Hovmoller diagram of the density anomaly at a depth of 20 m from 10 to 14 July, 2010. (The anomaly was calculated by removing the time mean density over exactly 8 M_2 tidal cycles for each location.) The middle panel shows the section's bathymetry (Georges Bank on the left) and the top panel shows the maximum M_2 speed during winter (black line) and summer (red line) predicted by Run2. Note the striations are clearly evident in the summer maximum speed. According to the Hovmoller diagram, the speed of propagation of signals away from the north edge of Georges Bank towards

the coast of Maine is about 0.93 m s^{-1}. This speed is similar to the speed of northward propagating internal waves (about 1 m s^{-1}) observed by *LaViolette et al.* (1990) in ocean photographs taken from the space shuttle.

Based on the above, I conclude that GoMSS does generate internal waves along the north edge of Georges Bank as observed even though it is a hydrostatic model.

Figure 5.11 also shows that the speed of the internal waves is not uniform. The wave appears to change speed in regions of rough bathymetry (Figure 5.11, compare the third and the second panel). I initially speculated that this could be caused by topographic bumps and hollows that generate more internal waves (moving in both directions) that interact with the propagating internal wave generated along the north slope of Georges Bank. I went on to speculate that this additional "bathymetric" forcing could also explain the striations in the δv map discussed above.

To test these speculations I use a Hovmoller diagram for the same depth and period calculated from the output of Run2s (i.e., Run2 with smooth bathymetry) and shown in Figure 5.12. It is clear that for Run2s, the speed of the forced internal wave is more uniform. Thus, my speculation that the apparent acceleration of the forced propagating internal waves generated north of Georges Bank is associated with localized bathymetric changes, is confirmed. However, striations are still evident in the M_2 tidal speed (see red line in top panel of Figure 5.12) for the model run with the smooth bathymetry. This is also shown in the left panel of Figure 5.13, similar to Figure 5.7. Thus, my initial speculation that the combination of propagating and locally generated forced internal waves causes the striations is wrong; it may alter the shape and intensity of the ridges in Figure 5.7 but it is not the main mechanism responsible for their formation. To determine the physical cause of the striations, I now examine another possible explanation: the superposition of barotropic and baroclinic tides.

Consider the idealized model of *Laurent et al.* (2003) of internal tide generation by barotropic tidal flow, at frequency ω, over a step in the seafloor (Figure 5.14, bottom panels). The water depth to the left and right of the step are denoted by H and $(1-\delta)H$, respectively, where δ is the normalized height of the step. The barotropic flow to the left and right of the step are assumed large scale and of the form $U_0 \cos(\omega t)$ and $(1-\delta)U_0 \cos(\omega t)$ respectively. To allow for stratification, *Laurent et al.* (2003) assumed that the background

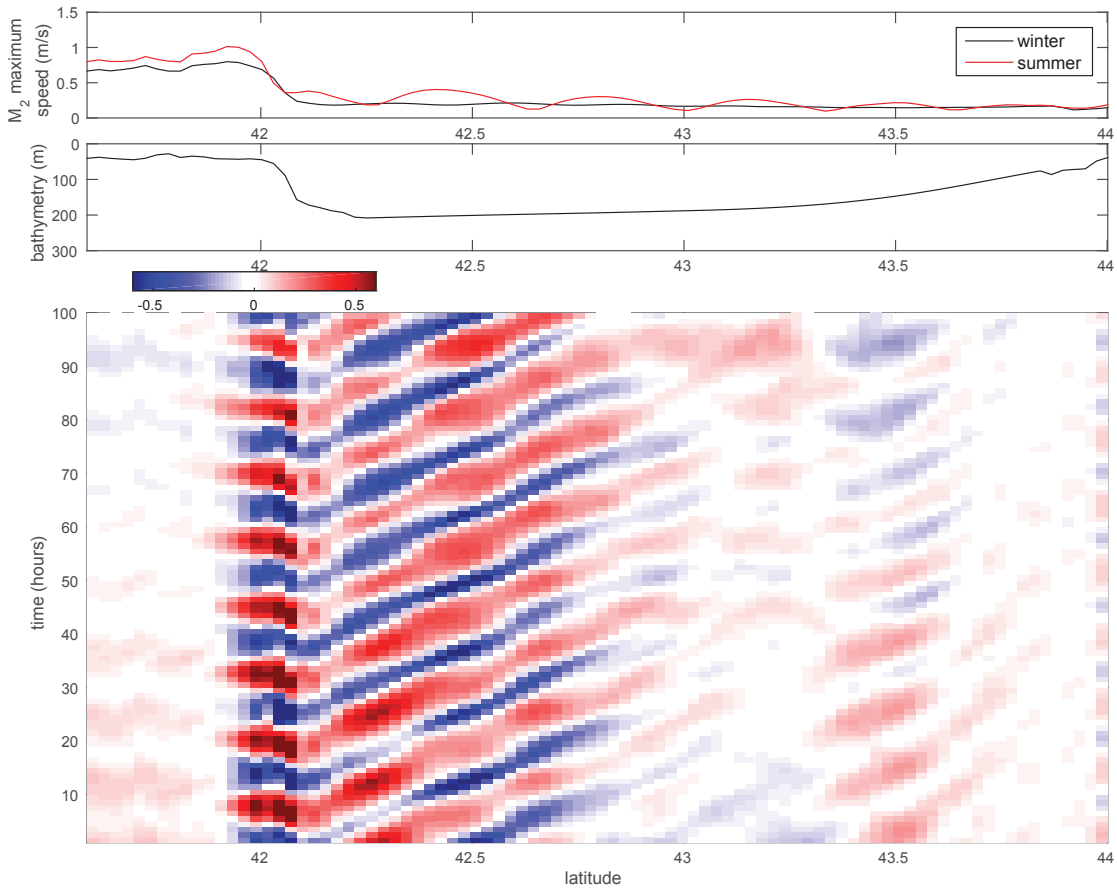

Figure 5.12: Effect of smoothing the bathymetry on the variation of density at 20 m depth along a section running from the top of Georges Bank to the Gulf of Maine. Similar format to Figure 5.11. Based on Run2s.

density field has a constant background buoyancy frequency (N). Under the assumption of a rigid lid, linear and hydrostratic flow, and $f < \omega << N$ where f is the inertial frequency, *Laurent et al.* (2003) derived explicit expressions for the baroclinic component of the flow by ensuring continuity of horizontal and vertical velocity directly above the step. Their solutions are expressed in terms of infinite sums of propagating baroclinic modes propagating away from the step in both directions. After nondimensionalizing time by ω^{-1}, the vertical coordinate by H, the horizontal coordinate by H/α where $\alpha = \sqrt{(\omega^2 - f^2)/(N^2 - \omega^2)}$ is the wave slope, the horizontal baroclinic velocity, after normalization by U_0, depends on only one parameter (the nondimensional step height δ).

Typical output from the *Laurent et al.* (2003) model is shown in the left panels of Figure 5.14 for $\delta = 1/\sqrt{2}$ and calculated using the first $n = 2000$ terms in the series

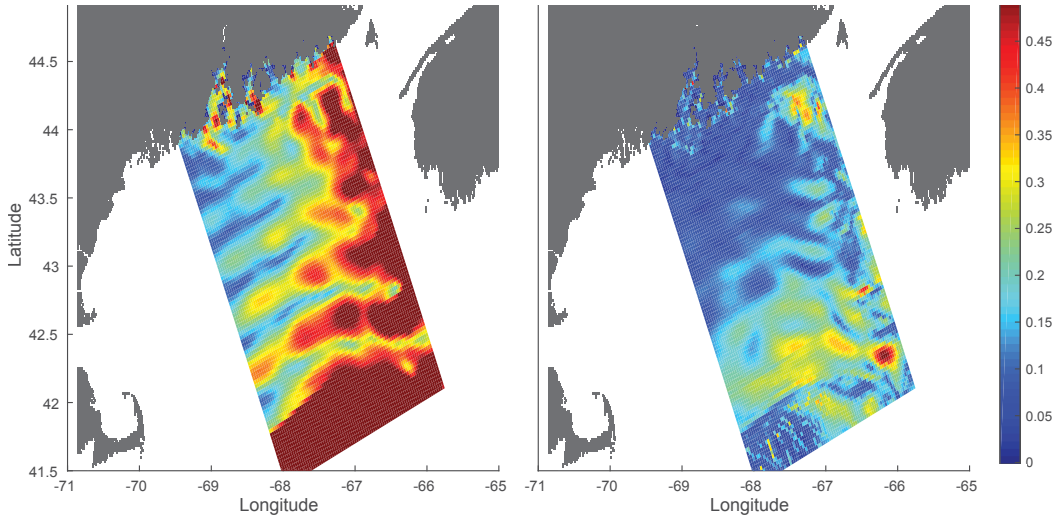

Figure 5.13: Effect of separating barotropic and baroclinic flow components on the striations. The left panel shows the maximum M_2 speed at the surface predicted by the run with smooth bathymetry (Run2s) during summer. The striations are still evident. The right panel shows the baroclinic component of the summer maximum M_2 current speed ($\max_t |\mathbf{u}'_s(0,t)|$). The striations are almost eliminated. Speeds are in m s $^{-1}$.

representation of horizontal baroclinic velocity. The bottom panel shows the step and a snapshot of the perturbation density at $t = 0$. The density changes are largest along the characteristic paths emanating from the top of the step as expected (*Laurent et al.*, 2003). The upper panel shows the amplitude of the tidal variations of the barotropic and baroclinic components of horizontal flow at the surface, and their sum (i.e., the total surface flow). As expected the baroclinic amplitude is high in the vicinity of locations where the characteristic paths reflect from the sea surface. The addition of the barotropic flow to the surface baroclinic flow modifies the spatial structure of surface current amplitude (red line) and results in locations where the total surface flow is zero.

The propagation speed of the baroclinic modes varies as the reciprocal of the mode number. Thus one might expect the higher modes to be dissipated close to their generation region, i.e., the step. To illustrate the effect of dissipation I have generated the solution using only the first baroclinic mode ($n = 1$) in the series representations. The bottom right panel of Figure 5.14 clearly indicates the propagation of the first baroclinic mode in the density perturbation as expected. The top right panel shows that the total velocity amplitude (red line) has a sinusoidal spatial structure reminiscent of the striations discussed

earlier.

In light of the above, I now assume that the total surface flow in the deep water away from the northern edge of the Bank is the sum of the barotropic flow and a contribution from the forced, first baroclinic mode:

$$U_T(x,t) = U_0\cos(\omega t) + U_1\cos(\omega t + kx)$$

where U_1 is the amplitude of the baroclinic flow and k is the associated wavenumber. The total flow can be written in the form $U_T(x,t) = A(x)\cos[\omega t + \phi(x)]$ where the spatially varying amplitude and phase are given by

$$\begin{aligned} A(x) &= \sqrt{U_0^2 + U_1^2 + 2U_0U_1\cos(kx)} \\ \phi(x) &= \arctan\left[\tfrac{U_1\sin(kx)}{U_0+U_1\cos(kx)}\right] \end{aligned} \tag{5.3}$$

If $U_0 > U_1$ it follows from (5.3) that $A(x)$ will range between $U_0 \pm U_1$ with distance from the Bank; if $U_1 > U_0$ then $A(x)$ will range between $U_1 \pm U_0$. For the special case $U_0 = U_1$, the barotropic and baroclinic components will cancel ($A(x) = 0$) when $x = \pi/k, 3\pi/k, \ldots$. In general (5.3) predicts spatial variations in $A(x)$ with a spacing equal to the wavelength of the baroclinic surface tidal current. This linear superposition of the phase locked barotropic and baroclinic tides provides a simple physical explanation for the striations in M_2 surface speed plotted in Figure 5.8. Note that from this figure I estimate the spacing between the striations to be about 40 km. Taking ω equal to the M_2 tidal frequency, a phase speed of 1.0 m s^{-1} is obtained, in good agreement with the internal tide speed from the Hovmoller plots and also the independent estimates of *LaViolette et al.* (1990).

As a further check on the linear superposition explanation, I approximate the barotropic M_2 tidal component of Run2s by vertically averaging the flow ($\overline{\mathbf{u}}(t)$) and define the baroclinic component by subtracting the depth average from the predicted M_2 tidal current at the surface($\mathbf{u}'(0,t) = \mathbf{u}(0,t) - \overline{\mathbf{u}}(t)$). The right panel of Figure 5.13 shows the summer maximum M_2 baroclinic current speed ($\max_t |\mathbf{u}'_s(0,t)|$). Clearly the striations are almost eliminated. This supports the above suggestion that the striations observed in the Gulf of Maine are caused by the linear superposition of phase-locked barotropic and baroclinic tides.

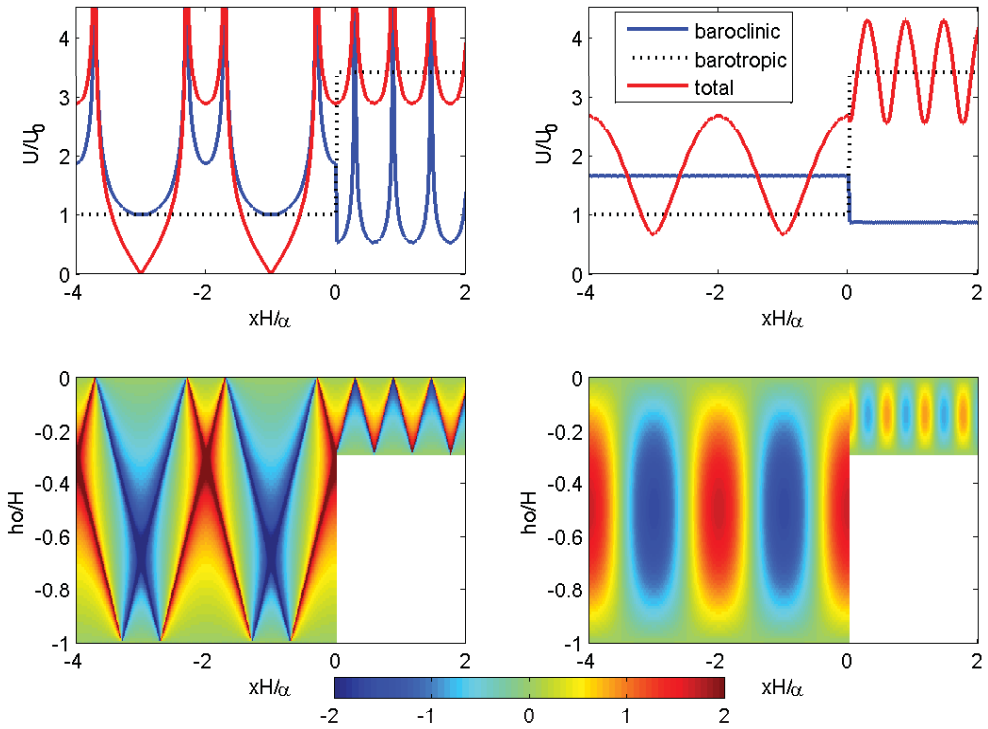

Figure 5.14: Predictions of perturbation density and surface velocity by the *Laurent et al.* (2003) model. The bottom panels show the step and pertutbation density at $t = 0$. The upper panels show the amplitudes of the surface velocity due to the barotropic and baroclinic flow and their sum. The left panels were calculated using $n = 2000$ baroclinic modes. The right panels were calculated using $n = 1$ baroclinic mode. The nondimensional step height is $\delta = 1/\sqrt{2}$.

On top of Georges Bank: The top of Georges Bank is well mixed in both summer and winter and so there is no generation or propagation of baroclinic tides in this region. Throughout the year, the phase of the M_2 current ellipses predicted by Run2 changes by less than 10° from top to bottom, and the semi-major axes decrease mononotically from the surface to the bottom, consistent with previous studies (e.g. *Marsden*, 1986). Figure 5.7 indicates an increase in M_2 current amplitude of about 0.1 m s^{-1} on top of the Bank during summer. Vertical profiles for each season (not shown) show the M_2 current speed is stronger throughout the water column, and has more shear, in summer compared to winter.

Prandle (1982) proposed an idealized, linear, barotropic model of the vertical structure of tidal currents, based on a constant eddy viscosity (A_v) and linear bottom drag formulation (coefficient r). The model is formulated in the frequency domain in terms of rotary tidal currents. This model provides a useful dynamical framework for interpreting the tidal

ellipses described in the previous paragraph. According to Prandle's model, the tidal ellipses are forced by a periodically-varying local sea level gradient. r primarily influences the amplitude of the modelled tidal currents and A_v their vertical structure.

The amplitude of the sea level gradient forcing, calculated directly from the output of Run2 is higher in summer by about 50(10)% in the along(cross) bank direction. The vertical eddy viscosity in GoMSS depends on wind and bottom stress, surface wave breaking, shear and buoyancy production. The vertical viscosity also depends on vertical convection; a large value (10 m^2 s^{-1}) is used if the column becomes gravitationally unstable (due to, for example, surface cooling). The net effect is that viscosity is larger in winter than summer.

The Prandle model, forced by sea level gradients from Run2, can accurately diagnose the seasonal changes in the overall amplitude, vertical structure, and phase of the M_2 tidal ellipses on top of Georges Bank using the seasonally varying sea level gradient and plausible values of A_v (higher in winter). I conclude that the seasonal variation of the M_2 tidal current on top of Georges Bank is due to a combination of stronger sea level gradients, and lower eddy viscosity, in summer compared to winter.

Outside the Gulf of Maine: The generation of internal tides is important not only on the north side of Georges Bank. One interesting feature is the region of relatively strong M_2 currents in the deep water offshore of the Northeast Channel in both summer and winter. This feature is absent in Run1 and is thus associated with the density field. Patterns resembling the striations are evident in the vicinity of the Northeast Channel (Figure 5.7). However their interpretation is beyond the scope of this thesis, because they are affected by (i) the complex bathymetry, resulting in waves coming from multiple directions, (ii) the time and spatially varying density field, (iii) more than just the first baroclinic mode. Although internal tides may be generated at other locations along the shelf break (e.g., *Sandstrom and Elliott*, 2011), their impact is most noticeable along the Northeast Channel because the M_2 tidal currents are very strong in this region.

5.1.6 Impact of Stratification on K_1

Stratification also impacts the other tidal constituents. However there is no indication that the changes in tides between summer (strong stratification) and winter (weak stratification) in the diurnal constituents are associated with internal wave generation in Run2. In the other semi-diurnal constituents (N_2 and S_2) striations are evident, as expected but their

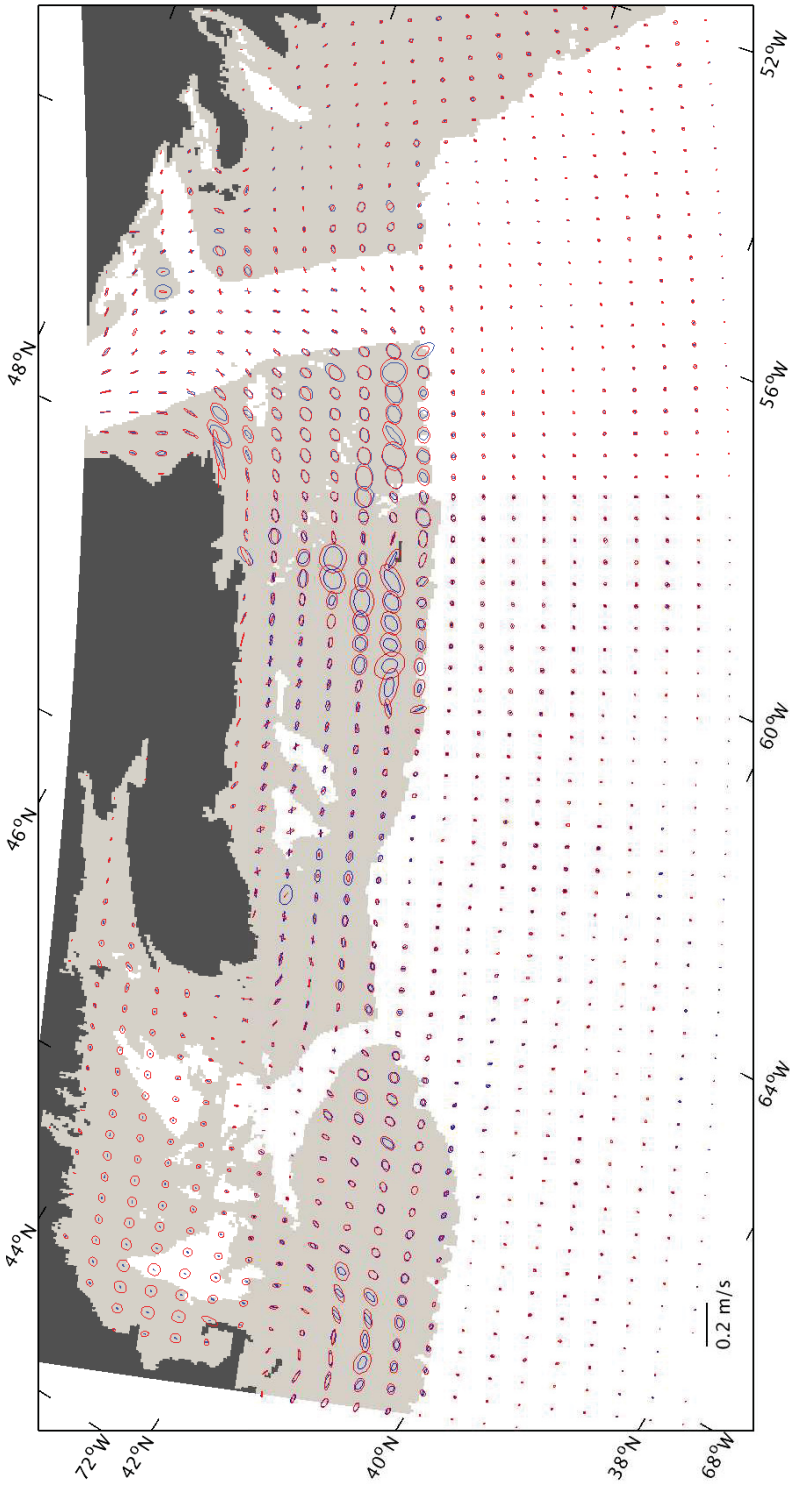

Figure 5.15: K_1 surface tidal current ellipses predicted by Run2 for winter (blue) and summer (red). Ellipses are shown every 10 grid points. The light gray shading shows areas shallower than 200 m.

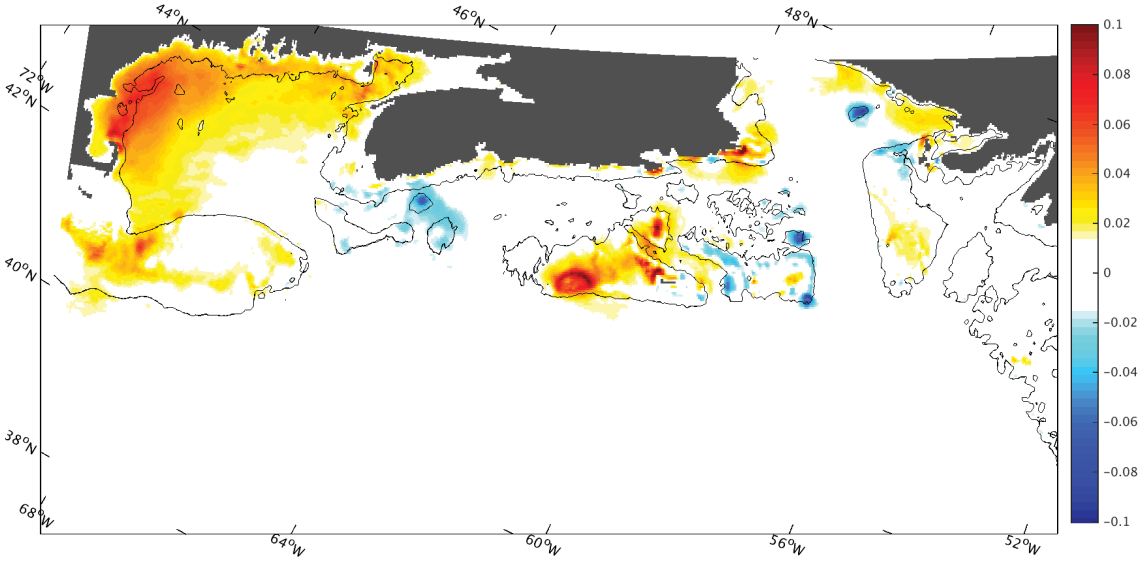

Figure 5.16: Seasonal differences in the speed of the K_1 surface current, summer - winter. The color shading shows δv (in m s^{-1}) based on Run2 for the period 2010-2012. The thin black line shows the 100 m isobath.

amplitude is much smaller than the striations in M_2. To highlight the difference of the stratification effect on M_2 with the diurnal constituents, I briefly discuss some results for K_1.

K_1 currents are generally weaker than M_2 currents. Relatively strong K_1 currents are found on the eastern Scotian Shelf (up to 0.18 m s^{-1}) and over Georges Bank (Figure 5.15). Overall the tidal current ellipses are aligned with the local bathymetry, with maximum currents found along the shelf break, and minimum currents in deep water off-shore and in the Gulf of Maine, consistent with *Daifuku and Beardsley* (1983). Comparison of Figures 5.7 and 5.16 shows that the spatial distribution of the seasonal variation in K_1 maximum speed is very different to that of M_2. This implies that the M_2 and K_1 seasonal variations are associated with different physical processes.

The map of δv (Figure 5.16) shows that the K_1 current is stronger during summer in the vicinity of Sable Island and the western part of the Gulf of Maine, and weaker over the Gully, the southern part of Scotian Shelf, and on the bank northeast of the Laurentian Channel. Over the Laurentian Channel there is a diurnal (K_1) amphidrome in the model that shifts position during summer due to changes in stratification. I believe that the shift

of the amphidrome causes the large seasonal changes in the K_1 maximum speed in this area. I do not have a physical explanation for the large seasonal variation in K_1 in the western Gulf of Maine and the Scotian Shelf.

5.2 Synoptic Variability

In this section I compare GoMSS's prediction of synoptic variability (time scales of hours to days) with observations from tide gauges, CTDs and a glider operating along the Halifax Line (see red line in Figure 4.3). Specifically, I assess the ability of GoMSS to simulate storm surges, and the synoptic variability of temperature and salinity, and then compare the performance of the global system and GoMSS. Although I focus on GoMSS with CFSR forcing, the impact of using high resolution atmospheric forcing is discussed briefly (GoMSS+RDPS).

5.2.1 Sea Level and Storm Surges

Hourly sea levels from GoMSS, and observations from four tide gauges (Halifax, Yarmouth, Portland and Boston; locations shown in Figure 4.11) for 2010 are shown in Figures 5.17 and 5.18. The Canadian tide gauges (A2 and A3) are operated by the Canadian Hydrographic Service and the American gauges (A4 and A5) are operated by NOAA. The inverted barometer effect and the tides have been removed from the observed and GoMSS time series. Some unrealistic noise near tidal frequencies is evident in the residual time series (especially the two Canadian stations) after removal of the tides. This noise is due in part to difficulties in separating harmonic constituents with close frequencies. To limit this problem, I adjusted the Rayleigh criterion in order to remove harmonic constituents with close frequencies in the tidal analysis package. Noise at near tidal frequencies persisted. This is not surprising because it has already been shown that the tide changes seasonally with stratification, an effect not modeled explicitly by the tidal analysis package. Some of the remaining tidal energy is probably due to small timing errors. Another source of high frequency energy is harbor seiching which is known to affect some of these gauges (e.g., *Mullarney et al.*, 2008).

Overall, GoMSS simulates well the observed sea level anomalies (Figures 5.17 and 5.18). It is encouraging to note that GoMSS captures with high accuracy the high frequency variability and generates most of the extreme events during winter. However, the

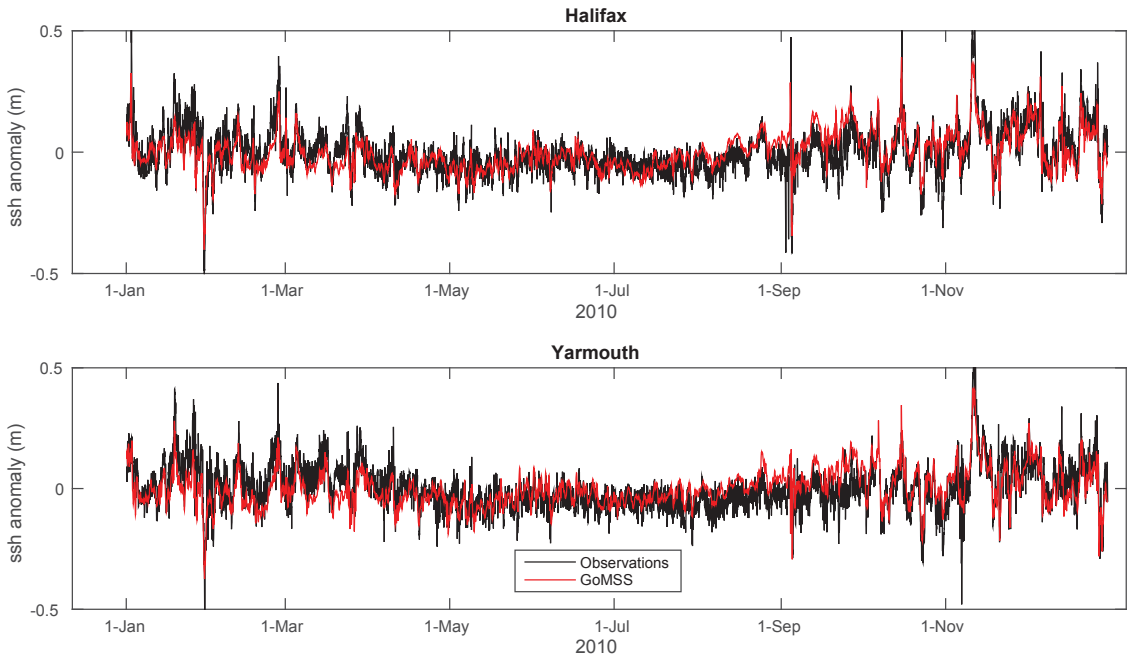

Figure 5.17: Comparison of observed (black) and predicted (red) hourly sea level anomalies at Halifax and Yarmouth for 2010. The inverted barometer effect and the tides have been removed.

model does not capture all of the high frequency variability. This missing high frequency variability is due in part to seiches, which the model does not simulate, and unremoved tides as discussed above.

To quantify the agreement between the observed and predicted sea level anomalies, the standard deviation of each series, and also the standard deviation of their difference, are presented in Tables 5.4 and 5.5. To provide a nondimensional measure of model performance, I have also calculated the ratio of the variance of the difference to the variance of the observed anomalies for each tide gauge (the normalized mean square error, NMSE). (Note that the model outputs and the observations are centred before estimating the NMSE.)

The model errors are larger for Halifax and Yarmouth. This is probably due to imperfections in GoMSS's northern boundary (i.e., the Gulf of St. Lawrence is missing). The imperfections introduced at the north boundary are expected to have a larger impact at the two tide gauges on the Scotian Shelf. The NMSE was also calculated for time series that include the inverse barometer effect (Table 5.5). As expected, the NMSE drops

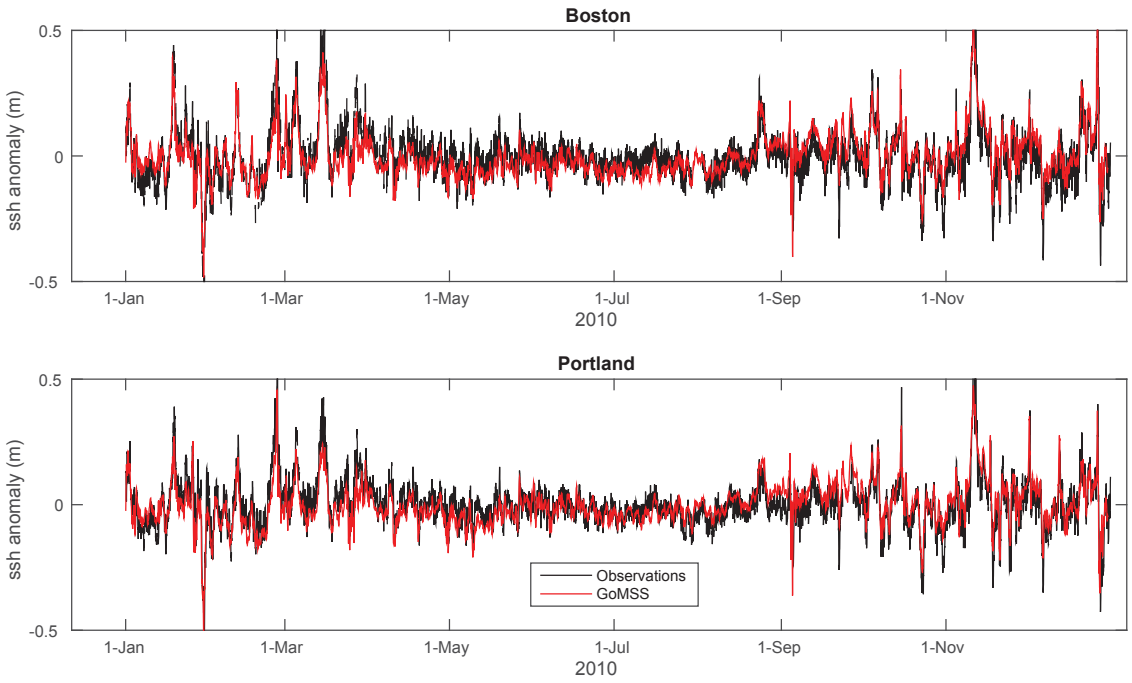

Figure 5.18: Comparison of observed (black) and predicted (red) hourly sea level anomalies at Portland and Boston for 2010. The inverted barometer effect and the tides have been removed. Same format as Figure 5.17.

Table 5.4: Comparison of observed and predicted sea level anomalies at four tide gauge locations. GoMSS was driven by CFSR atmospheric forcing. The tide and inverse barometer effect were removed before calculating standard deviations of the observed and predicted anomalies (columns 2 and 3) and their difference (column 4). The last column is the squared ratio of values in the fourth and second columns.

Station	σ obs (m)	σ GoMSS(m)	σ difference (m)	NMSE
Halifax	0.096	0.079	0.065	0.459
Yarmouth	0.095	0.078	0.071	0.559
Portland	0.100	0.088	0.063	0.397
Boston	0.113	0.096	0.070	0.384

significantly because the standard deviation of the observations has been increased but the standard deviation of the difference remains the same (the inverse barometer effect is the same for the observations and predictions).

When GoMSS is driven by the higher resolution RDPS atmospheric forcing (GoMSS+RDPS) the sea surface height error drops at all four tide gauges (not shown). This is because the RDPS has higher resolution and represents the wind forcing more accurately, particularly

Table 5.5: Comparison of observed and predicted sea level anomalies. GoMSS was driven by CFSR atmospheric forcing. The inverse barometer effect was *not* removed before calculating standard deviations. Otherwise same format as Table 5.4.

Station	σ obs (m)	σ GoMSS(m)	σ difference (m)	NMSE
Halifax	0.132	0.116	0.065	0.243
Yarmouth	0.128	0.111	0.071	0.308
Portland	0.121	0.110	0.063	0.271
Boston	0.133	0.120	0.070	0.277

during extreme winter storms. This shows that uncertainties in the small scale structure of the atmospheric forcing can contribute to errors in GoMSS's predictions of sea surface height.

I did not calculate sea level errors for the global system for the four tidal gauge locations because the global system outputs were only available daily. Thus, the comparison with GoMSS, where hourly outputs are used, would not have been fair.

5.2.2 Temperature and Salinity

The predictions of temperature and salinity from GoMSS are now compared with observations made by a glider, ship-deployed CTDs (see section 4.1 for details) and a buoy located in Halifax Harbour (i.e Halifax Harbour 44258). The buoy is operated by Environment Canada. Although GoMSS, driven by the higher resolution RDPS forcing, performs slightly better in areas where atmospheric forcing is important, its temperature and salinity fields are generally similar with results generated with CFSR forcing. The rest of this subsection focuses on GoMSS forced by the CFSR fields.

CTD profiles: Although I conducted comparisons with observed profiles from several hundreds of locations (Figure 5.19), I present 12 selected profiles from the six representative locations (C1 to C6) shown in Figure 4.3. The observed and predicted profiles of temperature are shown in Figure 4.4. Overall the predicted temperatures (blue line) are in good agreement with the observations (black line). At C4 (offshore of Halifax) GoMSS simulates accurately the mixed layer depth, the shape of the thermocline and its seasonal change. However, the model overestimates sea surface temperature by about 1°C during March and June. Additionally, the model overestimates the temperature at 75 m by about 2°C during late fall. At C1 (Northwest Channel) and C2 (western Scotian Shelf) GoMSS

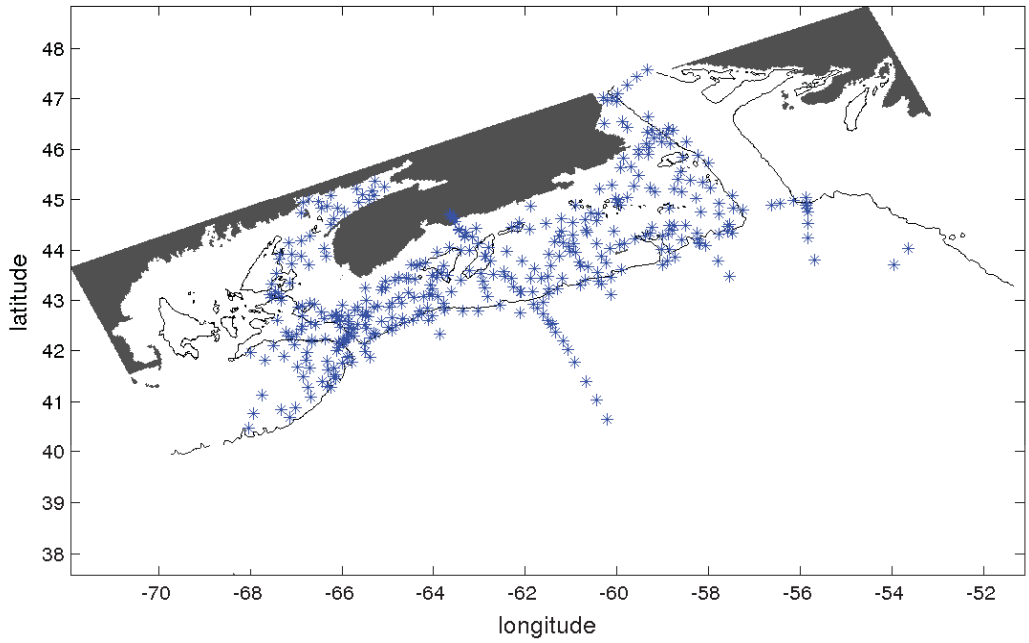

Figure 5.19: Locations of all available CTD profiles for 2012. These profiles are used to estimate the global system and GoMSS error. Black line is the 200 m isobath.

underestimates the depth of the mixed layer by about 20 m. At C5 (the Gully) the model reproduces the sharp thermocline during summer and early fall, however, it overestimates the sea surface temperature by 1°C, and overestimates the whole water column by about 2°C on October. At C6 (Laurentian Channel) the model generates a thermocline that is smoother than observed.

The corresponding profiles of salinity are shown in Figure 4.5. Overall the predictions are quite realistic. At C4 the model captures the overall vertical salinity gradient (i.e., fresher near surface) and the well mixed surface layer during winter and late fall. However, the model overestimates the surface mixed layer salinity by about 0.8. At C3 the model generates a deeper mixed layer, and has a sharper halocline, than the observed profile. At C2 GoMSS underestimate the salinity by about 1.8.

To quantify and compare the errors of the global system and GoMSS, I estimated the NMSE for all available CTD observed profile locations for the year 2012 (Figure 5.19, Tables 5.6 and 5.7). For both GoMSS and the global system the NMSE for temperature is larger for intermediate depths (21-100 m) due to the sharp vertical gradients associated with the thermocline. GoMSS has smaller temperature errors at intermediate depths compared

to the global system. By way of contrast, near the surface (0-20 m) and in deeper water (>100 m) the global system error is smaller. GoMSS has smaller salinity errors throughout the water column.

Table 5.6: The normalized mean square error (NMSE) for the global system and GoMSS based on the observed temperature profiles for 2012 (Figure 5.19), binned over three depth ranges.

Depth range	Global system	GoMSS
0-20 m	0.10	0.12
21-100 m	0.38	0.31
>100 m	0.12	0.13

Table 5.7: The NMSE of the global system and GoMSS based on the observed salinity profiles (Figure 5.19). Same as Table 5.6

Depth range	Global system	GoMSS
0-20 m	0.39	0.35
21-100 m	0.38	0.33
>100 m	0.54	0.29

Overall, GoMSS provides more realistic simulations of mixed layer depth and thermocline shape than the global system. This is because the model has higher resolution and because it includes tidal mixing that is absent from the global system. Nevertheless, the global system simulates better the sea surface temperature than GoMSS. This is because the global system assimilates satellite sea surface temperature. Some of the differences between GoMSS and the observations may be due to mismatches between the time of the observation and the time of the model output. (The 3D salinity and temperature fields are saved once daily for the whole model domain.) This time mismatch may have a large impact in areas with strong tidal mixing fronts and diurnal cycles forced by air sea fluxes.

Both the global system and GoMSS can generate small scale features that appear in the wrong place. For example, the surface temperature discrepancy with the observations at location C5 (the Gully) shown in Figure 4.3 are likely due to a misplaced surface front. Figure 5.20 shows the sea surface temperature from GHRSST (Group for High Resolution Sea Surface Temperature) near location C5 for 2 August 2012 and 13 October 2012. The C5 location is close to the front between shelf and Slope Water. In both summer and early fall, GoMSS places the Slope Water too close to the shelf (i.e., closer to the 200 m isobath).

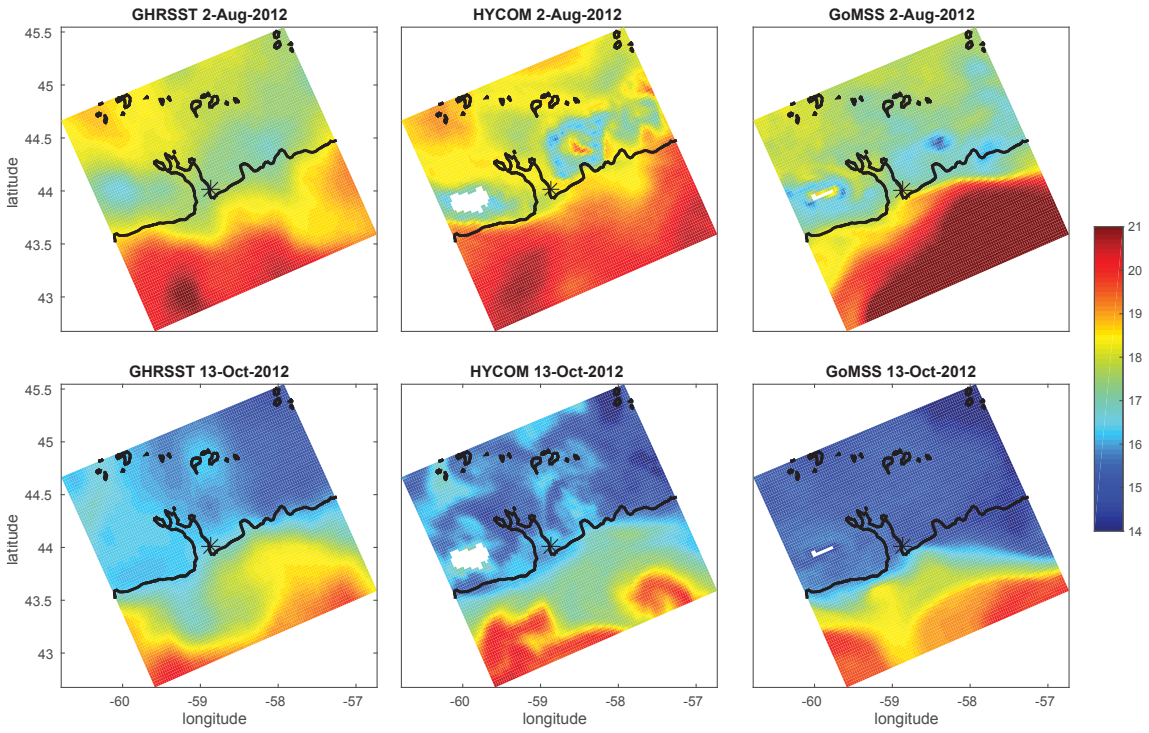

Figure 5.20: Snapshots of sea surface temperature from GHRSST (left panels), the global system (middle panels) and GoMSS (right panels) near Sable Island (represented by white color) and the Gully. The upper panels are for the 2/8/2012 and the lower panels are for the 13/9/2012. The black line is the 200 m isobath and the black star is the location of C5. The two dates correspond to the vertical temperature profiles at C5 shown in Figure 4.3. Temperature is in °C.

Thus, for locations near the shelf break (e.g., C5 and C6) errors in sea surface temperature may be associated with misplaced surface fronts. Although, errors in surface front position exist in the global system, the global system has a better representation of surface fronts because it assimilates satellite observations. Overall, Figure 5.20 shows that if the surface front is misplaced, the local, small scale variability is misrepresented. Details of a method to improve the position of surface fronts are given in Chapter 6.

Gliders: "Snapshots" of temperature and salinity, along a vertical section running along the Halifax Line (Figure 4.3), are shown in Figures 5.21 and 5.22 respectively. The glider observations were collected between 11 and 31 July, 2012. (Details of the glider observations are given in section 4.1.) For both figures, the left and center panels show the observed and predicted sections at the same times. Note that the glider's horizontal

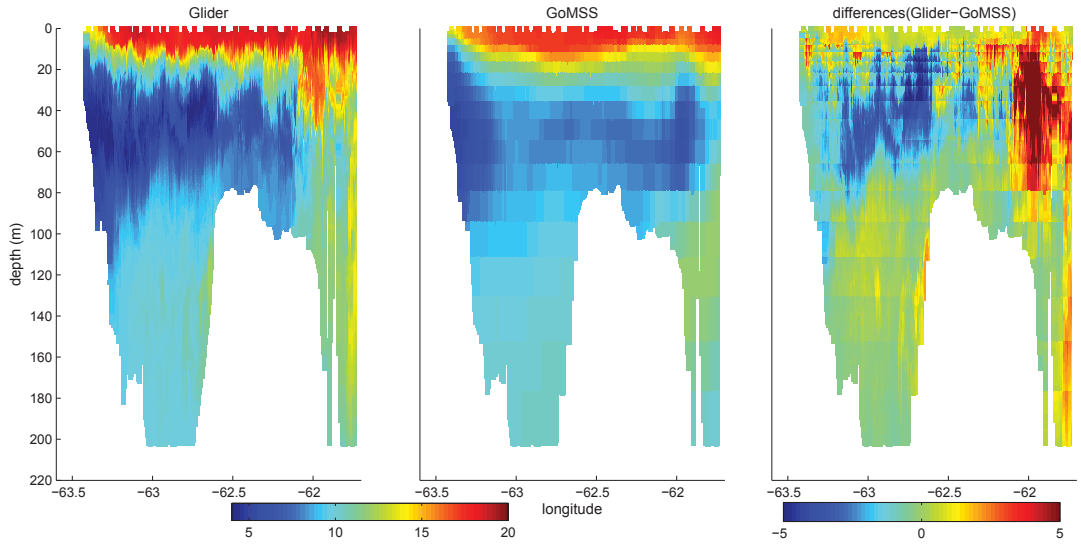

Figure 5.21: Temperature section observed by a glider (left panel) operating along the Halifax Line (red line in Figure 4.3), GoMSS (middle) along the same path, and their difference (right panel) during 11-31, July 2012. See text for details. Temperature is in °C.

and vertical resolution is very high and thus the model results appear much smoother. This is evident in the rightmost panel of each figure which shows the difference between observations and predictions. Overall, GoMSS generates a three layer structure during this summer period, consistent with the glider observations. Near the surface the model has a very warm (17°C and above) layer driven by surface heating. Between 30 and 100 meters, the model generates a cold intermediate layer, with temperature below 6°C and salinity below 33. This intermediate layer mainly consists of water from the Gulf of St. Lawrence. Near the bottom (below 100 m), and in Emerald Basin, the model generates warm (around 10°C), saline (around 35) water associated with the intrusion of dense water from the continental slope.

There are some noticeable discrepancies between GoMSS and the glider observations. The model's intermediate layer in Emerald Basin is too warm and the model underestimates the salinity by about 0.5. At 62°W the model captures accurately the sharp water front between the cold and fresh water on the shelf, and the warmer and saltier water offshore. Note that over the edge of the Emerald Bank (between 62 and 61.5°W) the model generates a realistic saline (around 35) water mass below 20 m; however, at the surface, it has lower salinity (by around 1) than the observations and it does not generate the pronounced

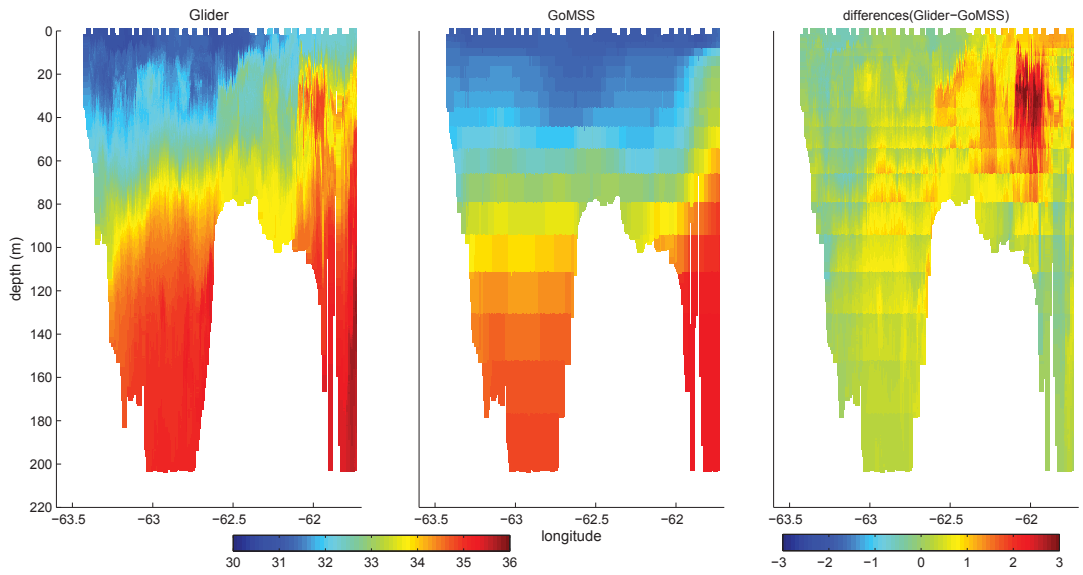

Figure 5.22: Salinity section from the glider and GoMSS. Same format as Figure 5.21. Salinity is in practical salinity units.

thermocline depression at 61.8°W.

Overall GoMSS is in better agreement with the glider observations than the global system (compare Figures 4.6 and 4.7 with Figures 5.21 and 5.22) and has a slightly smaller temperature and salinity NMSE than the global system (Table 5.8). GoMSS and the global system do not have any significant temperature bias (i.e small mean difference in Table 5.9). However, GoMSS and the global system systematically overestimate the salinity (i.e positive bias in Table 5.9) by 0.42 and 0.48 respectively. The main error of the global system is that it misplaces the sharp front observed at the shelf break. This is probably because the global system has a coarser resolution than GoMSS, and it does not include tidal mixing that is significant on top of Emerald Bank.

Table 5.8: The normalized mean square error (NMSE) of the global system and GoMSS based on the temperature and salinity glider observations.

NMSE	Global system	GoMSS
Temperature	0.254	0.223
Salinity	0.245	0.222

Surface buoy: Surface temperature predicted by the global system and GoMSS, and observed by a buoy located near Halifax Harbour, are shown in Figure 5.23 for 2010 to

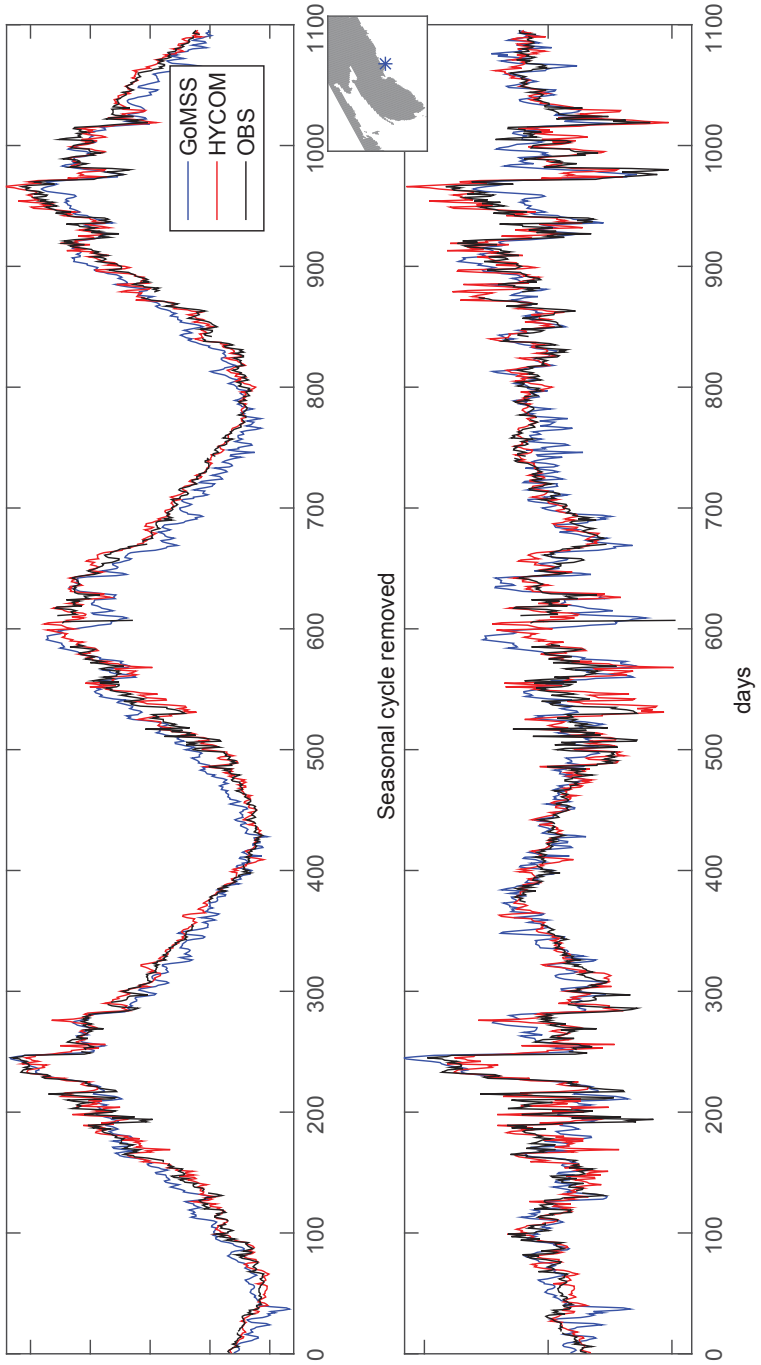

Figure 5.23: Surface temperature from GoMSS (blue), the global system (red) and observed by a buoy (black) located near Halifax Harbour (blue point on the inset). Time series cover the period 1/1/2010 to 31/12/2012. The top panel includes the seasonal cycle. In the bottom panel the seasonal cycle has been removed. Temperature is in °C.

Table 5.9: The mean difference between temperature and salinity glider observations and the global system and GoMSS.

Bias	Global system	GoMSS
Temperature	0.063	0.100
Salinity	0.417	0.487

2012. Overall, GoMSS is in good agreement with the observations and simulates well most of the upwelling events. The global system is in excellent agreement with the observations, probably because it assimilates in situ and satellite surface temperature. However, during some extreme events GoMSS outperforms the global system (e.g., the upwelling event around day 600). It is important to note that GoMSS does not exhibit significant drift (top panel, Figure 5.23). This is encouraging because GoMSS does not use any form of correction to suppress model bias and drift.

5.3 Seasonal Cycle and Mean State

GoMSS is now evaluated based on comparisons with observations from tide gauges, altimeters, current meters and observed seasonal climatologies. I also determine if the higher resolution of GoMSS leads to improvements in the seasonal cycle and the long term mean compared to the global system. Note that winter is defined between January and March, and summer between July and September.

5.3.1 Sea Level

Maps of the long term mean, standard deviation and skewness of sea level are shown in Figure 5.24 for GoMSS (daily sea level) and the gridded altimeter based products provided by AVISO (similar to Figure 4.2, see subsection 4.1.2 for details). The model mean dynamic height is in generally good agreement with the altimeter observations. By comparison, the AVISO mean is smoother due to its coarser resolution. The standard deviation of sea level is large near the shelf break due to the Gulf Stream influence (e.g., meandering, eddies and interaction between Gulf Stream water and the colder and fresher water inshore). The model standard deviation and skewness are higher than the AVISO in the vicinity of the Gulf Stream. This is probably because the model has high resolution and can resolve small scale eddies and meanders that are missing from the AVISO product. The model has negative skewness in the Gulf of Maine and on the Newfoundland shelf.

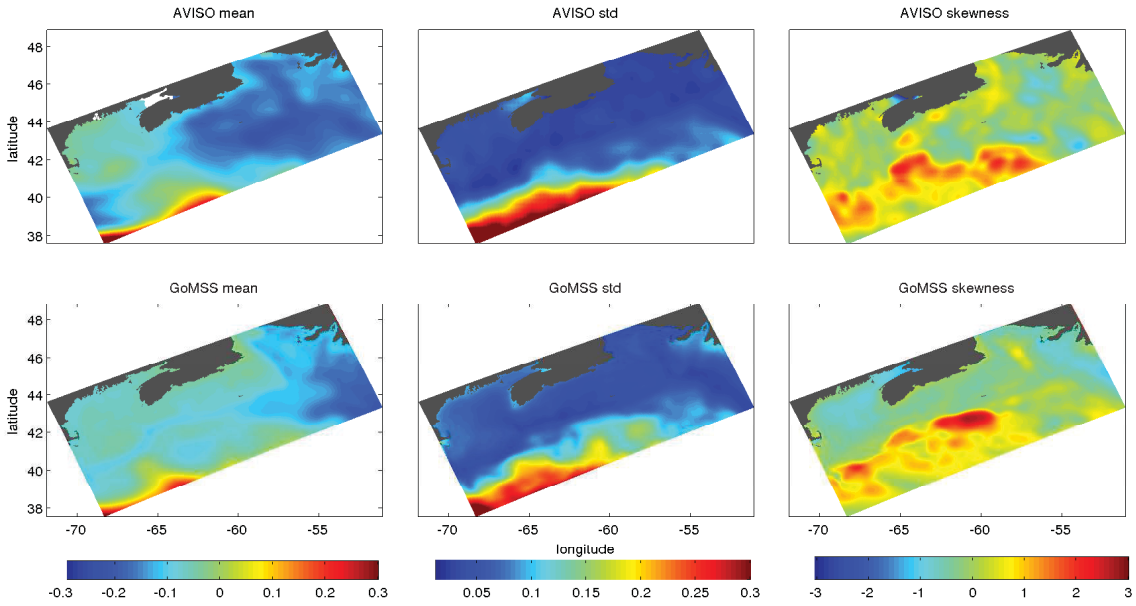

Figure 5.24: The mean, standard deviation and skewness of sea level based on satellite observations (AVISO, upper panels) and GoMSS (lower panels, tides removed). The mean and standard deviation are in meters. Skewness has no units. Same format as Figure 4.2.

This negative skewness, which is absent from the AVISO product, also occurs in the global system (Figure 4.2).

Results from the model with CFSR and RDPS atmospheric forcing are similar. However GoMSS+RDPS has slightly larger sea surface height variability. This is because RDPS includes the effect of atmospheric forcing occurring on small spatial scales not resolved by CFSR.

The seasonal cycle of sea level at three tide gauges (North Sydney, Halifax and Yarmouth; locations A1, A2 and A3 respectively in Figure 4.3) is shown in Figure 5.25. The data have been corrected for the inverse barometer effect and the diurnal and semi-diurnal tides were removed before the monthly means were calculated. The range of the sea level decreases moving down the shelf (i.e., about 20 cm at North Sydney and 10 cm at Yarmouth). Although the observed coastal sea level time series vary from year to year, they all exhibit a clear and repeatable annual cycle (generally higher in autumn and lowest in late winter, consistent with *Han et al.*, 2010). The maximum occurs approximately in October at North Sydney, November at Halifax, and late November to December at Yarmouth. This maximum is associated with the freshwater outflow from the Gulf of St.

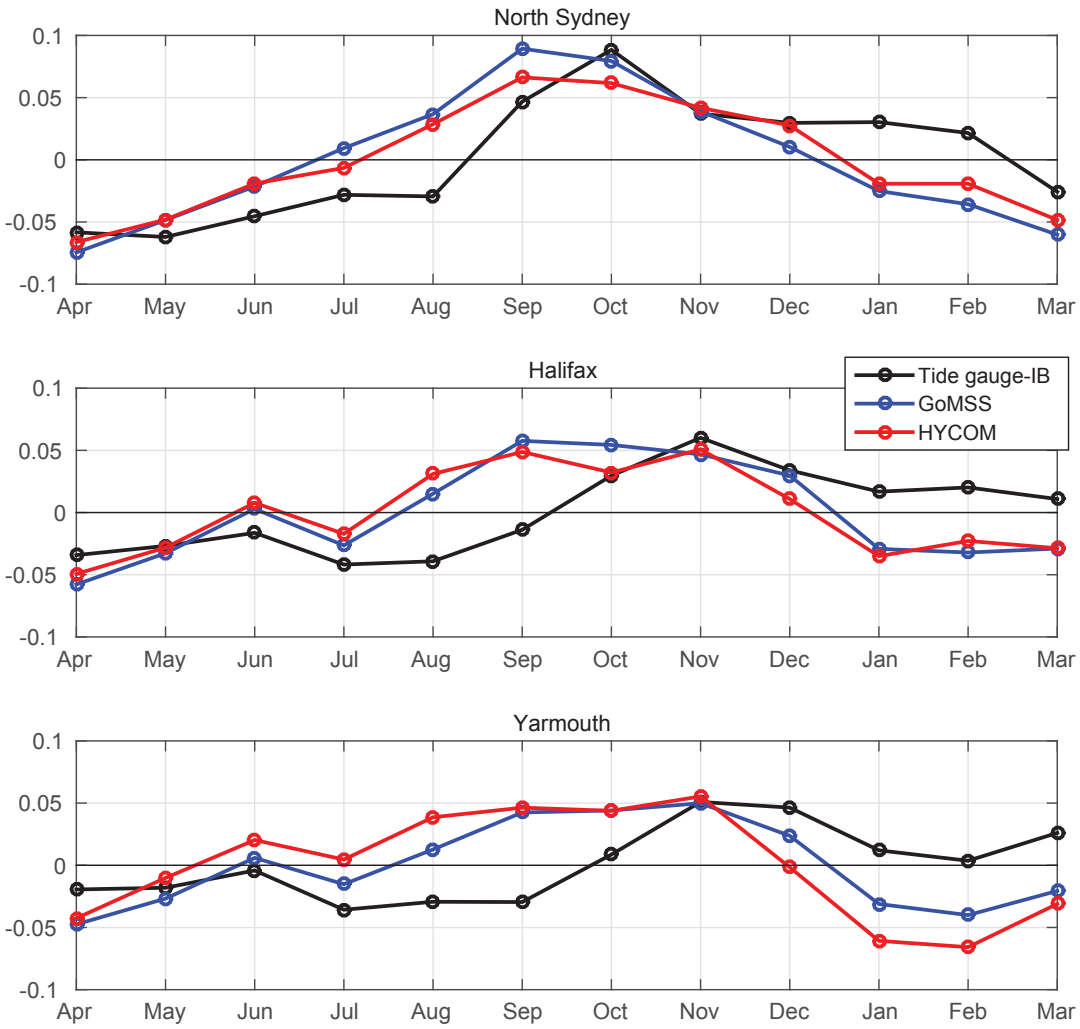

Figure 5.25: Variation of monthly mean sea level at North Sydney, Halifax, and Yarmouth based on tide gauge observations (black), and predictions from GoMSS (blue) and the global system (red). The monthy means are averaged over the years 2010, 2011 and 2012. The seasonal cycle is presented from April to March and is in meters.

Lawrence that flows down the shelf reaching first North Sydney and then Halifax and Yarmouth within 2-3 months similar to previous studies (e.g., *Drinkwater et al.*, 1979; *Smith and Schwing*, 1991).

The monthly means of sea level from the global system and GoMSS are generally similar to the tide gauge observations (Figure 5.25) in terms of their range and timing of the maximum. However, the global system and GoMSS signals have a time shift with respect to the observed signal: their maximum occurs one month earlier than observed

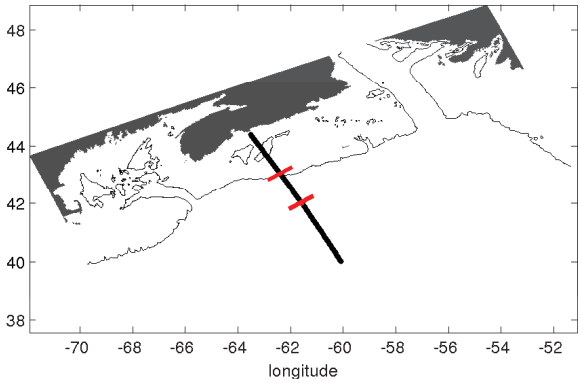

Figure 5.26: The altimeter track (black thick line). The black thin line represents the 200 m isobath. The red lines show the shelf break and foot of the the continental slope indicated by the horizontal red lines in Figure 5.27.

at North Sydney, and about two months earlier at Halifax and Yarmouth. This implies the freshwater signal from the Gulf of St. Lawrence is either advected faster in the global system and GoMSS (faster currents along the coast), or that most of the freshwater outflow is diffused before it reaches Halifax and Yarmouth (or probably a combination of the two). The source of both problems is likely found upstream near the north boundary (i.e biases and uncertainties in the Cabot Straight outflow and unrealistic recirculation along GoMSS north boundary).

Repeat profiles of sea level measured along the satellite altimeter track shown in Figure 5.26 were kindly made available by Dr Florence Birol from the Laboratoire d'Etudes en Geophysique et Oceanographie Spatiales (LEGOS) for the period 9 February, 2010 to 23 January, 2012. The tracks were provided every 9.9156 days with a grid spacing of approximately 6 km from the deep ocean to the coast, just offshore of Halifax (Figure 5.26). The profiles had been corrected for coastal effects and aliasing by the tide, storm surges and the inverse barometer effect.

A Hovmoller diagram of the coastal altimetry data set is shown in Figure 5.27. The strongest variability is evident in the deep water, beyond the foot of the continental slope (most southerly horizontal red line in each panel). This enhanced variability is due to eddies and meanders and is expected. The variability drops over the shelf (northward of the upper horizontal red line). Comparison of Figures 5.25 and 5.28 (a coastal zoom of Figure 5.27) shows that the seasonal cycle from the coastal altimeter track is generally

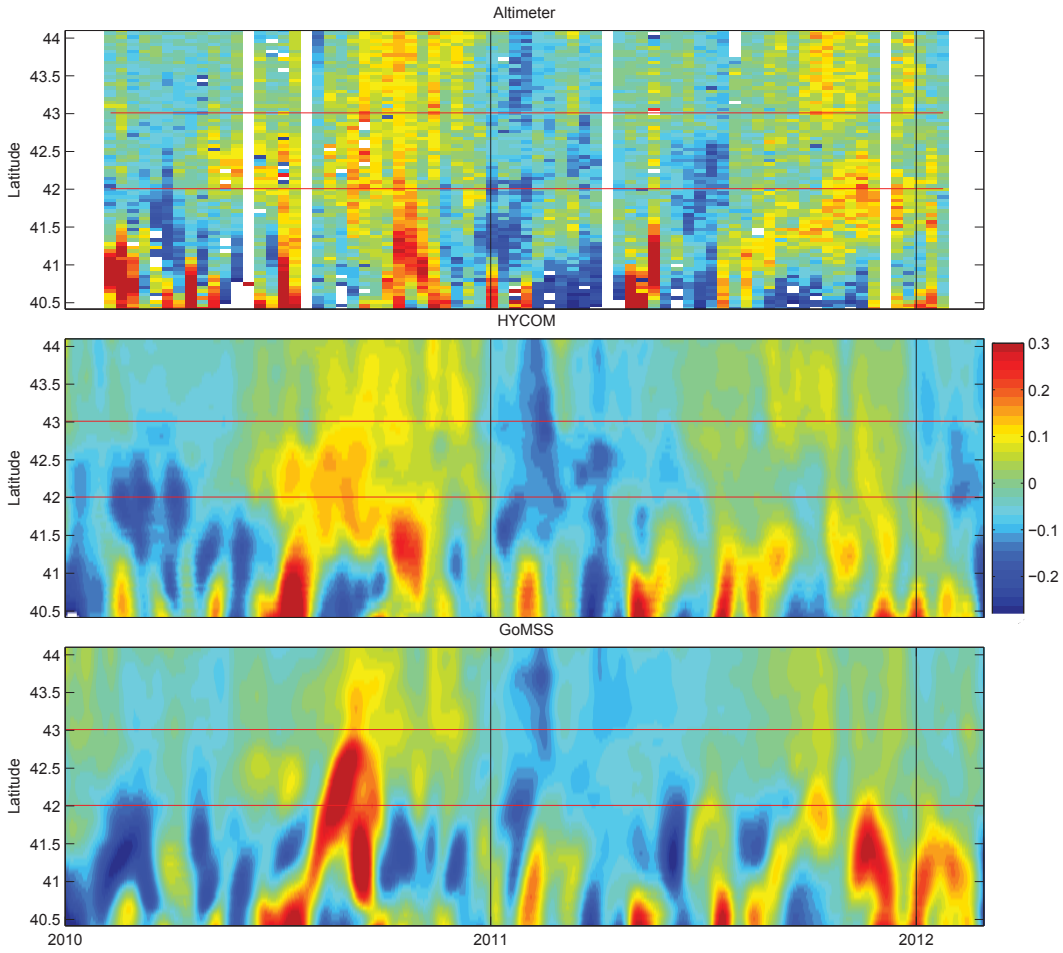

Figure 5.27: Hovmoller diagram of sea level along the Halifax Line (Figure 5.26) based on the coastal altimeter dataset (top panel), and predictions by the global system (middle panel) and GoMSS (bottom panel). High frequency variability of all model output was removed using a Butterworth filter with a cutoff frequency of 20 days. The horizontal red lines show the shelf edge (43°N, near 200 m isobath) and foot of the slope (42°N deeper than 1000 m). Sea level is in meters.

consistent with the seasonal cycle observed by the Halifax tide gauge. Note the sea surface height signal is approximately constant across the shelf, indicating a deep water origin.

Another view of the sea level data is provided by Figure 5.29 which shows the standard deviation of the grid point time series as a function of position along the altimeter track. It is clear that the global system and GoMSS are quantitatively in good agreement with the coastal altimeter observations. On the shelf (north of 43°) the global system and GoMSS have standard deviations very close to that observed. In deep water (south of 43°) the

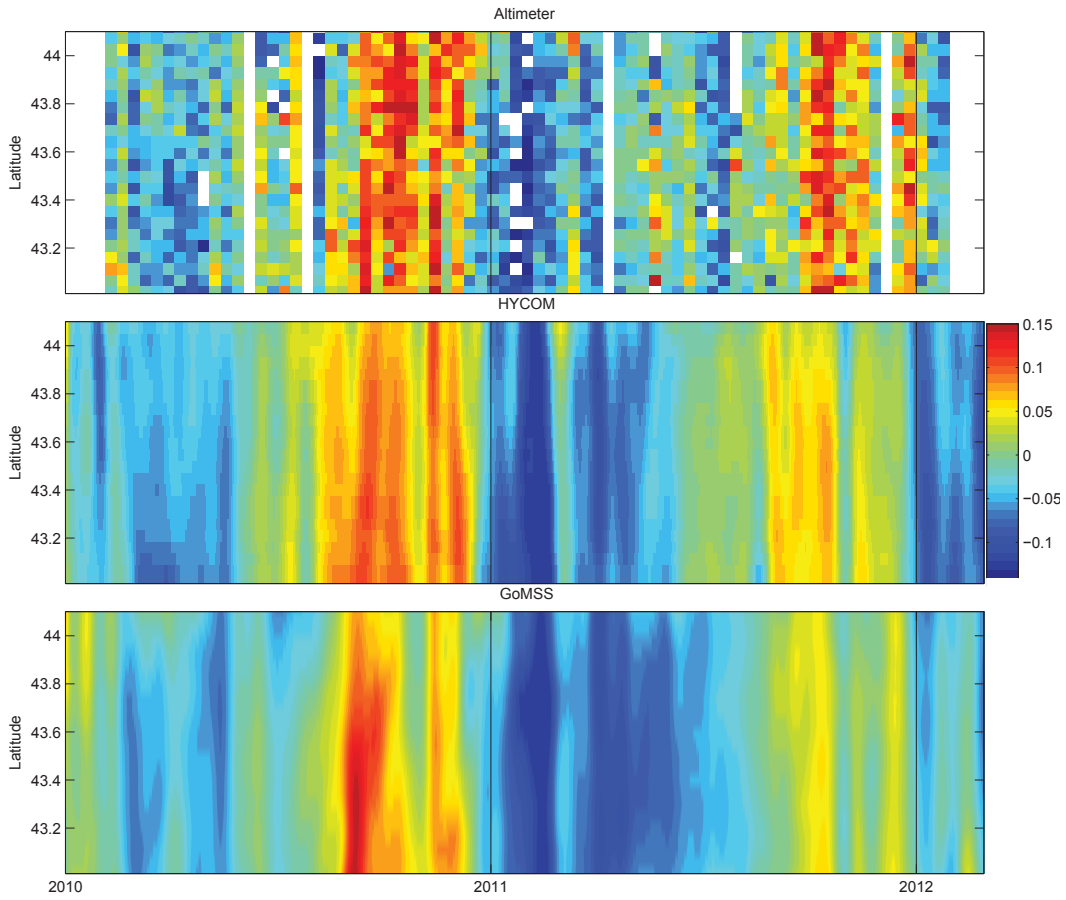

Figure 5.28: Hovmoller diagram of sea level along the Halifax Line (Figure 5.26) based on the coastal altimeter dataset (top panel), and predictions by the global system (middle panel) and GoMSS (bottom panel). Same format as Figure 5.27 but zoomed onto the shelf. Sea level is in meters.

global system is in good agreement with the observations; this is not surprising because it assimilates altimeter observations. Note the standard deviation of GoMSS is much larger than observed between 41 and 42°N. The high standard deviation is associated with an unrealistic extreme positive sea surface height event occurring between 41.5° and 43° latitude in the late summer of 2010.

Differences between predictions of the global system and GoMSS in deep water are not surprising because they place several eddies and meanders in different locations (Figure 5.27). Constraining the positions of GoMSS's eddies will improve the model's sea surface height variability as discussed in Chapter 6. The very good agreement between GoMSS

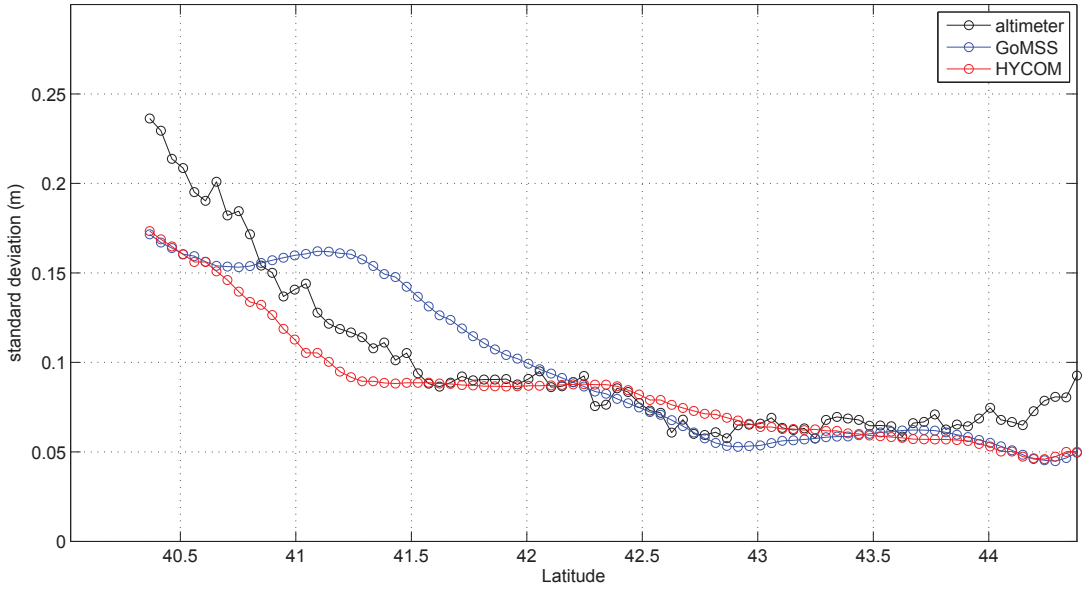

Figure 5.29: Standard deviation of sea level from coastal altimetry (black), the global system (red) and GoMSS (blue) along the altimeter track shown in Figure 5.26.

and the global system around 40.5° is due to the proximity to GoMSS's south open lateral boundary.

5.3.2 Temperature and Salinity

Mean temperature and salinity distributions for winter and summer, for four different regions (Figure 5.30), are now discussed. Note the model driven by CFSR and RDPS forcing generate very similar seasonal cycles; the following discusses only the CFSR model run.

GoMSS generates a seasonal cycle that is in good agreement with the global system and the Geshelin monthly climatology (*Geshelin et al.*, 1999, details in Appendix C). A detailed comparison of the global system and GoMSS predictions and the Geshelin climatology is presented in Appendix C. In summary, GoMSS captures accurately the summer heating and freshening of the surface layer. GoMSS also generates a fresher water outflow from the Gulf of St. Lawrence, and a fresher Labrador Current, during summer, consistent with the climatology and the global system. The summer upwelling along the Scotian Shelf coast is also realistically simulated in the model. In summer, GoMSS reproduces accurately the surface, fresh water mass along the west coast of the Gulf of Maine, which is missing from the global system. This is probably associated with the better

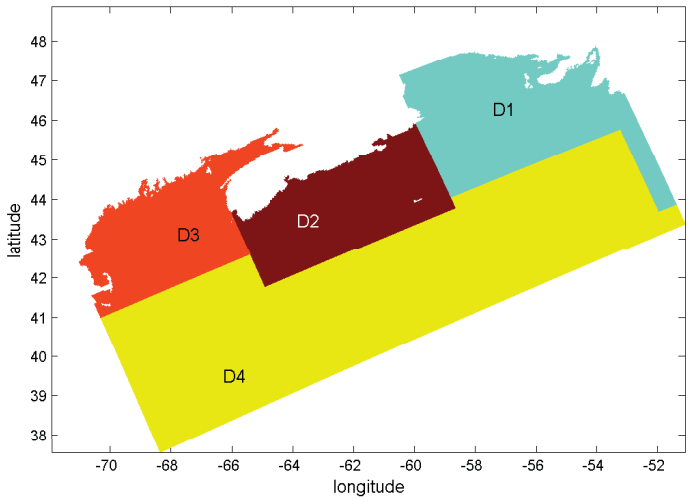

Figure 5.30: Separation of GoMSS domain into 4 sub-domains used to examine the seasonal variation of temperature and salinity.

representation of river discharge in GoMSS than in the global system. At depths below 100 m, the model simulates well the warm, saline water (i.e., Slope Water) in Emerald Basin, and the penetration of Slope Water into the Gulf of Maine through the Northeast Channel. This penetration of Slope Water into the Gulf of Maine and Emerald Basin is more intense in GoMSS than in the global system. This is probably associated with tidal advection that is absent from the global system. Additionally, on top of Georges Bank GoMSS has a well mixed water layer that extends down to the bottom during summer, due to mixing caused by strong tidal currents. The global system has some mixing in the area but not as intense, because it does not have tides. It is difficult to conclude if the global system or GoMSS is more realistic based only on the analysis discussed in Appendix C. However, all the figures in Appendix C show that the largest discrepancies between the global system and GoMSS are located close to the shelf break and are mainly due to their different predictions of the position of the front between the slope and shelf water.

I now focus on TS diagrams (5.31 and 5.32) for winter and summer for the four sub-areas defined in Figure 5.30. The TS diagrams are for depth greater than 50 m. The TS diagrams are used to summarize the observed and predicted water mass characteristics over the whole domain, and to determine if GoMSS develops significant biases. Only three years (2010-2012) are used to estimate the seasonal means of both the global system and GoMSS

and so some discrepancies with the climatology are due to discrepancies in the averaging period.(Details about the climatology are given in Appendix C.)

Sub-domain D1: GoMSS predicts temperature between 1°C and 8°C and salinity 31.2 and 34.8 in winter (see light blue panels in Figure 5.31). In shallow water, the simulated water temperature and salinity generally increase with depth consistent with the observed climatology. The GoMSS fresh (< 32) and cold (< 2°C) water mass is associated with outflow from the Gulf of St. Lawrence and is found along the coast of Nova Scotia. The water mass with temperature below 2°C and salinity around 33 is found in the Newfoundland coast, and consists mainly of inshore Labrador Current. Warm (> 2°C) and salty (> 33) water is found in deeper regions along the Laurentian Channel and it is formed due to mixing with penetrating Slope Water. Overall, during winter, GoMSS temperature and salinity is consistent with the climatology and the global system. The climatology has slightly colder (around 0.5°C) and more saline (around 0.5) water outflow from the Gulf of St. Lawrence.

In summer, the salinity and temperature distribution is similar to winter for sub-domain D1. However, the water along the Nova Scotian coast is generally about 1.5°C warmer. This is because during summer, the outflow from the Gulf of St. Lawrence is warmer. Additionally, in GoMSS, near North Sydney (A1 in Figure 4.3), the water reaches temperatures as high as 7.5° at about 50 m depth. This increase in temperature is due to intense tidal mixing and is absent in the climatology, probably due to lack of resolution. Although, the global system has increased temperature in the area, it cannot capture accurately the local temperature and salinity changes that are associated with tidal mixing.

Sub-domain D2: There is a wide distribution of temperature and salinity in this sub-domain chosen to coincide with the Scotian Shelf. Generally, GoMSS fields are in good agreement with the observed climatology and the global system. In more detail, the dark red panels in Figures 5.31 and 5.32 show that, below 100 m, the temperature and salinity distribution do not change significantly with season consistent with *Loder et al.* (1997). At 50 m the water is fresher, and the salinity increases with depth reaching up to 35.5). In the northeastern part of the Scotian Shelf, the water is fresh and cold, influenced by the outflow from the Gulf of St. Lawrence. The water becomes warmer and saltier as it flows downstream and mixes with penetrating Slope Water which is consistent with

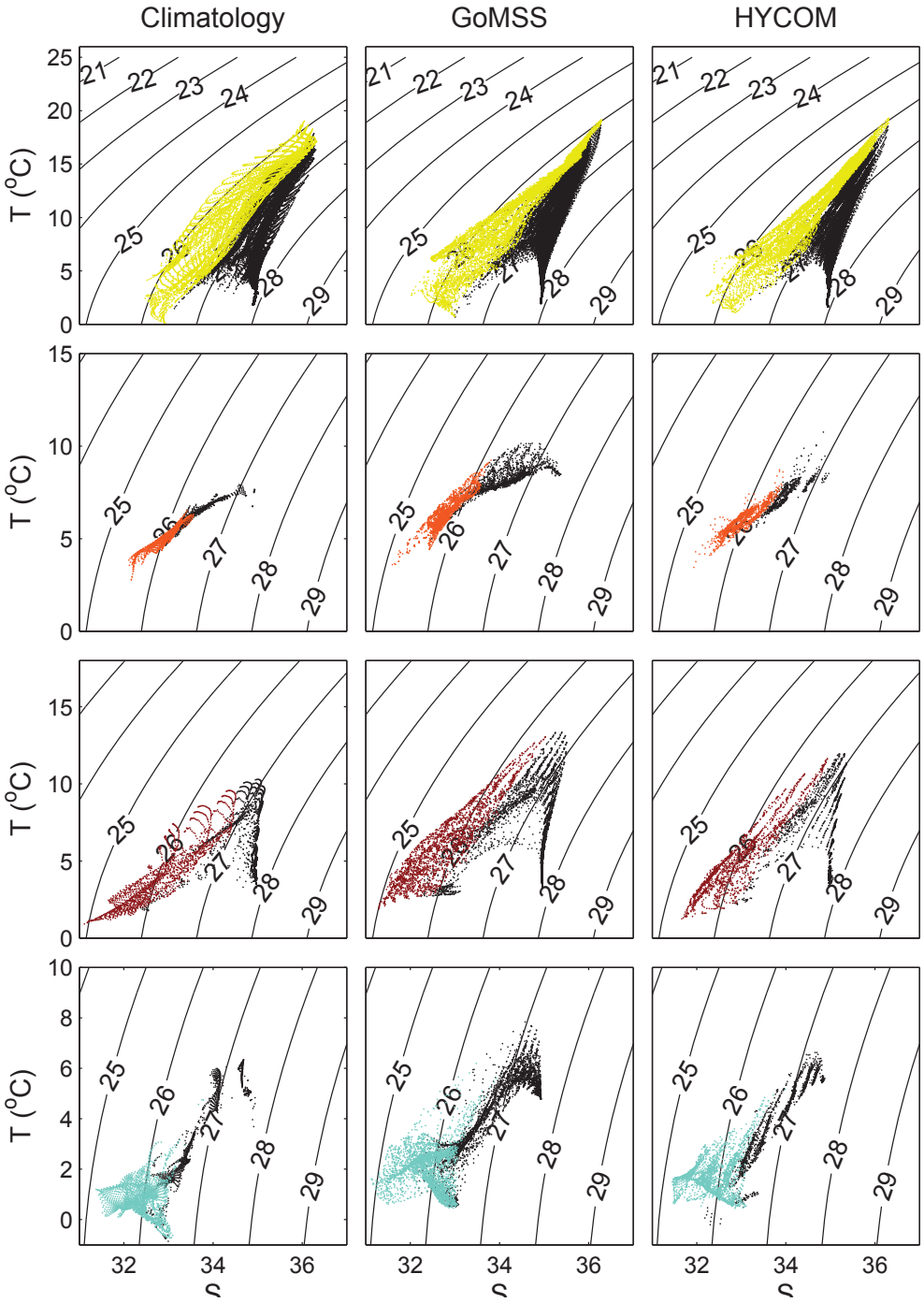

Figure 5.31: TS diagrams for winter for the climatology (left panels), GoMSS (middle panels) and the global system (right panels) for depths greater than 50 m. The colors (and hence rows) correspond with the color coding of the four sub-domains defined in Figure 5.30. Coloured dots are for depths 50-100 m and black dots are for depths greater than 100 m.

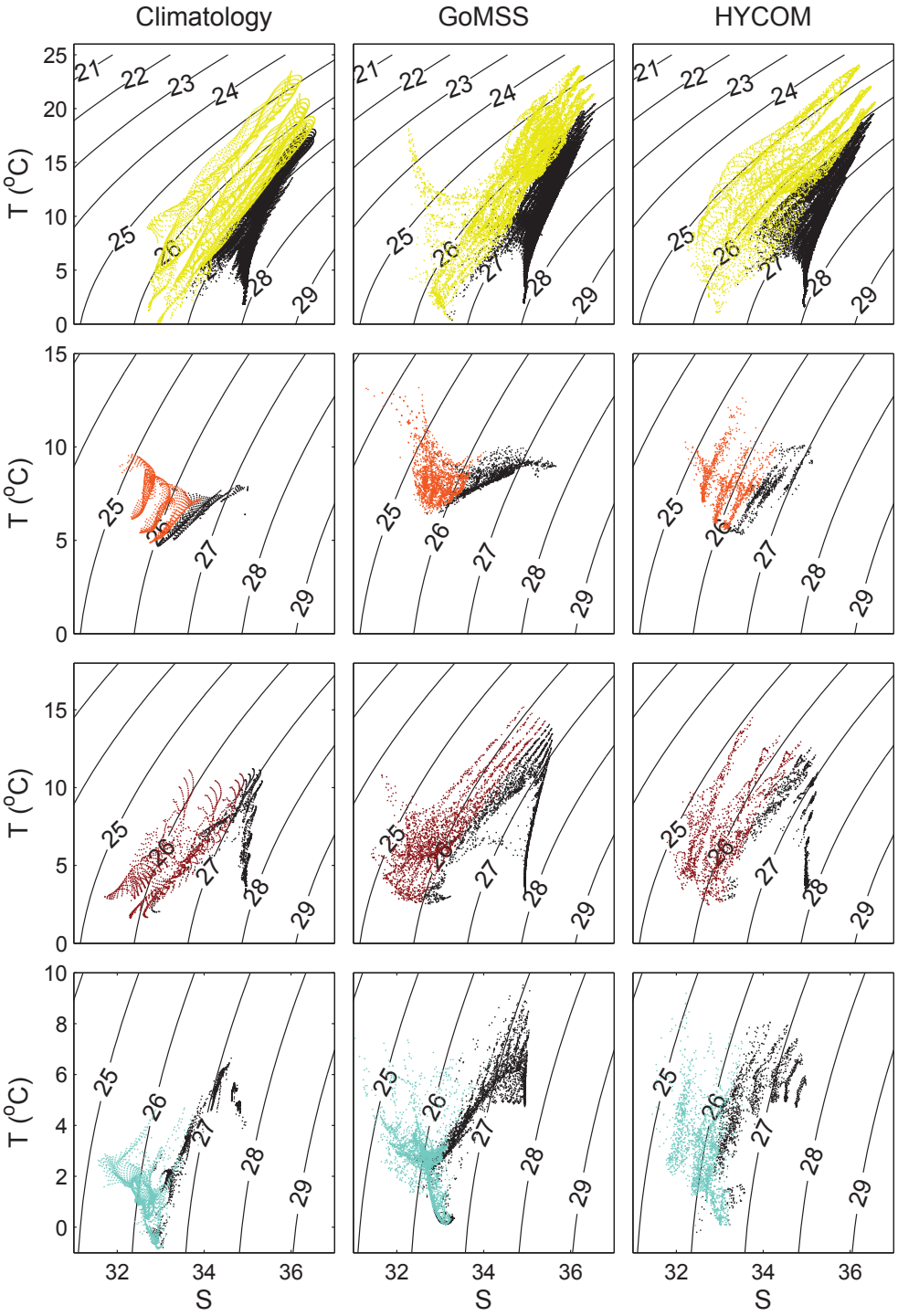

Figure 5.32: TS diagrams for summer. Same format as Figure 5.31

observations (*Loder et al.*, 1997). Along the coast, the water is fresh and cold; the salinity and temperature increase moving from the coast towards the shelf break, due to interaction with Slope Water.

Sub-domain D3: During summer, the salinity and temperature do not change significantly below 50 m. Overall, GoMSS temperature and salinity are consistent with the climatology and the global system, both in summer and winter. The winter and summer GoMSS TS diagrams are in good agreement with previous observations (i.e., *Brown and Irish*, 1993). Both GoMSS and the global system have higher temperature than the climatology close to the shelf break by about 1°C and 2°C, respectively. Figure 5.31 shows that during winter, the temperature below 50 m is between 4°C and 8°C and the salinity between 32 and 35. The temperature and salinity both increase with depth. The water mainly consists of Nova Scotia Current water. The water in sub-domain D3 is better mixed than the other sub-domains due to the very strong tides in the area. In summer (Figure 5.32), the global system and GoMSS generate warmer water between 50-100 m (black dots) throughout D3 due to intense tidal mixing with upper layer water, consistent with the climatology and previous studies (e.g. *Loder et al.*, 1997). GoMSS large increase in the summer temperature (up to 10°C at 50 m depth) is associated with intense tidal mixing on top of Georges Bank and is consistent with observations (e.g., *Loder et al.*, 1997; *Flagg*, 1987). This summer temperature increase is absent in the climatology, probably due to the lack of resolution.

Sub-domain D4: In this area the temperature and salinity variability is large mainly because the water over the slope is a highly variable mixture of water from the Gulf Stream and the Labrador Current, and also the effect of advection due to current meandering and eddies. During both winter and summer the temperature and salinity from GoMSS is consistent with the observed climatology. However during summer, GoMSS generates a water mass between 50 and 100 m depth with high temperature and salinity around 32.3, that does not exist in the observed climatology. This water mass is on top of Georges Bank and it is generated by intense tidal mixing.

Overall, the global system fits the observed climatology better. However both the climatology and the global system are coarser than GoMSS and so they miss several small scale features resolved by GoMSS. To investigate if the differences in the TS diagram between the climatology and GoMSS are due to the small scales features that

are absent in the climatology and the global system, I generated new TS diagrams after smoothing GoMSS temperature and salinity fields (not shown) by applying the same level of smoothing as the climatology. The smoothed GoMSS fit to the climatology was now similar to the global system fit. However, the global system's TS diagrams still agreed more closely with the climatology. This shows that GoMSS has large scale errors, especially off the shelf in deep water. This is further discussed in Chapter 6.

5.3.3 Currents

The seasonal variation of the circulation of the global system and GoMSS are now evaluated based on available current meters observations. (I focus on the model forced by CFSR because it gives very similar results to RDPS forcing.) Because the observations are sparse, and do not cover the whole domain, I also use previous studies (e.g. *Lynch et al.*, 1996; *Han et al.*, 1997; *Loder et al.*, 1997, 1998; *Hannah et al.*, 2001; *Urrego-Blanco and Sheng*, 2014) to evaluate GoMSS and global system.

The observed seasonal currents are estimated based on monthly means of observed currents archived by the Department of Fisheries and Ocean Canada (Ocean Data Inventory). I only consider locations that are on the shelf and have multiple months records between 1960 and 2014. The observations are separated into three vertical layers: i) 0-20 m, ii) 21-100 m and iii) 101-300 m. Figure 5.33 shows the winter and summer observed mean currents for the three vertical levels. As expected, the observations show circulation patterns consistent with previous studies (e.g., *Lynch et al.*, 1996; *Han et al.*, 1997; *Loder et al.*, 1997, 1998; *Hannah et al.*, 2001; *Urrego-Blanco and Sheng*, 2014), including the inflow-outflow through Cabot Strait, the general southwestward flow over the Scotian Shelf, and the inflow-outflow along the Northeast Channel.

Figures 5.34 to 5.37 show 0-100m depth averaged seasonal currents calculated from the global system, GoMSS and the observations. Note that the observed means are based on averages of different depths (depending of data availability for each location). However for the inset scatterplots, and the R^2 values discussed below, the model results were averaged over the same depths as the available observations for each location.

Overall, the seasonal mean circulation of the global system and GoMSS are similar, and consistent with previous studies (e.g., *Lynch et al.*, 1996; *Han et al.*, 1997; *Loder et al.*, 1997, 1998; *Hannah et al.*, 2001; *Urrego-Blanco and Sheng*, 2014). GoMSS general

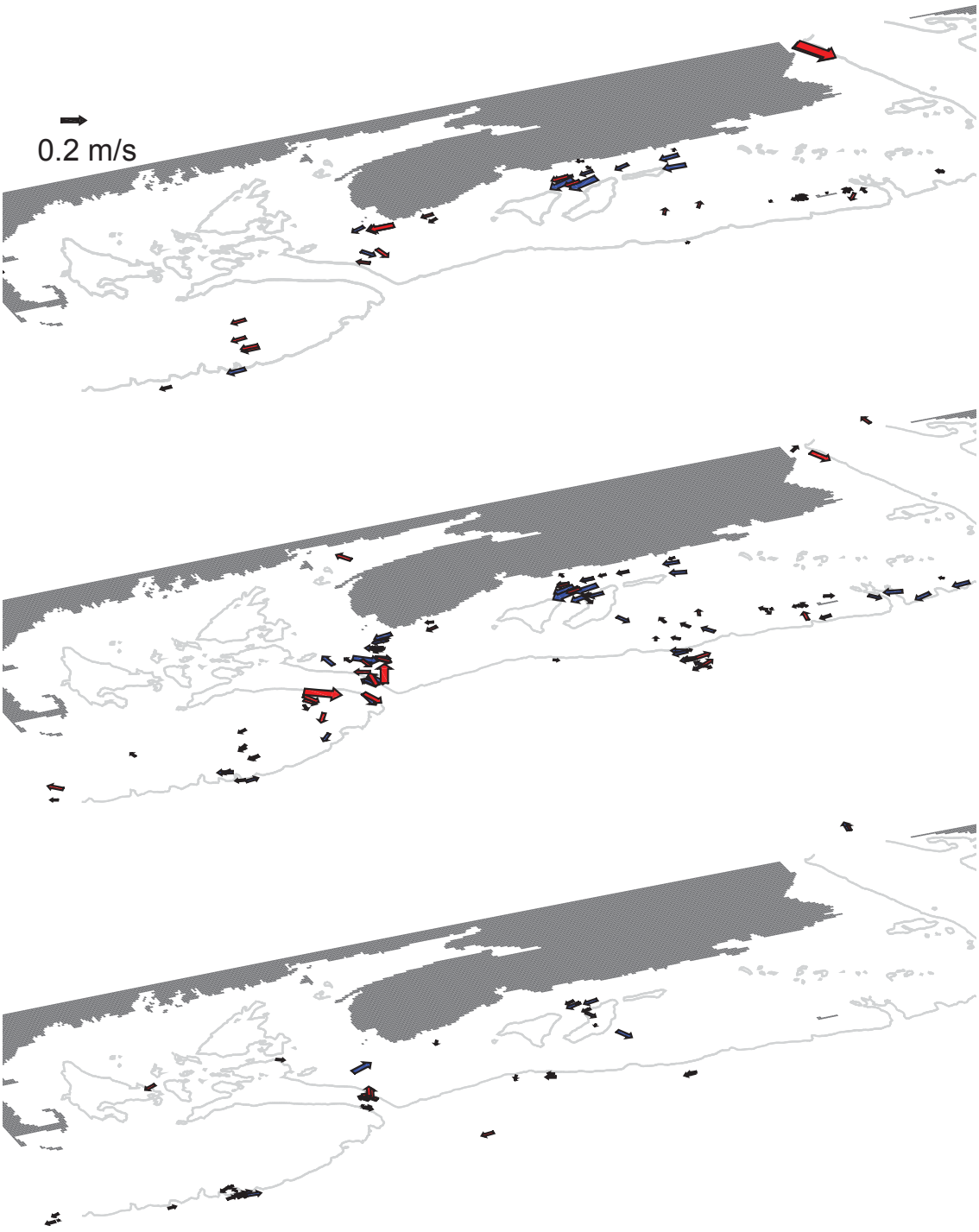

Figure 5.33: Seasonal mean currents based on current meters observations. The blue and red vectors are for winter and summer respectively. The top, middle and bottom panels are for 0-20 m, 21-100 m, and 101-300 m respectively. The grey contour is the 200 m isobath.

circulation on the shelf is towards the southwest and strongly influenced by the wind and tidal rectification in shallow areas. Off the shelf, the predicted circulation is generally to the northeast as expected.

The global system and GoMSS agree on the outflow from the Gulf of St. Lawrence on the west side of Cabot Strait (Figures 5.34 to 5.37). This outflow supplies the inner and the outer currents on the Scotian Shelf. During summer, the outflow from the Gulf of St. Lawrence is stronger in both the global system and GoMSS, however, some of this flow is recirculated within the Laurentian Channel and does not enter the Scotian Shelf consistent with the study of *Loder et al.* (1997). During winter, the global system does not reproduce the observed inflow of Labrador Current water into the Gulf of St. Lawrence, along the east side of Cabot Strait. In summer, although the global system generates some weak inflow into the Gulf of St. Lawrence, this flow is not confined along the east side of Cabot Strait. GoMSS generates a northward current along the east side of the Laurentian Channel, however, much of this flow recirculates southward at the model's north boundary (i.e., along Cabot Strait) and does not exit the model domain. This feature is unrealistic and demonstrates how biases introduced through the lateral boundary conditions can affect GoMSS solution.

Figures 5.34 to 5.37 show that the model simulates well the observed clockwise circulation around the Sable Island, with typical values between 0.08 (winter) and 0.2 m s^{-1} (summer). As discussed in section 5.1, this clockwise current is driven by tidal rectification. Over the Gully the model simulates a cyclonic circulation that varies seasonally, in agreement with *Han et al.* (2001) and *Shan et al.* (2014). In summer, off the shelf, the model generates a strong northward flow (0.15 m s^{-1}).

GoMSS predicts a cyclonic circulation along the coast of the Gulf of Maine, that is intensified during summer, in agreement with *Brooks* (1985) and *Lynch et al.* (1996). The global system does not capture accurately this cyclonic circulation during summer. Consistent with *Lynch et al.* (1996), the model simulates the cyclonic partial gyre over the Jordan Bank and its intensification during summer. Additionally, the model simulates well the observed clockwise circulation over the Georges Bank (a peak speed above 0.4 m s^{-1} along the north side of the Bank that reaches up to 0.65 m s^{-1} along the northeast side, during summer) that is due to tidal rectification. This is consistent with previous studies (e.g., *Loder*, 1980; *Butman et al.*, 1982; *Greenberg*, 1983; *Naimie et al.*, 1994; *Hannah*

et al., 2001). The global system also has currents with clockwise tendency above Georges Bank but these currents are much weaker that the observed presumably because it does not have tides.

Flow across the Halifax Line: Seasonal mean currents normal to the Halifax Line for GoMSS and the global system are shown in Figure 5.38. During winter, GoMSS simulates well the position and vertical structure of the strong southward current along the coast of Nova Scotia. However, GoMSS underestimates the current velocity (model maximum speed is 0.17 m s^{-1}). In summer, GoMSS simulates accurately the observed weakening of the southwards flow along the coast. Figure 5.38 shows that in winter, near the edge of Emerald Basin (near 43.7°N), GoMSS generates the observed weak northwards flow. This flow is associated with a cyclonic gyre above Emerald Basin that has been observed in previous studies (e.g., *Han et al.*, 1997; *Loder et al.*, 1997; *Hannah et al.*, 2001). Additionally, in summer, at around 44.3°N and near the surface, the model generates northward flow of order of 0.1 m s^{-1} that is not present in the observations. This flow has large interannual variability (i.e., the flow disappears in 2011 and intensifies in 2012).

Overall, the flow across the Halifax Line predicted by the global system is consistent with GoMSS and the observations. Nevertheless, the predictions of GoMSS (Figures 5.38) are in better agreement with the observations than the global system. In fact, during summer, the global system has a very weak southward flow along the coast (almost zero flow).

In terms of the integrated flow of the Nova Scotia Current across the Halifax Line, *Hebert et al.* (2013) estimated the transport to be 0.61 and 0.24 Sv in winter and summer respectively, based on acoustic Doppler current profiles (ADCP) from 2010-2012. GoMSS predicts winter and summer transports of 0.55 Sv and 0.25 Sv respectively, in good agreement with the observed transport. The global model predicts transport in better agreement with the observed in winter (0.60 Sv). However during summer the global system significantly underestimates the transport, predicting a transport of 0.15 Sv.

Flow across the Cape Sable section: Seasonal mean currents normal across a line radiating from Cape Sable are shown in Figure 5.39. The line crosses Browns Bank and the Northeast Channel. Near Cape Sable, GoMSS simulates the flow from the Scotian Shelf

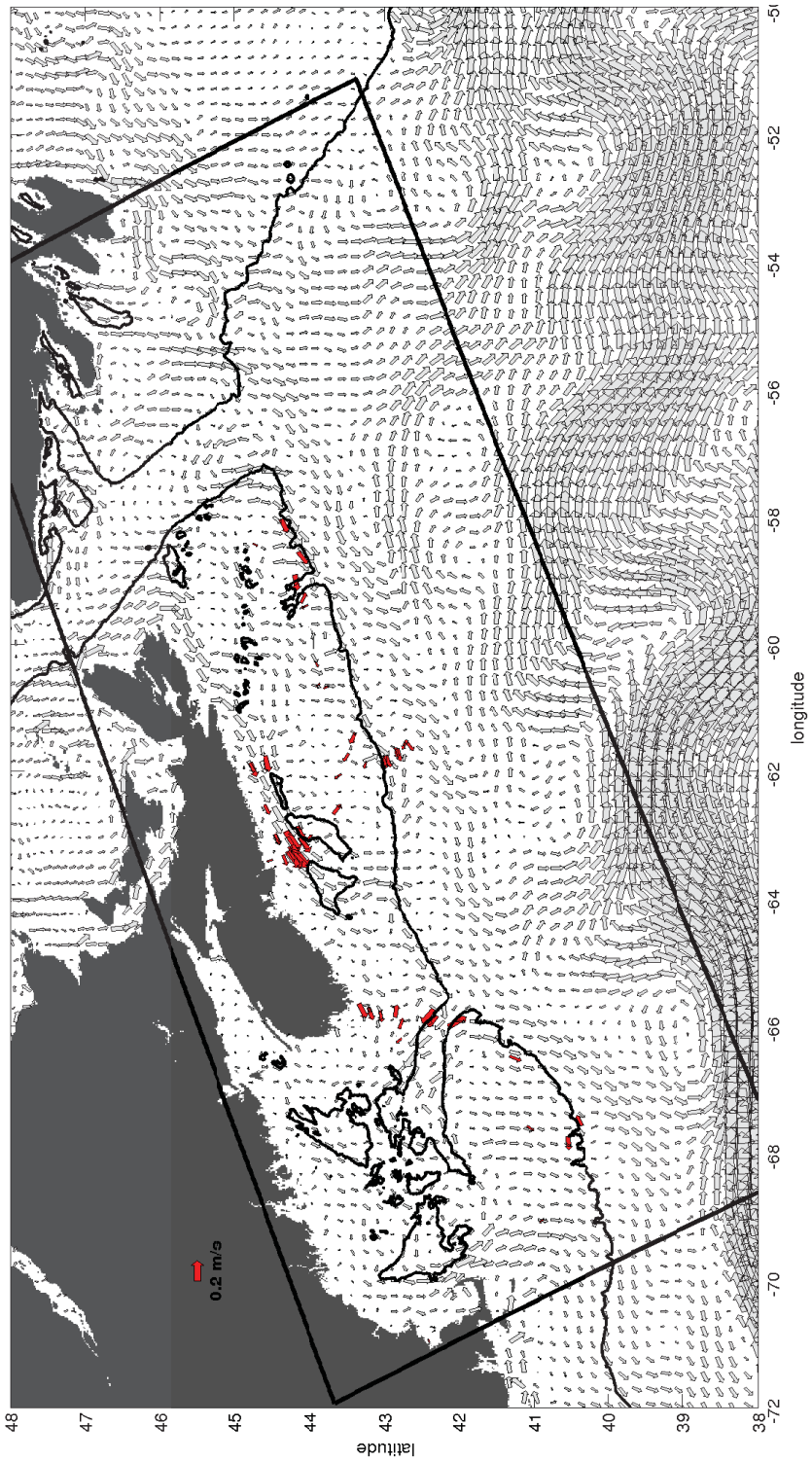

Figure 5.34: The observed (red arrows) and the global system (every 3 grid points) winter mean currents averaged over the top 100 m. The black line shows the 200 m isobath. The black squares indicates the domain of GoMSS. The global system mean currents are based on the 2010-2012 time period.

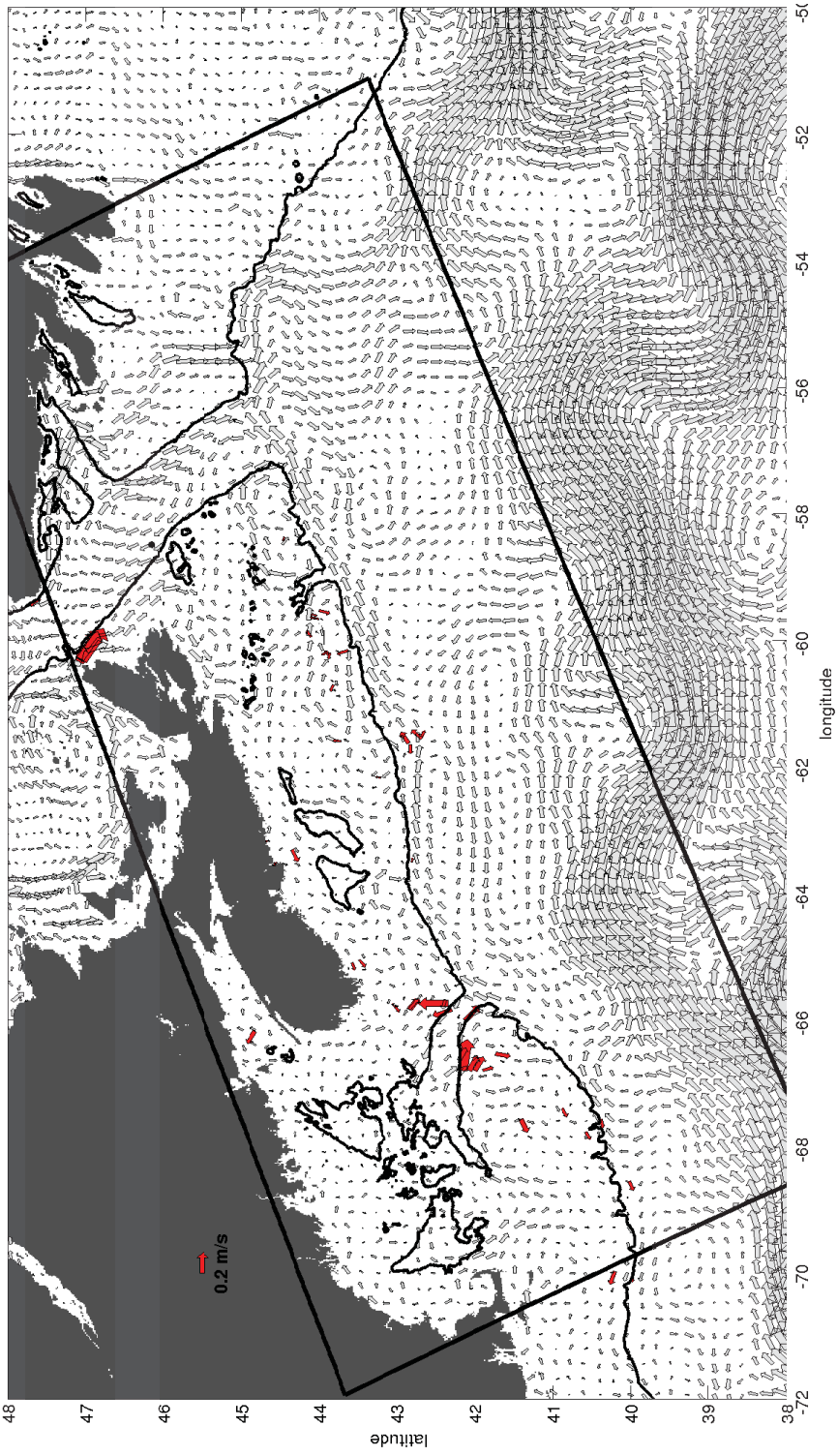

Figure 5.35: The observed (red arrows) and the global system (every 3 grid points) summer mean currents averaged over the top 100 m. Same format as 5.34

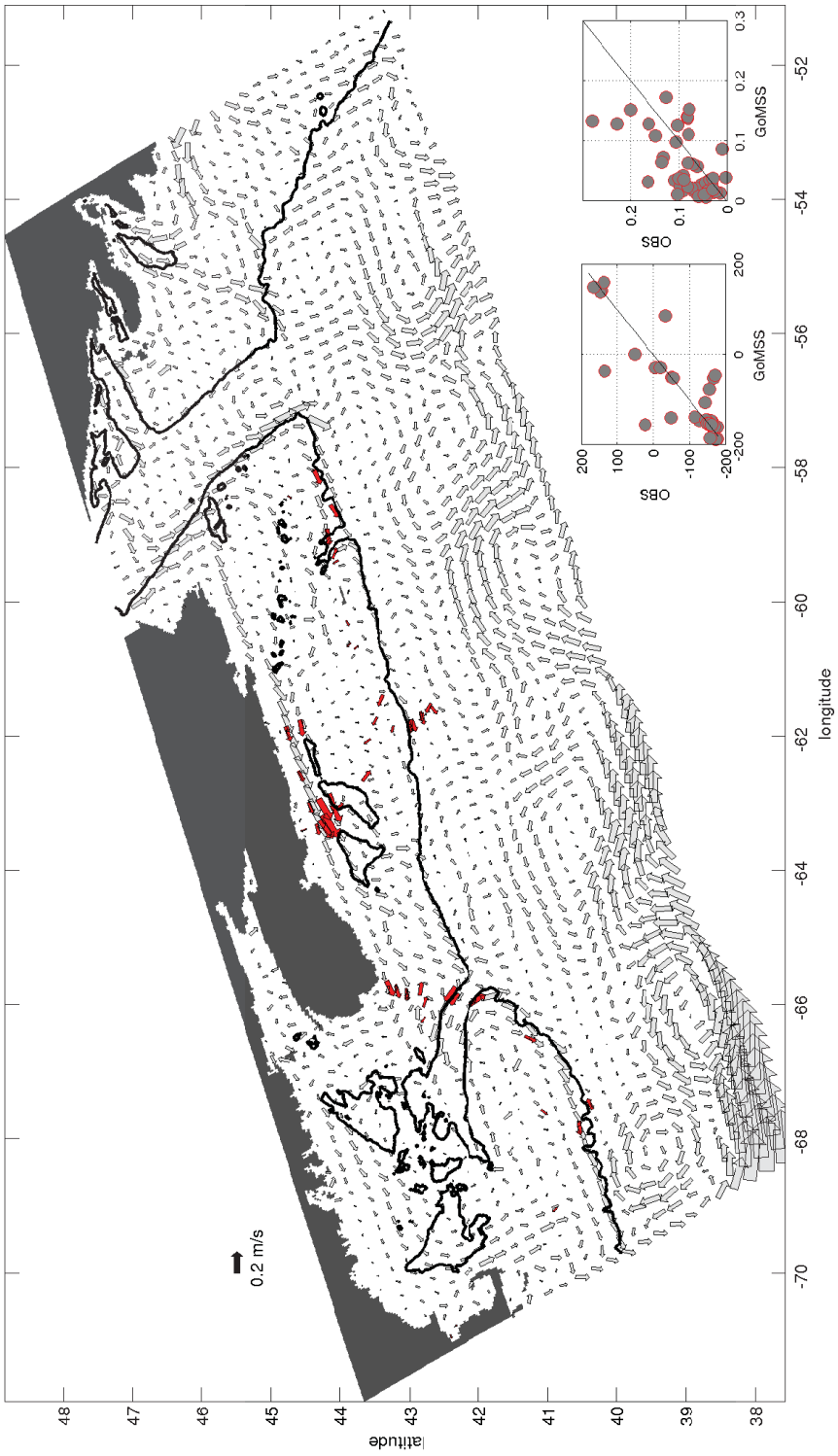

Figure 5.36: The observed (red arrows) and GoMSS (every 8 grid points) winter mean currents averaged over the top 100 m. The black line shows the 200 m isobath. The insets are scatterplots of observed and predicted speed (m s^{-1}) and direction (degrees, clockwise from eastward). GoMSS mean currents are based on the 2010-2012 time period.

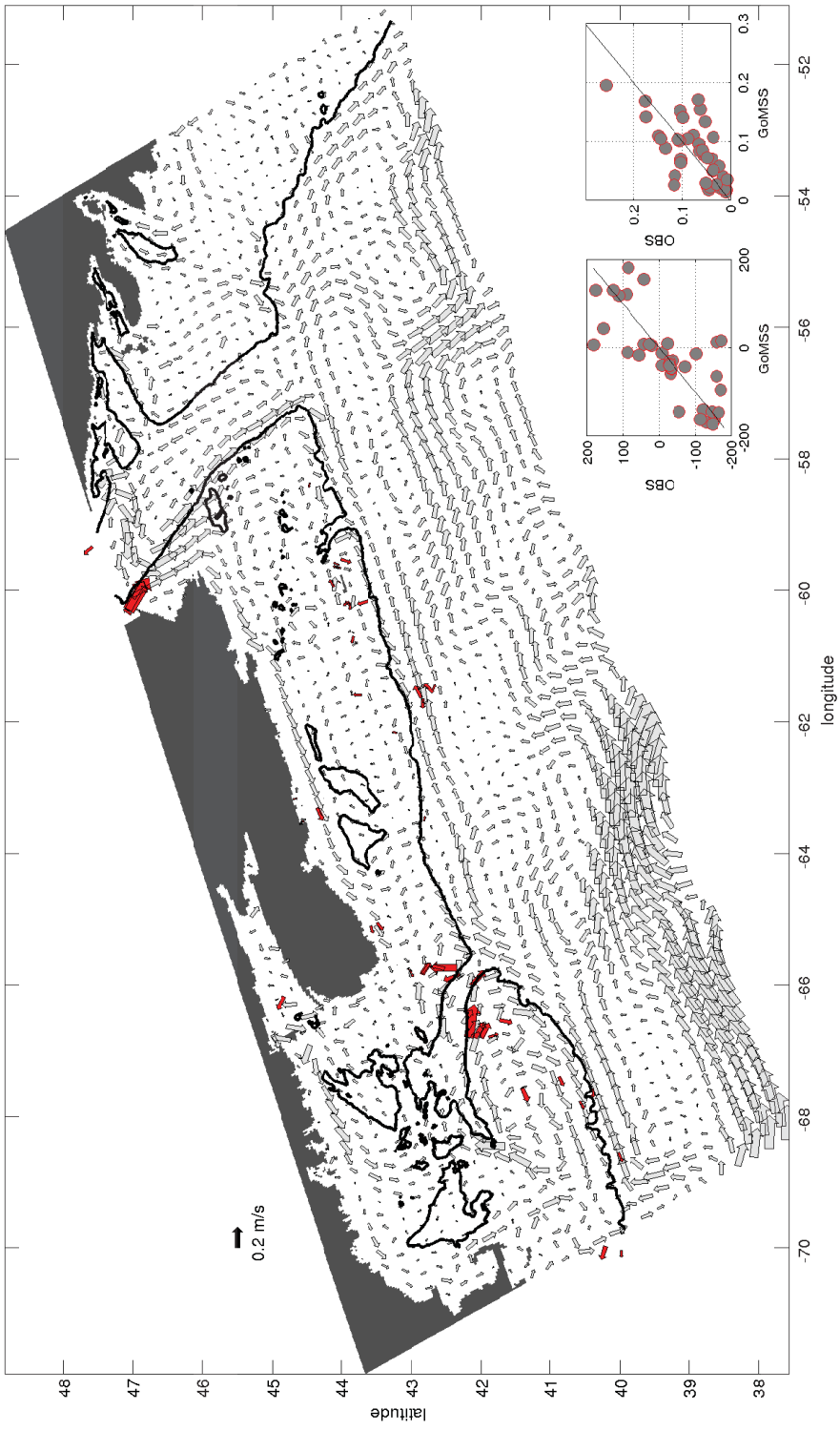

Figure 5.37: The observed (red arrows) and GoMSS (every 8 grid points) summer mean currents averaged over the top 100 m. Same format as 5.36.

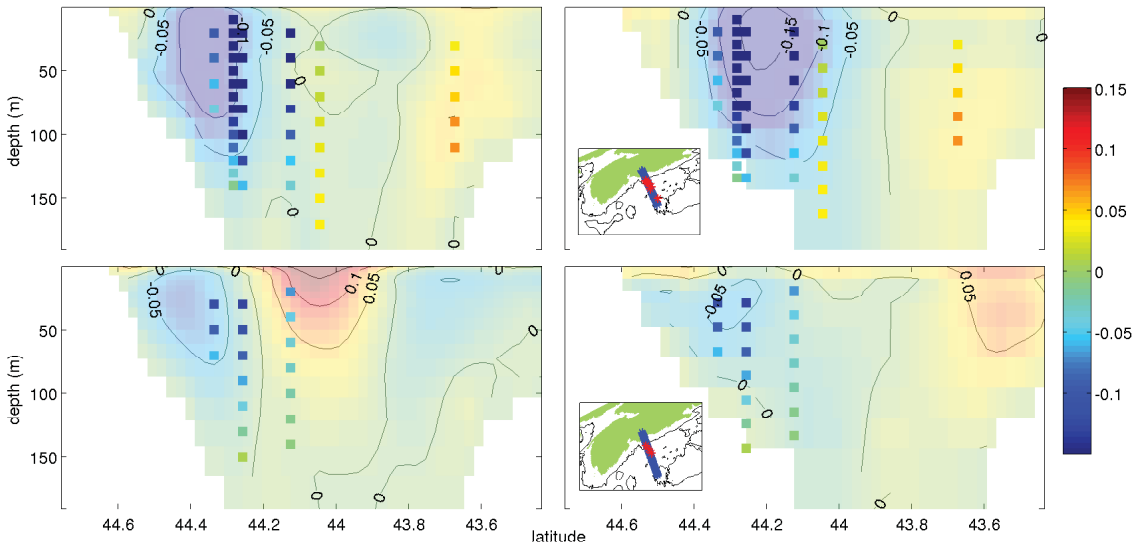

Figure 5.38: Seasonal mean currents normal to a section crossing the Scotian Shelf (see inset). Results from the global system and GoMSS are shown in the left and right panels respectively. Winter and summer means are shown in the top and bottom panels respectively. The bold boxes show the velocities calculated from current meter observations (red dots on the inset panel). The velocity is in m s^{-1}.

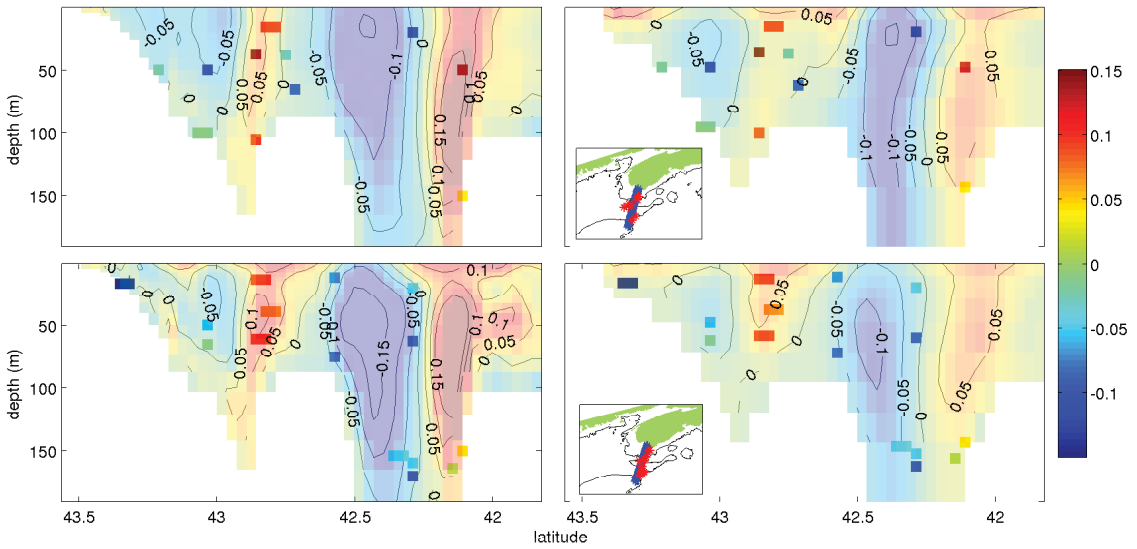

Figure 5.39: Seasonal mean currents normal to a section radiating from Cape Sable at the western end of Nova Scotia. Same format as Figure 5.38.

into the Gulf of Maine throughout the year, consistent with observations. Although the model captures the weakening of this flow during summer, it underestimates the speed of the flow by around 0.1 m s^{-1} during winter.

The model simulates the clockwise circulation above Browns Bank (i.e., eastwards flow on the north side of the Bank and westwards flow on the south side of the Bank, Figure 5.39) that persist throughout the year. This flow is associated with tidal rectification and has been observed in previous studies (e.g., *Greenberg*, 1983; *Hannah et al.*, 2001). The global system underestimates the clockwise flow on top of Browns Bank, because it does not include tides. Both the global system and GoMSS simulate well the observed circulation along the Northeast Channel that persists throughout the year: inflow towards the Gulf of Maine along the north side of the channel, and outflow along the south side of the channel. In both summer and winter the global system generates a weaker outflow than GoMSS. This is because the outflow is part of the clockwise current above the Georges Bank that is associated with tidal rectification as discussed in subsection 5.1.2 (a process absent in the global system).

Quantitative comparison: Although visual comparison of the global system and GoMSS with observations is informative, a quantitative comparison is required. To quantify the error we need to take into account discrepancies in *i)* current speed, *ii)* current direction, and *iii)* the absence of an observed large scale mean flow. To satisfy the above criteria, I define the following linear regression model:

$$\mathbf{u}_{obs} = \boldsymbol{\beta}_0 + \mathbf{u}_{mod}\boldsymbol{\beta}_1 + \epsilon \tag{5.4}$$

where $\mathbf{u}_{obs}$ and $\mathbf{u}_{mod}$ denote the colocated observed and predicted seasonal mean currents respectively, and ϵ denotes the error. The currents and error, and the regression coefficients $\boldsymbol{\beta}_0$ and $\boldsymbol{\beta}_1$, are assumed to be complex (e.g., $\mathbf{u} + i\mathbf{v}$). The intercept $\boldsymbol{\beta}_0$ corresponds to a large scale flow not captured by the ocean model. The coefficient $\boldsymbol{\beta}_1$ allows for scaling and rotation of the predicted flow by the same amount at all locations in order to bring the model flows into better agreement with the observed mean flows.

The estimates for $\boldsymbol{\beta}_0$ and $\boldsymbol{\beta}_1$ were obtained using complex least squares and denoted by $\hat{\boldsymbol{\beta}}_0$ and $\hat{\boldsymbol{\beta}}_1$. The predicted mean flow is then given by $\hat{\mathbf{u}} = \hat{\boldsymbol{\beta}}_0 + \mathbf{u}_{mod}\hat{\boldsymbol{\beta}}_1$ and we use the

following measure of model fit:

$$R^2 = \frac{\sum_{i=1}^{N_{obs}} |\hat{\mathbf{u}}|_i^2}{\sum_{i=1}^{N_{obs}} |\mathbf{u}_{obs}|_i^2} \tag{5.5}$$

Note that this metric corresponds to the proportion of kinetic energy of the observed mean flow that is accounted by the model. It is constrained to be between 0 and 1.

Table 5.10: Fit of the global system and GoMSS to observed mean flows in winter for three depth ranges. The regression coefficient $\hat{\beta}_1$ is given in polar form (vector scale and rotation, in degrees).

R^2	Global system	GoMSS	β_1	Global system	GoMSS
0-20 m	0.82	0.68	0-20 m	(1.40, 3.5)	(0.90, 1.6)
21-100 m	0.62	0.62	21-100 m	(0.98 -1.5)	(0.82, 0.9)
101-300 m	0.06	0.21	101-300 m	(0.44, 24.2)	(0.81, 15.9)

Table 5.11: Fit of the global system and GoMSS to observed mean flows in summer. Same format as Table 5.10.

R^2	Global system	GoMSS	β_1	Global system	GoMSS
0-20 m	0.47	0.46	0-20 m	(1.31, 16.7)	(0.83, 14.4)
21-100 m	0.39	0.51	21-100 m	(1.36 -9.6)	(0.75, -0.6)
101-300 m	0.45	0.45	101-300 m	(0.78, 6.4)	(0.48, -9.5)

The estimates of β_1 and R^2 for three depth ranges, and winter and summer, are listed in Tables 5.10 and 5.11. Note that β_0 is approximately zero for all depth ranges during winter and summer.

For the top 20 m, during winter, the global system and GoMSS have an R^2 index equal to 0.82 and 0.68, respectively. This indicates that their circulation is in good agreement with the observations. However, during winter, the number of the observations at the surface is relatively small (See Figure 5.33). In summer, where there are more observations GoMSS and the global system skill drops to 0.47 and 0.46, respectively. For the intermediate depths (21-100 m) and winter, the global system and GoMSS have an R^2 index equal to 0.62, which implies that they both simulate well the intermediate depth circulation. For the intermediate depths and summer, GoMSS skill is significantly higher than the

global system. For the bottom layer (101-300 m) GoMSS has higher skill than the global system in winter. The low skill of the global system and GoMSS during winter is probably associated with the limited number and location of observations.

GoMSS generally overestimates the current speed ($\beta_1 < 1$), but it has a small angle error, which shows that the model simulates well the orientation of the circulation. Overall the global system has a larger angle error than GoMSS.

5.4 Summary

GoMSS provides realistic simulations of tidal heights and tidal currents. Notably, the model simulates well the impact of stratification on tides (e.g., the internal tide generation over abrupt topography in areas with strong density stratification) and provides realistic predictions of tidal residual currents. GoMSS resolves well the variability associated with small scales. However, in areas with many observations (e.g., at the ocean surface where satellite data are available), the global system generates more realistic fields due to the assimilation of the observations.

Overall, the predictions of the global system and GoMSS are similar over the shelf. GoMSS provides better simulations of the circulation in areas where the interaction of strong tidal currents with local bathymetry is important (e.g., Georges Bank, Browns Bank, Sable Island). Additionally, GoMSS simulates better the temperature and salinity fields where tidal mixing is important (e.g., Gulf of Maine). Off the shelf the global system and GoMSS predict very different circulation patterns. GoMSS is often not able to accurately simulate the location and timing of eddies or meanders. This is associated with the unrealistic internal variability that develops in all regional models as discussed in Chapter 2. Furthermore, GoMSS also generates some unrealistic features near its open lateral boundaries, e.g., a persistent anti-cyclonic gyre off the shelf near the western lateral boundary.

The unrealistic internal variability, and the unrealistic features near some lateral boundaries, both reduce the predictive skill of GoMSS. In the next chapter I introduce a method to constrain these undesirable features in order to achieve a more accurate form of downscaling.

CHAPTER 6

DOWNSCALING THE NORTHWEST ATLANTIC AND ADJACENT SHELF SEAS

I now investigate the generation of unrealistic internal variability, and recirculation along the lateral boundaries of the GoMSS regional model, and implement a new method (described in Chapter 2) to eliminate them. The method is similar to atmospheric spectral nudging but it has been modified for ocean applications. Specifically, the large scales of GoMSS are relaxed towards the state provided by the global system using spectral nudging. The new downscaling system will henceforth be referred to as GoMSS$^+$. Extensive comparisons of the predictions of GoMSS and GoMSS$^+$ with observations are described. However, in the deep water the observations are limited and the global system assimilates these observations. Thus not surprisingly the global system generates fields in very close agreement with these observations (e.g., along the altimeter line described in Chapter 5). This complicates the comparison between the global system and GoMSS$^+$. For this reason, and to better understand the impact of spectral nudging on the length scales that are not directly affected by the spectral nudging, I also quantify the distribution of variance on different length scales in the three systems using wavenumber spectra.

In section 6.1 the generation of unrealistic internal variability by GoMSS, and the impact of the ill-posed lateral boundary conditions, are discussed. I also investigate if the assimilation of observations in the global system can generate dynamical inconsistencies. In section 6.2 the implementation of the new downscaling method in GoMSS is discussed. The benefit of the new downscaling method over one-way nesting is discussed in section 6.3,

where GoMSS$^+$ results are evaluated based on observations and comparisons with GoMSS and the global system fields. In section 6.4 I investigate the impact of spectral nudging on energy and enstrophy transfer through the analysis of wavenumber spectra. The results of the chapter are summarized in section 6.5.

6.1 Motivation for the New Downscaling Method

GoMSS is more realistic than the global system because it includes tides and has higher resolution, thereby better resolving the small scale variability. However, it misplaces some of the small scale variability, not because its dynamics are flawed, but because the large scale patterns are misplaced (e.g., the position of the front between the shelf and slope water). On the other hand, the large scale patterns of the global system are more accurate (at least closer to the surface) because the global system assimilates all available in situ and satellite observations. It is important to note however that the assimilation of observations may lead to unrealistic variability in the fields that are not directly observed. In this section I investigate the variability of the global system and GoMSS for different length scales, focusing on the manifestation of unrealistic internal variability and recirculation along the open lateral boundaries of GoMSS, and unrealistic features in output from the global system caused by data assimilation.

6.1.1 Spatial and Temporal Variability

To examine the spatial and temporal variability of temperature and salinity, I now describe the autocorrelations of the global system and GoMSS for different times (temporal lag) and for different grid points (spatial lag). (See Appendix D for details.)

The spatial autocorrelation of temperature and salinity are shown in Figures 6.1 and 6.2, respectively, for the global system and GoMSS. Correlation contours are shown for six reference points (indicated by black stars): two on the shelf, two at the shelf break, and two in deep water. Temperature and salinity were averaged over the top 20 m and the annual and semi-annual cycles were removed before calculating the autocorrelations.

On the Scotian Shelf, the GoMSS temperature autocorrelation is high over most of the shelf. This pattern is due to the advective effect of the Scotian Shelf current flowing to the southwest along the shelf. GoMSS salinity autocorrelation is limited to smaller

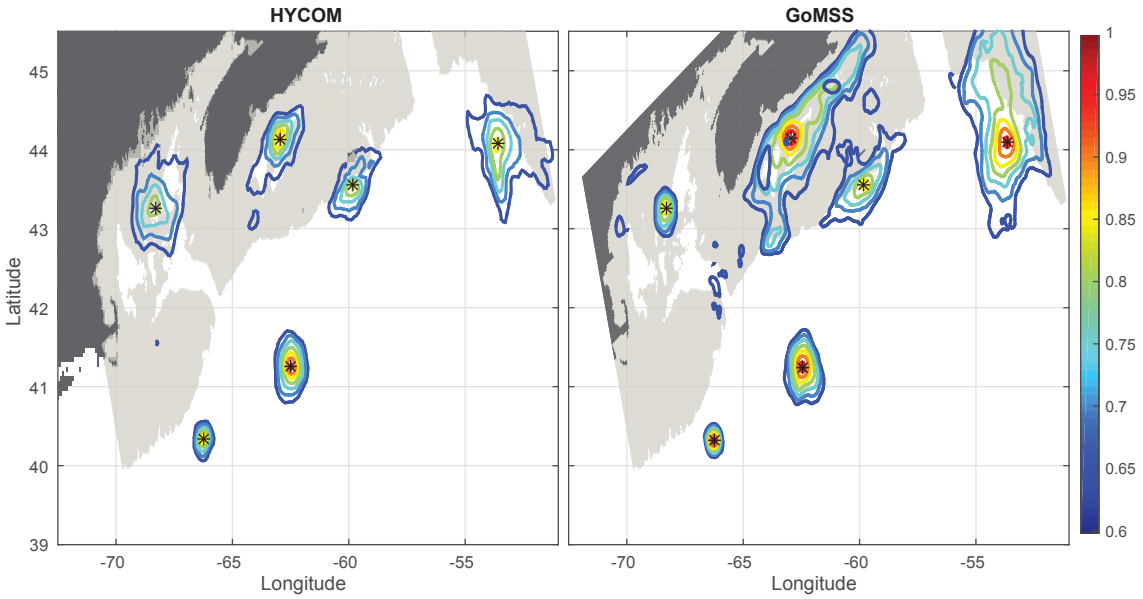

Figure 6.1: Spatial autocorrelations for temperature for the global system (left panel) and GoMSS (right panel) for the 6 reference locations indicated by the black stars. Temperature and salinity were averaged over the top 20 m and the annual and semiannual cycles were removed before calculating the autocorrelations. Light gray shows areas shallower than 200 m.

scales than the temperature, however it is still extended downstream due to advection. The corresponding decorrelation length scales for the global system, for both temperature and salinity, are shorter than GoMSS on the Scotian Shelf. The global system's decorrelation length scales are limited to around 35 km (close to the first Rossby radius of deformation in the area). This is not dynamically consistent with the advective effect of the local circulation and is due to the assimilation of observations. Specifically, in the global system, the salinity and temperature are horizontally adjusted based on observations using correlation length scales specified by the first Rossby radius of deformation. Furthermore, altimeter derived synthetic profiles observations are used to adjust the temperature and salinity profiles below the surface (*Fox et al.*, 2002) in areas with no in situ observations. Thus, although the assimilation may keep the global system temperature fields close to observations it also introduces features that are not consistent with the local circulation. An example is shown in Figure 5.20, where, in summer, near the Gully the global system has an unrealistic circular water mass of cold water with a warm core that does not appear

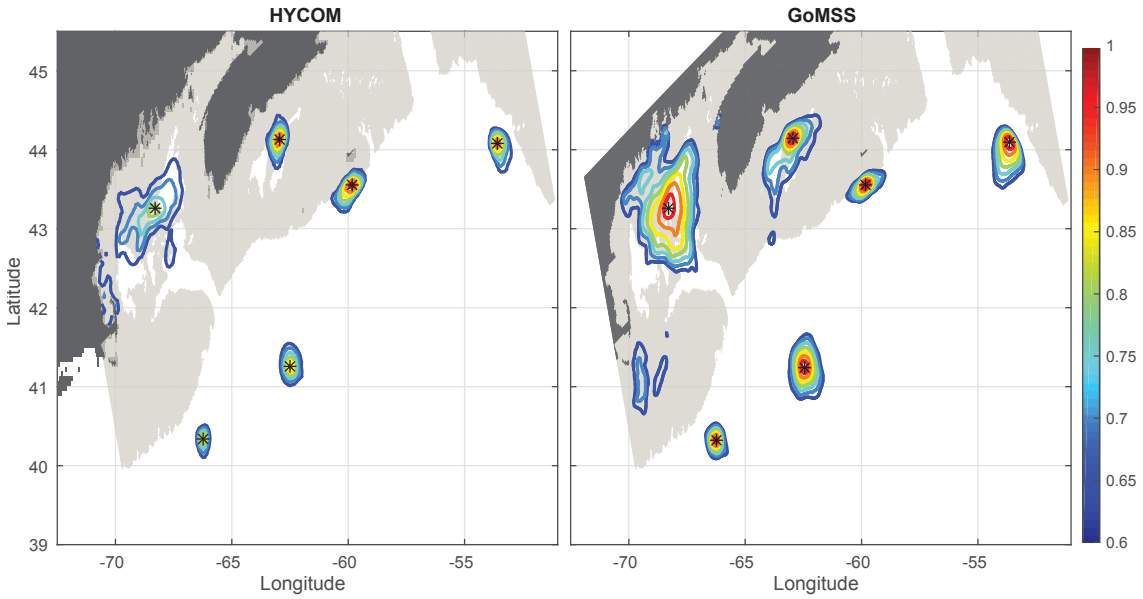

Figure 6.2: Spatial autocorrelation for salinity for the global system (left panel) and GoMSS (right panel). Same format as Figure 6.1.

in the temperature satellite observations.

In the Gulf of Maine, the decorrelation length scales of the global system and GoMSS for temperature are relatively small. However the GoMSS salinity autocorrelation is high over most of the Gulf, suggesting the salinity fields are dominated by advection by the large scale circulation. The global system's salinity decorrelation length scales are similar to its temperature length scale but somewhat shorter.

Near the shelf break, the GoMSS decorrelation length scale for temperature is elongated along the slope indicating the effect of advection. Again, the global system decorrelation length scales are shorter due to the effect of assimilation. The decorrelation length scale in deeper water is generally short in both the global system and GoMSS. This is not surprising because, in deep water, non-linear processes are dominant leading to the generation of small scale features.

The temporal autocorrelation of temperature and salinity are shown in Figures 6.3 and 6.4 respectively for the global system and GoMSS. Autocorrelations are shown for five time series: two from the shelf, two from the shelf slope, and one in deep water. Temperature and salinity were averaged over the top 20 m. The temporal autocorrelations of the global

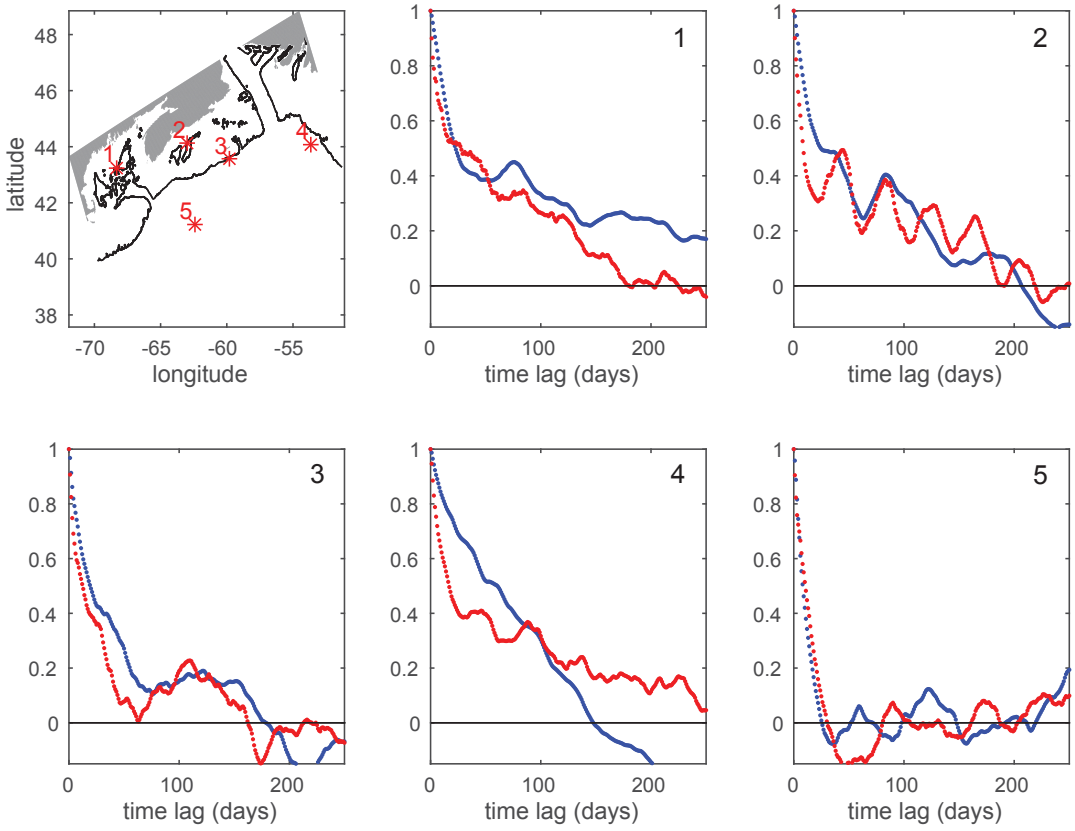

Figure 6.3: Temporal autocorrelation of temperature for the global system (red) and GoMSS (blue) for the five locations shown by red stars. The temperatures were averaged over the top 20 m, and the annual and the semiannual cycles were removed, before calculating the autocorrelation.

system and GoMSS are generally similar. On the shelf (locations 1 and 2) there are two dominant correlation time scales for temperature. The first one is about 20 days and is associated with the influence of the atmosphere (e.g., wind mixing, net incoming solar radiation). The second one is of about 150 days and longer, and I attribute it to the local circulation (advection from the north, flowing along the Scotian Shelf and into the Gulf of Maine). In the Gulf of Maine (location 1), the global system temperature decorrelates faster than GoMSS. Salinity autocorrelation also has two dominant time scales, similar to temperature. Overall salinity decorrelates somewhat faster than the temperature.

At the Scotian Shelf break (location 3) the global system and GoMSS have very similar temperature and salinity autocorrelation. At the Newfoundland Shelf break (location 4) the

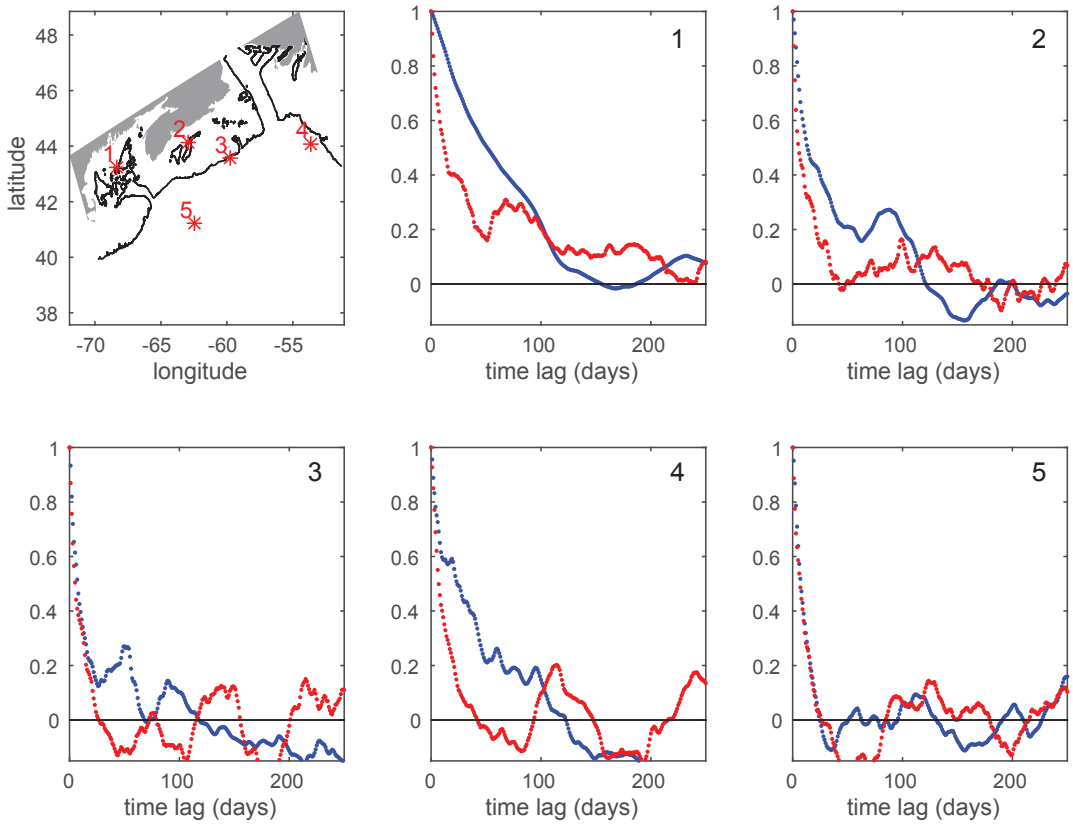

Figure 6.4: Temporal autocorrelation of salinity for the global system (red) and GoMSS (blue) for the five locations shown by red stars. Same format as Figure 6.3.

GoMSS temperature decorrelation time scale is significantly shorter than that of the global model; this is probably associated with the proximity of the open boundary. In deep water (location 5) the autocorrelation of GoMSS and the global system drops quickly (20 days decorrelation time scale, associated with atmospheric forcing). This is expected because in deep water the non-linearity causes high frequency variability e.g., eddies.

6.1.2 Internal Variability

As discussed in the Introduction and Chapter 2, all realistic regional models generate internal variability. Figure 6.5 maps the correlation between colocated values of temperature and salinity from GoMSS and the global system. Temperature and salinity were averaged over the top 20 m, and the annual and semi-annual cycles were removed, before calculating the correlation. The global system and GoMSS temperatures are strongly correlated along the lateral boundary sponge layer, as expected. However the correlation

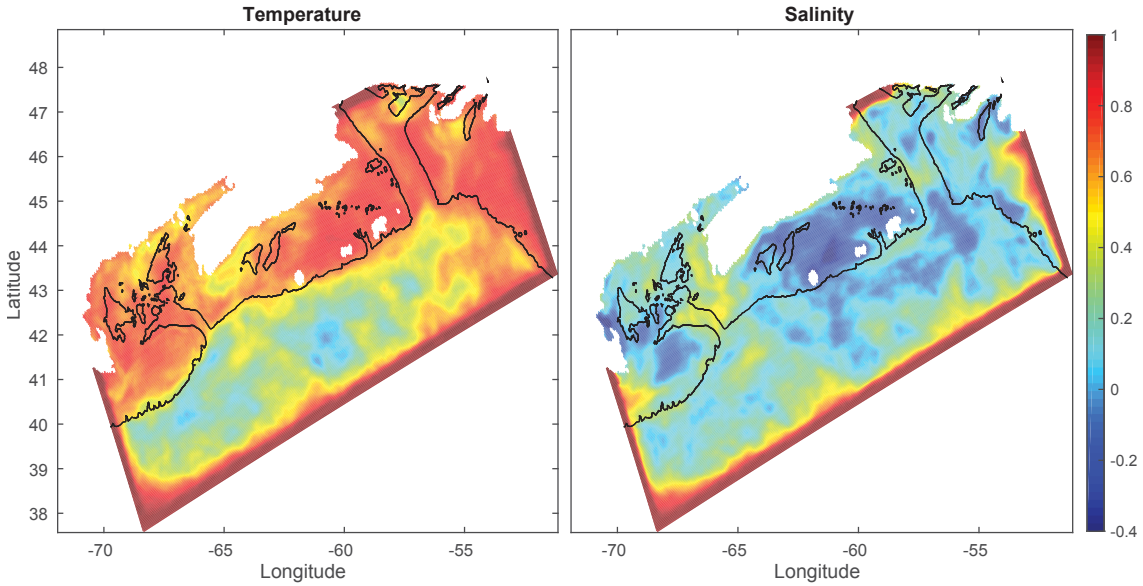

Figure 6.5: Correlation of colocated temperature (left panel) and salinity (right panel) from the global system and GoMSS. The black lines show the 200 m isobath. The temperatures and salinities were averaged over the top 20 m, and the annual and the semiannual cycles were removed, before calculating the correlation. Based on 2010-2012 time period.

drops quickly beyond the sponge layer in the deep water where the circulation is influenced by nonlinear eddies and meanders. This reduced correlation between the two models is the manifestation of internal variability: GoMSS and the global system both generate eddies, meanders and fronts, but they place them at different locations.

On the shelf, near the surface, temperature is driven primarily by the atmospheric forcing, mixing and the local circulation. Both the global system and GoMSS have similar atmospheric forcing and general circulation on the shelf (see Chapter 5). GoMSS represents better the mixing on the shelf because of its tides and higher resolution, however the global system compensates for the absence of tides and resolution by assimilating observations (e.g., surface temperature from satellites). Thus it is not surprising that GoMSS and the global system temperature is strongly correlated on the shelf.

On the shelf the global system and GoMSS salinities are not correlated. The global system has generally a larger salinity error than GoMSS (see Chapter 5, Tables 5.6, 5.7 and 5.8). This is not surprising because (i) salinity is sensitive to river run-off and it is specified differently in the two models, (ii) the global system does not include tidal mixing, and (iii)

less observations for salinity than temperature are available at the ocean surface (satellite and in-situ observations are available for temperature while only in-situ observations are available for salinity) and thus larger uncertainty is expected in the global system salinity fields.

Overall, the cross-correlation maps for salinity and temperature of the global system and GoMSS are consistent with the conclusions of Chapter 5. GoMSS and the global system have similar temperature over the shelf but different temperature in deep water. The global system's large scale patterns (e.g., meanders and the front between slope and shelf water) are consistent with the assimilated satellite observations of temperature; GoMSS misplaces some of these large scale patterns.

6.1.3 Lateral Open Boundaries

A radiation algorithm, with different relaxation coefficients for inflow and outflow, was used at the GoMSS lateral boundaries in an attempt to allow perturbations to leave the model domain (Chapter 4). However, perturbations are sometimes trapped within the domain leading to unrealistic recirculation near the open boundaries. This recirculation occurs in areas where GoMSS has large outflow (out of the model domain) while the global system (the source of the open boundary condition) has weaker outflow, or even inflow. To illustrate, Figure 5.36 shows an unrealistic anti-cyclonic eddy located adjacent to the west boundary.

I conducted several sensitivity experiments based on varying the outflow relaxation strength. Very strong relaxation leads to more unrealistic recirculation near the boundaries, however it keeps the model outflow locations consistent with the global system. Very weak relaxation limits the recirculation but it leads to areas of outflow that are inconsistent with the global system. Additionally, for each boundary the optimal relaxation time scale is different.

The inflow boundary conditions are not perfect either. For example, Figures 5.35 and 5.37 show that at GoMSS's north boundary there is a strong inflow from the Gulf of Saint Lawrence on the east side of Cabot Strait. In the global system, this inflow is mainly confined to the Newfoundland Shelf (some recirculation does occur). By way of contrast, a substantial part of this inflow in GoMSS travels southwards along the north boundary and is combined with inflow from the west side of Cabot Strait. The global system inflow

at the east side of Cabot Strait is not consistent with observations as discussed in Chapter 5. Thus this unrealistic inflow, forced by the north lateral boundary condition, follows a path that is dynamically consistent with the local circulation in the model but different from that of the global system.

GoMSS and the global system generate small scales variability differently because GoMSS has higher resolution and includes tides. Additionally, the GoMSS fields are always dynamically consistent because the model does not assimilate observations. However, the realism of GoMSS could be improved by suppressing the recirculation of trapped perturbations, and constraining the internally generated variability. In the next section I discuss a different method for downscaling the ocean conditions. This method is designed to be easily relocatable and eliminates the necessity of treating each boundary differently.

6.2 Spectral Nudging and its Implementation in GoMSS

The downscaling method introduced in Chapter 2 is now applied to GoMSS to overcome the problems associated with one-way nesting discussed in the previous section. The goal is to relax the large scale state of GoMSS towards the global model state and permit the small scales to evolve freely. I already showed in Chapter 3 that this method can be used successfully to downscale conditions in an idealized ocean model. However, there are several challenges in applying the method to a realistic ocean model. For example, the model's coastline is convoluted and so the two dimensional Fourier transform (used in Chapter 3 and in atmospheric modelling) has to be replaced by some other method of separating length scales. Additionally, the spectral nudging coefficient should be allowed to depend on horizontal (e.g., distance from shore) and vertical position (e.g., proximity to seafloor or surface).

6.2.1 Regional Model Primitive Equations with Spectral Nudging

In this study, two variables are influenced directly by spectral nudging: temperature and salinity. Thus only the temperature and salinity governing equations need to be modified directly by the spectral nudging. Based on discretizing equations (4.1) and also (2.11), the

Table 6.1: Main characteristics of GoMSS with spectral nudging (GoMSS$^+$).

	GoMSS$^+$
Model Framework	NEMO
Resolution	1/36°
Domain	Gulf of Maine, Scotian Shelf, and adjacent deep ocean
Atmospheric forcing	CFSR
Tidal forcing	FES2004
Spectral Nudging	global system
Nudging time step	12 minutes
Cutoff wavelength	90 km
Relaxation time	1 hour

model governing equations for temperature and salinity take the form

$$T_t = \mathcal{D}_t(T_{t-1}) + \gamma\langle T_t^{GS} - \mathcal{D}_t(T_{t-1})\rangle_L \tag{6.1}$$

$$S_t = \mathcal{D}_t(S_{t-1}) + \gamma\langle S_t^{GS} - \mathcal{D}_t(S_{t-1})\rangle_L \tag{6.2}$$

where T^{GS} and S^{GS} are the temperature and salinity fields from the global system, γ is the nudging coefficient and $\langle\cdot\rangle_L$ denotes a quantity that has been spatially smoothed to provide its large scale component. Note that in my experiments I use the same γ for salinity and temperature but this is not required by the method.

For computational reasons, the nudging term is not estimated every time step. After some experimentation it was found that estimating and applying the nudging every 4 model time steps (i.e., every 12 minutes, Table 6.1) was sufficient. This reduced significantly the computation cost of running GoMSS$^+$.

6.2.2 Length Scale Separation

A two dimensional Fourier transform was used in Chapter 3 to define the large and small scales. This approach is used in atmosphere downscaling, and with idealized models with simple rectangular model domains. However, in the real ocean, near the shore, the complexity of the coastline prohibits the use of Fourier transforms. I have used a two dimensional low-pass, second order Butterworth filter to define the large and small scales (similar to *Thompson et al.*, 2006).

Figure 6.6 shows the response of different order Butterworth filters. The low-pass

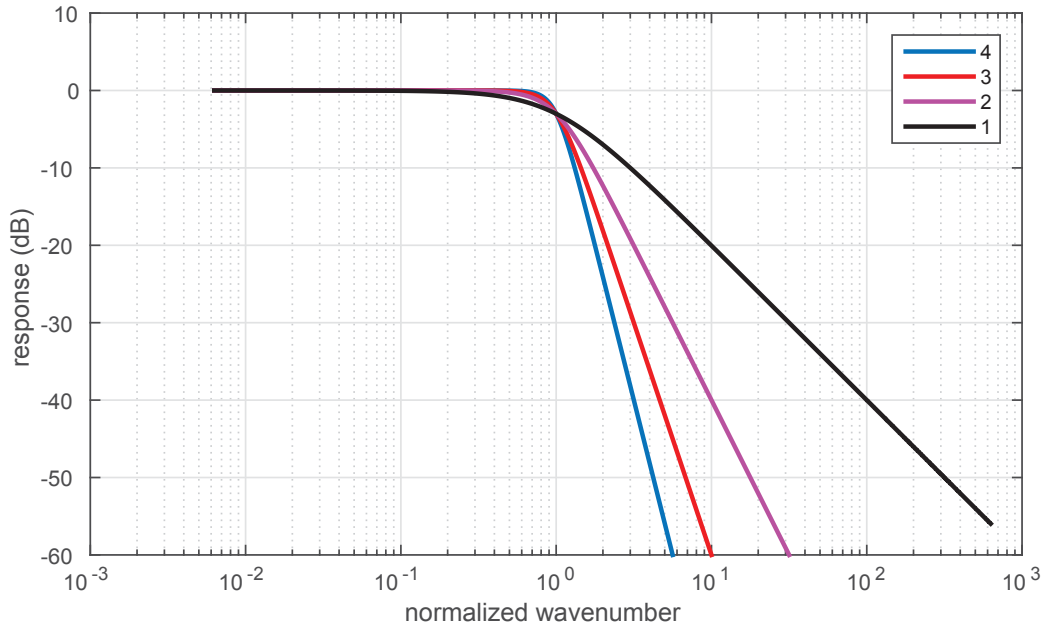

Figure 6.6: Response of the 1st to 4th order low-pass Butterworth filters as a function of wavenumber normalized by the cutoff wavenumber.

Butterworth filter allows all wavenumbers below a wavenumber cutoff to pass undisturbed (the pass band) while blocking the wavenumbers higher than the cutoff wavenumber (the stop band). The transition from stop band to pass band is smooth and it is controlled by the order of the filter as shown in Figure 6.6. The higher the order of the filter, the steeper the transition between the pass and stop band.

6.2.3 Parameter Choices

Length scale separation: GoMSS has higher resolution and thus resolves better the eddy variability. However, it does not always places the eddies at the correct location. To ensure that the spectral nudging does not suppress the variability on eddy scales and smaller, the cutoff wavelength (λ^c) must be larger than the first baroclinic Rossby radius of deformation, which is of the order of 30km in our domain. In this study I used $\lambda^c = 90\ km$. This choice was based on some sensitivity experiments that are not discussed further in this study.

Nudging horizontal variability: The discrepancy between the global system and GoMSS is most profound in deep water for the reasons given above. Near the coast GoMSS has more realistic hydrography and circulation than the global system because it has a higher resolution coastline. Thus, it is reasonable to increase the strength of nudging from the

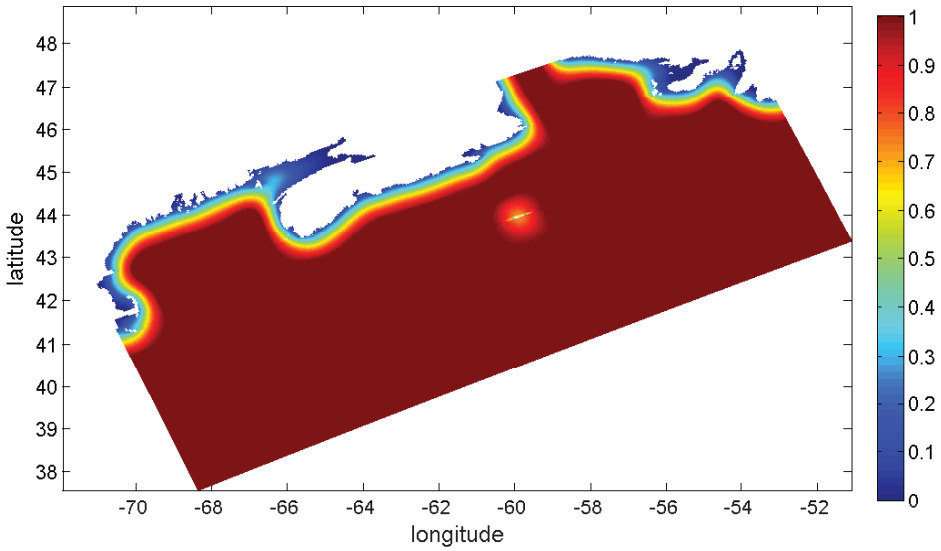

Figure 6.7: Coastal attenuation of the nudges by the Butterworth filter.

coast to deep water. This can be achieved in two ways i) by setting γ as a function of distance from the coast (with zero γ at the coast) or ii) by setting $\langle T^{GS} - \mathcal{D}_t(T_{t-1})\rangle_L = 0$ at the coast and letting it increase with distance from shore. Either way, the effect on the nudge $\gamma\langle T^{GS} - \mathcal{D}_t(S_{t-1})\rangle_L$ will be the same. I decided to use the second approach because it is straightforward to implement using a recursive Butterworth filter, by setting the land temperature and salinity values equal to zero and repeating the filtering over several passes. (Note the land points are reset to zero each pass.) The number of passes controls the distance from the coast over which the nudge is attenuated. I used 10 passes leading to an attenuation distance of around 70 km from the coast. Figure 6.7 illustrates this coastal attenuation. For this example I assumed the unfiltered nudge was equal to 0 and 1 for land and wet points respectively. After filtering ten times, the nudge is zero at the coast and increases toward 1 over a coastal band that is about 70 km wide. (An experiment with no nudging on the shelf is described in Appendix E.)

Nudging vertical variability: The global system's fields are most realistic at the surface because the system assimilates all available observations and most of them are made at, or close to, the sea surface. At greater depths, far fewer observations are available leading to an increase in global system errors with depth, especially off the shelf. For this reason I applied stronger spectral nudging near the surface, where the global system is trustworthy,

and reduced the strength of the nudging with depth such as that there is no nudging at the bottom in deep water (but the nudging is still significant at the bottom in shallow areas). Specifically the depth dependence of the nudging coefficient is assumed to be of the form

$$\gamma(z) = \gamma_0 \left[\frac{z_{max} - z}{z_{max}} \right]^{\frac{1}{4}} \tag{6.3}$$

where z and z_{max} are the model depth and the maximum model depth respectively. (In GoMSS $z_{max} = 4000.$)

The parameter γ_0 can be interpreted as the ratio of the nudging time step divided by the nudging relaxation time scale. In this study the nudging time step is equal to 12 minutes. The value of the relaxation time scale depends on the application and is usually estimated based on trials. The optimal value of the relaxation time scale is the subject of ongoing research (*Omrani et al.*, 2012). Because the purpose of this study is to show if spectral nudging can address weaknesses in the one way nesting, I decided to apply relatively strong nudging and used a relaxation time of one hour leading to γ_0=0.2. Similar results were obtained with other reasonable values of γ_0 (i.e., $1 \geq \gamma \geq 0.05$) .

6.3 Impact of Spectral Nudging on Prediction Skill

I now check if spectral nudging of the large scales keeps the GoMSS solution consistent with the global system and constrains the unrealistic variability in the deep ocean and adjacent to the model's open boundaries. More generally, I check if GoMSS with spectral nudging (GoMSS$^+$) successfully ingests the information on the large scales and predicts more accurate results. GoMSS$^+$ is evaluated by comparing its predictions with i) the global system, ii) GoMSS without spectral nudging and iii) observations. To simplify the comparison I discuss the deep water and shelf circulation and hydrography separately.

6.3.1 Deep Water and Shelf Break

Snapshots of surface temperature from satellite observations, the global system, GoMSS and GoMSS$^+$ are shown in Figure 6.8 for the same date. The observations are based on daily MODIS (Moderate Resolution Imaging Spectroradiometer) data at 5 km resolution, gridded into 1/12° and kindly provided by Dr. Emmanuel C. Devred. This snapshot was selected because of good satellite coverage; similar results are obtained for different

dates. Off the shelf, the global system's surface temperature is consistent with the satellite observations. A more quantitative assessment of the global system is shown in the bottom panel of Figure 6.8, where the global system's surface temperature time series from a typical deep water location (shown by the star in the top panels of Figure 6.8) is compared with the observed values. Overall the global system is consistent with the observations. This is expected because the global system assimilates the satellite observations.

The GoMSS predictions of sea surface temperature differ from the satellite observations, and the global system predictions, in the deep water: it misplaces the front between the warm slope water and the cold shelf water, and several associated eddies and meanders. The bottom panel in Figure 6.8 shows that the discrepancy between GoMSS and the global system is greater when GoMSS misses the eddies at this specific location.

The GoMSS$^+$ predictions of sea surface temperature (Figure 6.8) place the front and associated eddies at locations consistent with the observations and the global system, e.g., spectral nudging has removed an unrealistic meander around 56°W and 42.5°N and places the slope water further south off the Sable Island. Furthermore, GoMSS$^+$ generates a time series closer to the observations and the global system (Figure 6.8). This implies that GoMSS$^+$ successfully ingests the large scale information from the global system, and that the spectral nudging of the large scales removes some of the unrealistic internal variability. This is more apparent in Figure 6.9 which shows the temperature-temperature and salinity-salinity correlations from the global system and GoMSS$^+$. Comparison of Figures 6.9 and 6.5 (note the different colorbar limits) shows that spectral nudging eliminates the temperature and salinity decorrelation between the model and the global system in deep water. This is not surprising because the large scales of temperature and salinity from the global system are assimilated by GoMSS$^+$. The correlation between GoMSS$^+$ and the global system decreases with depth (not shown) but it is higher than the correlation between GoMSS and the global system at the same depth.

GoMSS$^+$ generates variability with finer scales than the global system (Figure 6.8). This is because GoMSS$^+$ has higher resolution than the global system. The same figure also confirms that spectral nudging has not suppressed the small scale variability and that GoMSS$^+$ generates more small scale variability than GoMSS. I speculate that the reason is that GoMSS energy at the small scales is quickly transferred to smaller scales

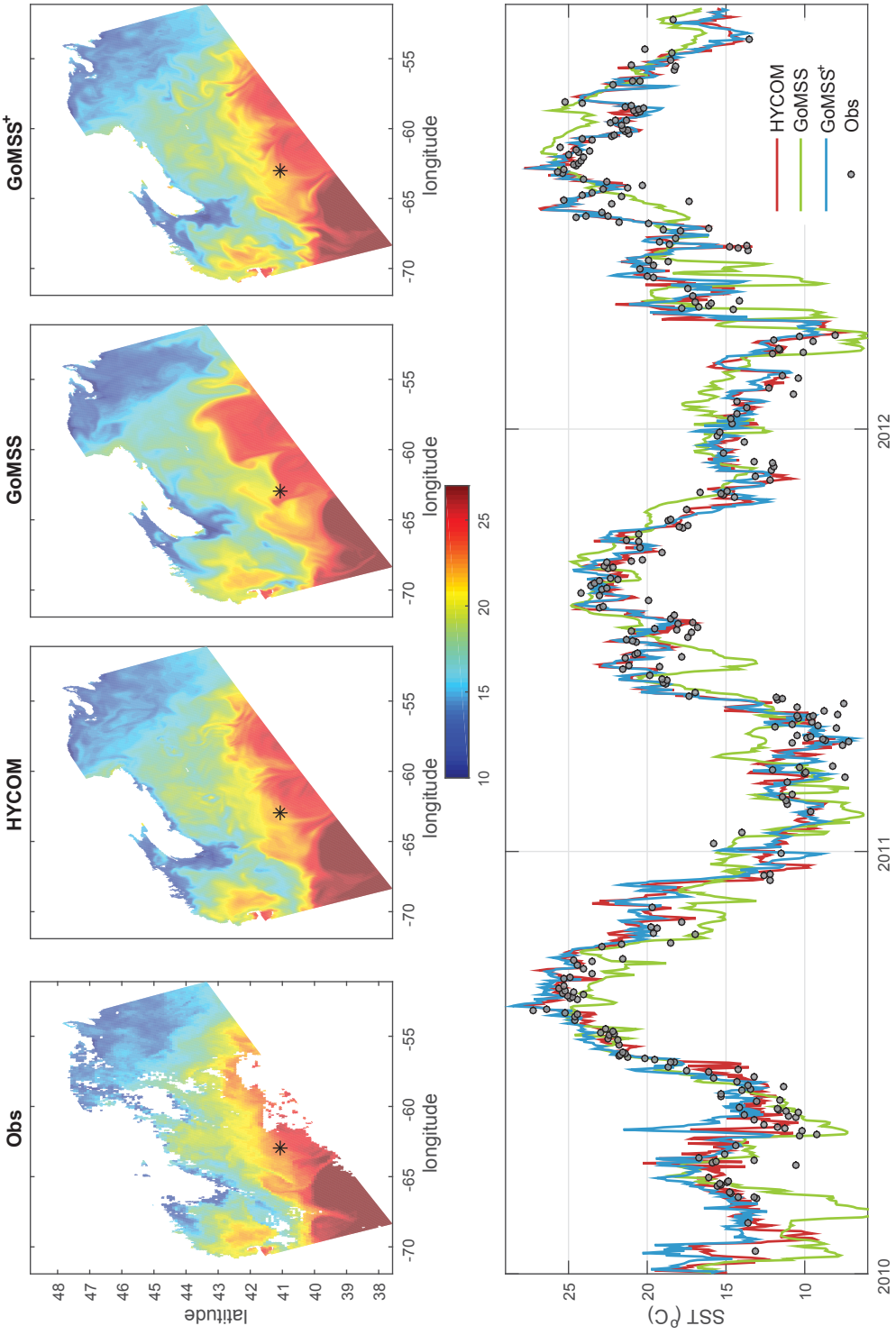

Figure 6.8: Sea surface temperature snapshots for 29 July, 2010 from satellite observations, the global system, GoMSS and GoMSS$^+$ (top panels). The bottom panel shows the sea surface temperature time series for the location shown by the black star on the top panels.

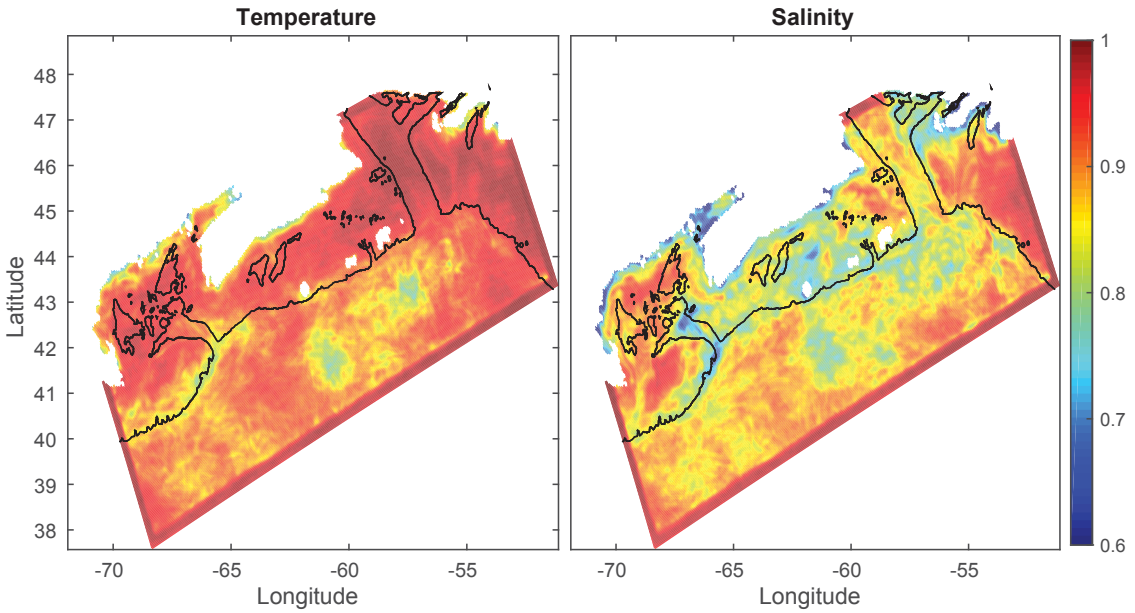

Figure 6.9: Correlation of colocated (left panel) temperature and (right panel) salinity from the global system and GoMSS$^+$. The black line is the 200 m isobath. Same format as 6.5.

(or even to large scales in an inverse cascade process) where it is finally dissipated by the model. However in GoMSS$^+$ the assimilation of large scales keeps "feeding" energy to the small scales leading to the GoMSS$^+$ small scales being more energetic than GoMSS. This implies that spectral nudging may help with imperfections in the parametrization of mixing of regional models. (More discussion in section 6.4).

To demonstrate, I now describe the sea surface temperature variability for different length scales. Figure 6.10 shows the cumulative variance for temperature for wavelengths shorter than 110 km (equivalent to the integrated power spectral density) for the observations, the global system, GoMSS and GoMSS$^+$, in deep water. The temperature cumulative variance (from small to large scales) is estimated for one image by:

$$\Phi(\lambda_n) = \sum_{i=1}^{n} \text{var}(T(\lambda_i)) \tag{6.4}$$

where var$(T(\lambda_i))$ corresponds to the temperature variance for a specific wavelength and $n = 1, 2 \cdots, N$. Note that the variance in (6.4) is in space and the time average is over several images ($\overline{\Phi(\lambda_n)}$).

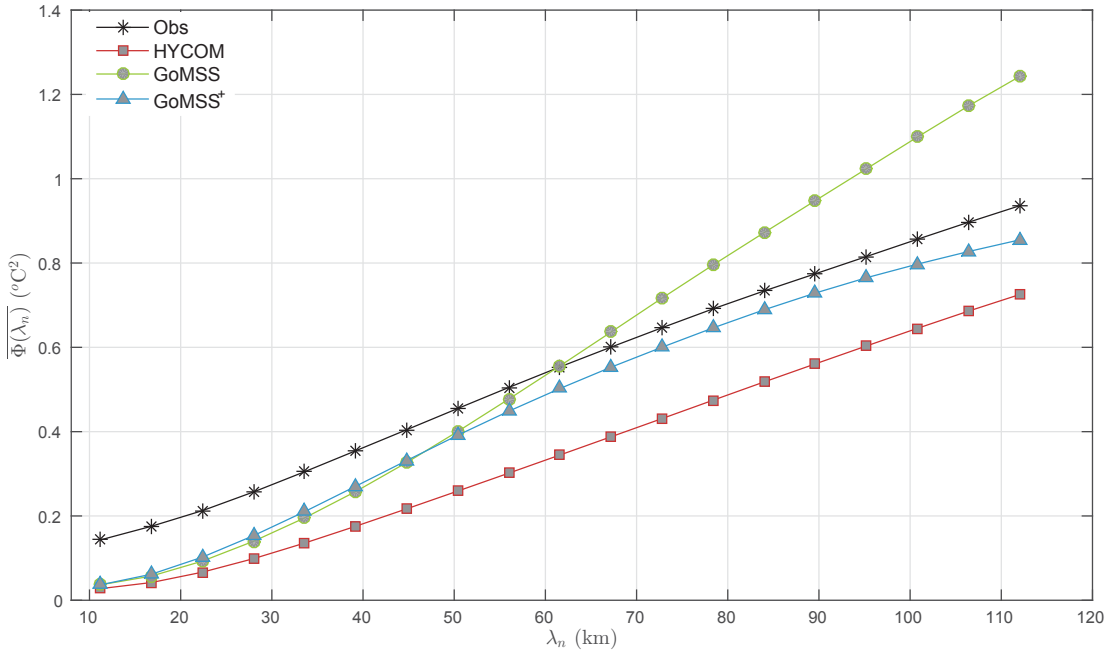

Figure 6.10: The cumulative variance of sea surface temperature in the deep water as a function of wavelength ($\overline{\Phi(\lambda_n)}$), determined by the footprint of the moving average filter. Results are shown for the satellite observations and corresponding predictions by the global system, GoMSS and GoMSS$^+$.

This estimate is similar to the small scale variance as a function of critical wavenumber discussed in Chapter 3. To separate the variance distribution according to different length scales, a simple moving average filter was used. This is because the satellite images have many missing data due to cloud cover and the use of a Butterworth filter (or Fourier transform) is problematic. Only satellite images with more than 4/5 area coverage on the deep water were used between the year 2010-2012 (45 days in total). The variance of the model and the global system was estimated based on the areas observed by the satellite (i.e., excluding the area covered by clouds) in deep water.

Figure 6.10 shows that $\overline{\Phi(\lambda_n)}$ in deep water drops with λ_n as expected. The observed variance is relatively large for $\lambda_n \leq$20 km; this is due to noise in the satellite data. Overall the GoMSS$^+$ variance is closer to the observed than the global system and GoMSS. GoMSS variance is about 20% larger than the observed at length scales around 110 km. This overestimation is due to unrealistic internal variability and the trapped eddies associated with ill-posed open lateral boundary conditions. GoMSS variance drops faster than the

observed which suggests that GoMSS baroclinic energy cascade to smaller scales and dissipation may be too fast. This is probably associated with the diffusion scheme used in the model. GoMSS$^+$ variance drops slower than GoMSS and is more consistent with the observations because the assimilation of the large scales keeps providing energy to the small scales. This is encouraging because it shows that the assimilation of large scales can significantly impact the small scale variability even through no information on the small scales has been assimilated. The energy transfer between the different length scales is discussed further in section 6.4.

Table 6.2: Correlation between sea level from the global system, GoMSS and GoMSS$^+$ and the satellite observations in the deep water, the shelf break and the shelf (areas separated by the horizontal lines in Figure 6.11). High frequency variability of all model output was removed using a Butterworth filter with a cutoff frequency of 20 days. Based on the time period 9 February 2010 to 23 January 2012.

Area	Global system	GoMSS	GoMSS$^+$
Shelf	0.57	0.58	0.59
Shelf break	0.53	0.44	0.54
Deep water	0.66	0.34	0.58

It is not surprising that spectral nudging significantly changes GoMSS temperature and salinity because it assimilates information on their large scale. However, the spectral nudging also modifies variables that are not directly assimilated into the model. To demonstrate, Figure 6.11 is a Hovmoller diagram of sea level from satellite observations, and predictions by the global system, GoMSS and GoMSS$^+$ along the coastal altimetry path shown in 5.26. Clearly the GoMSS$^+$ sea level is in better agreement with the observations in deep water and the shelf break than GoMSS. For example, spectral nudging eliminates the unrealistic positive sea surface height event occurring between 41.5 and 43° in the late summer of 2010. A more quantitative view is provided in Figures 6.12 which shows the standard deviation of the sea level. GoMSS$^+$ has a standard deviation closer to the observed than GoMSS on the shelf break and in the deep water. Table 6.2 shows that the correlation between GoMSS$^+$ and the satellite observations is higher than GoMSS in the deep water and the shelf break.

Sea level from the global system is in somewhat better agreement with the observations than GoMSS$^+$ in the deep ocean. This is not surprising because the global system

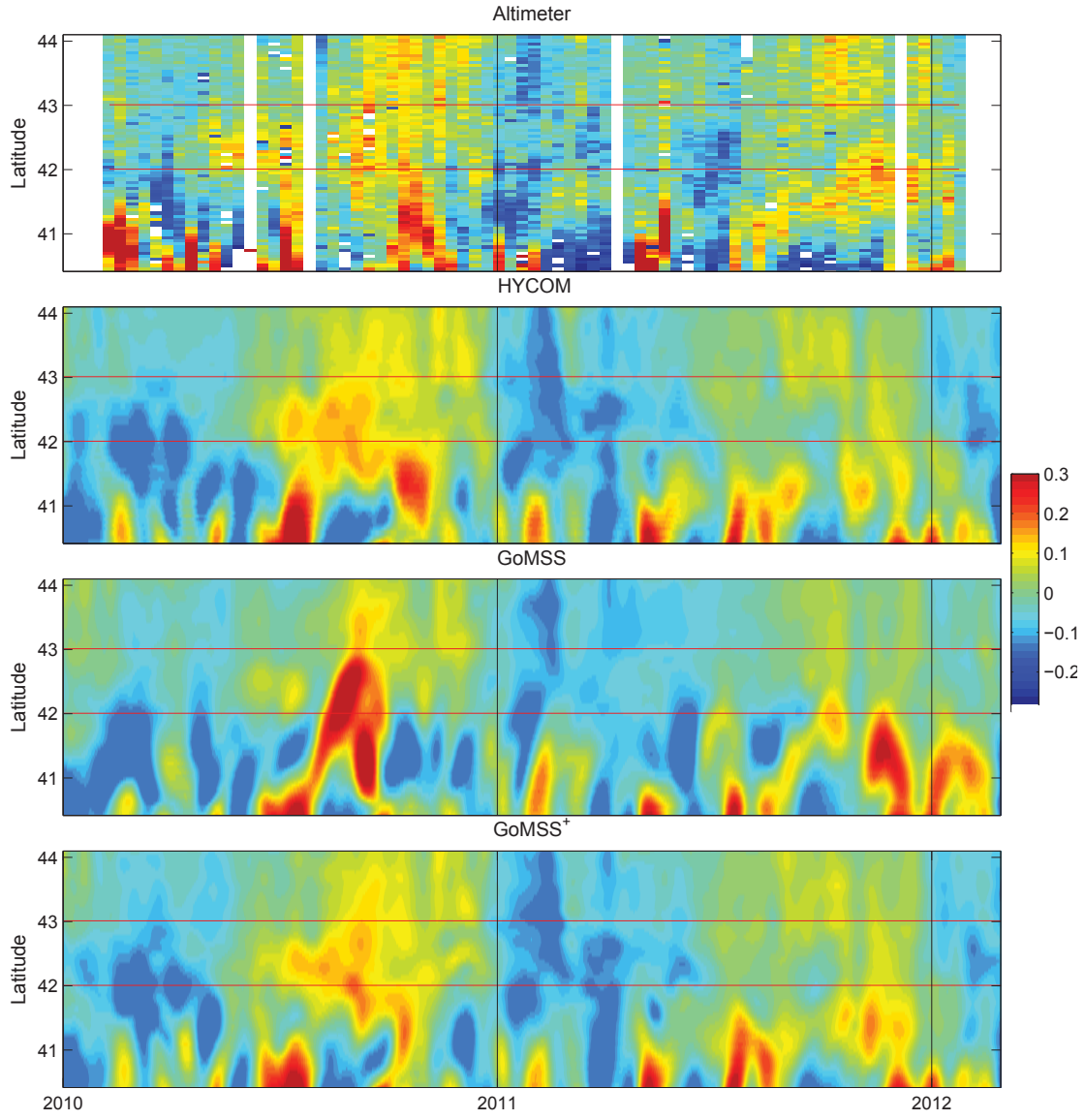

Figure 6.11: Hovmoller diagram of sea level along the Halifax Line (Figure 5.26) based on the coastal altimeter dataset (first panel), and predictions by the global system (second panel), GoMSS (third panel) and GoMSS$^+$ (fourth panel). High frequency variability of all model output was removed using a Butterworth filter with a cutoff frequency of 20 days. The horizontal red lines show the shelf edge (43°N, near 200 m isobath) and foot of the slope (42°N deeper than 1000 m). Sea level is in meters.

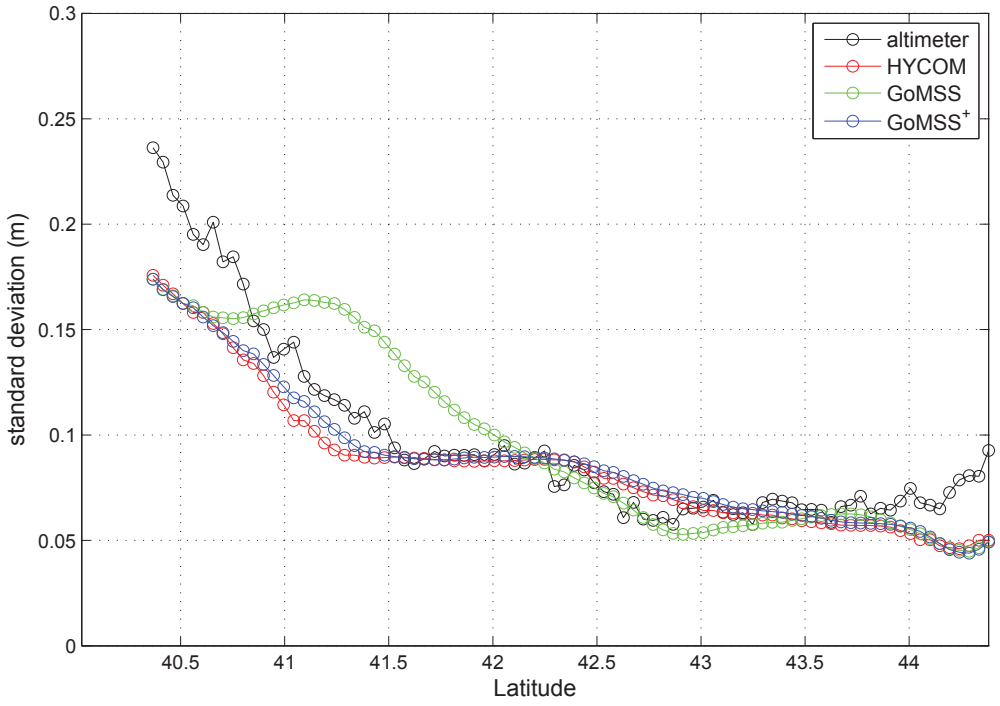

Figure 6.12: Standard deviation of sea level from coastal altimetry (black), the global system (red), GoMSS (green) and GoMSS$^+$ (blue) along the altimeter track shown in Figure 5.26. High frequency variability of all model output was removed using a Butterworth filter with a cutoff frequency of 20 days. Based on the time period 9 February 2010 to 23 January 2012.

assimilates this information. To investigate the realism of the sea level of GoMSS$^+$ for the small scales (wavelengths less than 90 km) I tried to estimate the correlation coefficients between the global system, GoMSS, and GoMSS$^+$ and the altimetric observations for different length scales (not shown) using different approaches (e.g., Butterworth and moving average filters). However it was hard to reach any conclusions because noise and missing data contaminate the observed variability on small scales leading to insignificant correlation coefficients (r <0.15). I note however that GoMSS$^+$ correlation with the observations for small scales is higher than the global system and GoMSS in the deep water. The sea level variance distribution on different length scales in the three systems is examined further in section 6.4 using wavenumber spectra.

GoMSS$^+$ prediction of the mean circulation for winter and summer are shown in Figures 6.13 and 6.14 respectively. Comparison of GoMSS$^+$ with GoMSS (Figures 5.36 and 5.37),

and the global system (Figures 5.34 and 5.35) shows that in deep water GoMSS$^+$ is more consistent with the global system than GoMSS in both winter and summer. For example, GoMSS$^+$ generates eddies and meanders in roughly the same locations as the global system. Close to the shelf break, during winter, GoMSS$^+$ captures the Labrador Current as it crosses the Laurentian Channel and continues southwards along the shelf break, consistent with previous studies (e.g., *Loder et al.*, 1998). This flow is very limited in GoMSS. GoMSS$^+$ does not generate unrealistic recirculation along the west and the south boundaries. This is encouraging because it shows that spectral nudging eliminates the trapped eddies associated with ill-posed boundary conditions.

6.3.2 Shelf

The impact of the spectral nudging on temperature and salinity is not as large on the shelf as in the deep water and the shelf break. Comparison of Figures 6.9 and 6.5 shows that, overall, the salinity and temperature correlations between GoMSS$^+$ and the global system are higher than the correlations between GoMSS and the global system on the shelf. The salinity correlation is lower than the temperature due to the impact of river run-off (different in the model and the global system). For both temperature and salinity the correlation between GoMSS$^+$ and the global system drops near the coast. This is because near the coast the spectral nudging is weaker.

The global system, GoMSS and GoMSS$^+$ predict similar surface temperatures on the shelf and they are in good agreement with the observations (see Figure 6.8 for a typical snapshot). Comparison with different snapshots (not shown) reveals that this is true for the 3 years of the model integration (2010-2012). However, there are areas, like the east side of the Gulf of Maine and on Georges Banks where GoMSS$^+$ generates sea surface temperatures that are in slightly better agreement with the observations.

To investigate further the impact of spectral nudging I now discuss changes in the model's local synoptic temperature and salinity. I use observations from CTDs and a glider (see Chapters 4 and 5 for details).

Figures 6.15 and 6.16 show 12 temperature and salinity profiles, respectively, from CTD measurements, GoMSS and GoMSS$^+$ for six representative locations (C1 to C6, Figure 4.3). Overall GoMSS$^+$ predicts temperature and salinity that is in good agreement with

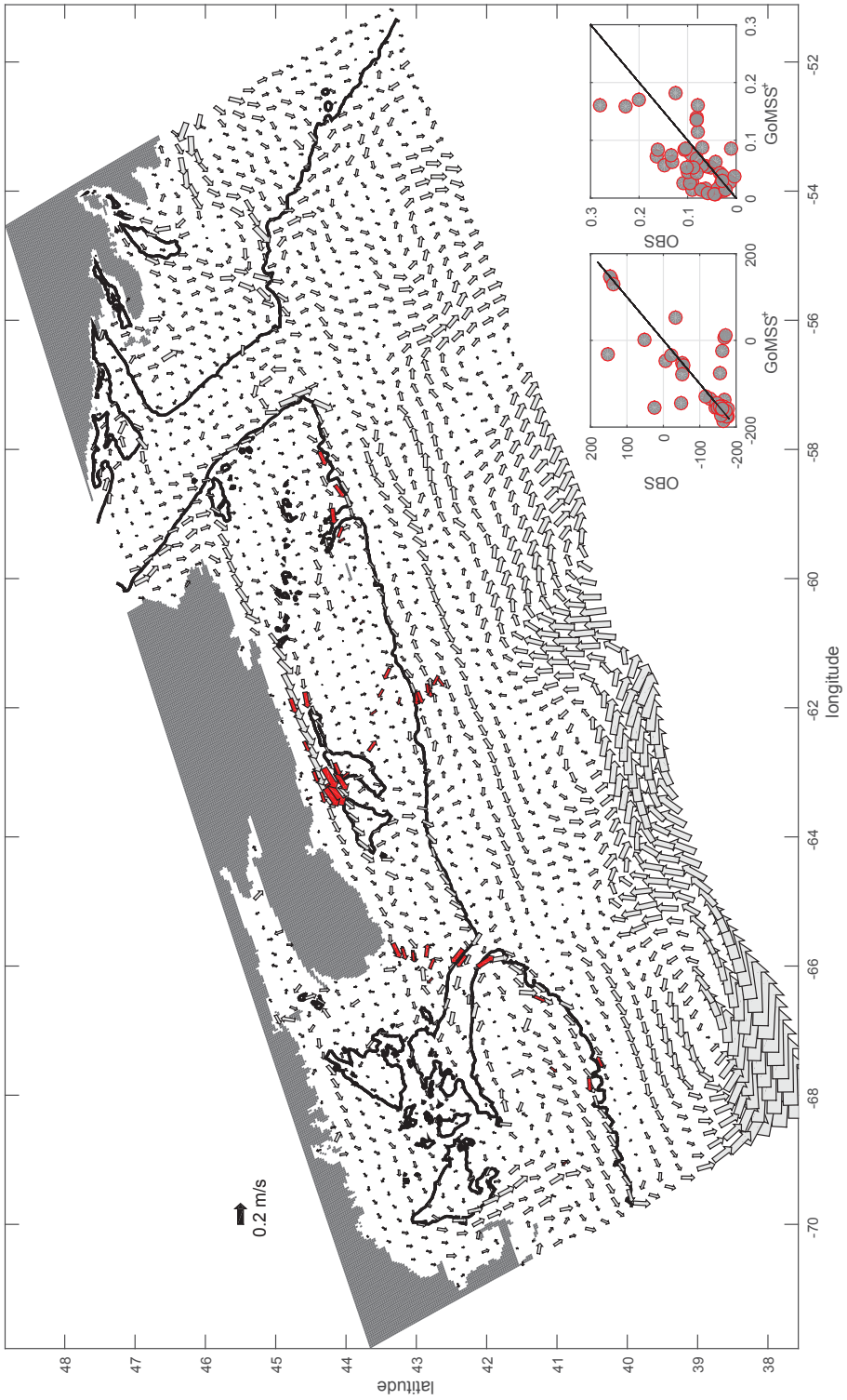

Figure 6.13: The observed (red arrows) and GoMSS$^+$ (every 8 grid points) winter mean currents averaged over the top 100 m. The black line is the 200 m isobath. The insets are scatterplots of observed and predicted speed (m s^{-1}) and direction (degrees, clockwise from eastward). GoMSS$^+$ mean currents are based on the 2010-2012 time period.

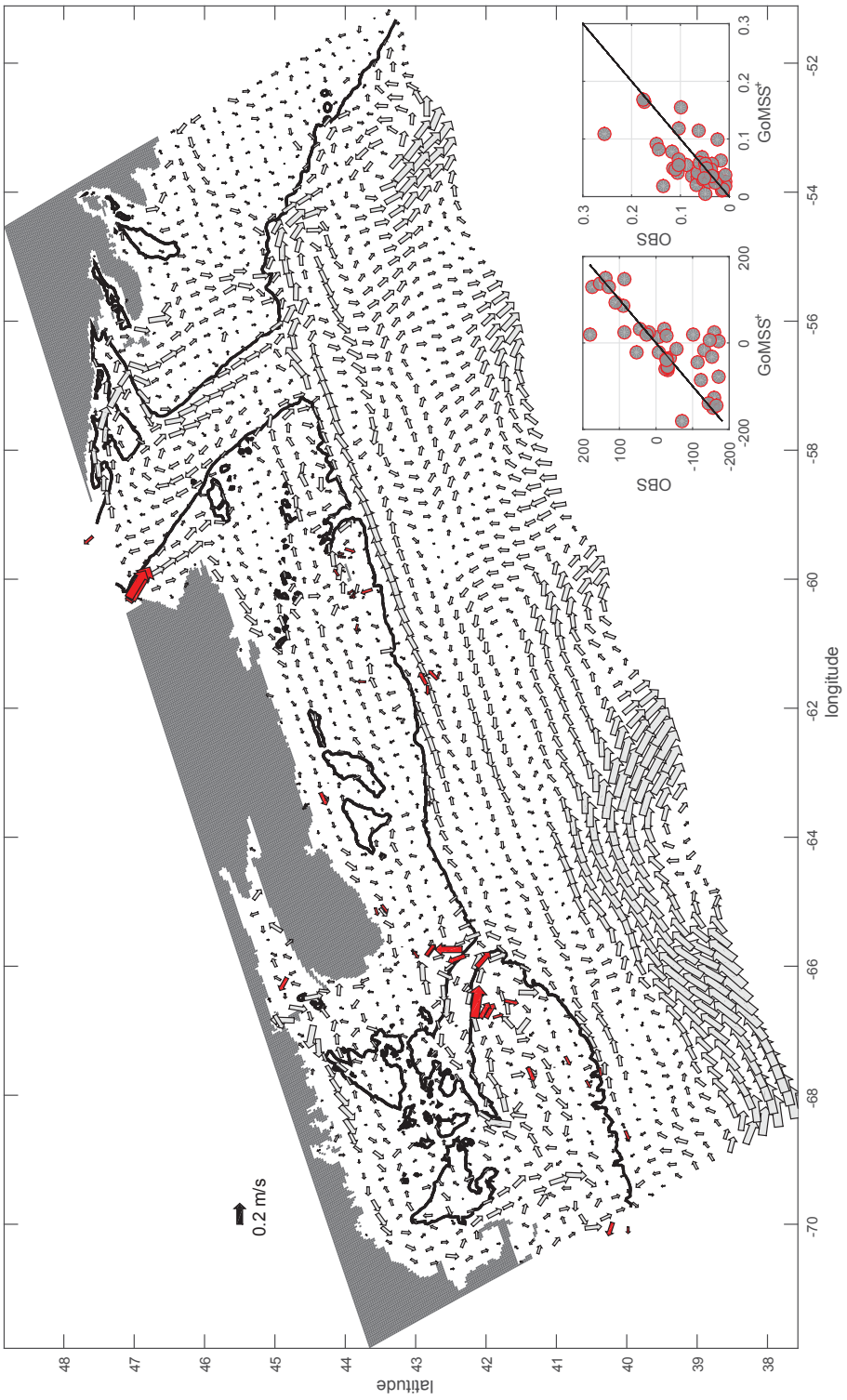

Figure 6.14: The observed (red arrows) and GoMSS^{+} (every 8 grid points) summer mean currents averaged over the top 100 m. Same format as 6.13

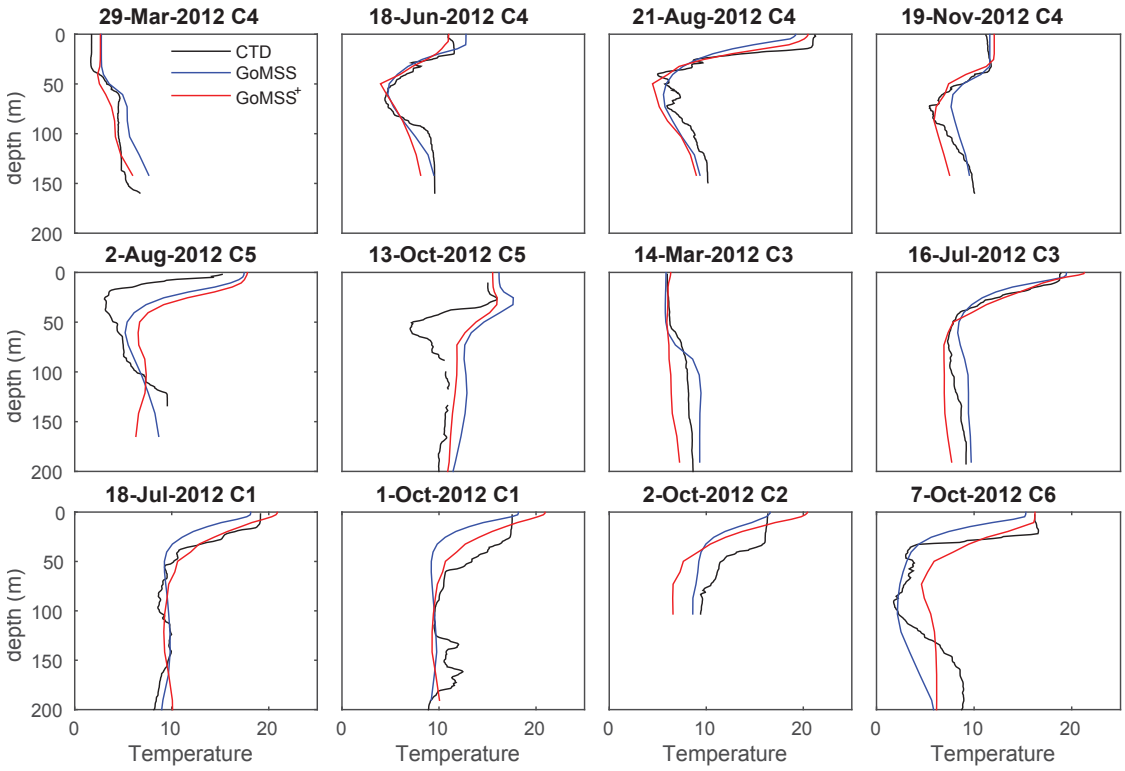

Figure 6.15: Temperature vertical profiles from CTD measurements (black), and predictions by GoMSS (blue) and GoMSS$^+$ (red). The six locations of the profiles are shown in Figure 4.3.

the observations. Comparison of Figures 4.4, 4.5, 6.15 and 6.16 shows that GoMSS$^+$ temperature and salinity profiles are very similar to the global system profiles. GoMSS$^+$ generates sea surface temperature that are in better agreement with the observations than GoMSS at C4 during summer, and C5 in early fall. At C1 and C2 GoMSS$^+$ significantly overestimates the sea surface temperature (by around 4°C) in early fall. GoMSS and GoMSS$^+$ generate similar thermoclines at the 6 locations, in good agreement with the observations. At C4 GoMSS$^+$ overestimates the salinity of the surface mixed layer by about 1 in late winter and late fall. At C2 GoMSS$^+$ generates a sharper salinity gradient than the observed and underestimates the salinity by around 0.8 in early fall. Overall GoMSS$^+$ and GoMSS generates similar haloclines, in good agreement with the observations.

To quantify the error for GoMSS$^+$, I estimated the normalized mean square error (NMSE) for all available CTD observed profiles locations for the year 2012 (Figure 5.19, Table 6.3). The NMSE for GoMSS$^+$ for temperature is larger for intermediate depths

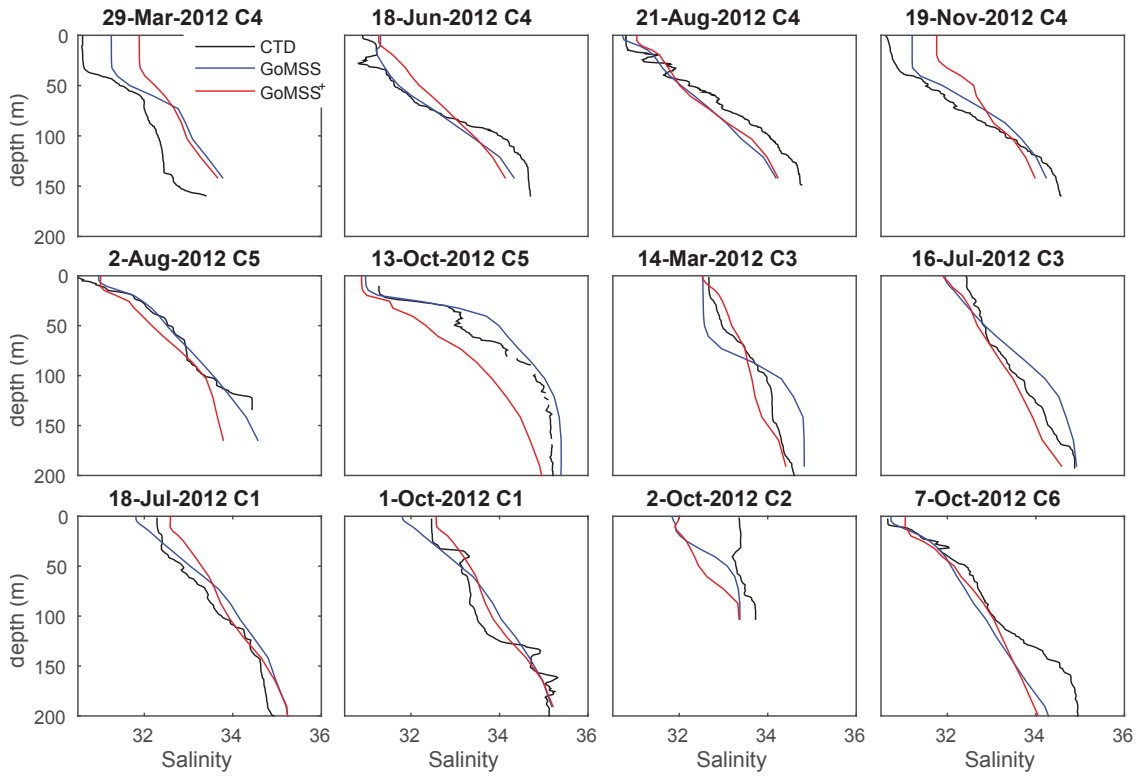

Figure 6.16: Salinity vertical profiles from CTD measurements (black), GoMSS (blue) and predictions by GoMSS$^+$ (red). The six locations of the profiles are shown in Figure 4.3.

(21-100 m) due to the sharp vertical gradient associated with the thermocline. Comparison of Tables 5.6 and 6.3 shows that GoMSS$^+$ gives better predictions of temperature than the global system below 20 m. GoMSS$^+$ has larger errors at intermediate depths (20-100 m) than GoMSS. GoMSS$^+$ generates temperature with smaller errors than GoMSS in greater depth ($>$100 m). Near the surface (0-20 m) GoMSS$^+$ generates lower temperature errors than GoMSS but the same errors as the global system. This is probably associated with the very strong spectral nudging imposed at the surface which somewhat constrains the model adjustment to the atmospheric conditions. This shows that further sensitivity studies are required to estimate the optimal strength of spectral nudging.

GoMSS$^+$ has larger salinity error than GoMSS throughout the water column. This implies that the strong spectral nudging degraded the model results for salinity, (especially in shallow depths where the nudging is stronger) and even led to higher error than the global system above 100 m (comparison of Tables 5.7 and 6.3). This maybe associated

with the strong nudging and because the salinity is significantly affected by river run-off on the shelf which differs between the regional and global models. In future, implementation a more elaborate form of nudging that takes account the location of river mouths should be considered or even a scheme that implements salinity spectral nudging only in the deep water (see Appendix E).

Table 6.3: Normalized mean square error (NMSE) for GoMSS$^+$ based on comparison with the observed temperature and salinity profiles for 2012 (Figure 5.19), binned over three depth ranges.

Depth range	Temperature	Salinity
0-20 m	0.10	0.48
21-100 m	0.36	0.40
$>$100 m	0.10	0.40

Snapshots of temperature and salinity collected from a glider, along a vertical section running along the Halifax Line (Figure 4.3) are shown in Figure 6.17 and Figure 6.18 respectively. The glider observations were collected between 11 and 31 of July, 2012. (Details of the glider observations are given in section 4.1). Overall GoMSS$^+$ generates a three layer structure: a warm layer near the surface (17° and above) driven by the atmosphere heating, a cold, fresh intermediate layer (between 30 and 100 m), which is a mixture of Labrador Current and water from St. Lawrence, and a saline (above 34) bottom layer in Emerald Basin that mainly consists of Slope Water. Comparison with the global system profiles (Figures 4.6 and 4.7) shows that GoMSS$^+$ generates temperature and salinity profiles that are consistent with the global system but with finer detail and in better agreement with the glider observations. GoMSS$^+$ captures the warming of the intermediate layer from the coast to the shelf break, and the deepening of the thermocline near the edge of Emerald Bank, better than GoMSS. However GoMSS$^+$ generates a colder and fresher bottom layer than the observations and GoMSS. This characteristic is inherited from the global system. Although GoMSS$^+$ captures the freshening of the surface layer along the shelf break, it does not predict accurately the sharp halocline front at 62°W. GoMSS$^+$ NMSE and bias are shown in Table 6.4. Comparison of Tables 5.8, 5.9 and 6.4 shows that overall GoMSS$^+$ has smaller temperature and salinity error and bias than the global system and GoMSS along the glider path.

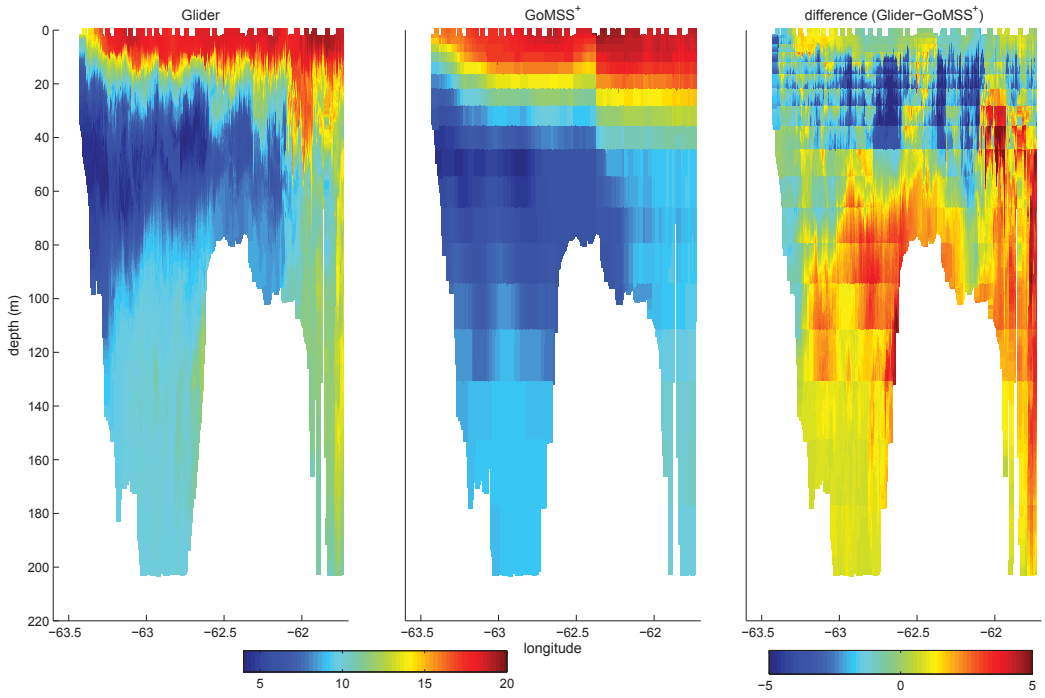

Figure 6.17: Temperature section observed by a glider (left panel) operating along the Halifax Line (red line in Figure 4.3), GoMSS$^+$ (middle) along the same path (and times), and their difference (right panel) during 11-31, July 2012. Temperature is in °C.

Table 6.4: The normalized mean square error (NMSE), and the mean difference, between the temperature and salinity glider observations and GoMSS$^+$.

GoMSS$^+$	NMSE	Bias
Temperature	0.202	0.013
Salinity	0.219	0.390

I now examine the impact of spectral nudging in the model variables that are not directly affected by nudging (e.g., sea surface height, currents), on the shelf. Figure 6.19 shows that on the shelf along the altimeter line (Figure 5.26), GoMSS$^+$ generates a seasonal cycle of sea surface height that is similar to GoMSS and the global system, and in good agreement with the coastal altimeter observations. Figure 6.12 shows that GoMSS$^+$, GoMSS and the global system are quantitatively similar on the shelf (north of 43N). Overall GoMSS$^+$ has slightly higher correlation with observations than both GoMSS and the global system on the shelf (Table 6.2).

The seasonal circulation on the shelf in winter and summer predicted by the three

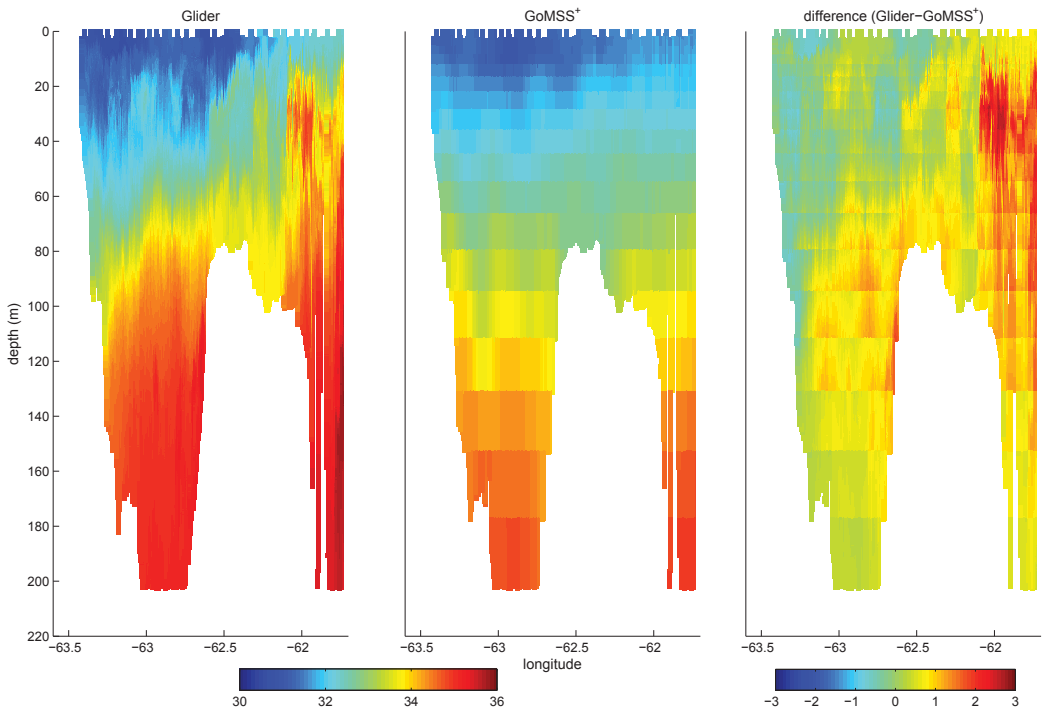

Figure 6.18: Salinity section from the glider and GoMSS$^+$. Same format as Figure 6.17. Salinity is in practical salinity units.

systems are similar (compare Figures 5.34, 5.35, 5.36, 5.37, 6.13 and 6.14), and generally consistent with previous studies (e.g. *Lynch et al.*, 1996; *Han et al.*, 1997; *Loder et al.*, 1997, 1998; *Hannah et al.*, 2001; *Urrego-Blanco and Sheng*, 2014). Along Cabot Strait (north boundary) GoMSS$^+$ predicts a circulation similar to the global system with outflow from the Gulf of St. Lawrence at both east and west side of the Strait in summer. The outflow at the east side of Cabot Strait is not realistic and it is due to a problem with the global system (as noted earlier in Chapter 5) that the model inherits through the open lateral boundary conditions and the spectral nudging. In summer GoMSS$^+$ generates weak inflow into the Gulf of St. Lawrence at Cabot Strait (similar to the global system) however, this outflow is not confined along the east side of the Cabot Strait.

GoMSS$^+$ simulates well the observed clockwise circulation around Sable Island (similar to GoMSS), that intensifies during summer and the cyclonic circulation and its seasonal variation over the Gully, consistent with *Hannah et al.* (2001). Similar to GoMSS, GoMSS$^+$ generates the overall cyclonic circulation in the Gulf of Maine and its intensification during

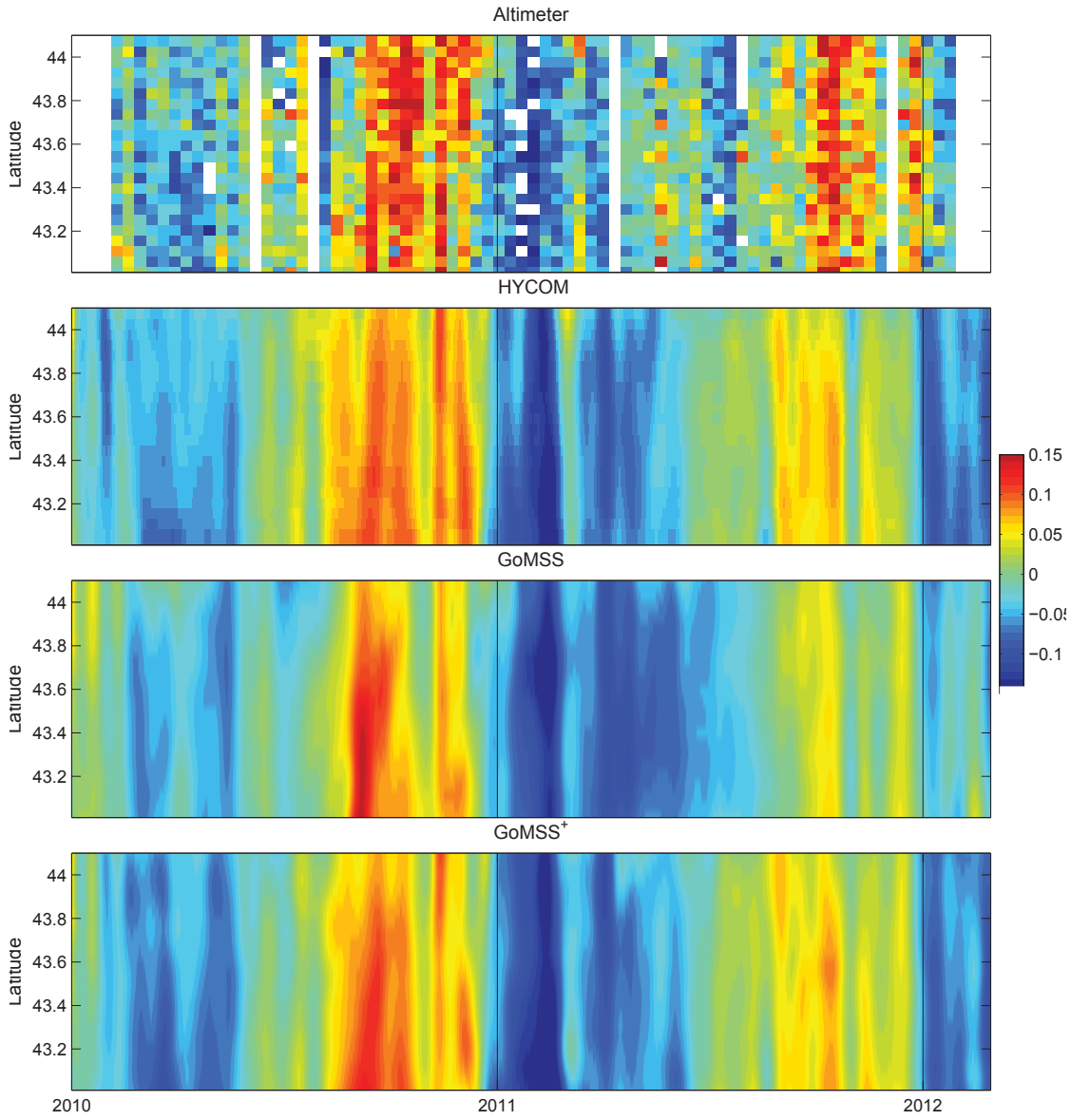

Figure 6.19: Hovmoller diagram of sea level along the Halifax Line (Figure 5.26) based on the coastal altimeter dataset (first panel), and predictions by the global system (second panel), GoMSS (third panel) and GoMSS$^+$ (fourth panel). Same format as Figure 5.27 but zoomed onto the shelf.

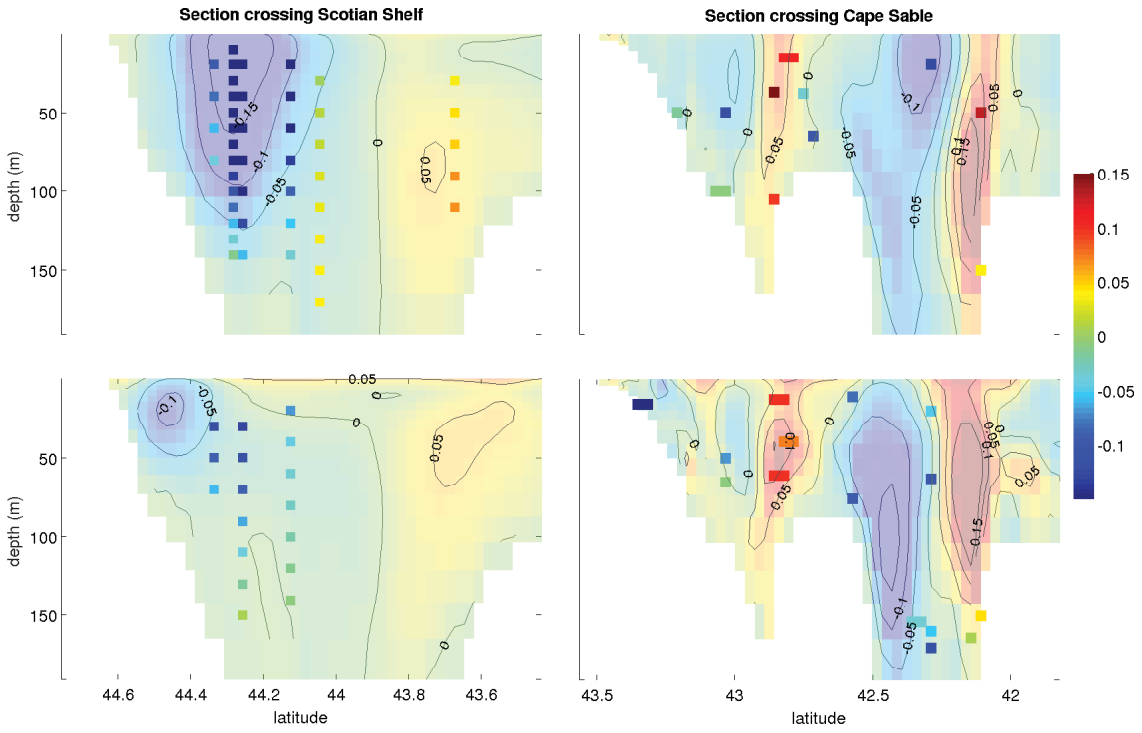

Figure 6.20: GoMSS$^+$ Seasonal mean currents normal to a section crossing the Scotian Shelf (see Figure 5.38) and to a section radiating from Cape Sable (see Figure 5.39). Winter and summer means are shown in the top and bottom panels respectively. The bold boxes show the velocities calculated from current meter observations. The velocity is in m s^{-1}.

summer, which is absent from the global system. Additionally GoMSS$^+$ generates the clockwise circulation over Georges Bank (associated with tidal rectification) that persists throughout the year.

GoMSS$^+$ predictions of the seasonal mean currents normal to Halifax Line, and across a line radiating from Cape Sable, are shown in Figure 6.20. Comparison of Figures 5.38 and 6.20 shows that during winter GoMSS$^+$ captures better the position and the intensity of the strong southwards current along the coast of Nova Scotia than GoMSS and the global system. In winter GoMSS$^+$ also generates the observed weak northwards flow near the edge of Emerald Basin associated with the cyclonic gyre above Emerald Basin noted by previous studies (e.g., *Han et al.*, 1997; *Loder et al.*, 1997; *Hannah et al.*, 2001). This flow is slightly stronger in GoMSS$^+$ than GoMSS and the global system. In summer GoMSS$^+$ generates a weaker southward current along the coast of Nova Scotia consistent

Table 6.5: Fit of GoMSS$^+$ to observed mean flows in winter and summer for three depth ranges. The regression coefficient $\hat{\beta}_1$ is given in polar form (vector scale and rotation, in degrees). Same format as Tables 5.10, 5.11.

R^2	Winter	Summer
0-20 m	0.73	0.53
21-100 m	0.60	0.51
101-300 m	0.08	0.47

β_1	Winter	Summer
0-20 m	(0.87, 4.5)	(1.03, 17.0)
21-100 m	(0.77, 4.9)	(0.82, 5.3)
101-300 m	(0.26, 22.2)	(0.53, -11.9)

with observations. GoMSS$^+$ does not generate the near surface northward flow around 44.3°N that is present in GoMSS but not in the global system or the observations. GoMSS$^+$ generates a summer weak northwards flow near the edge of the Emerald Basin (similar to the global system) that is absent from GoMSS.

GoMSS$^+$ and GoMSS generate similar currents across the line radiating from Cape Sable (compare Figures 5.39 and 6.20). GoMSS$^+$ captures the observed flow from the Scotian Shelf into the Gulf of Maine throughout the year and its weakening during summer. GoMSS$^+$ underestimates the speed of this flow during winter, similar to GoMSS. Also similar to GoMSS, GoMSS$^+$ simulates well the clockwise circulation above Brown Banks (associated with tidal rectification) that persists throughout the year (not captured accurately in the global system). GoMSS$^+$ simulates well the observed circulation along the Northeast Channel (inflow towards the Gulf of Maine along the north side and outflow along the south side of the Channel) that persists throughout the year. In winter, GoMSS$^+$ predictions are closer to the observed position of the inflow along the north side of the channel than GoMSS. GoMSS$^+$ has stronger outflow in the south side of Northeast channel than the global system because it simulates the tidal rectification above Georges Bank.

To quantify the overall accuracy of GoMSS$^+$ seasonal currents on the shelf, I use the R^2 statistics introduced in Subsection 5.3.3. The R^2 statistics is estimated based on the observations shown in Figure 5.33. The GoMSS$^+$ R^2 statistics and the regression coefficient $\hat{\beta}_1$, for three depth ranges during winter and summer are shown Table 6.5.

Overall GoMSS$^+$ and GoMSS have similar skill in simulating the seasonal mean circulation (compare Tables 5.10, 5.11 and 6.5) at the observation locations shown in Figure 5.33. For winter and the top 20 m, GoMSS$^+$ has higher R^2 than GoMSS. For intermediate depths (21-100 m) GoMSS$^+$ has slightly lower skill than GoMSS and the

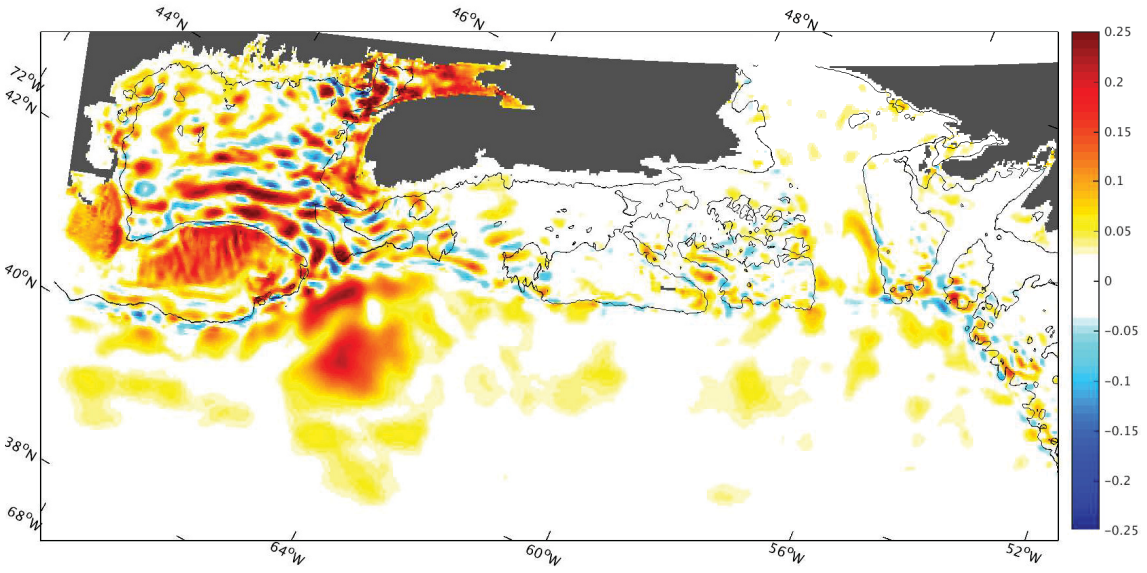

Figure 6.21: Seasonal differences in the maximum speed of the M_2 surface current, summer - winter predicted by GoMSS$^+$. The color shading shows δv (in m s^{-1}) for the period 2010-2012. The thin black line is the 100 m isobath.

global system in winter, however the R^2 is still significant. For the bottom layer (101-300 m) and in winter, GoMSS$^+$ skill is much lower than GoMSS but slightly higher than the global system. The low skill in the bottom layer during winter is probably associated with the limited number of observations (see Figure 5.33). In summer GoMSS$^+$ has generally higher skill than GoMSS and the global system. Overall GoMSS$^+$ and GoMSS have similar angle error, which means that they both generate currents with similar orientation.

Although spectral nudging affects the hydrography and the circulation of the model as discussed above, it does not suppress the tides and their interaction with the seasonal variability. GoMSS$^+$ generates similar tidal elevation and tidal currents to GoMSS for the five major tidal constituents (M_2, N_2, S_2, K_1 and O_1). GoMSS$^+$ also captures the impact of the seasonal changes in stratification in the tidal elevation and currents. Figure 6.21 shows GoMSS$^+$ difference in the maximum M_2 surface current speed between winter and summer (δv, similar to Figure 5.7). This map is very similar to the δv map predicted by GoMMS; note the striations are at the same locations and the largest values are found over Georges Bank, the Bay of Fundy, and the Northeast Channel. This is because the small scales (<90 km) evolve freely in GoMSS$^+$ and so the regional dynamics can generate

locally important features like the internal tide.

GoMSS$^+$ also captures the impact of the tides on the seasonal hydrography and circulation. For example, GoMSS$^+$ does not suppress the tidal mixing on top of Georges Bank and generates a well mixed water column similar to GoMSS on top of the Bank (not shown); this is not captured by the global system. GoMSS$^+$ accurately generates the rectified tidal currents on top of shallow banks. For example GoMSS$^+$ simulates the known clockwise gyres on top of Georges and Browns Banks, and in the vicinity of the Sable Island similar to GoMSS and previous studies (e.g., *Loder*, 1980; *Butman et al.*, 1982; *Greenberg*, 1983; *Hannah et al.*, 2001). Thus the spectral nudging does not suppress the effect of tides on the local hydrography and circulation.

Overall the spectral nudging is less significant on the shelf but it still impacts the local hydrography, sea level and circulation. Comparisons with observations on the shelf shows that weaker spectral nudging may be necessary on the shelf. An experiment discussed in Appendix E shows that "switching off" the spectral nudging on the shelf still suppresses the unrealistic internal variability and places several eddies and meanders at locations consistent with the observations and the global system in the deep water, but also allows the regional model dynamics to control the fields on the shelf.

6.4 Effect of Spectral Nudging on Wavenumber Spectra of Sea Level, Current and Vorticity

In the previous Section it was shown that, overall, GoMSS$^+$ generates fields that are more consistent with the observations and global system than GoMSS, particularly in the deep water where GoMSS is affected by unrealistic internal variability and recirculation due to ill-posed boundary conditions. In the deep water the available observations (i.e., sea surface height and temperature from satellite observations) are assimilated into the global system. Thus, using these observations alone does not provide a useful comparison of the global system and GoMSS$^+$. My approach is to address the performance of GoMSS$^+$ on length scales that are not directly affected by the spectral nudging. For example, the sea surface temperature cumulative variance in wavelength (Figure 6.10) shows that GoMSS$^+$ generates sea surface temperature variance in better agreement with the observations than the global system and GoMSS for length scales below the spectral nudging cutoff (90 km)

in deep water. This led me to speculate that spectral nudging provides additional energy to the small scales. To further investigate this speculation I now examine the wavenumber spectra of sea level, currents and vorticity predicted by the global system, GoMSS and GoMSS$^+$.

Different mechanisms are responsible for the supply and distribution of energy in the three systems. In GoMSS the energy supply (or removal) and distribution are associated with the model's open boundaries (i.e., surface, bottom and lateral open boundaries) and the model dynamics. In the global system the assimilation of observations can act as an additional energy source (or sink), and the strength and distribution depends on the covariance function used in the assimilation. In GoMSS$^+$ spectral nudging acts as an additional energy source (or sink) that has been designed to directly affect the large scales but also drive the energy distribution on small scales through the model's non-linear dynamics.

To investigate how spectral nudging impacts the distribution of energy on different length scales I first discuss the dynamical background for transfer of energy between length scales. I then investigate the variance of the sea surface height, velocity and vorticity predicted by the global system, GoMSS and GoMSS$^+$ and the associated wavenumber spectra.

6.4.1 Dynamical Background

As discussed in Chapter 2 the non-linearity of the governing equations leads to coupling amongst length scales, and ultimately turbulence. To investigate the distribution of variability over the different length scales, it is important to understand how these length scales exchange energy in a turbulent flow. Before I discuss how turbulence manifests in the real ocean where rotation and stratification are important, I consider the simpler fundamental theories of non-rotating three dimensional (3D) and two dimensional (2D) turbulence. The following discussion is based on *Vallis* (2006).

Non-rotating 3D flow: Assume a 3D flow with large scale forcing, setting in motion a large scale flow. Instability in the flow leads to the growth of smaller eddies and so on. Thus kinetic energy is transferred to smaller and smaller scales in a forward cascade process until it reaches very small scales where energy is dissipated by viscosity. The vortex stretching mechanism plays an important role in the transfer of energy to smaller scales.

Turbulence causes the elongation of fluid elements rather than compression. Thus on average turbulence leads to vortex stretching. For an incompressible flow this implies that the turbulent length scales decrease in the directions perpendicular to the vortex stretching, and because of conservation of angular momentum, the kinetic energy is transferred towards smaller scales.

Assuming that the flow is statistically isotropic and homogeneous, and the scale at which energy is supplied to the flow (forcing scale) is much larger than the dissipation scale, there will be an intermediate scale at which neither the forcing nor the dissipation are important: the inertial scale. It can be shown that over this inertial scale the energy spectrum $\mathcal{E}(k)$ is given by

$$\mathcal{E}(k) = \mathcal{K}\epsilon^{2/3}k^{-5/3} \tag{6.5}$$

where $\mathcal{K}$ is a dimensionless constant, ϵ is the energy flux (supplied at large scales), and k is the wavenumber. The above equation is the so called "Kolmogorov -5/3 spectrum" which shows that the spectrum of energy in the inertial range has a slope of -5/3.

2D flow: The vortex stretching responsible for the transfer of energy in smaller scales is absent in two dimensions. In an incompressible 2D flow, turbulence will elongate a fluid band but, because its area is preserved, the band narrows. The vorticity of the band is preserved and so the vorticity gradient increases. Defining enstrophy as the square of the vorticity (just as kinetic energy is associated with the square of velocity), the above argument implies that enstrophy is transferred to smaller scales but the energy to larger scales.

Thus in 2D turbulence with two inertial ranges, (one for energy that carries energy to large scales, and one for enstrophy that carries enstrophy to small scales) it can be shown that the energy spectrum over the enstrophy inertial range is given by

$$\mathcal{E}(k) = \mathcal{K}_\eta\eta^{2/3}k^{-3} \tag{6.6}$$

and over the energy inertial range is given by

$$\mathcal{E}(k) = \mathcal{K}_\epsilon\epsilon^{2/3}k^{-5/3} \tag{6.7}$$

where K_η and K_ϵ are constants and η is the enstrophy flux.

Rotating, stratified flow: Because the large scale circulation of the ocean is influenced by rotation and stratification, neither of the above theories applies exactly. To describe turbulence in stratified and near geostrophic balanced flow, geostrophic turbulence theory (*Vallis*, 2006; *Ferrari and Wunsch*, 2009) is used. Geostrophic turbulence predicts that at very large scales a source (e.g., surface heat fluxes and winds) provides energy to the system's baroclinic modes (e.g., baroclinic instability) which is then transferred to smaller baroclinic scales (forward cascade). At length scales comparable to, and larger, than the first Rossby radius of deformation some of the energy is then transferred to the barotropic mode (barotropization of the flow). The energy in the barotropic mode is then transferred back to the large barotropic scales (inverse cascade). The enstrophy is always transferred towards the small scales. In the limit of the energy inverse cascade, the energy follows a $k^{-5/3}$ spectrum, while in the limit where the enstrophy is tranfered to smaller scales, the energy follows a k^{-3} spectrum (similar to 2D turbulence theory). Although the theory has limitations (e.g., ignores interaction with topography), observations and numerical models broadly support it (Ferrari et al., 2009). Thus I will use it to help interpret my model results.

6.4.2 Variance

To investigate the overall variability of sea surface height, current velocity and vorticity across my domain I first examine their variance through time at the ocean surface. Using Reynolds decomposition it is straightforward to show that the total variance of the current velocity is proportional to the eddy kinetic energy (EKE) defined by

$$\text{EKE} = \frac{1}{2}\overline{|\mathbf{u}'|^2} \tag{6.8}$$

where $\mathbf{u}$ is the horizontal velocity vector, overbar denotes the time average and $'$ denotes the temporal perturbation about this average.

Similarly, the variance of the vertical component of vorticity (ζ) is proportional to the eddy enstrophy (EZ) per unit area defined by

$$\text{EZ} = \frac{1}{2}\overline{\zeta'^2} \tag{6.9}$$

Figure 6.22 shows maps of the variance of sea surface height, EKE and EZ generated

by the global system, GoMSS and GoMSS$^+$ at the ocean surface. The sea surface height variance, EKE and EZ are estimated based on daily fields (snapshots). The tides have been removed from GoMSS and GoMSS$^+$ using a simple regression analysis with five tidal constituents (M_2, N_2, S_2, K_1 and O_1) and a sliding time window of two months (to account for the seasonal variation in tides).

The three systems' sea surface variance, EKE and EZ are larger in the deep water due to the influence of the unstable Gulf Stream and associated eddies and meanders. Both GoMSS and GoMSS$^+$ appear to have more structure on smaller scales. This is not surprising because the regional model has higher resolution than the global system. The sea surface height variance from the global system and GoMSS$^+$ are similar due to the temperature and salinity nudging. GoMSS has somewhat larger sea surface height variance that the global system in the deep water probably associated with the unrealistic internal variability and trapped perturbations due to ill-posed lateral boundary conditions. The large sea surface height variance in the Bay of Fundy is associated with tidal elevation not removed by the above tidal analysis.

GoMSS$^+$ has generally lower EKE than the global system and GoMSS in the deep water. GoMSS generates a jump between low and high EKE along the south boundary, which reflects the influence of the lateral boundary conditions. GoMSS$^+$ has a smoother transition between the interior and the boundary sponge layer (10 grid points), which shows that spectral nudging helps to suppress the trapped perturbations. On the shelf the global system has higher EKE. The differences in EKE between the systems are primarily associated with the different mechanisms that supply energy in each system, as discussed in the beginning of the section. Thus, the assimilation of the currents based on the multivariate correlation function with the dynamic height, is probably responsible for the high EKE at the global system surface.

GoMSS and GoMSS$^+$ generate higher EZ than the global system. GoMSS generates large EZ along the west and the south lateral boundaries (outside the boundary sponge layers). This is again associated with trapped eddies near the lateral boundaries. The transition of EZ between the interior and the boundary sponge layer is smoother in GoMSS$^+$. The EZ from GoMSS$^+$ is higher than GoMSS, implying that spectral nudging supplies enstrophy to the system. On the shelf GoMSS and GoMSS$^+$ generate large EZ

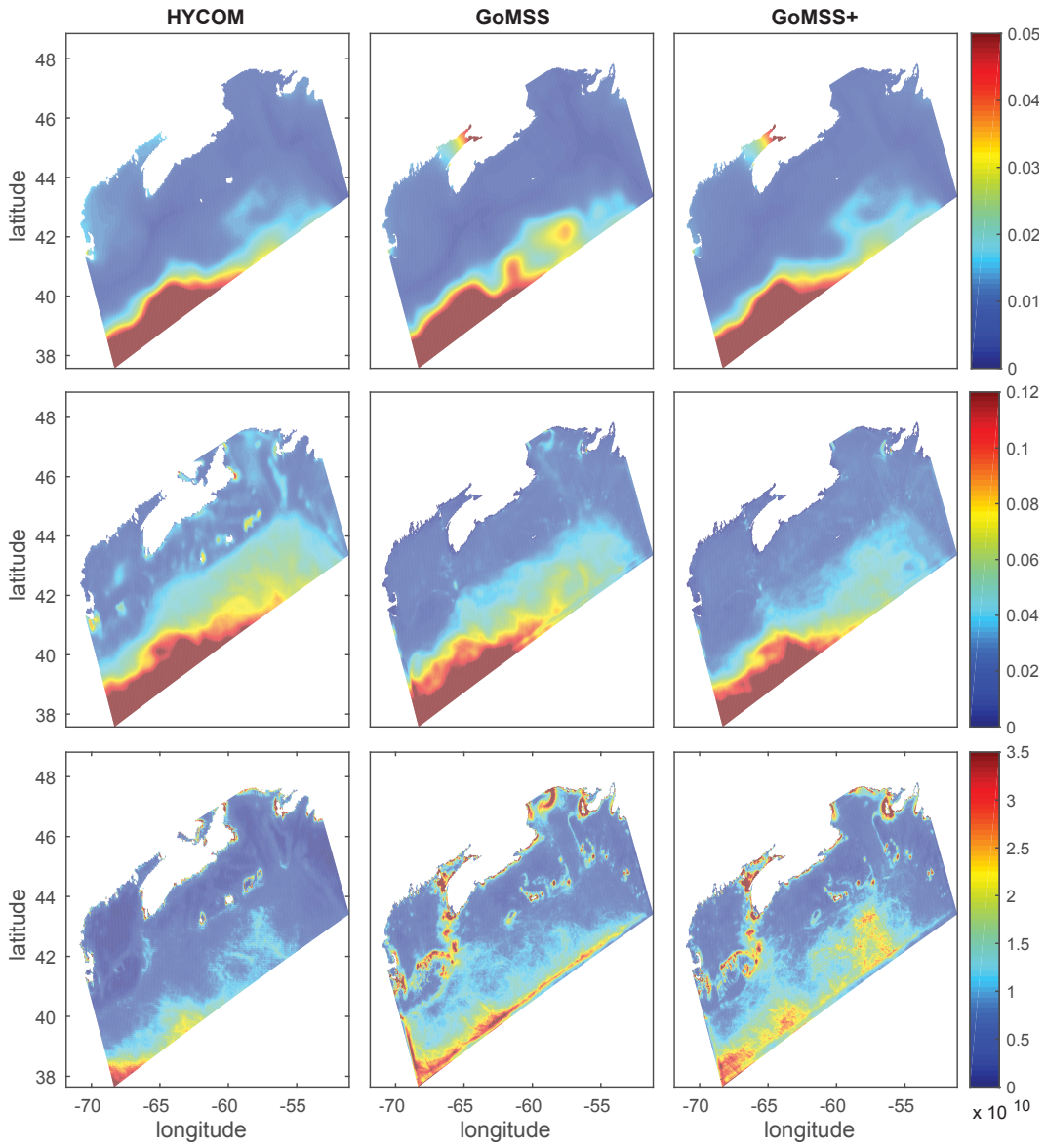

Figure 6.22: Sea surface height variance (top panels), eddy kinetic energy (middle panels) and eddy enstrophy (bottom panels) for the global system, GoMSS and GoMSS$^+$ at the ocean surface. The sea surface height variance is in m^2, the eddy kinetic energy is in m^{2}s^{-2} and the eddy enstrophy is in s^{-2}. Based on 2010-2012 time period.

in areas where the tidal rectification is important (missing in the global system) probably because of the seasonal fluctuations in the tidal residual currents.

6.4.3 Wavenumber Spectra

Although finer scale details are present in the GoMSS and GoMSS$^+$ temporal variance maps (Figure 6.22), it is difficult to confirm that indeed GoMSS and GoMSS$^+$ generate more energetic small scales from these maps. I now decompose the sea surface height, velocity and vorticity variance by wavenumber.

Suppose that $f(x)$ is a function of x and $F(k)$ is its Fourier transform. Then according to Parseval's theorem:

$$\int |f(x)|^2 dx = \int |F(k)|^2 dk \tag{6.10}$$

where k is the wavenumber. The above equation shows that the energy contained in $f(x)$ summed across x is equal to the energy of its Fourier components summed across all of wavenumbers. The Wiener-Khinchin theorem applies the idea behind (6.10) to statistically random processes (Appendix D). The left hand side of (6.10) is replaced by the variance of the process and the right hand side by the integral of the wavenumber spectrum across all wavenumbers.

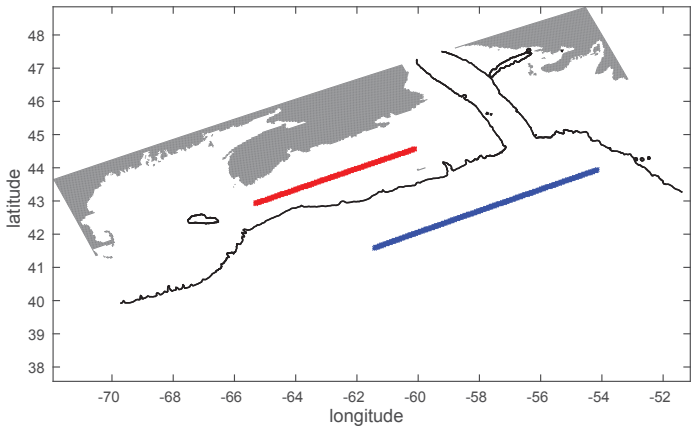

Figure 6.23: The two lines (red and blue) along which the wavenumber spectra are estimated. The thin black lines show the 300 m isobath.

Based on (6.10) I can define the spectra $\mathcal{S}(k)$, $\mathcal{E}(k)$ and $\mathcal{Z}(k)$ for the sea level variance, the velocity variance (corresponding to turbulent kinetic energy) and the vorticity variance

(corresponding to turbulent enstrophy per unit area), respectively. (Note that in this section I consider variance in space, so I remove the spatial mean. I also remove the time average from each time series. Thus "turbulent" refers to the perturbation around both the spatial and the time average.) In practical terms I estimate the spectra for a given geographic line by i) removing the spatial and time average of each variable, ii) applying discrete Fourier transform in the spatial direction, iii) calculating the square absolute value of each Fourier component and iv) average through time. For $\mathcal{E}(k)$ and $\mathcal{Z}(k)$, I divided by a 1/2 factor to be consistent with the definition of energy and enstrophy.

Figure 6.24 shows wavenumber spectra along the blue line shown in Figure 6.23 (deep water). This line was chosen because its eddy variances (Figure 6.22) are roughly uniform. Investigation of spectra along several other lines in deep water (with different size and in different locations) reveal that the results from this line are typical for the deep water outside the boundary sponge layer.

Figure 6.24 shows that overall GoMSS has higher sea level variance than the global system and GoMSS$^+$ for all length scales (consistent with Figure 6.22), probably due to GoMSS unrealistic internal variability. GoMSS$^+$ has a sea surface variance spectrum that is similar to the global system, due to the temperature and salinity nudging of GoMSS$^+$ to the global system on wavelengths longer than 90 km. There is not much variability left in the sea surface height below wavelength (λ) of 100 km. Thus it is difficult to conclude which system generates higher resolution features from sea surface height. Note that for λ <250 km the sea surface height follows a $k^{-11/3}$ spectrum which is consistent with observations from altimeters *LeTraon et al.* (2008).

Figure 6.24 shows that the global system, GoMSS and GoMSS$^+$ energy generally follows a $k^{-5/3}$ spectrum for λ between 250 km and 80 km and a k^{-3} spectrum for λ between 80 km and 15 km. Thus according to geostrophic turbulence theory, the inverse energy cascade occurs at length scales above 80 km which is around 3 times larger than the first Rossby radius of deformation (around 30 km in the region). The reasons for this are not clear but *Vallis* (2006) notes that the wavelength of maximum instability can be expected to be larger than the first deformation radius (e.g., in the Eady problem the wavelength of maximum instability is a few times the first deformation radius). For λ >250 km the inverse cascade is halted probably due to the influence of the β-effect and bottom friction. For λ <15 km, where ageostrophic dynamics becomes important,

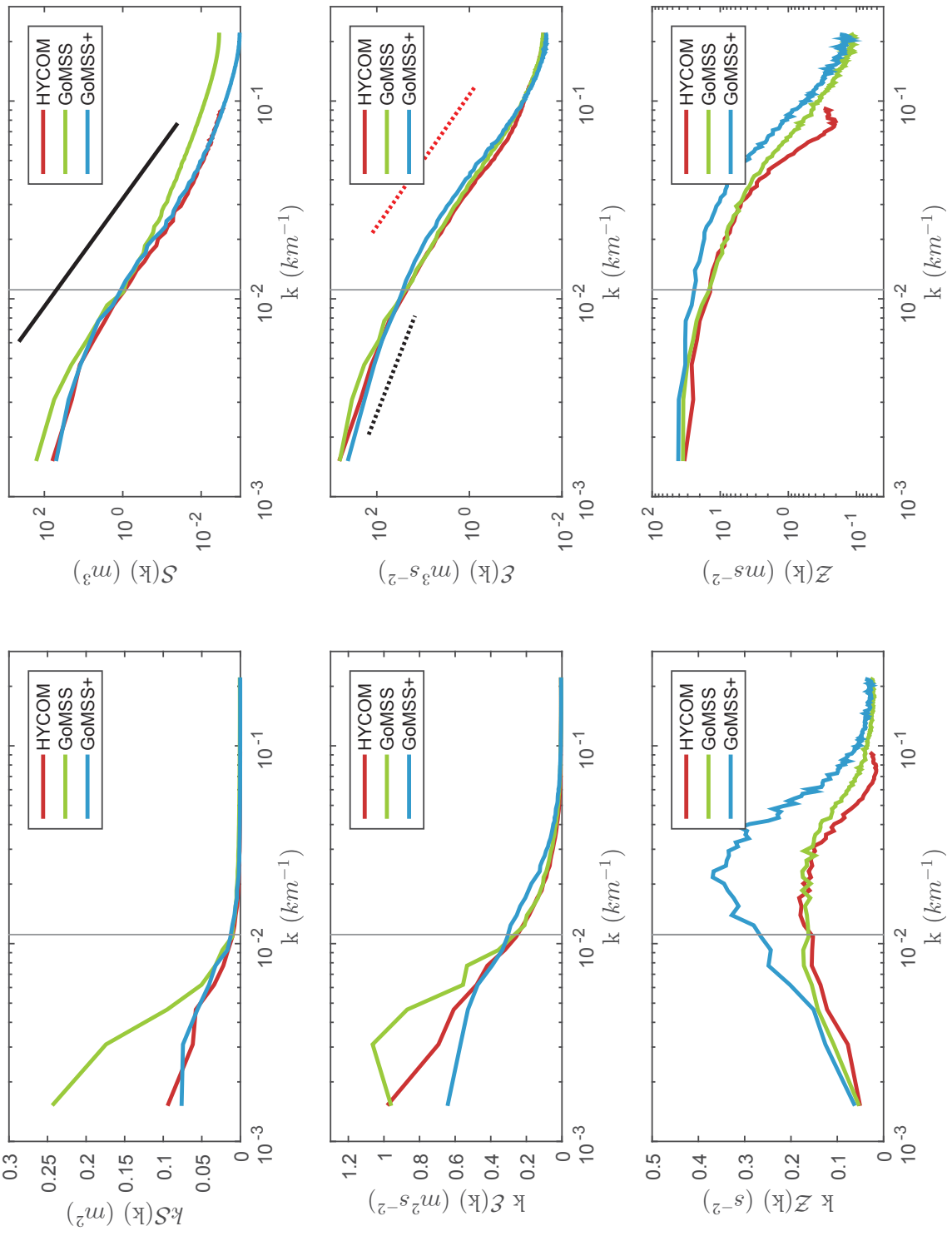
HYCOM
GoMSS
GoMSS+
$\mathcal{S}(\mathrm{k})\ (m^3)$
$\mathcal{E}(\mathrm{k})\ (m^3 s^{-2})$
$\mathcal{Z}(\mathrm{k})\ (ms^{-2})$
$k\mathcal{S}(\mathrm{k})\ (m^2)$
$\mathrm{k}\ \mathcal{E}(\mathrm{k})\ (m^2 s^{-2})$
$\mathrm{k}\ \mathcal{Z}(\mathrm{k})\ (s^{-2})$
k (km^{-1})

the energy spectra has a slope close to $-5/3$ implying a forward energy cascade which is consistent with previous studies (e.g., *Capet et al.*, 2008).

The energy spectra show that, overall, GoMSS is more energetic than the global system. This is expected for the small scales because GoMSS has higher resolution than the global system. However, for the large wavelengths this is associated with the trapped eddies formed due to problems with the lateral boundary conditions that lead to unrealistic high variability in the deep water. For $\lambda >$160 km GoMSS$^+$ is somewhat less energetic than the global system. This is because spectral nudging does not directly constrain the barotropic component of the kinetic energy. However GoMSS$^+$ has more energy than the global system, and GoMSS for λ between 100 and 10 km. This implies that i) the spectral nudging does not suppress the variability for $\lambda <$90 km and ii) spectral nudging acts as a source of energy for the eddies for 100 km$< \lambda <$10 km. This leads me to speculate that spectral nudging acts as a source of potential energy that then "feeds" the kinetic energy (i.e., baroclinic instability) and so the formation of eddies for 100 km$< \lambda <$10 km. However, below 10 km and above 100 km GoMSS$^+$ has lower energy than GoMSS. The physical mechanisms for this are not clear and further analysis beyond the scope of this thesis is necessary (e.g., energy budget analysis). I speculate that GoMSS$^+$ transfer less kinetic energy to larger ($\lambda >$90 km) and smaller scales ($\lambda <$10 km).

The global system and GoMSS have similar enstrophy variance distribution above 30 km. All systems have an enstrophy variance preserving spectrum peak at $\lambda \approx$50 km. However GoMSS$^+$ generally has more enstrophy than both the global system and GoMSS and a steeper variance preserving peak. This implies that spectral nudging acts as an additional enstrophy source in the deep water. This is because, in deep water, the eddies are primarily generated by baroclinic instability (i.e., transfer of potential energy to kinetic energy), while on the shelf other mechanisms primarily force the small scale motion (e.g., winds),

---

Figure 6.24 *(preceding page)*: Sea level variance (top panels), turbulent kinetic energy (middle panels) and turbulent enstrophy (bottom panels) wavenumber spectra from the global system (red), GoMSS (green) and GoMSS$^+$ (blue) at the ocean surface along the line in deep water (blue line) shown in Figure 6.23. The left panels show the spectra in variance-preserving form. The right panels show the spectra on traditional logarithmic scales. The straight solid black, dashed red and dashed black lines indicate the -11/3, -3 and -5/3 slopes, respectively. The grey line shows the spectral nudging cutoff wavenumber. The wavenumber is in cycles per km.

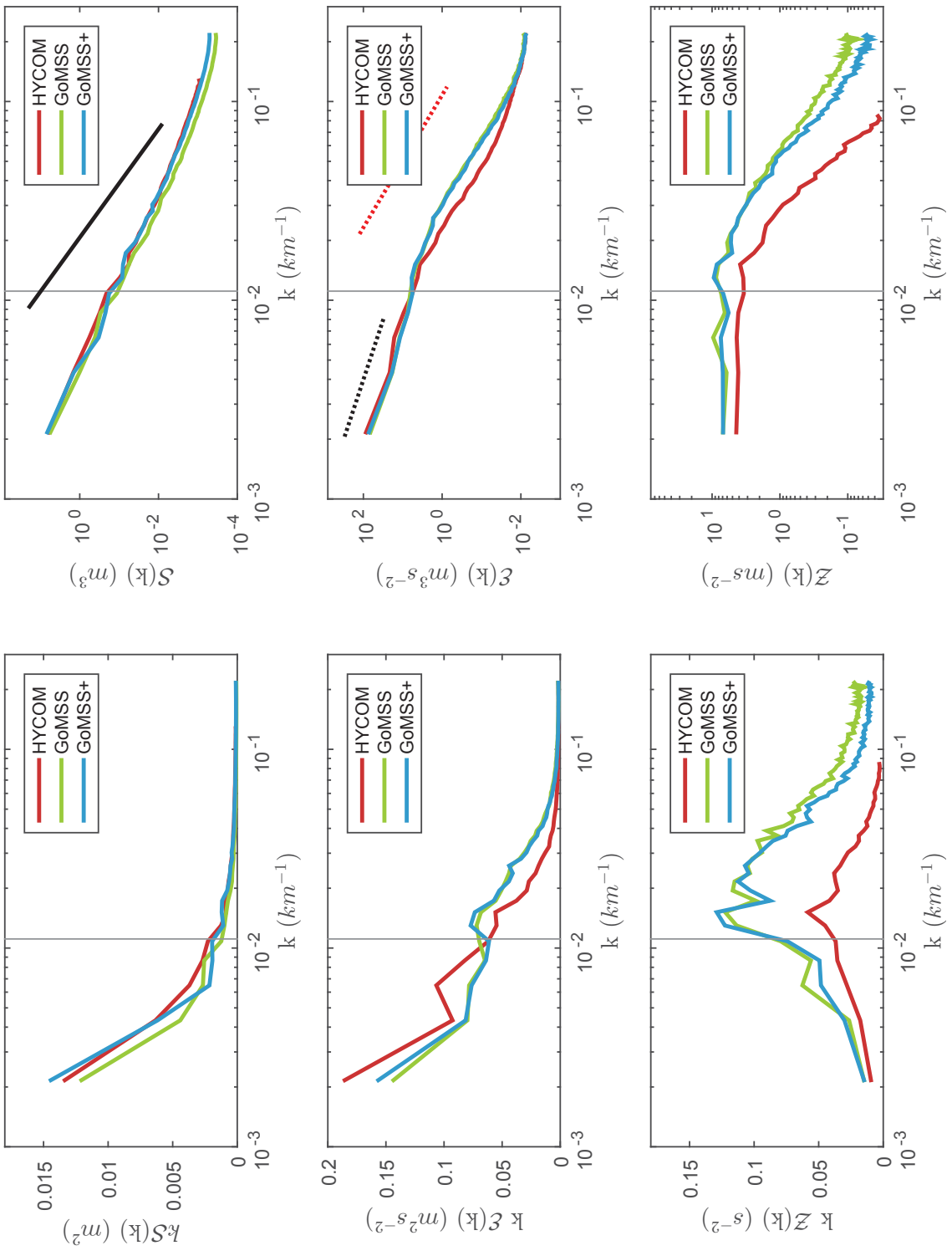
HYCOM
GoMSS
GoMSS+
$\mathcal{S}(\mathrm{k})\ (m^3)$
$\mathcal{E}(\mathrm{k})\ (m^3 s^{-2})$
$\mathcal{Z}(\mathrm{k})\ (m s^{-2})$
$k\mathcal{S}(\mathrm{k})\ (m^2)$
$\mathrm{k}\ \mathcal{E}(\mathrm{k})\ (m^2 s^{-2})$
$\mathrm{k}\ \mathcal{Z}(\mathrm{k})\ (s^{-2})$
$\mathrm{k}\ (km^{-1})$

which are the same in GoMSS and GoMSS$^+$.

Figure 6.25 shows spectra estimated along the line on the shelf (red line, Figure 6.23). Estimates for several lines on the shelf indicate that the spectra along this line are typical for the shelf. Figure 6.25 shows that the global system and GoMSS$^+$ sea surface height variance spectra are very similar. GoMSS generally has lower sea surface height variance in all the length scales. There is almost no sea surface variance left for λ <100 km. On the shelf GoMSS and GoMSS$^+$ energy spectra are almost identical. GoMSS and GoMSS$^+$ have more energy for λ <100 km compared to the global system. GoMSS and GoMSS$^+$ enstrophy spectra are very similar. Generally GoMSS and GoMSS$^+$ have higher enstrophy than the global system on the shelf.

In summary, in deep water the enstrophy and energy spectra show that GoMSS$^+$ generates more variability than the global system and GoMSS for length scales between 100 and 10 km. This confirms that GoMSS$^+$ has more energetic eddies and finer scale detail than the global system and GoMSS in this wavelength band. On the shelf, GoMSS and GoMSS$^+$ energy and enstrophy spectra are very similar. This is not surprising because on the shelf other dynamical effects dominate the variability on small scales (e.g., advection, atmospheric forcing, tidal rectification and mixing) rather than the spectral nudging. Both GoMSS and GoMSS$^+$ have more energy and enstrophy for λ <100 km than the global system on the shelf, which confirms that the regional model generates more variability in smaller scales than the global system because it has higher resolution.

As expected, the spectra show that higher order quantities, like velocity and vorticity reflect higher wavenumber variability than sea level. For example, Hovmoller diagrams for sea surface height (Figure 6.11) show that there is not much variability on the small scales. To relate the above discussion to the other variables, I present Hovmoller diagrams for the vertical component of the relative vorticity (ζ) normalized by the planetary vorticity (Figure 6.26), at the ocean surface along the blue line in Figure 6.23. Figure 6.26 clearly shows that GoMSS and GoMSS$^+$ generate higher vorticity on the small scales than the

---

Figure 6.25 *(preceding page)*: Sea level variance (top panels), turbulent kinetic energy (middle panels) and turbulent enstrophy (bottom panels) wavenumber spectra from the global system (red), GoMSS (green) and GoMSS$^+$ (blue) at the ocean surface along the line on the shelf (red line) shown in Figure 6.23. Same format as Figure 6.24.

global system. Additionally, Figure 6.26 shows that GoMSS^{+} has more energetic small scales than GoMSS. This is consistent with the bottom panels in Figure 6.24.

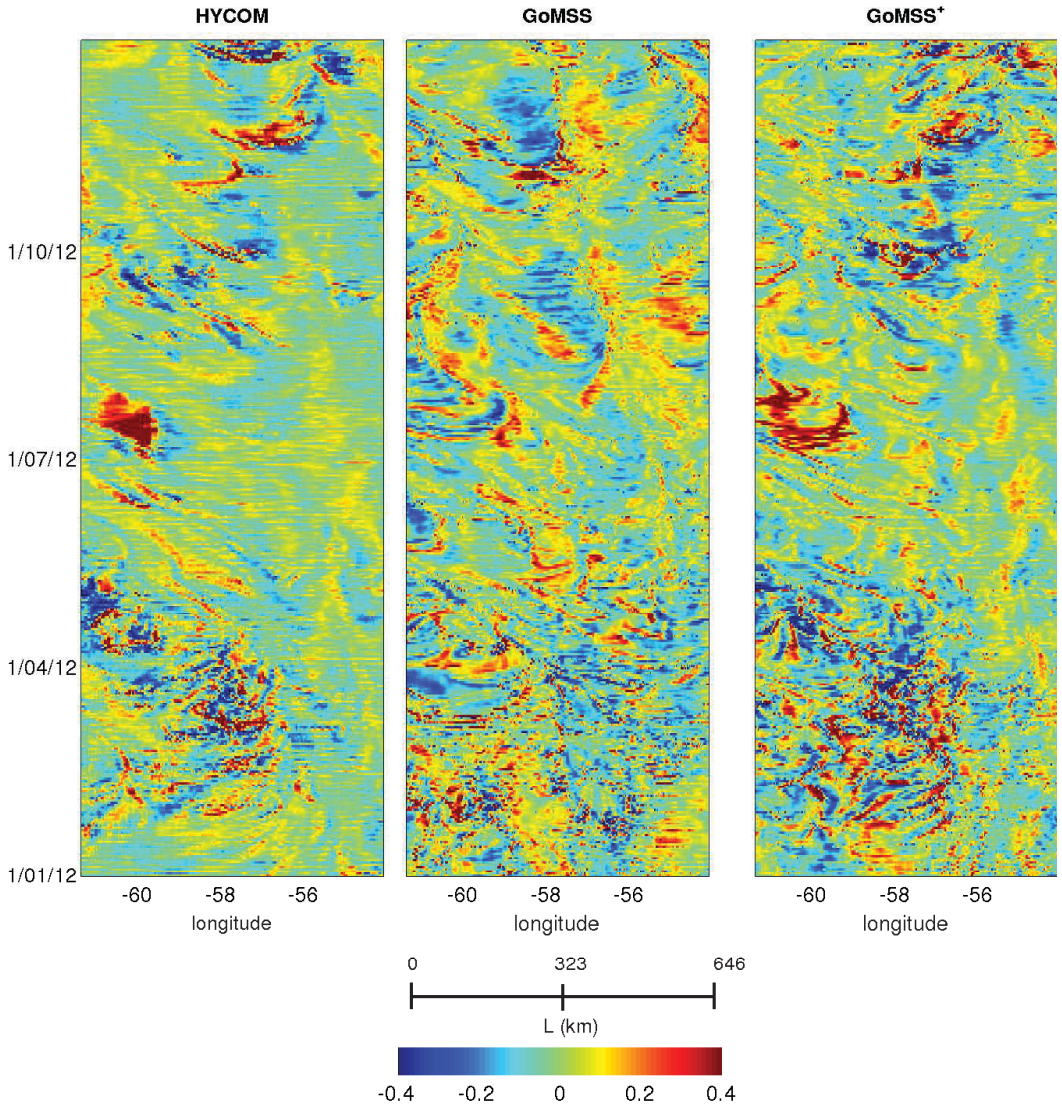

Figure 6.26: Hovmoller diagrams of vertical relative vorticity at the surface normalized by the planetary vorticity, along the deep ocean line (blue line) in Figure 6.23 based on the global system (left panel), GoMSS (middle panel) and GoMSS^{+} (right panel). The scale L shows the distance in km along the line. The fields are for 2012.

6.5 Summary

Assimilation may keep the global system close to the observations (wherever they are available) but it can also result in dynamical inconsistencies. GoMSS generates more dynamically consistent fields, and finer scale features, on the Scotian Shelf and the Gulf of Maine than the global system because it has higher resolution and does not assimilate data. However, the GoMSS solution is affected by unrealistic internal variability and recirculation along the lateral open boundaries. Spectrally nudging the large scales of the global system into GoMSS eliminates these unrealistic features.

Overall, GoMSS$^+$ (GoMSS with spectral nudging) generates temperature and salinity fields that are in better agreement with the observations than GoMSS in the deep water. The spectral nudging placed the front between the slope and the shelf water, and the associated eddies and meanders, in positions consistent with satellite observations. GoMSS$^+$ also generates better sea level and circulation than GoMSS in the deep water. Additionally spectral nudging supplied energy and enstrophy on the length scales between 100 and 10 km.

The impact of spectral nudging is less significant on the shelf, but it still affects the local circulation and hydrography. Wavenumber spectra showed that spectral nudging did not have a significant impact on the transfer of energy and enstrophy on the shelf. It is difficult to conclude if spectral nudging improved the temperature and salinity fields on the shelf. (Comparison with observations from CTD's showed that GoMSS$^+$ error is higher than GoMSS at intermediate depths (21-100 m), but comparison with a glider showed that GoMSS$^+$ error is lower than GoMSS.) Overall spectral nudging, led to slightly better circulation and sea level on the shelf and did not remove important features generated due to the interaction between the tides and the local bathymetry (tidal rectification) and the seasonal stratification (tidal mixing and generation of internal waves).

I conclude by noting that different spectral nudging parameters may lead to better results. Additionally applying weaker nudging on the shelf may be necessary (see Appendix E). Further sensitivity experiments are necessary to evaluate the optimal spectral nudging strength and its horizontal and vertical variation over the model domain.

CHAPTER 7

SUMMARY AND DISCUSSION

Despite the rapid advances in global ocean modelling, there is still need for higher resolution and the explicit representation of processes absent from existing global forecast systems (e.g., tides interaction with the regional scale fields and higher resolution topography) in order to accurately simulate, and ultimately predict variability in regional scales. From a practical perspective, it is easier, and computationally more efficient, to use a higher resolution regional model than increase the resolution of a global model. However, the variability on regional scales is often controlled by processes operating on basin or possibly global scales. This leads to a multi-scale problem, where higher resolution regional models, driven by global systems, are needed to downscale the ocean conditions. The standard approach is to introduce information from the global system at the lateral open boundaries of the regional model, which is often referred to as one-way nesting. As discussed in the introduction, the one-way nesting method has many practical problems: ill-posedness (e.g., *Davies*, 1976; *Marchesiello et al.*, 2001; *Blayo and Debreu*, 2005), unrealistic internal variability (*Giorgi and Bi*, 2000; *Caya and Biner*, 2004; *Rinke et al.*, 2004; *Alexandru et al.*, 2009; *Laprise et al.*, 2012, e.g.,) and propagation of errors from the global system to the regional model.

These problems motivated me to develop and evaluate new methods for downscaling ocean conditions. The methods are inspired in part by the recent study of *Henshaw et al.* (2003) which used theoretical arguments and numerical models to show that the time history of the large scales can be used to reconstruct a portion of the small scales. The idea proposed by *Henshaw et al.* (2003) has similarities with an approach used by the atmospheric community to downscale the atmospheric conditions: atmospheric spectral

nudging.

Two-way nesting provides an alternative way of keeping the regional model state consistent with the fields introduced at the lateral boundaries (e.g., *Urrego-Blanco*, 2014). However, as mentioned in Chapter 2, two-way nesting is computationally demanding because it requires both the high resolution regional and the coarser resolution global (or basin scale) models to run in parallel (i.e., online exchange). Most importantly because of the required online integration of the regional and global models, available analysis products from realistic operational systems, such as the the global system used in this study, cannot be used in two-way nesting. For these reasons in this thesis I did not explore two-way nesting.

A brief summary of the thesis is given below followed by answers to the questions posed in the Introduction and suggestions for future work.

7.1 Summary

I summarize below the technical and the scientific achievements of the thesis separately. Note however that these two aspects often overlap and so the distinction is somewhat blurred.

Technical Objectives: My first attempt at downscaling was statistical. My second approach was based on dynamical downscaling using an idealized and a realistic ocean model.

The statistical approach was used to confirm that there is predictability of small scales from the large scales in ocean variability. More specifically, a multivariate regression based approach was used to quantify the proportion of small scale variability of a sequence of sea level fields (obtain from an along track satellite altimeter) that can be linearly predicted by the large scales. The encouraging level of predictability provided motivation for the subsequent dynamical downscaling.

An idealized ocean model was used to extend the analysis of *Henshaw et al.* (2003) to flow regimes closer to the real ocean. Specifically a quasi-geostrophic ocean model that generates a double gyre was used [1]. Based on numerical experiments it was shown that the

[1] Material from the downscaling experiments using the idealized ocean model has been published as:

position and the intensity of the model's unstable mid-ocean jet, and the associated eddies, could be recovered from the time history of the large scales.

For most practical applications the large scales are not known perfectly. To address the imperfections in the large scales a traditional data assimilation method was combined with the nudging of large scales, using a "hybrid" and applied to the idealized model. I conducted several experiments where time series of sea level from a fixed array of locations obtained, from a model run that was treated as the "truth" (i.e. pseudo-observations), were assimilated using the ensemble optimal interpolation (EnOI) and the hybrid methods. Not surprisingly it was shown that traditional data assimilation methods can effectively recover all the scale of variability of the quasi-geostrophic model given a sufficiently dense observing array. However, when a small number of observations is used (that alone alias or completely miss some of the eddies) the predictability of the small scales is reduced significantly. By way of contrast, experiments with the hybrid method showed that when the large scale features are ingested into the model, the assimilation of limited point observations improves significantly the accuracy of the recovered small scales. The hybrid method also outperformed the simple spectral nudging of large scales.

A realistic model of the Gulf of Maine, Scotian Shelf and adjacent deep ocean (GoMSS), was developed within the NEMO framework. GoMSS has a horizontal resolution of approximately 1/36° and 52-z vertical levels with spacing that varies from 0.7 m at the surface and 233 m at the deepest level. Tides are explicitly resolved in the model. A simple one-way nesting was first performed by introducing GoMSS's initial and lateral open boundary conditions from daily temperature salinity, sea surface height and horizontal current velocity fields from 1/12° HYCOM/NCODA analysis system (referred to as the global system in the thesis). Because the global system does not have tides, five important tidal constituents (M_2, N_2, S_2, K_1 and O_1) obtained from FES2004 were also used to drive the model at its lateral open boundaries.

The global system was chosen because previous studies have shown that it provides realistic ocean fields (e.g., *Chassignet et al.*, 2007, 2009; *Kelly et al.*, 2007; *Metzger et al.*, 2008). To ensure the global system has no major biases in the Gulf of Maine and Scotian Shelf I conducted comparisons with local observations. Overall the global system

---

Katavouta, A., and K. R. Thompson, Downscaling ocean conditions: Experiments with a quasi-geostrophic model, *Ocean Modelling*, 72, 231-241, 2013.

fields were reasonably realistic (within the limits of its resolution), especially closer to the surface. This is not surprising because the global system assimilates all available satellite and in-situ observations. However, the global system does not have tides and so it cannot simulates several important features and phenomena in the area (e.g., intense mixing on top of Georges Bank, residual currents, internal tides). Furthermore, the spatial autocorrelation function of the global system reveals that the assimilation may keep the model close to the observations, but it also introduces some unrealistic local features and limits the dynamical consistency between the circulation and the tracers (temperature and salinity).

Comparisons of GoMSS, observations and a monthly hydrographic climatology showed that GoMSS provides realistic simulations of the tides, and captures accurately the synoptic and seasonal variability. GoMSS generates more accurate currents and hydrography than the global system in areas where the tides are large (further discussion is provided in the scientific objectives). GoMSS resolves well the variability associated with small scales not resolved by the coarser resolution in the global system. However, in areas with many available observations (e.g., ocean surface), the global system generated more realistic fields due to the assimilation of observations. Off the shelf, in the deep ocean, GoMSS is often not able to accurately simulate the location and timing of the eddies or meanders. (The global system produces realistic positions of eddies and meanders because of the assimilation of satellite observations.) Misplacement of eddies and meanders is the manifestation of unwanted internal variability in highly non-linear areas. Furthermore GoMSS generates some unrealistic features near its open lateral boundaries e.g., unrealistic recirculation near the western lateral open boundary.

Additional experiments were conducted to evaluate the benefits of the atmospheric spectral nudging approach in GoMSS. The method was modified for ocean applications. GoMSS large scale ($>$90 km) temperature and salinity were relaxed towards the global system fields. It was shown that off the shelf, in the deep ocean, several eddies and meanders are placed closer to their observed position. Furthermore spectral nudging suppressed the unrealistic features near the lateral boundaries. On the shelf, the impact of spectral nudging was not as pronounced as in the deep ocean. Spectral nudging led to somewhat better representation of the sea surface height and the circulation on the shelf. I was encouraged to find that spectral nudging did not smooth out the small scale variability associated with tides (e.g., mixing on top of Georges bank, the striations). This is not

surprising because spectral nudging does not affect directly the small scales, but it allows them to adjust based on the model's dynamics. Overall the spectral nudging method leads to more accurate downscaling than one-way nesting alone.

Scientific Objectives:

As I addressed the technical issues I noticed several interesting phenomena in the GoMSS output that were absent from the global system. Particularly, the interaction between tides and seasonal variability caused the formation of features of both scientific and practical interest. Some of these features have been observed and discussed extensively in the past. However, to my surprise the model generated some features that have not been identified before. This motivated me to investigate the physical mechanisms responsible for these features[2].

The effect of the tides on the seasonal mean state was clearly evident in GoMSS's prediction of well mixed water mass on top of Georges Bank and the generation of tidally rectified flows on top of shallow banks (e.g., Georges Bank and Brown Banks). I demonstrated, for the first time, the important role played by tidal rectification in controlling the mean circulation around Sable Island on the outer Scotian Shelf. GoMSS simulates better the temperature and salinity in areas where tidal mixing is important and the circulation in areas strongly affected by tidal rectification. Most notably the global system does not capture accurately the well mixed water column, or the clockwise gyre on top of Georges Bank.

GoMSS prediction of tidal elevation and currents are generally consistent with previous studies and observations from coastal tide gauges, fixed moorings and land-based HF radar systems. Experiments with constant and varying water density showed that tides vary with season due to seasonal changes in stratification. For M_2, changes of tidal elevation amplitude are less than 10%. On the other hand the effect on tidal currents is more important, particularly in the Gulf of Maine and the deep water adjacent to the Northeast Channel. For both locations the maximum M_2 tidal current in summer can exceed the colocated winter maxima by more than 0.1 m s^{-1}.

One of the surprising model predictions was an alternating pattern of highs and lows in the surface M_2 summer maximum speed aligned with Georges Bank (the "striations"). The

[2]Material based on the interaction between the seasonal variability and tides has been submitted for publication in the *Journal of Physical Oceanography.*

striations are absent in winter and for diurnal constituents. The striations are also observed in HF radar radial velocities. To my knowledge this is the first time that such a pattern has been explicitly identified and observed in this region. It was argued that the striations are linked to the generation of internal tides along the north side of Georges Bank and their propagation towards the coast of Maine. An idealized model based on *Laurent et al.* (2003) was used to confirm that the striations are caused by the linear superposition of the barotropic and forced, phase-locked baroclinic tide. Additionally, the seasonal changes in tidal current on top of Georges Bank are associated with seasonal changes in the model sea level gradient and vertical viscosity, in agreement with the simple model of *Prandle* (1982).

In my attempt to understand how spectral nudging influences the various length scales and the fields that are not directly assimilated in the regional model I examined the wavenumber spectra. The wavenumber spectra for velocity and vorticity revealed that although spectral nudging directly affects only the length scales exceeding 90 km, it indirectly modifies the energy and enstrophy of the smaller scales in deep water. More specifically, spectral nudging indirectly supplies kinetic energy to the wavelengths between 100 and 10 km. Additionally, spectral nudging supplies enstrophy to the system. Therefore, due to the non-linearity of the governing equations spectral nudging not only did not suppress the length scales below the cutoff length (90 km) in deep water but rather energized them. In contrast, on the shelf spectral nudging did not have any significant impact on the enstrophy and kinetic energy transfer. This is because in deep water non-linearity is dominant while on the shelf other phenomena (i.e. advection, atmospheric forcing, tidal rectification and mixing) are more important.

7.2 Answer to Questions posed in the Introduction

To summarize the main conclusions of the thesis let us refer back to the Introduction and address the questions that motivated this study. I now answer the technical questions. For all the technical questions the answer is yes. To elaborate:

Is there evidence of coupling across length scales in the real ocean on which to base effective downscaling methods? I showed based on observations and theoretical arguments that there is coupling between the different length scales in the real ocean.

Can the time history of the large scales be used to recover the small scale variability (as proposed by Henshaw et al., 2003) of flow regimes that exist in the real ocean? By extending the analysis of *Henshaw et al.* (2003) to a highly non-linear idealized ocean model (quasi-gestrophic model) I proved that indeed some of the small scale variability can be recovered successfully from the time history of the large scales. However, isolated small scale features (e.g., eddies that have been advected away from the region of their formation) can not be recovered from the large scales.

Is spectral nudging of large scales a viable method for ocean downscaling? If so can it be supplemented by the assimilation of local observations to produce more accurate simulations of the small scales? Based on the idealized model experiments, I conclude that the spectral nudging of the large scales is a viable method for ocean downscaling. Furthermore using the same idealized model I demonstrated that by supplementing the large scale nudging with assimilation of limited local observations (that are too sparse to improve the small scales when used in a traditional assimilation experiment) using EnOI (i.e., hybrid method) can significantly improve the accuracy of the small scales.

Can the existing global ocean forecast systems, in particular the 1/12° HYCOM/NCODA global operational system, provide realistic large scales for the Northwest Atlantic? The global system provides reasonable realistic fields in the study area, within the limits of its resolution. However, the global system does not have tides and so it cannot simulate several important features and phenomena in the area (e.g., intense mixing on top of Georges Bank, residual currents, internal tides).

Can the global system's representation of the hydrography and circulation of the Northwest Atlantic be improved by high resolution and explicit representation of tides? Overall GoMSS improves the global system fields, at least on the shelf, because it has tides and higher resolution.

Does one-way nesting lead to unrealistic features? How does it compare with the spectral nudging method? One-way nesting leads to physically unrealistic fields and circulation in the deep water. More specifically, one-way nesting generates unrealistic internal variability off the shelf in deep water (i.e., misplaced eddies and meanders) and unrealistic recirculation along the lateral boundaries of GoMSS. Although it is possible that further adjustment of the lateral boundary conditions parameters along each boundary may lead to more accurate simulations a method that eliminates the necessity of "tuning"

along each boundary, like the spectral nudging, is preferable. The atmospheric spectral nudging method improves the results from the one-way nesting and removed most of the unrealistic internal variability and recirculation along the lateral boundaries, without suppressing important small scale variability.

Turning now into the scientific questions that were posed at the introduction.

How does the spectral nudging method modify the transfer of energy between large and small scales? Wavenumber spectra showed that spectral nudging acts as a source of kinetic energy and enstrophy for the eddies with wavelength between 100-10 km. In particular, spectral nudging acts as a source of potential energy that is then transferred to kinetic energy through baroclinic instability for wavelengths between 100-10 km. By way of contrast, it appears that spectral nudging acts as a "sink" of kinetic energy for length scales larger than 100 km and smaller than 10 km. This suggests that spectral nudging limits the kinetic energy transfer to larger and smaller scales but the reasons for this are not clear and further analysis is necessary.

How large are the seasonal changes in the tides and what is their spatial distribution? The seasonal change in the M_2 tidal elevation is less than 10% and not of practical significance. The effect of seasonal stratification on the M_2 tidal currents is relatively more important (more than 0.1 m s^{-1}) in the Gulf of Maine and the deep water adjacent to the Northeast Channel.

What are the physical mechanism responsible for large seasonal variations in tidal currents in the Gulf of Maine and on top of Georges Bank? I showed that the physical mechanism responsible are the linear superposition between barotropic and forced, phase-locked, baroclinic tide (in the Gulf of Maine), and seasonal changes in the sea level gradient and vertical eddy viscosity (on top of Georges Bank).

7.3 Future Work

I have shown that spectral nudging, modified for ocean applications, has great potential for downscaling. However, more sensitivity studies are necessary to estimate the optimal parameters (i.e., nudging coefficient, large scale length). Additionally, more work is required to explore any potential benefit of temporal smoothing of the large scale fields introduced through spectral nudging.

Although, the unrealistic internal variability and the recirculation along the lateral boundaries were constrained using spectral nudging, some unrealistic features persist. More specifically the global system has erroneous inflow-outflow at Cabot Strait. This erroneous feature is subsequently introduced to GoMSS through the north lateral boundary condition. Spectral nudging cannot solve this problem (i.e. imperfect large scales). The "hybrid" (combination of spectral nudging and assimilation of local observations) that was developed and tested using the idealized model has the potential to correct imperfections in the large scale. Thus, in future implementation of spectral nudging, the incorporation of observations near GoMSS north boundary, or possibly the modification of the form of the open lateral condition at the north boundary, should be considered.

Furthermore, the benefit of spectral nudging on downscaling the ocean conditions needs to be further explored and verified using high resolution observations in the deep water. Hopefully, such observations may become available in the near future given the progress in ocean observing systems.

Given that computational power will keep increasing in the future, even higher resolution can be used to explicitly simulate smaller scale processes absent from GoMSS (e.g., filaments associated with coastal upwelling, personal communication with Shiliang Shan). Additionally, to explore further the interaction of seasonal stratification and tides a non-hydrostatic model that can generate tidal bores is recommended.

Based on our analysis GoMSS has been proven to produce reliable seasonal mean states and extremes and so can be used for surge storm prediction, design of off shore structures etc.. In this study all the results were discussed using an Eulerian representation of fluid flow. However, for some applications (e.g., oil spill mitigation) the Lagrangian frame of reference is more relevant. To show that GoMSS is able to produce a reasonable Lagrangian description, Figure 7.1 shows trajectories from virtual particles released along the 200 m isobath on the shelf break. The trajectories were generated using the GoMSS output discussed in this thesis (the trajectories were generated by Erica Rogers using the Ariane computational tool of *Blanke and Raynaud* (1997)). The particles were released on 1-July-2010 and the trajectory paths are for 90 days. Several circulation features that were discussed in this thesis are evident in the trajectories shown in Figure 7.1, e.g., the exchange between shelf and deep water along the Northeast Channel and the Emerald Basin, the clockwise current on top of Georges Bank, the northwards flow along the east

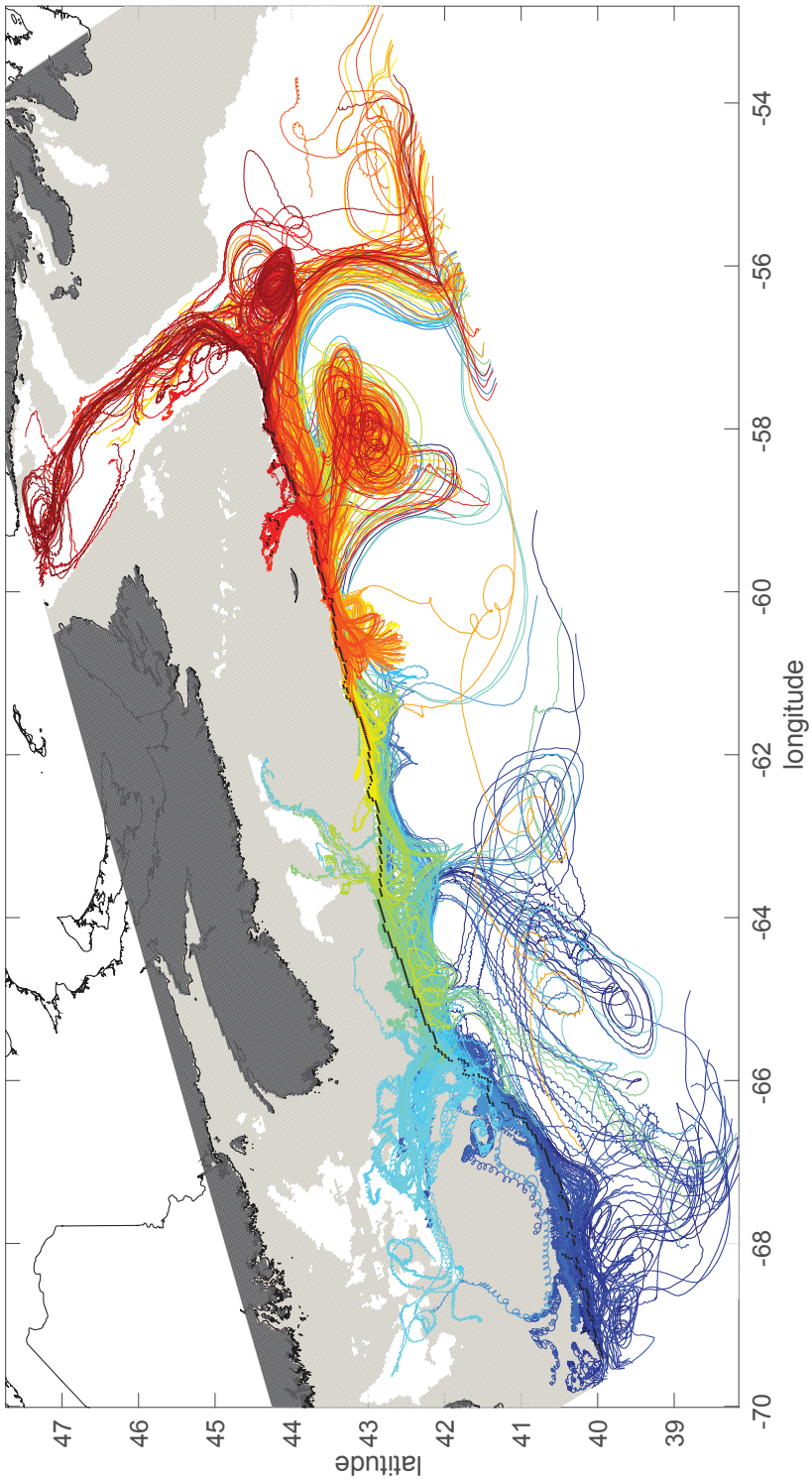

Figure 7.1: Trajectories of particles released along the shelf break 200 m isobath (thick black line) based on GoMSS. The particles were released on 1-July-2010 and the trajectory paths are for 90 days. The different colors indicate different release area. The light gray shading shows areas shallower than 200 m.

side of the Laurentian Channel, and the impact of eddies and meanders near the shelf break. Thus, GoMSS can also be used for a range of applications where Lagrangian flow is necessary, like oil spill mitigation and marine animal movement.

As a final remark, it is to be expected that the combined use of the downscaling method described in this thesis and assimilation of local observations into higher resolution models will lead to even more realistic simulations and predictions.

APPENDIX A

OPTIMAL ENSEMBLE SIZE

The sensitivity of the EnKF and EnOI to the ensemble size has been the subject of many studies (e.g., *Houtekamer and Mitchell*, 1998; *Mitchell et al.*, 2002; *Evensen*, 2003; *Oke et al.*, 2007), and generally, the quality of the analysis increases with increasing ensemble size. To illustrate, consider the ensemble mean as the best estimate, and the ensemble spread as the error of the ensemble. An ensemble of finite size will provide only an approximation to the error covariance matrix. Thus, a very large ensemble is necessary to minimize the error. However, several studies (e.g., *Houtekamer and Mitchell*, 1998; *Oke et al.*, 2007) have demonstrated that a moderate size ensemble can be used effectively if the long range spurious correlations are filtered out (localization).

I performed a sensitivity experiment to investigate the optimal ensemble size for the EnOI application in the quasi-geostrophic model (Chapter 3). Although several twin experiments with varying ensemble size, and number and location of pseudo-observations were performed, I discuss results for 3 ensembles (small, medium, and large), and a pseudo-observation array with 344 observations, laid out in a roughly equispaced grid. The model runs described in Chapter 3 were used to generate the forecast, the truth (pseudo-observations), and the ensemble run (Table 3.2).

- **Small ensemble:** The ensemble members were generated by subsampling run EN every 500 days (14 members). The correlation function based on the ensemble is shown in the right panel of Figure A.1. The correlation between neighbouring points is strong and decreases with distance. However, strong correlation persists between long range points. This is not realistic and is caused by the limited ensemble size.

- **Medium ensemble:** The ensemble members were generated by subsampling run EN

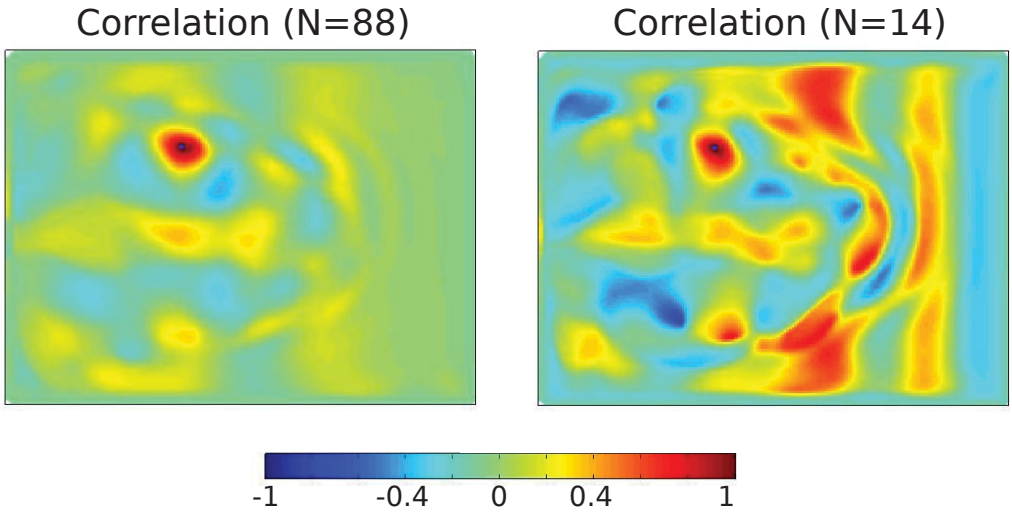

Figure A.1: Correlation function between the point represented by black dot and the rest of the grid points. Left is for the large ensemble and right is for the small ensemble.

every 250 days (27 members). The correlation between long range points is reduced; however, there is still significant long range spurious correlation (not shown).

- **Large ensemble:** The ensemble members were generated by subsampling run EN every 75 days (88 members). The use of a large ensemble limited significantly the long range unrealistic correlation; however, some weak correlation between long distance points recurs (Figure A.1).

The effectiveness of each ensemble is assessed by checking how closely the true state is represented in each analysis run. Typical snapshots of sea level differences, between the true fields and the forecast, and analysis fields, for day 200, are shown in Figure A.2. When a small ensemble is used EnOI does not lead to any significant improvement. As the ensemble size increases, EnOI leads to more accurate analysis. The differences between the truth and the forecast runs are almost eliminated when a large ensemble (88 members) is used.

The mean square differences of the true sea level and the forecast, and the analysis sea level through time, is shown in Figure A.3. For a large and a medium ensemble, EnOI reduced significantly the mean square difference. Particularly, for a large ensemble, EnOI almost eliminates the differences between the forecast and the true sea level. For a

small ensemble, the fit of the EnOI to the truth is not much better than the forecast and at times the analysis degrades the forecast. After day 700, the small ensemble leads to some improvement on the forecast. However, note that if the experiment continues further in time there will be periods where the difference is inflated again.

Implementation of EnOI with the large ensemble (88 members) leads to an accurate analysis. However the 88 member ensemble is still affected by some long range spurious correlation (Figure A.1). To eliminate this long range correlation, the ensemble based covariance is multiplied element by element by a function of distance C (localization). In this study the function proposed by *Gaspari and Cohn* (1999) is used:

$$C = \begin{cases} -\frac{1}{4}\left(|z|/R_o\right)^5 + \frac{1}{2}\left(|z|/R_o\right)^4 + \frac{5}{8}\left(|z|/R_o\right)^3 - \frac{5}{3}\left(|z|/R_o\right)^2 + 1 & : 0 \leq |z| \leq R_o \\ \frac{1}{12}\left(|z|/R_o\right)^5 - \frac{1}{2}\left(|z|/R_o\right)^4 + \frac{5}{8}\left(|z|/R_o\right)^3 + \frac{5}{3}\left(|z|/R_o\right)^2 & \\ -5\left(|z|/R_o\right) + 4 - \frac{2}{3}\left(R_o/|z|\right) & : R_o < |z| \leq 2R_o \\ 0 & : 2R_o < |z| \end{cases}$$

where z represents distance between grid points and R_0 represents a radius of influence.

Localization is important when the observation array is sparse. However, localisation can remove essential information if the length scales of the localising function are too short (e.g. *Oke et al.*, 2007). Therefore, the length scale of localization varies depending on the observation array-size, and the critical wavenumber in Chapter 3 (Table 3.1).

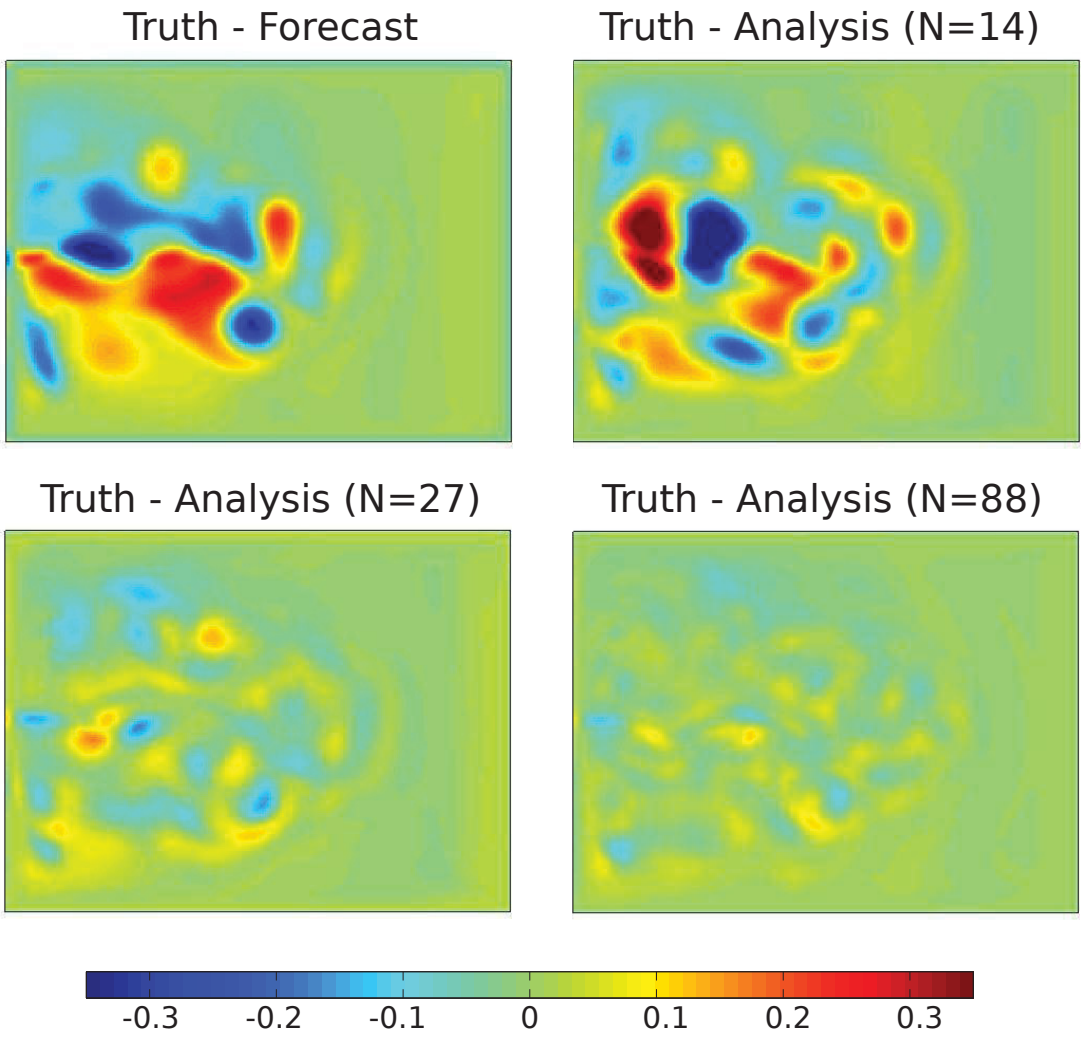

Figure A.2: Typical snapshots (day 200) of sea level difference between the truth and forecast (left top panel), the analysis using the small ensemble (right top panel), the medium ensemble (left bottom panel), and the large ensemble (right bottom panel).

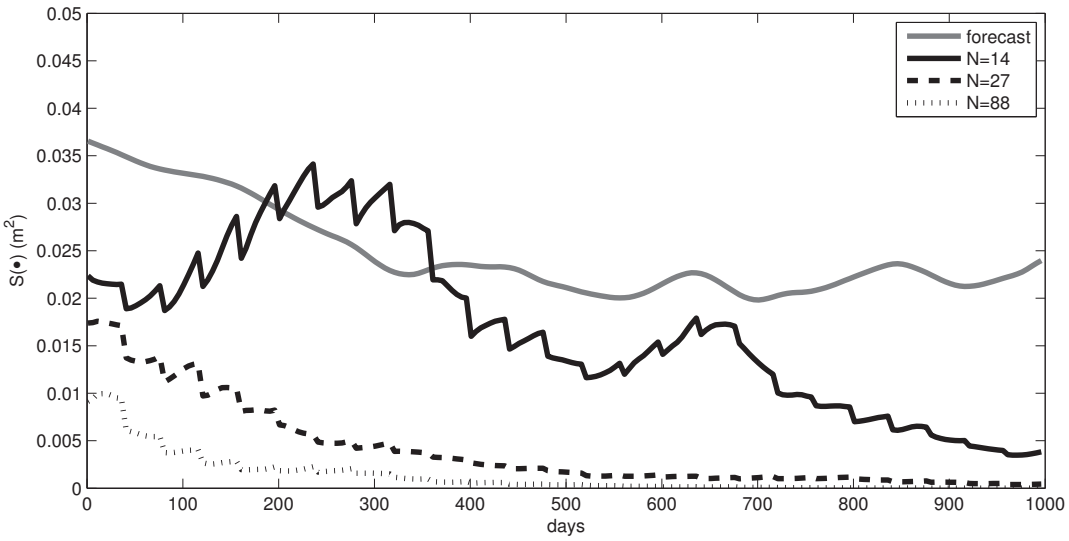

Figure A.3: Time variation of the mean square difference between the truth run and the forecast and the analysis runs, for different ensemble sizes.

APPENDIX B

COMPARISON OF TIDAL CURRENTS AND OBSERVATIONS

I now check the realism of the tidal current variations predicted by GoMSS and shown in Chapter 5 through comparison with current observations made by moored current meters and HF radar. I first define a simple metric that quantifies the discrepancy between observed and predicted error ellipses.

Define

$$\gamma^2 = \frac{\int_0^P |\mathbf{u}_{obs}(t) - \mathbf{u}_{mod}(t)|^2 \, dt}{\int_0^P |\mathbf{u}_{obs}(t)|^2 dt} \tag{B.1}$$

where P is the period of the tidal constituent of interest, and $\mathbf{u}_{obs}(t)$ and $\mathbf{u}_{mod}(t)$ are the observed and predicted, time-varying tidal currents respectively. Note that this scalar measure of fit takes into account errors in ellipse size and shape, inclination and phase, and corresponds to the GoMSS mean kinetic energy error scaled by the mean kinetic energy of the observations for a given frequency. In general γ^2 is bounded below by 0 and unbounded above. If $\gamma^2 << 1$ the model predicts well the observed tidal ellipse; if $\gamma^2 = 0$ the model is perfect. By way of contrast, if $\gamma^2 >> 1$ the predicted tidal ellipses are a poor representation of reality. $\gamma^2 = 1$ is the same as a prediction of no tidal current. Note however that it is straightforward to show that $\gamma^2 = 1$ can also result from a predicted ellipse that is perfect apart from an overestimation of amplitude by a factor of 2, or a phase error of 45°. Thus, $\gamma^2 \approx 1$ does not necessarily mean that the model has no prediction skill but rather the model may simply be overestimating the tidal amplitude, or subject to a phase or ellipse inclination error.

To compare the performance of Run2 and Run1 I use scatterplots of their γ^2 values with each plotted point corresponding to a location for which observed tidal ellipse information is available (e.g., Figure B.1). Assume γ^2_{Run1} is on the x-axis and γ^2_{Run2} is on the y-axis. If the points fall below the 1:1 line, then Run2 fits the observations better. In an absolute sense, a good model will have γ^2 values less than 1 (i.e., γ^2 to the left of $x = 1$ for Run1 and below $y = 1$ for Run2). Note that if the points cluster near the 1:1 line, the performance of the two models is very similar.

B.1 Model Evaluation using Moored Current Meter Observations

Observed tidal ellipse parameters estimated from current time series are used. The ellipse parameters are based on various Bedford Institute of Oceanography technical reports (*Drozdowski et al.*, 2002). I use only those parameters estimated from records that are at least 30 days long and have a known start date. Additionally, only observations near the surface (0-20 m) were used. For winter, observations that meet the above criteria are available only on the Scotian Shelf (15 locations shown in Figure 4.11). For summer, observations are available for Georges Bank, between Cape Sable and Georges Bank, and on the Scotian Shelf (19 locations shown in Figure 4.11).

The scatterplots of γ^2 for Run2 and Run1 are shown in Figure B.1 for winter (top panel) and summer (bottom panel). In winter there are locations with $\gamma^2 > 1$. However, visual comparison (not shown) of the observed and the predicted tidal ellipses reveals that the large γ^2 values in these location is due primarily to differences in phase and magnitude but, overall, the model still captures the shape and inclination of the observed tidal ellipses. Generally Run2 has smaller γ^2 than Run1 (most points are below the 1:1 line) indicating better perfomance of Run2 for all five constituents considered. In summer, γ^2 is generally smaller for both Run2 and Run1 for all the constituents. The difference between the two models is larger (increased spread of points) in summer; this is to be expected because stratification is enhanced in summer. Overall, the Run2 tidal currents are closer to observations than the Run1 currents in summer. Note that some of the discrepancies between the observed and Run2 tidal currents are due to interannual variability in the density fields (observations and predictions are generally for different years).

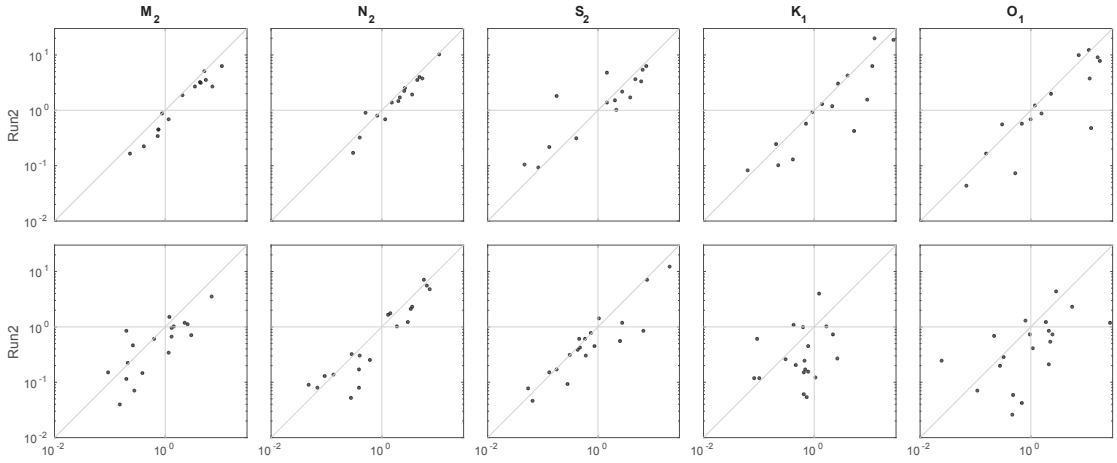

Figure B.1: Evaluation of the surface tidal currents predicted by Run2 and Run1. Model predictions are compared with ellipse parameters estimated from observed mooring data. Each panel is a scatterplot of γ^2 for Run1 (x-axis) and Run2 (y-axis). Results are shown for 5 tidal constituents. The top row is for winter and the bottom row is for summer. Run2 is for 2010 to 2012.

B.2 Model Evaluation using HF Radar Observations

Surface currents measured by three high frequency radar antennae in the Gulf of Maine (see Figure 4.11 for locations) were kindly provided to us by Dr Neil Fisher (University of Maine, 2014, personal communication). The present system is supported by the Northeastern Regional Association of Coastal and Ocean Observing Systems (NERACOOS) in partnership with the University of Maine. Hourly data were provided in two forms: velocities resolved along specific radii emanating from a given antenna ("radial" data) and also vector means formed from overlapping radial data ("total" data).

Hourly radial data measured by the Greens Island antenna (see Figure 5.7 for location and the four selected radii) were available for the summers and winters of 2011 to 2014. The size of the averaging bins is 4.53 km radially (maximum of 52 range bins) and $\pm 2^\circ$ with respect to direction. Hourly total data were available for the summers and winters of 2013 and 2014. The hourly total data are weighted averages of the radial data from the 3 antennae shown in Figure 4.11 and estimated only at the locations that the 3 antennae beams intercept. The hourly total data provide a surface velocity field presented on a 10 km grid. Note that because the averaging area of the radial data increases as the distance from the antennae increases, the amount of the smoothing that is applied to obtain the tidal data

varies across the grid. In the vicinity of the striations (for all the three antennae) the spatial averaging occurs on scales of around 20 km.

The M_2 tidal ellipses were estimated by harmonic analysis of the hourly total data. One of the challenges of the radial and total data sets is that there are far fewer hourly observations between about 8 pm and 6 am local time. To separate the three semi-diurnal constituents I only analyzed grid point time series with at least 662 hourly values (1500 in winter for the total data). The grid points that meet these criteria cover roughly the northeast part of the Gulf of Maine (Figure 4.11, gridded area).

The scatterplot of γ^2 for the surface M_2 currents predicted by Run2 and Run1, using the observed total velocity data, is shown in the left panels of Figure B.2. Both Run1 and Run2 are in good agreement with observed ellipses ($\gamma^2 < 1$) in winter and summer. Overall Run1 agrees better with the observations in both winter and summer. However, when the small scale variability (length scales less than 15 km) is spatially filtered from the velocities predicted by Run2, the performance of Run2 improves and matches that of Run1 (see right panels of Figure B.2).

One possible reason for the poorer perfomance of Run2 is the smoothing of small scale features in the observed surface currents: the total data have an averaging radius of 20 km in the vicinity of the striations and the distance between a consecutive maximum and minimum in the striations is about 20 km. The radial data are subject to less spatial smoothing and so they are used to evaluate the striations in Chapter 5

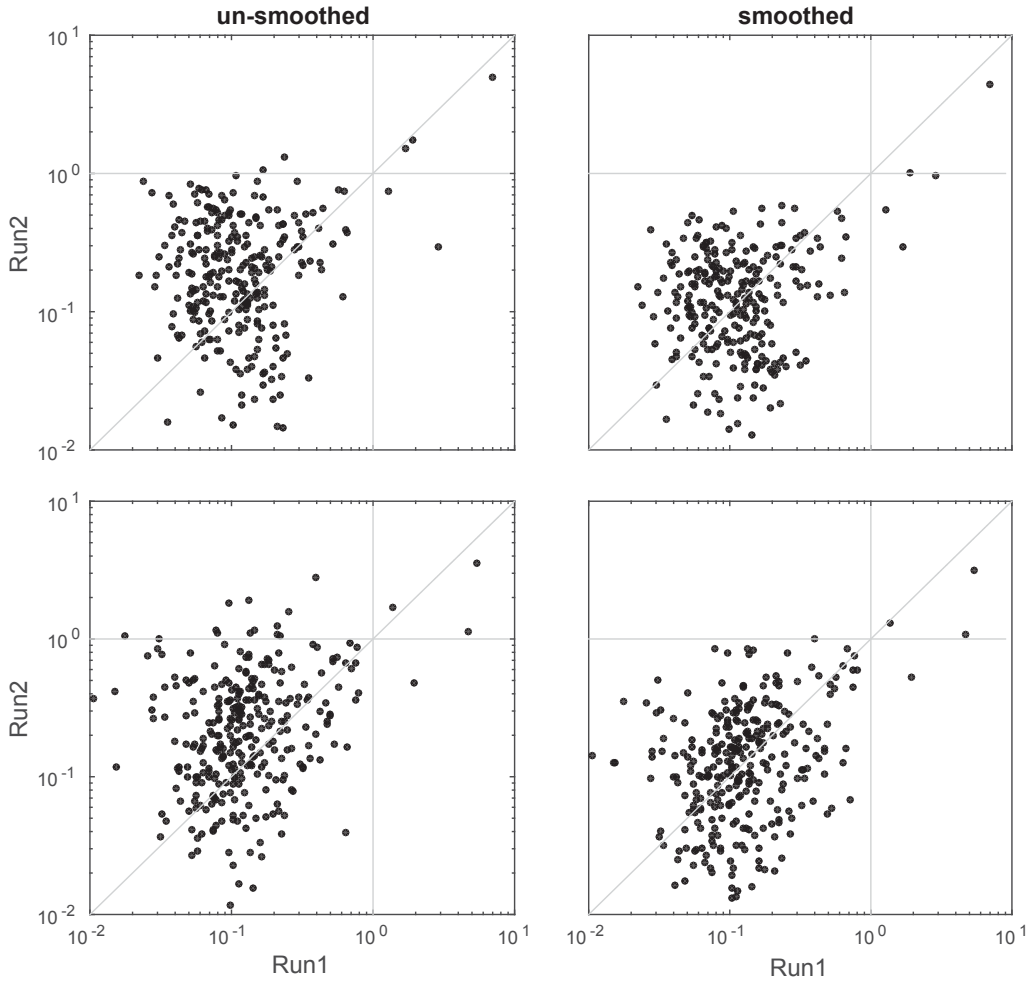

Figure B.2: Evaluation of the M_2 surface tidal currents predicted by Run2 and Run1 using the total radar data as observations. The left panels are for Run2 and the right panels are for Run2 after spatial smoothing of the surface flow fields as explained in the text. The top panels are for winter and the bottom panels are for summer. Run2 is for 2010 to 2012.

APPENDIX C

REGIONAL MODEL SEASONAL CYCLE: COMPARISON WITH CLIMATOLOGY

The monthly mean climatology produced by *Geshelin et al.* (1999) is used to validate the seasonal cycle of GoMSS. The Geshelin monthly climatology was calculated using a modified form of Barnes algorithm (*Barnes*, 1964) applied to all available hydrographic observations from the US National Oceanographic Data Center (NODC). Observations from three consecutive months were used, weighted based on their temporal distance (in days) relative to the mid-point of each month. The resulting monthly mean climatological fields are defined on to a 1/6° horizontal grid and 32 vertical levels. Only three years (2010-2012) of data are available from GoMSS and so some discrepancies with the observed climatology will be due to differences in averaging period. The winter is defined for January-March and the summer for July-September.

The comparison between the climatology, GoMSS and the global system annual temperature and salinity fields, is presented in Figures C.2 to C.13 (at the ocean surface, at 100 m depth and for 4 different sections shown in Figure C.1). Figures C.2 and C.3 show that off the shelf, the model simulates accurately the warm saline Slope Water. During winter, at the ocean surface, GoMSS captures the fresh (around 31), cold (around 2^{o}C) water on top of the Scotian Shelf. This water outflows from the Gulf of St. Lawrence and continues downstream along the Scotian Shelf. GoMSS simulates well the entrainment of this water into the Gulf of Maine, along the Scotian coast.

Figure C.3 shows that during summer, on the Scotian Shelf, GoMSS has fresher water

that extends further offshore than during winter. This is associated with the summer freshening of the outflow from the gulf of St. Lawrence. In summer, GoMSS surface temperature increases by about 15^oC on the Scotian Shelf, due to the heating of the ocean surface. Along the Nova Scotia coast, the presence of cold water is associated with upwelling events, that have been observed in previous studies (e.g, *Petrie et al.*, 1987). In the Gulf of Maine, along the coast, the presence of cold water is associated with transport from the Scotian shelf, local upwelling, intense tidal mixing and river discharge.

During summer the model simulates accurately the fresh water along the west coast in the Gulf of Maine (Figure C.3). This fresh water is probably associated with rivers run-off and is missing from the global system. This is because GoMSS and the global system have different river run-off. For the interior of the Gulf of Maine, at the surface, GoMSS generates slightly fresher water than the global system.

The GoMSS interface between warm, saline water off-shore and cold, fresh water on-shore is more complex than in the global system, due to higher horizontal resolution. Some discrepancies between the climatology, and GoMSS and the global system (e.g. the high temperature water in the west side of the Gulf of Maine) are probably due to local atmospheric effects during the 2010-2012 time period.

Figures C.4 and C.5 show that at 100 m depth the model does not generate any significant seasonal variability, as expected. For the north Scotian Shelf GoMSS predicts water with salinity around 33 and temperature around 1^oC, in agreement with the climatology. In the Laurentian Channel the GoMSS temperature and salinity are higher due to intrusion of Slope Water. In the Emerald Basin, at 100 m depth, the model simulates realistically the intrusion of warm, saline Slope Water. Additionally, the model captures the intrusion of warm off shore water into the Gulf of Maine through the Northeast channel. However, this intrusion is more intense in GoMSS than in the global system and the climatology.

To evaluate the model seasonal variability along the water column, I examine the temperature and salinity vertical profiles along 4 sections (shown in Figure C.1). In the Gulf of Maine, in winter, GoMSS predicts temperature and salinity that increase with depth (Figures C.6 and C.7) due to the intrusion of Slope Water through the Northeast Channel. During summer, a surface layer develops due to surface heating. In GoMSS, this warm layer extends down to the bottom on top of Georges Bank due to mixing generated by strong tidal currents. This summer feature is consistent with observations (e.g. *Loder*

et al., 1997; *Flagg*, 1987) but absent from the climatology, presumably due to lack of horizontal and vertical resolution. This feature is not captured accurately in the global system because it does not have tides.

Figures C.8 and C.9 show that for section S2, GoMSS is in good agreement with the climatology and the global system, and it captures well the seasonal cycle. GoMSS generates accurately the fresh cold water layer near the surface during winter, and in particular the very fresh water along the coast that is missing in the global system. Also, the model simulates well the warming of the surface layer and the upwelling along the coast, during summer.

Along S3 (Figures C.10 and C.11), GoMSS predicts relatively fresh and cold water above 100 m that extends to the shelf break in winter. Near the shore the water is colder (2°) and fresher (31) and consists mainly of outflow from the Gulf of St. Lawrence. During summer, a near surface layer of warm water develops due to surface heating, and the cold fresh water is confined to intermediate depths (40-100 m), consistent with the observed climatology and previous studies (e.g. *Loder et al.*, 1997, 2003). In summer, the near surface water is fresher than in winter, due to freshening of the outflow from the Gulf of St. Lawrence and the overall increase in river discharge. Below 100 m, GoMSS simulates the saline (34.5), warm (8-10°) water in Emerald Basin that comes from the slope region, consistent with observations (*Loder et al.*, 2003).

Figures C.12 and C.13 show that in section S4, GoMSS sea surface temperature and salinity varies with season; however below around 70 m depth, there is no profound seasonal cycle. In summer, at the surface, the temperature increases due to heating from the atmosphere. Additionally GoMSS surface salinity decreases (by around 1) along the coast of the Gulf of Maine, probably due to an increase in the river discharge during summer. This is consistent with the climatology. Overall, in S4 section GoMSS, the climatology and the global system generate similar results. GoMSS and the global system have warmer water filling the Emerald Basin and the deep areas of the Gulf of Maine than the climatology. This maybe associated with the different time periods that were used to estimate each fields.

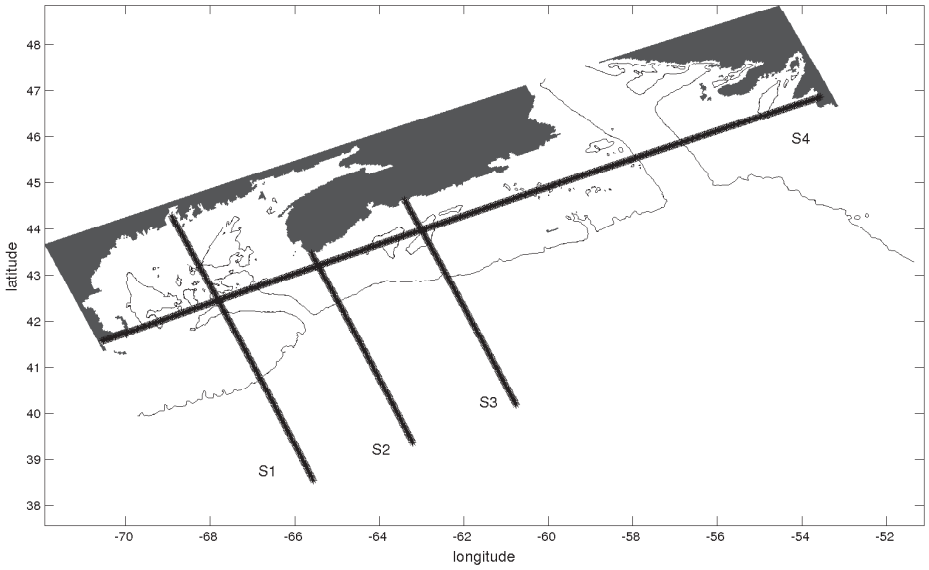

Figure C.1: The 4 sections for which the vertical profiles for temperature and salinity are presented.

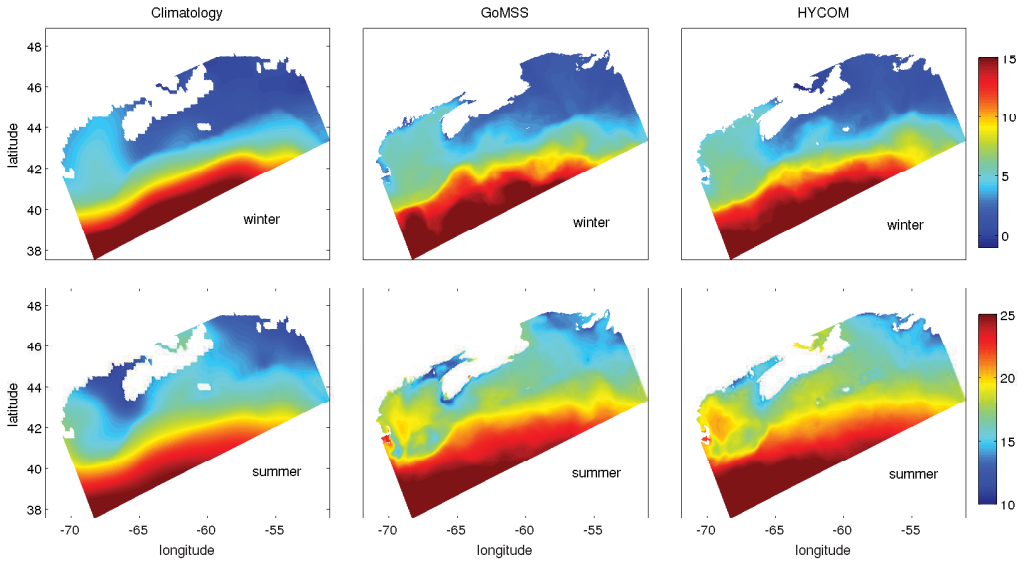

Figure C.2: The seasonal mean surface temperature from the climatology (left panels), GoMSS (middle panels) and the global system (right panels), during winter (top panels) and during summer (bottom panels).

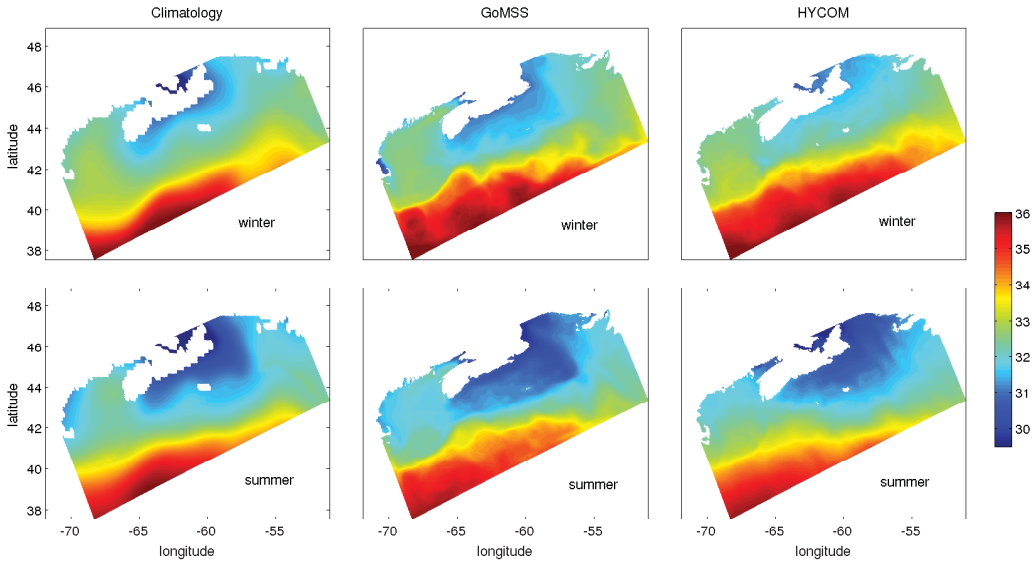

Figure C.3: Similar to Figure C.2 for salinity.

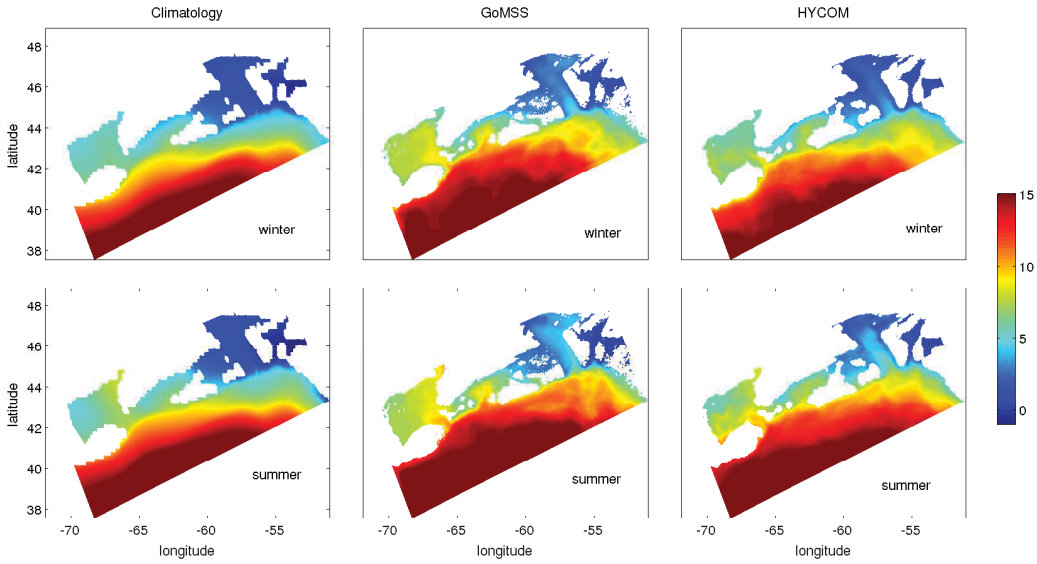

Figure C.4: The seasonal mean temperature from the climatology (left panels), GoMSS (middle panels) and the global system (right panels) at 100 m depth, during winter (top panels) and during summer (bottom panels).

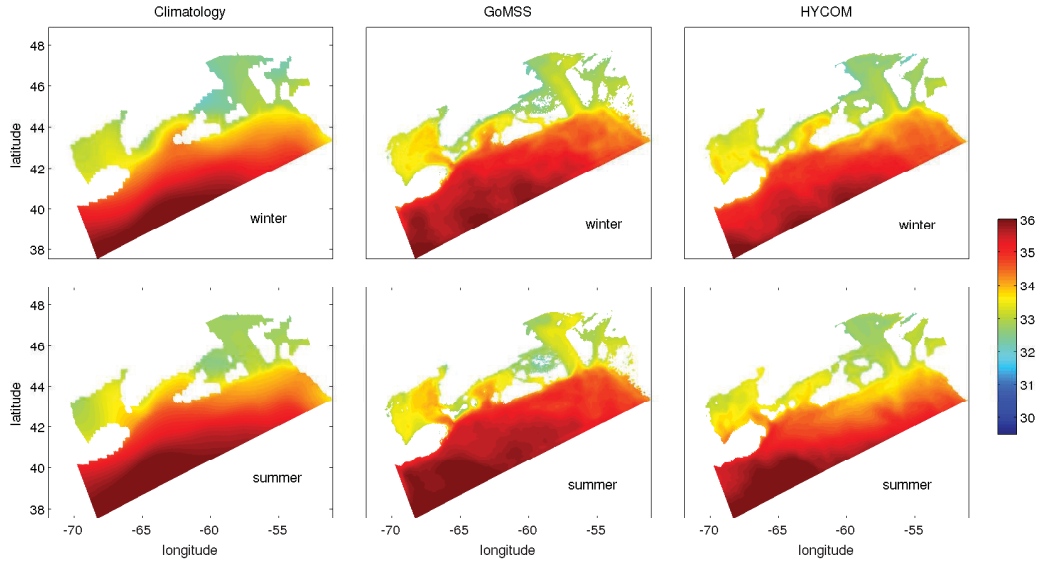

Figure C.5: Similar to Figure C.4 for salinity

.

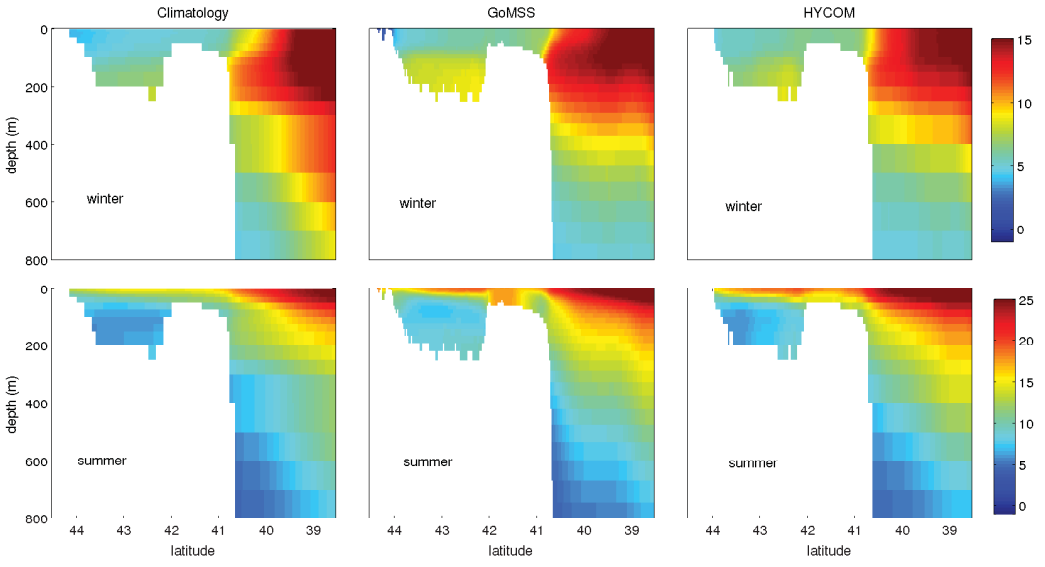

Figure C.6: The seasonal mean temperature profile along section S1, from the climatology (left panels), GoMSS (middle panels) and the global system (right panels), during winter (top panels) and during summer (bottom panels).

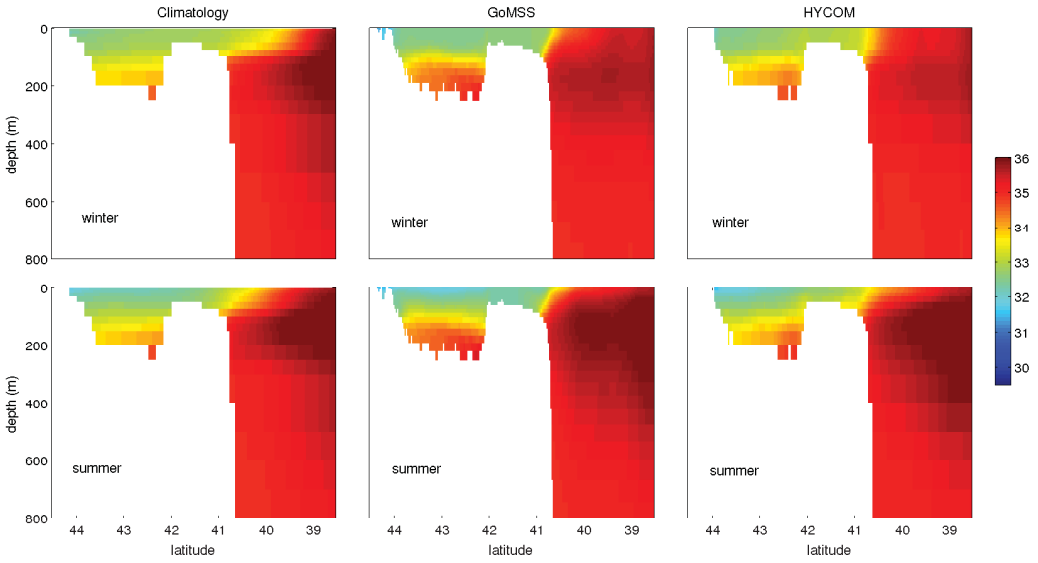

Figure C.7: The seasonal mean salinity profile along section S1, similar to Figure C.6.

.

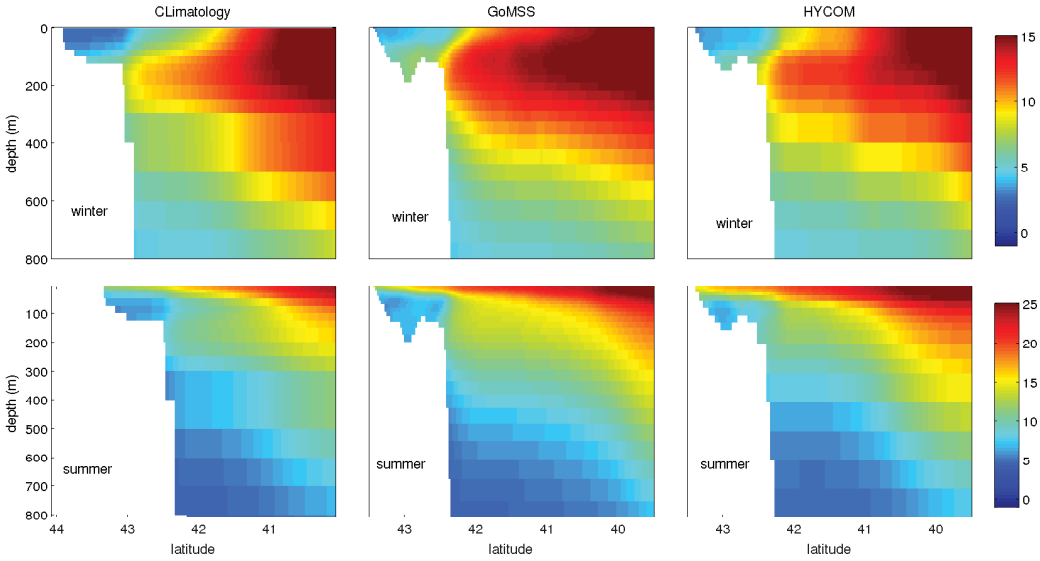

Figure C.8: The seasonal mean temperature profile along section S2, similar to Figure C.6.

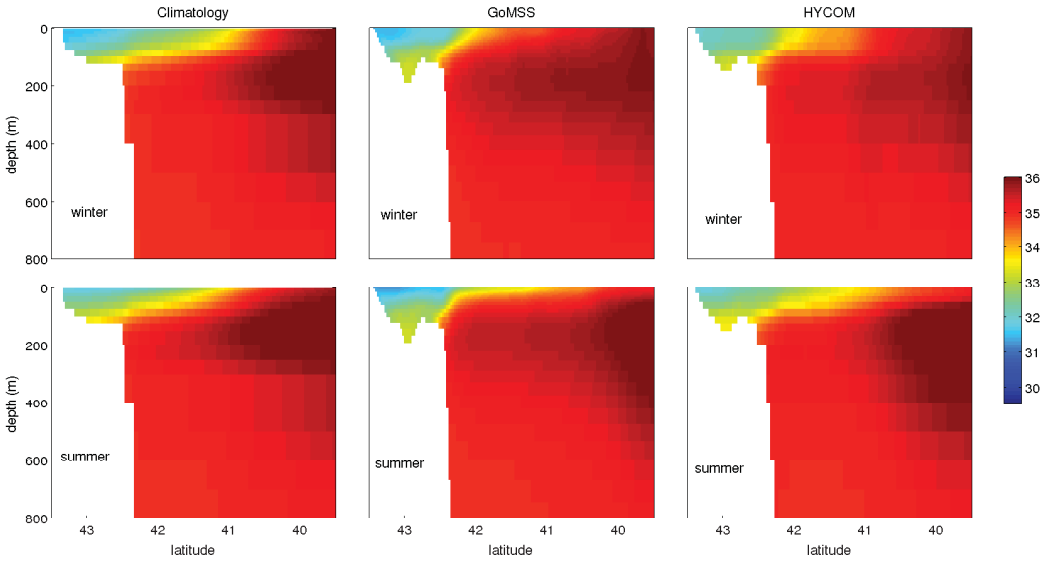

Figure C.9: The seasonal mean salinity profile along section S2, similar to Figure C.6.

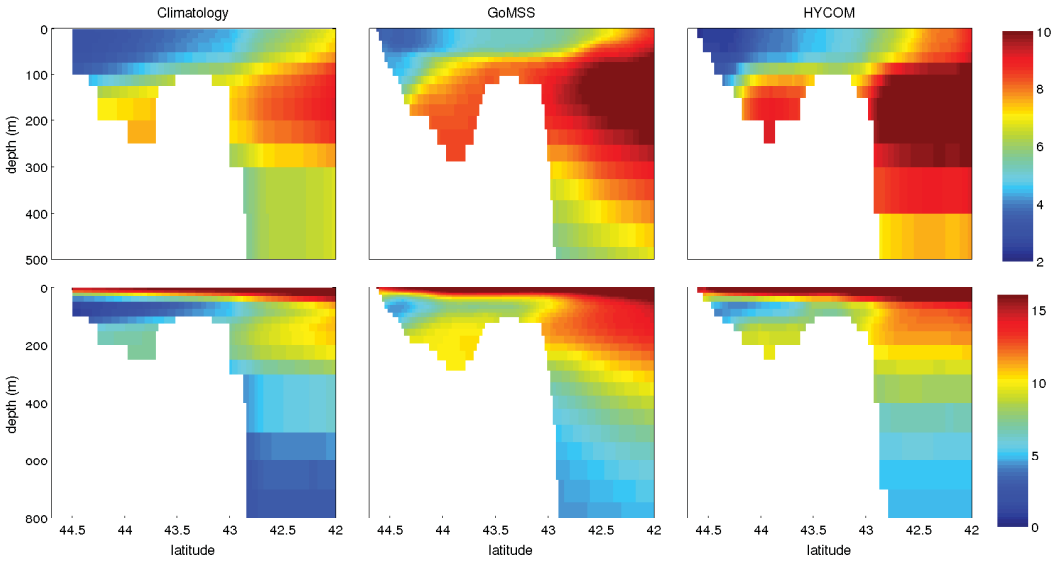

Figure C.10: The seasonal mean temperature profile along section S3, similar to Figure C.6.

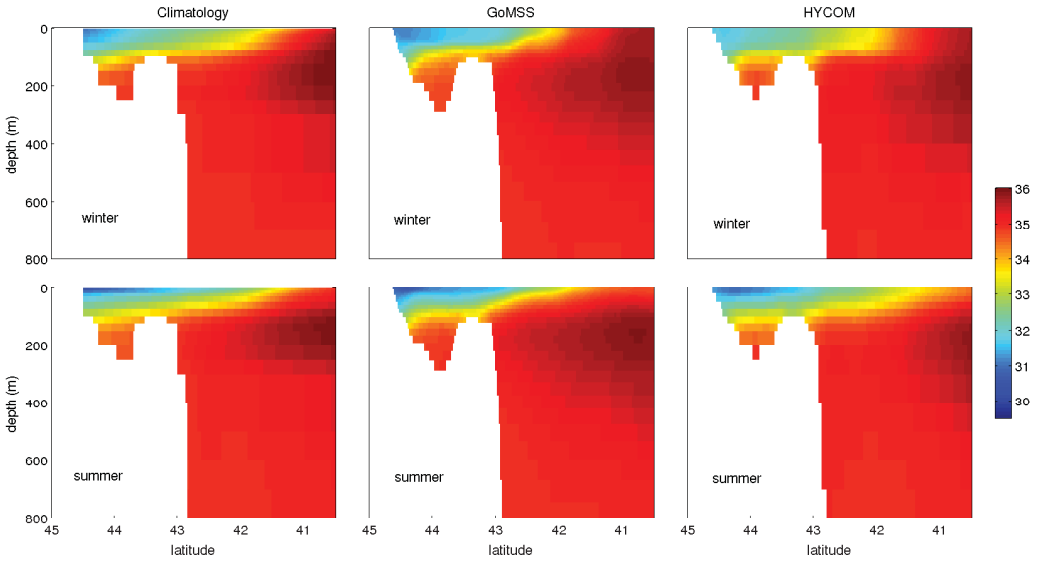

Figure C.11: The seasonal mean salinity profile along section S3, similar to Figure C.6.

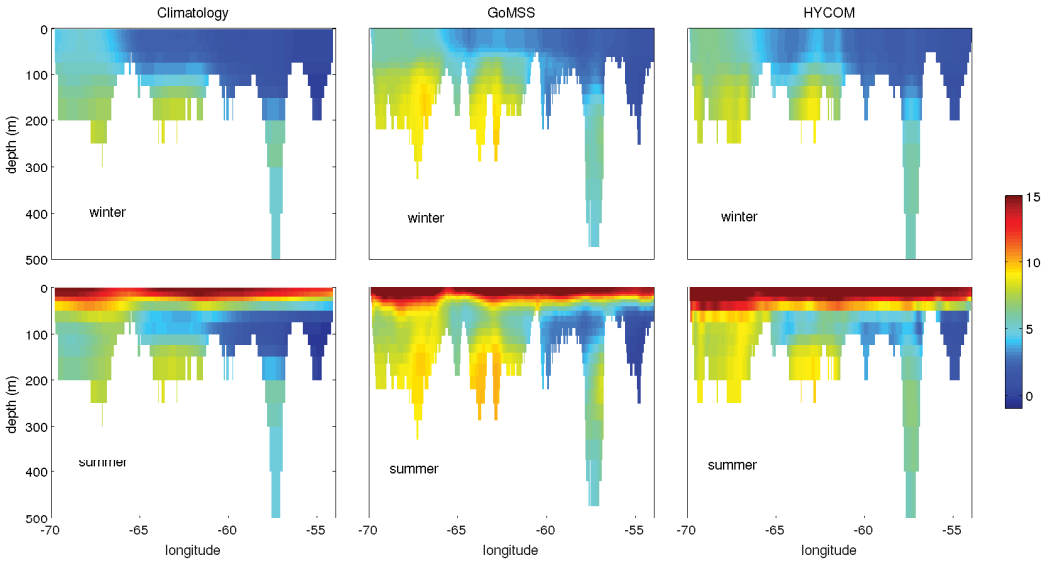

Figure C.12: The seasonal mean temperature profile along section S4, similar to Figure C.6.

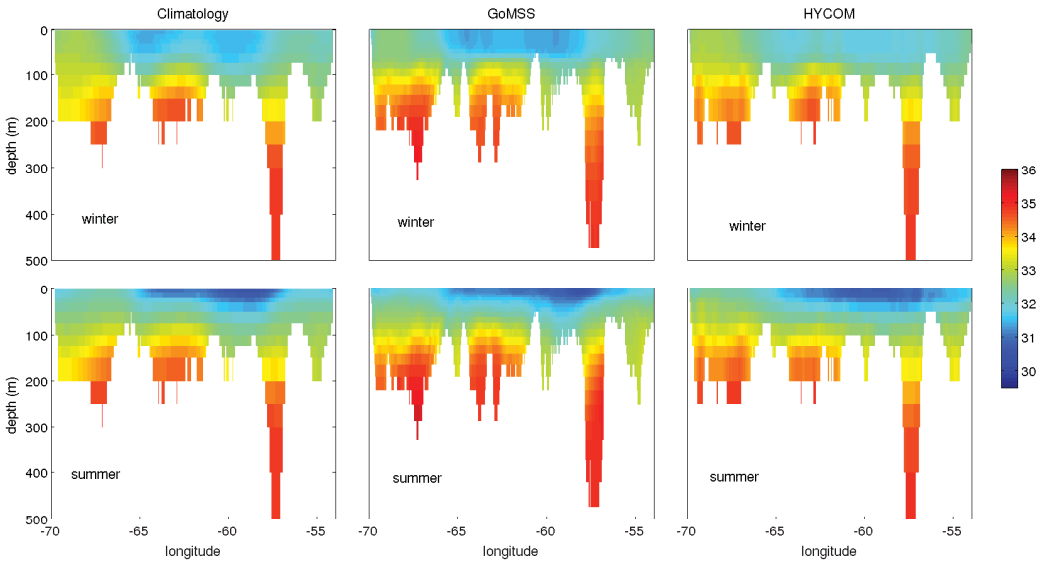

Figure C.13: The seasonal mean salinity profile along section S4, similar to Figure C.6.

APPENDIX D

AUTOCOVARIANCE AND POWER SPECTRAL DENSITY

To demonstrate how the autocovariance function is related to the power spectral density, assume the model predictions can be treated as a stationary random process with zero mean. The temporal autocovariance function of the model is then defined as

$$R(\tau) = E[X(t)X(t+\tau)] \tag{D.1}$$

where τ is the time lag, E denotes the expected value, and X is the field value (e.g. temperature, salinity) at a given time t and for a specific grid point. The Wiener-Khinchin theorem states that the covariance is related to the power spectral density (or frequency spectrum) by

$$R(\tau) = \int_{-\infty}^{+\infty} S(f)e^{2i\pi\tau f}\, df \tag{D.2}$$

where $S(f)$ is the power spectral density and f the frequency.

Similarly the spatial autocovariance function for lag χ is related to the wavenumber spectrum by

$$R(\chi) = \int_{-\infty}^{+\infty} S(k)e^{2i\pi\chi k}\, dk \tag{D.3}$$

where k is the wavenumber.

Equations (D.2) and (D.3) show that the spectrum and the autocovariance function form Fourier transform pairs. Thus, the more concentrated the spectrum the more spread out is the autocovariance function (uncertainty principle).

In this thesis I discuss results based on the autocorrelation functions r (i.e., autocovariance normalized by the variance), because I find it more intuitive.

APPENDIX E

SPECTRAL NUDGING IMPLEMENTED ONLY IN THE DEEP WATER

GoMSS generates more realistic hydrography, sea level and currents on the shelf than the global system because it has higher resolution, tides and better representation of the topography and coastlines, and is not affected by dynamical inconsistencies introduced through the assimilation of observations. As discussed in Chapter 6, when strong spectral nudging is applied on the shelf GoMSS inherits some unrealistic characteristics from the global system (e.g., a very fresh bottom layer in the Emerald Basin) that can degrade GoMSS^{+} accuracy. Thus, a scheme that implements spectral nudging only in the deep water, while allowing GoMSS dynamics to evolve freely on the shelf, may be beneficial.

This motivated me to conduct an experiment where spectral nudging is "switched off" on the shelf. This was achieved by setting γ as a function of bathymetry and depth:

$$\gamma(x,y,z) = \gamma_0 \phi(x,y) \left[\frac{z_{\text{max}} - z}{z_{\text{max}}}\right]^{\frac{1}{4}}$$

$$\phi(x,y) = \frac{1}{2}\left[1 + \tanh\left(\frac{h(x,y) - h_0}{\Delta h}\right)\right]$$

where γ_0 is a constant (i.e., the ratio of the nudging time step divided by the nudging relaxation time scale), $h(x,y)$ is the model bathymetry, h_0 is the bathymetry cutoff set equal to 2000 m, except along the Laurentian Channel where $h_0 = 350$m, Δh controls the smoothness of the transition between no-nudging and nudging areas and is set equal to 1200 m, z is the model depth and z_{max} is the maximum model depth (equal to 4000 m in the

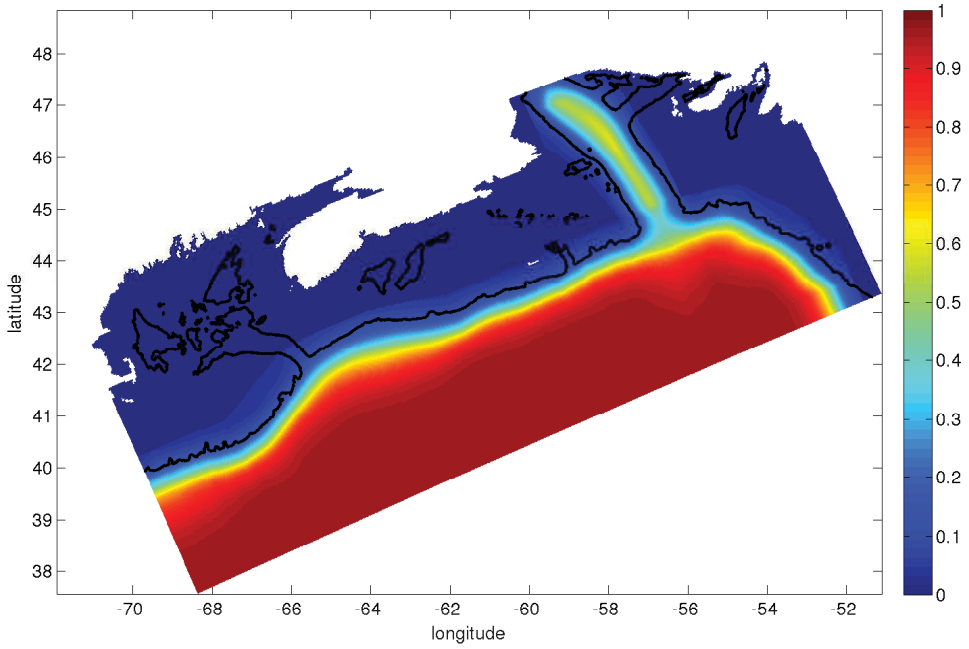

Figure E.1: Horizontal attenuation of γ ($\phi(x, y)$).

regional model). For smoother transitions, the regional model bathymetry was smoothed using a central moving average filter with a 100 km spatial window.

Figure E.1 illustrates the horizontal attenuation of γ ($\phi(x, y)$). Comparison between Figures E.1 and 6.7 shows that in this new experiment spectral nudging is only applied in the deep water and in a transition zone that extends around 50 km from the shelf break onto the shelf. The remaining parameters (i.e., γ_0, cutoff wavelength) are the same as the experiment discussed in Chapter 6 (see Table 6.1).

Limiting the spectral nudging in the deep water does not have a major impact on the GoMSS$^+$ accuracy off the shelf. Figure E.2 shows that spectral nudging eliminates the temperature and salinity decorrelation in the deep water. This is because, as expected, spectral nudging constrains the unrealistic internal variability and recirculation along the open lateral boundaries. Additionally, GoMSS$^+$ with no-nudging on the shelf generates more realistic hydrography, sea level and circulation in the deep water than GoMSS (e.g., comparison of Tables E.1 and 6.2).

The difference between the two GoMSS$^+$ runs (i.e., nudging and no-nudging on the

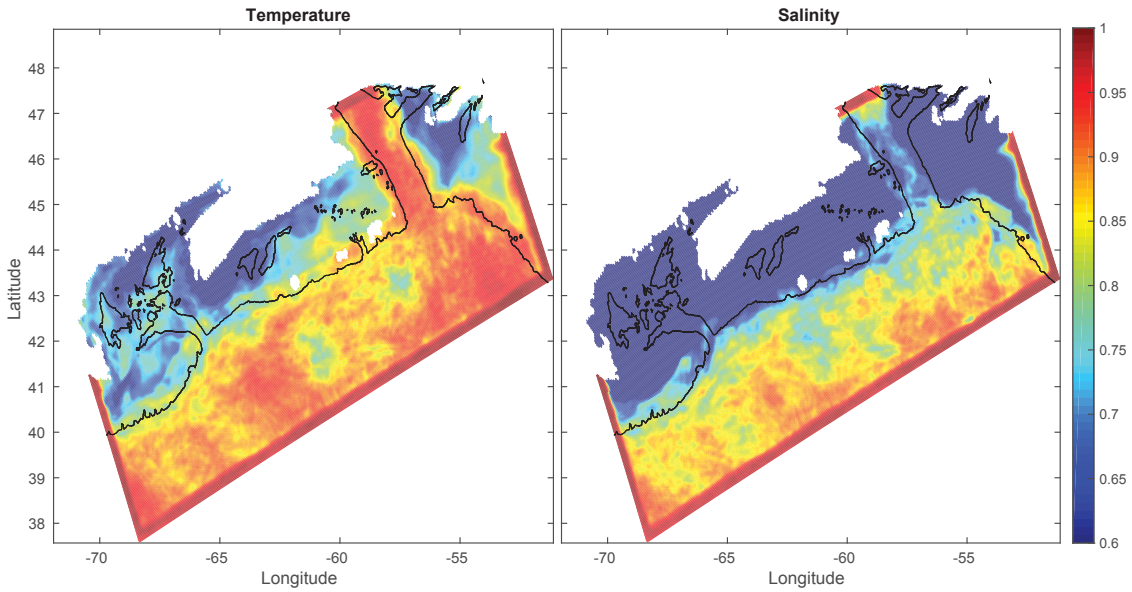

Figure E.2: Correlation of colocated temperature (left panel) and salinity (right panel) from the global system and GoMSS$^+$ with no-nudging on the shelf. The black lines show the 200 m isobath. Same format as Figure 6.5

Table E.1: Correlation between sea level from GoMSS$^+$ (with no-nudging on the shelf) and the satellite observations in the deep water, the shelf break and the shelf (areas separated by the horizontal lines in Figure 6.11). High frequency variability of all model output was removed using a Butterworth filter with a cutoff frequency of 20 days. Based on the time period 9 February 2010 to 23 January 2012.

Area	GoMSS$^+$
Shelf	0.62
Shelf break	0.55
Deep water	0.58

shelf) is more profound on the shelf. Figures E.3 and E.4 show 12 temperature and salinity profiles from CTD measurements, and predicted from GoMSS and GoMSS$^+$ with no-nudging on the shelf for six representative locations (C1 to C6, Figure 4.3). Comparison of Figures E.3, E.4, 6.15 and 6.16 shows that the run with no-nudging on the shelf generates sea surface temperature and salinity in better agreement with the observations than the run with nudging on the shelf and captures better the thermocline and halocline at all locations. Additionally the run with no-nudging on the shelf has, overall, smaller normalized mean square error than the run with nudging on the shelf (compare Tables E.2 and 6.3).

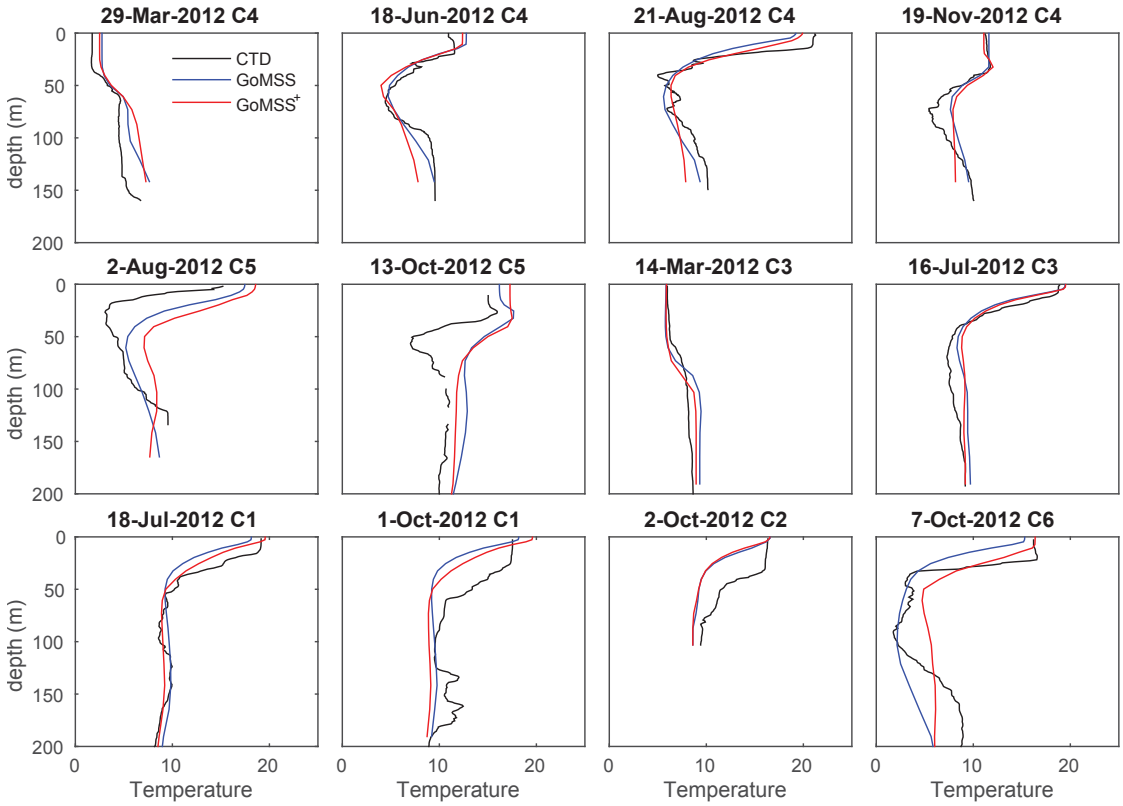

Figure E.3: Temperature vertical profiles from CTD measurements (black), and predictions by GoMSS (blue) and GoMSS$^+$ with no-nudging on the shelf (red). The six locations of the profiles are shown in Figure 4.3.

Table E.2: Normalized mean square error (NMSE) for GoMSS$^+$ with no-nudging on the shelf based on comparison with the observed temperature and salinity profiles for 2012 (Figure 5.19), binned over three depth ranges.

Depth range	Temperature	Salinity
0-20 m	0.10	0.34
21-100 m	0.35	0.37
>100 m	0.09	0.35

Turning to the variables that are not directly affected by spectral nudging, comparison of Tables E.1 and 6.2 shows that "switching off" the nudging on the shelf leads to sea levels that are in better agreement with the observations on the shelf. The seasonal currents of GoMSS$^+$ with no-nudging on the shelf are very similar to GoMSS on the shelf as expected, and similar to GoMSS$^+$ in the deep water (not shown).

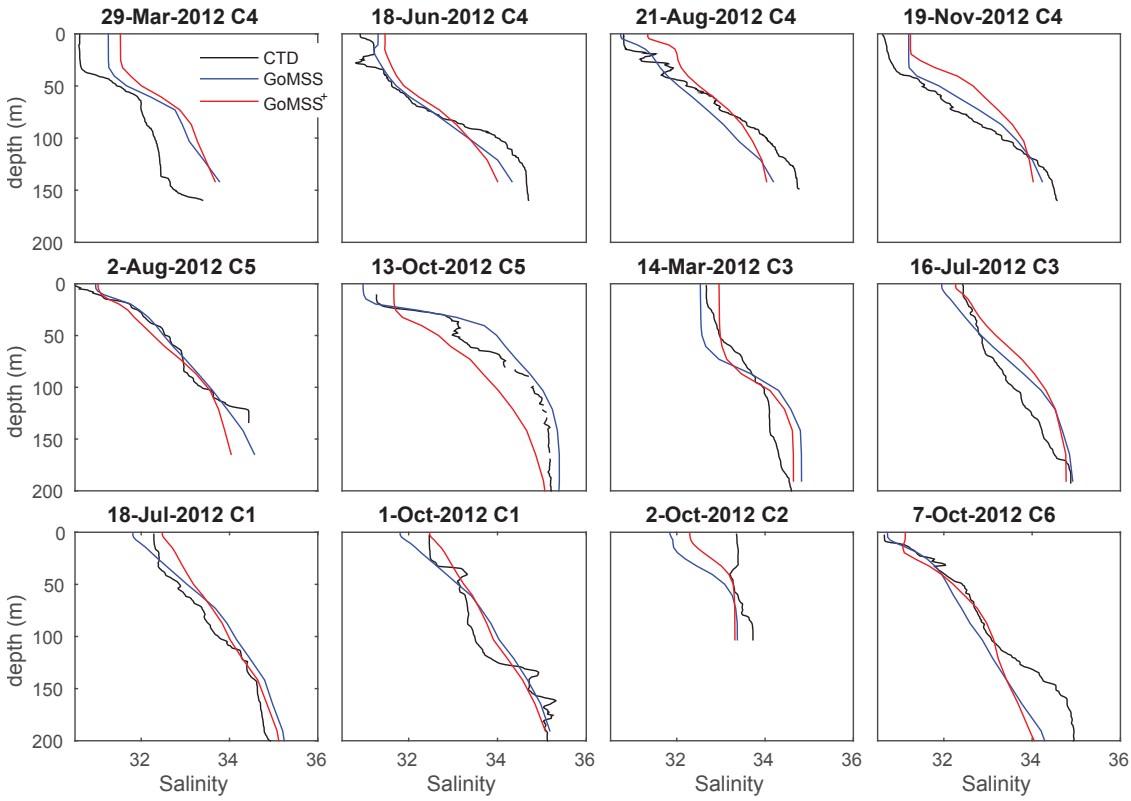

Figure E.4: Salinity vertical profiles from CTD measurements (black), GoMSS (blue) and predictions by GoMSS$^+$ with no-nudging on the shelf (red). The six locations of the profiles are shown in Figure 4.3.

Enstrophy and energy spectra from the line in the deep water (blue line Figure 6.23) from GoMSS$^+$ with no-nudging on the shelf (not shown) show that it generates very similar spectra with GoMSS$^+$ with nudging on the shelf, and that it has more variability than the global system and GoMSS for length scales between 100 and 10 km. This confirms that GoMSS$^+$ with no-nudging on the shelf has more energetic eddies and finer scale details than the global system and GoMSS in the deep water.

Overall, GoMSS$^+$ with no-nudging on the shelf generates more realistic fields in the deep water than GoMSS (similar to GoMSS$^+$ with nudging on the shelf). However on the shelf, the run with no-nudging on the shelf generates better fields than the run with nudging on the shelf. This suggests that allowing GoMSS$^+$ fields to evolve freely on the shelf based on the model dynamics (i.e., no nudging) leads to overall better results.

BIBLIOGRAPHY

Adlandsvik, B., and M. Bentsen, Downscaling a twentieth century global climate simulation to the North Sea, *Ocean Dyn.*, *57*, 453–466, 2007.

Alexandru, A., R. de Elia, R. Laprise, L. Separovic, and S. Biner, Sensitivity study of regional climate model simulations to large-scale nudging parameters, *Mon. Wea. Rev.*, *137*, 1666–1686, 2009.

Baines, P. G., The generation of internal tides by flat-bump topography, *Deep-Sea Res.*, *20*, 179–205, 1973.

Barnes, S. L., A technique for maximizing details in numerical weather map analysis, *J. Appl. Meteor.*, *3*, 396–409, 1964.

Barron, C. N., and L. F. Smedstad, Global river inflow withing the Navy Coastal Model, *Proceedings of the Oceans 2002 MTS/IEEE Conference*, Biloxi, MS, USA, 2002.

Blanke, B., and S. Raynaud, Kinematics of the Pacific Equatorial Undercurrent: An Eulerian and Lagrangian approach from GCM results, *J. Phys. Oceanogr.*, *27*, 1038–1053, 1997.

Blayo, E., and L. Debreu, Revisiting open boundary conditions from the point of view of characteristic variables, *Ocean Modell.*, *9*, 231–252, 2005.

Bleck, R., An oceanic general circulation model framed in hybrid isopycnal-Cartesian coordinates, *Ocean Modell.*, *4*, 55–88, 2002.

Brickman, D., and J. W. Loder, Energetics of the internal tide on northern Georges Bank, *J. Phys. Oceanogr.*, *23*, 409–424, 1993.

Brooks, D. A., Vernal circulation in the Gulf of Maine, *J. Geophys. Res.*, *90*, 4687–4706, 1985.

Brown, W. S., and J. D. Irish, The annual variation of water mass structure in the Gulf of Maine:1986-1987, *J. Mar. Res.*, *51*, 53–107, 1993.

Burnett, W., J. Harding, and G. Heburn, Overview of operational ocean forecasting in the US Navy: Past, present and furure, *Oceanography*, *15*, 4–12, 2002.

Butman, B., R. C. Beardsley, B. Magnell, D. Frye, J. A. Vermersch, R. Schlitz, R. Limeburner, W. R. Wright, and M. A. Noble, Recent observations of the mean circulation on Georges Bank, *J. Phys. Oceanogr.*, *12*, 569–591, 1982.

Capet, X., J. C. McWilliams, M. J. Molemaker, and A. F. Shchepetkin, Mesoscale to submesoscale transition in the California Current system. Part III: energy balance and flux, *J. Phys. Oceanogr.*, *38*, 2256–2269, 2008.

Carnes, M. R., Description and evaluation of GDEM-V 3.0, *Memorandum report*, Naval Research Laboratory, Stennis Space Center, 2009.

Caya, D., and S. Biner, Internal variability of RCM simulations over an annual cycle, *Climate Dyn.*, *22*, 33–46, 2004.

Chassignet, E. P., H. E. Hurlburt, O. M. Smedstad, G. R. Halliwell, P. J. Hogan, A. J. Wallcraft, R. Baraille, and R. Bleck, The HYCOM (HYbrid Coordinate Ocean Model) data assimilative system, *J. Mar. Syst.*, *65*, 60–83, 2007.

Chassignet, E. P., H. E. Hurlburt, E. J. Metzger, O. M. Smedstad, J. A. Cummings, G. R. Halliwell, R. Bleck, R. Baraille, A. J. Wallcraft, C. Lozano, H. L. Tolman, A. Srinivasan, S. Hankin, P. Cornillon, R. Weisberg, A. Barth, R. He, F. Werner, and J. Wilkin, US GODAE global ocean prediction with the HYbrid Coordinate Ocean Model (HYCOM), *Oceanography*, *22*, 64–75, 2009.

Chen, C., H. Huang, R. C. Beardsley, Q. Xu, R. Limeburner, G. W. Cowles, Y. Sun, J. Qi, and H. Lin, Tidal dynamics in the Gulf of Maine and New England Shelf: An appliction of FVCOM, *J. Geophys. Res.*, *116*, 2011.

Cooper, M., and K. Haines, Altimetric assimilation with water property conservation, *J. Geophys. Res.*, *101*, 1059–1077, 1996.

Cummings, J. A., Operational multivariate ocean data assimilation, *Quart. J. Roy. Meteor. Soc.*, *131*, 3583–3604, 2005.

Cummings, J. A., and O. M. Smedstad, Variational data assimilation for the global ocean, in *Data Assimilation for Atmospheric, Oceanic and Hydrologic Applications Vol II*, edited by S. K. Park and L. Xu, pp. 303–343, Springer, 2013.

Cummins, P. F., D. Masson, and M. G. G. Foreman, Stratification and mean flow effects on diurnal tidal currents off Vancouver Island, *J. Phys. Oceanogr.*, *30*, 15–30, 2000.

Daifuku, P. R., and R. C. Beardsley, The K_1 tide on the continental shelf from Nova Scotia to Cape Haterras, *J. Phys. Oceanogr.*, *13*, 3–17, 1983.

Davies, H. C., A lateral boundary formulation for multi-level prediction models., *Quart. J. Roy. Meteor. Soc.*, *102*, 405–418, 1976.

de Elia, R., R. Laprise, and B. Denis, Forecasting skill of nested limited-area models: a perfect model approach, *Mon. Wea. Rev.*, *130*, 2006–2023, 2002.

Deleersnijder, E., and P. F. J. Lermusiaux, Multi-scale modeling: nested-grid and unstructured-mesh approaces, *Ocean Dyn.*, *58*, 335–336, 2008.

Dengo, J., The problem of Gulf Stream seperation: a barotropic approach, *J. Phys. Oceanogr.*, *23*, 2182–2200, 1993.

Denis, B., R. Laprise, D. Caya, and J. Côté, Downscaling ability of one-way nested regional climate models: The big-brother experiment, *Climate Dyn.*, *18*, 627–646, 2002.

Drinkwater, K. F., B. Petrie, and W. H. Sutcliffe, Seasonal geostrophic volume transports along the Scotian Shelf, *Estuarine Coastal Mar. Sci.*, *9*, 17–27, 1979.

Drozdowski, A., C. G. Hannah, and J. W. Loder, The northwest Atlantic tidal current database, *Can. Tech. Rep. Hydrogr. Ocean Sci. 222*, Department of Fisheries and Oceans, Bedford Institute of Oceanography, Darmouth, NS, Canada, 2002.

Evensen, G., Advanced data assimilation for strongly nonlinear dynamics, *Mon. Wea. Rev.*, *125*, 1342–1354, 1997.

Evensen, G., The Ensemble Kalman Filter: theoretical formulation and practical implementation, *Ocean Dyn.*, *53*, 343–367, 2003.

Ferrari, R., and C. Wunsch, Ocean circulation kinetic energy: reservoirs, sources and sinks, *Annu. Rev. Fluid Mech.*, *41*, 253–282, 2009.

Flagg, C. N., Hydrographic structure and variability, in *Georges Bank*, edited by R. H. Backus and D. W. Bourne, pp. 108–124, MIT Press, Cambridge, 1987.

Flather, R. A., A tidal model of the northwest European continental shelf, *Mem. Soc. R. Sci. Liege*, *10*, 141–164, 1976.

Fox, D. N., W. J. Teague, C. N. Barron, M. R. Carnes, and C. M. Lee, The Modular Ocean Data Assimilation System (MODAS), *J. Atmos. Oceanic Technol.*, *19*, 240–252, 2002.

Garrett, C. J., Tidal resonance in the Bay of Fundy and Gulf of Maine, *Nature*, *238*, 441–443, 1972.

Gaspari, G., and S. E. Cohn, Construction of correlation functions in two and three dimensions, *Quart. J. Roy. Meteor. Soc.*, *125*, 723–757, 1999.

Geshelin, Y., J. Sheng, and R. J. Greatbatch, Monthly mean climatologies of temperature and salinity in the western North Atlantic, *Canadian Data Report of Hydrography and Ocean Sciences 153*, Department of Fisheries and Oceans, Bedford Institute of Oceanography, Darmouth, NS, Canada, 1999.

Gill, A. E., *Atmosphere-Ocean*, Academic Press, 1982.

Giorgi, F., and X. Bi, A study of internal variability of a regional climate model, *J. Geophys. Res.*, *105*, 29503–29521, 2000.

Greenberg, D. A., Modelling the mean barotropic circulation in the Bay of Fundy and Gulf of Maine, *J. Phys. Oceanogr.*, *13*, 886–904, 1983.

Griffies, S. M., Chapter 2: Some ocean model fundamentals, in *Ocean Weather Forecasting*, edited by E. P. Chassignet and J. Verron, pp. 19–73, Springer, Netherlands, 2006.

Griffies, S. M., M. Winton, B. Samuels, G. Danabasoglu, S. Yeager, S. Marsland, and H. Drange, Dataset and protocol for the CLIVAR WGOMD Coordinate Ocean-sea ice Reference Experiment (COREs), *WCRP report 21*, 2012.

Griffies, S. M., A. Gnanadesikan, K. W. Dixon, J. P. Dunne, R. Gerdes, M. J. Harrison, A. Rosati, J. L. Russel, B. L. Samuels, M. J. Spelman, M. Winton, and R. Zhang, Formulation of an ocean model for global climate simulation, *Ocean Sci.*, *1*, 45–79, 2005.

Haines, K., Ocean data assimilation, in *Data Assimilaton: Making Sense of Observations*, edited by W. A. Lahoz, B. Khattatov, and R. Ménard, pp. 517–547, Springer, 2010.

Han, G., C. G. Hannah, J. W. Loder, and P. C. Smith, Seasonal variation of the three-dimensional mean circulation over the Scotian Shelf, *J. Geophys. Res.*, *102*, 1011–1025, 1997.

Han, G., P. Roussel, and J. W. Loder, Modeling tidal currents and seasonal-mean circulation in the Sable Gully region, in *Estuarine and Coastal Modeling: Proceedings of the seventh International ASCE Conference*, pp. 22–34, American Society of Civil Engineers, Petersburg, FL, 2001.

Han, G., J. W. Loder, and B. Petrie, Tidal and non-tidal sea level variability along the coastal Nova Scotia from satellite altimetry, *Int. J. of Rem. Sens.*, *31*, 4791–4806, 2010.

Hannah, C. G., J. A. Shore, J. W. Loder, and C. E. Naimie, Seasonal circulation on the western and central Scotian Shelf, *J. Phys. Oceanogr.*, *31*, 591–615, 2001.

Hebert, D., R. Pettitas, D. Brickman, and M. Dever, Meteorological, sea ice and physical oceanographic conditions on the Scotian Shelf and in the Gulf of Maine during 2012, *DFO Can. Sci. Advis. Sec. Res. Doc. 2013/058*, Bedforf Institute of Oceanography, Darmouth, Nova Scotia, Canada, 2013.

Henshaw, W., H. . Kreiss, and J. Ystrom, Numerical experiments on the interaction between the large- and small-scale motions of the Navier-Stokes equations., *Multiscale Model. Simul.*, *1*, 119–149, 2003.

Higginson, S., K. R. Thompson, J. Huang, M. Véronneau, and D. G. Wright, The mean surface circulation of the North Atlantic subpolar gyre: A comparison of estimates derived from new gravity and oceanographic measurements, *J. Geophys. Res.*, *116*, C08016, 2011.

Holland, W. R., The role of mesoscale eddies in the general circulation of the ocean - numerical experiments using a wind-driven quasi-geostrophic model, *J. Phys. Oceanogr.*, *8*, 363–392, 1978.

Houtekamer, P. L., and H. L. Mitchell, Data assimilation using and Ensemble Kalman Filter technique, *Mon. Wea. Rev.*, *126*, 796–811, 1998.

Howarth, M. J., The effect of stratification on tidal current profiles., *Cont. Shelf Res.*, *18*, 1235–1254, 1998.

Kelly, K. A., L. Thompson, W. Cheng, and E. J. Metzger, Evaluation of HYCOM in the Kuroshio Extention region using new metrics, *J. Geophys. Res.*, *112*, C01004, 2007.

Lamb, K. G., Numerical experiments of internal wave generation by strong tidal flow across a finite amplitude edge, *J. Geophys. Res.*, *99*, 843–864, 1994.

Laprise, R., Resolved scales and nonlinear interactions in limited-area models, *J. Atmos. Sci.*, *60*, 768–779, 2003.

Laprise, R., D. Kornic, M. Rapaic, L. Separovic, M. Leduc, O. Nikiema, A. D. Luca, E. Diaconescu, A. Alexandru, P. Lucas-Picher, R. de Elia, D. Caya, and S. Biner, Considerations of domain size and large-scale driving for nested regional climate models: impact on internal variability and ability at developing small-scale details, in *Climate Change: Inferences from Paleoclimate and Regional Aspects*, edited by A. Berger, F. Mesinger, and D. Sijacki, Springer, Heidelberg (2012), 2012.

Laurent, L. S., S. Stringer, C. Garrett, and D. Perrault-Joncas, The generation of internal tides at abrupt topography, *Deep-Sea Res. Part I*, *50*, 987–1003, 2003.

LaViolette, P. E., D. R. Johnson, and D. A. Brooks, Sun-glitter photographs of Georges Bank and the Gulf of Maine from the space shuttle, *Oceanography*, *3*, 43–49, 1990.

LeTraon, P. Y., P. Klein, B. L. Hua, and G. Dibarboure, Do altimeter wavenumber spectra agree with the interior of surface quasigeostrophic theory?, *J. Phys. Oceanogr.*, *38*, 1137–1142, 2008.

Levier, B., A. M. Treguier, G. Madec, and V. Garnier, Free surface and variable volume in the NEMO code, *MERSEA IP report WP09-CNRS-STR-03-1A*, 2007.

Loder, J. W., Topographic rectification of tidal currents on the sides of Georges Bank, *J. Phys. Oceanogr.*, *10*, 1399–1416, 1980.

Loder, J. W., and E. P. W. Horne, Skew eddy fluxes as signatures of non-linear tidal current interactions, with application to Georges Bank, *Atmos. Ocean*, *29*, 517–546, 1991.

Loder, J. W., and D. G. Wright, A depth-dependent study of the topographic rectification of tidal currents, *Geophys. Astrophys. Fluid Dyn.*, *31*, 169–220, 1985.

Loder, J. W., D. Brickman, and E. P. W. Horne, Detailed structure of currents and hydrography on the northern side of Georges Bank, *J. Geophys. Res.*, *97*, 14331–14351, 1992.

Loder, J. W., G. Han, C. G. Hannah, D. A. Greenberg, and P. C. Smith, Hydrography and baroclinic circulation in the Scotian Shelf region: winter versus summer, *Can. J. Fish. Aquat. Sci.*, *54*, 40–56, 1997.

Loder, J. W., B. Petrie, and G. Gawarkiewicz, Chapter 5, the coastal ocean off northeastern North America: A large-scale view, in *The sea*, edited by A. R. Robinson and K. H. Brink, vol. 11, pp. 105–133, John Wiley and Sons, Inc., 1998.

Loder, J. W., C. G. Hannah, B. D. Petrie, and E. A. Gonzalez, Hydrographic and transport variability on the Halifax section, *J. Geophys. Res.*, *108*, 2003.

Lyard, F., F. Lefevre, T. Letellier, and O. Francis, Modelling the global ocean tides: modern insight from FES2004, *Ocean Dyn.*, *56*, 394–415, 2006.

Lynch, D. R., J. T. C. Ip, C. E. Naimie, and F. E. Werner, Comprehensive coastal circulation model with application to the Gulf of Maine, *Cont. Shelf Res.*, *16*, 875–906, 1996.

Madec, G., NEMO ocean engine., *Note du Pole de modélisation 27 ISSN*, Institut Pierre-Simon Laplace (IPSL), France, 2008.

Madec, G., P. Delecluse, M. Imbard, and C. Levy, OPA8.1 ocean general circulation model reference manual, *Note du Pole de modélisation 11*, Institut Pierre-Simon Laplace (IPSL), France, 1998.

Marchesiello, P., J. C. McWilliams, and A. Shchepetkin, Open boundary conditions for long-term integration of regional oceanic models., *Ocean Modell.*, *3*, 1–20, 2001.

Marsden, R. F., The internal tide on Georges Bank, *J. Mar. Res.*, *44*, 35–50, 1986.

Mason, E., J. Molemaker, A. F. Shchepetkin, F. Colas, J. C. McWilliams, and P. Sangrà, Procedures for offline grid nesting in regional ocean models, *Ocean Modell.*, *35*, 1–15, 2010.

McCalpin, J. D., On the adjustment of azimuthally perturbed vortices, *J. Geophys. Res.*, *92*, 8213–8225, 1987.

McCalpin, J. D., The statistics and sensitivity of a double-gyre model: the reduced-gravity, quasigeostrophic case, *J. Phys. Oceanogr.*, *25*, 806–824, 1995.

McCalpin, J. D., and D. B. Haidvogel, Phenomenology of the low-frequency variability in a reduced-gravity quasigeostrophic double-gyre model, *J. Phys. Oceanogr.*, *26*, 739–752, 1996.

Metzger, E. J., H. E. Hurlburt, A. J. Wallcraft, J. F. Shriver, and L. F. Smedstad, Validation test report for the global ocean prediction system v3.0-1/12° HYCOM/NCODA: Phase I, *Memorandum report*, Naval Research Laboratory, Stennis Space Center, 2008.

Miguez-Macho, G., G. L. Stenchikov, and A. Robock, Spectral nudging to eliminate the effects of domain position and geometry in regional climate model simulations, *J. Geophys. Res.*, *109*, D13, 2004.

Miguez-Macho, G., G. L. Stenchikov, and A. Robock, Regional climate simulations over the North America: interaction of local processes with improved large-scale flow, *J. Climate*, *18*, 1227–1246, 2005.

Mitchell, H. L., P. L. Houtekamer, and G. Pellerin, Ensemble size, balance , and model-error representation in an Ensemble Kalman Filter*, *Mon. Wea. Rev.*, *130*, 2791–2808, 2002.

Molines, J. M., B. Barnier, T. Penduff, A. M. Treguier, and J. L. Sommer, ORCA12.L46 climatological and interannual simulations forced with DFS4.4: GJM02 and MJM88, *Drakkar group experiment report GDRI-DRAKKAR-2014-03-19*, LGGE-Grenoble, LPO, France, 2014.

Mullarney, J. C., A. E. Hay, and A. J. Bowen, Resonant modulation of the flow in a tidal channel, *J. Geophys. Res.*, *113*, 2008.

Müller, M., J. Y. Cherniawsky, M. G. G. Foreman, and J.-S. von Storch, Seasonal variation of the M_2 tide, *Ocean Dyn.*, *64*, 2014.

Naimie, C. E., J. W. Loder, and D. R. Lynch, Seasonal variation of the three-dimentional residual circulation on Georges Bank, *J. Geophys. Res.*, *99*, 15967–15989, 1994.

Nutter, P., D. Stensrud, and M. Xue, Effects of coarsely resolved and temporally interpolated lateral boundary conditions on the dispersion of limited-area ensemble forecasts, *Mon. Wea. Rev.*, *132*, 2358–2377, 2004.

Ohashi, K., J. Sheng, K. R. Thompson, C. G. Hannah, and H. Ritchie, Effect of stratfication on the tidal circulation over the Scotian Shelf and Gulf of St. Lawrence: a numerical study using a three-dimentional shelf circulation model, *Ocean Dyn.*, *59*, 809–825, 2009.

Oke, P. R., P. Savok, and S. P. Corney, Impacts of localisation in the EnKF and EnOI: experiments with a small model, *Ocean Dyn*, *57*, 32–45, 2007.

Oke, P. R., G. B. Brassington, D. A. Griffin, and A. Schiller, The Bluelink ocean data assimilation system (BODAS), *Ocean Modell.*, *21*, 46–70, 2008.

Omrani, H., P. Drobinski, and T. Dubos, Spectral nudging in regional climate modelling: how strongly should we nudge?, *Quart. J. Roy. Meteor. Soc.*, *138*, 1808–1813, 2012.

Orlanski, I., A rational subdivision of scales for atmospric processes, *Bull. Amer. Meteor. Soc.*, *56*, 527–530, 1975.

Özgökmen, T. M., E. P. Chassignet, and A. P. Paiva, Impact of wind forcing, bottom topography, and inertia on midlatitude jet seperation in a quasigeostrophic model, *J. Phys. Oceanogr.*, *27*, 2460–2476, 1997.

Pedlosky, J., *Geophysical Fluid Dynamics*, Springer-Verlak, New York, 1987.

Petrie, B., B. J. Topliss, and D. G. Wright, Coastal upwelling and eddy development off Nova Scotia, *J. Geophys. Res.*, *29*, 12979–12991, 1987.

Prandle, D., The vertical structure of tidal currents and other oscillatory flows, *Cont. Shelf Res*, *1*, 191–207, 1982.

Richardson, L. F., *Weather prediction by numerical processes*, Cambridge University Press, 1922.

Rinke, A., P. Marbaix, and K. Dethloff, Internal variability in Arctic regional climate simulations: case study of SHEBA year, *Climate Res.*, *27*, 197–209, 2004.

Rockel, B., C. L. Castro, R. A. S. Pielke, H. von Storch, and G. Leoncini, Dynamical downscaling: assesment of model system dependent retained and added variability for two different regional climate models, *J. Geophys. Res.*, *113*, D21107, 2008.

Saha, S., S. Moorthi, H.-L. Pan, X. Wu, J. Wang, S. Nadiqa, P. Trpp, R. Kistler, J. Woollen, D. Behringer, H. Liu, D. Stokes, R. Grumbine, G. Cayno, J. Wang, Y.-T. Hou, H.-Y. Chuang, H.-M. H. Juang, J. Sela, M. Iredell, R. Treadon, D. Kleist, P. V. Delst, D. Keyser, J. Derber, M. Ek, H. W. J. Meng, R. Yang, S. Lord, H. V. D. Dool, A. Kumar, W. Wang, C. Long, M. Chelliah, Y. Xue, B. Huang, J.-K. Schemm, W. Ebisuzaki, R. Lin, P. Xie, M. Chen, W. H. S. Zhou, C.-Z. Zou, Q. Liu, Y. Chen, Y. Han, L. Cucurull, R. W. Reynolds, G. Rutledge, and M. Goldberg, The NCEP climate forecast system reanalysis, *Bull. Amer. Meteor. Soc.*, *91*, 1015–1057, 2010.

Sandstrom, H., and J. A. Elliott, Production, transformation and dissipation of energy in internal tides near the continental shelf edge, *J. Geophys. Res.*, *116*, 2011.

Semtner, A. J., Modeling ocean circulation, *Science*, *269*, 1379–1385, 1995.

Shan, S., J. Sheng, and B. J. W. Greenan, Physical processes affecting circulation and hydrography in the Sable Gully of Nova Scotia, *Deep Sea Res. II*, *104*, 35–50, 2014.

Simpson, J. H., and J. R. Hunter, Fronts in the Irish Sea, *Nature*, *250*, 404–406, 1974.

Smedstad, O. M., H. E. Hurlburt, E. J. Metzger, R. C. Rhodes, J. F. Shriver, A. J. Wallcraft, and A. B. Kara, An operational eddy-resolving 1/16° global ocean nowcast/forecast system, *J. Mar. Syst.*, *40-41*, 341–361, 2003.

Smith, P. C., The mean and seasonal circulation off southwest Nova Scotian, *J. Phys. Oceanogr*, *13*, 1034–1054, 1983.

Smith, P. C., and F. B. Schwing, Mean circulation and variability on the eastern Canadian continental shelf, *Cont. Shelf Res.*, *11*, 977–1012, 1991.

Smith, P. C., B. Petrie, and C. R. Mann, Circulation, variability, and dynamics of the Scotian Shelf Slope, *J. Fish. Res. Board of Can.*, *35*, 1067–1083, 1978.

Staniforth, A., Regional modelling: a theoretical discussion, *Meteor. Atmos. Phys.*, *63*, 15–29, 1997.

Sun, C., M. Feng, R. J. Matear, M. A. Chamberlain, P. Craig, K. R. Ridgway, and A. Schiller, Marine downscaling of a future climate scenario for Australias Boundary Currents, *J. Climate*, *25*, 2947–2962, 2012.

Thompson, K. R., and E. Demirov, Skewness of sea level variability of the world's oceans, *J. Geophys. Res.*, *111*, C5, 2006.

Thompson, K. R., D. G. Wright, Y. Lu, and E. Demirov, A simple method for reducing seasonal bias and drift in eddy resolving ocean models, *Ocean Modell.*, *13*, 109–125, 2006.

Urrego-Blanco, J., and J. Sheng, Study on subtidal circulation and variability in the Gulf of St. Lawrence, Scotian Shelf, and Gulf of Maine using a nested-grid shelf circulation model, *Ocean Dyn.*, *64*, 385–412, 2014.

Urrego-Blanco, J. R., Subtidal circulation, hydrography, sea ice and associated variability over the eastern Canadian Shelf using a coupled ocean-ice model, *Doctoral thesis, Dalhousie University*, 2014.

Vallis, G. K., *Atmospheric and Oceanic Fluid Dynamics*, Cambridge University Press, 2006.

von Storch, H., H. Langenberg, and F. Feser, A spectral nudging technique for dynamical downscaling purposes, *Mon. Wea. Rev.*, *128*, 3664–3673, 2000.

Waldron, K. M., J. Peagle, and J. D. Horel, Sensitivity of a spectral filtered and nudged limited-area model to outer model options, *Mon. Wea. Rev.*, *124*, 529–547, 1996.

Wikle, C. K., and L. M. Berliner, A Bayesian tutorial for data assimilation, *Physica D: Nonlinear phenomena*, *230*, 1–16, 2007.

Wilby, R. L., and T. M. L. Wigley, Downscaling general circulation model output: a review of methods and limitations, *Prog. Phys. Geogr.*, *21*, 530–548, 1997.

Wunsch, C., Internal tides in the ocean, *Rev. Geophys. and Space Phys.*, *13*, 167–182, 1975.